

---

**Geophysical and Geoscientific Investigations in the  
Ejina Basin, Inner Mongolia, NW China  
with Focus on  
Processing of TEM-Data in the Wavelet Domain  
and on 2D Modeling**

---

VORGELEGT VON  
DIPLOM-GEOPHYSIKER  
**SEBASTIAN HÖLZ**  
AUS BERLIN

VON DER FAKULTÄT VI - PLANEN BAUEN UMWELT  
DER TECHNISCHEN UNIVERSITÄT BERLIN  
ZUR ERLANGUNG DES AKADEMISCHEN GRADES  
DOKTOR DER NATURWISSENSCHAFTEN  
(DR. RER. NAT.)  
GENEHMIGTE DISSERTATION

BERLIN, AUGUST 2007

Promotionsausschuss:

Prüfungsvorsitzender	Prof. Dr. W. Dominick
1. Gutachter:	Prof. Dr. H. Burkhardt
2. Gutachter:	Prof. Dr. P. Weidelt

Datum der Disputation:	19.7.2007
------------------------	-----------

# Table of Contents

<b>Abstract</b>	<b>3</b>
<b>Zusammenfassung</b>	<b>5</b>
<b>1 Introduction</b>	<b>7</b>
<b>2 Theory &amp; Methods</b>	<b>9</b>
2.1 TEM - General Introduction.....	9
2.2 1D Modeling & Inversion.....	11
2.2.1 Extension of 1D Modeling Code .....	13
2.2.2 1D Inversion.....	18
2.3 2.5D Modeling - TEMDDD .....	22
2.3.1 TEMDDD - General Description.....	24
2.3.2 Numerical Testing .....	26
2.3.3 2D - Model Generator .....	29
2.3.4 Parallelization.....	32
2.3.5 2.5D Model Study .....	34
2.4 Processing of TEM Signals in the Wavelet Domain.....	38
2.4.1 Common Processing Techniques for TEM Signals .....	38
2.4.2 Wavelet Transformation - General Concept .....	41
2.4.3 TEM Signals in the Wavelet Domain .....	49
2.4.4 Filtering in the Wavelet Domain.....	53
2.4.5 Examples .....	59
<b>3 Regional Geology &amp; Tectonical Framework</b>	<b>63</b>
3.1 Regional Geology of Central Asia .....	63
3.1.1 Tectonic Evolution.....	64
3.1.2 Stratigraphy & Plutonism .....	68
3.2 The Ejina Basin .....	69
3.2.1 Tectonical Framework, Topography and Seismicity .....	69
3.2.2 Previous Geophysical Studies .....	72
<b>4 Results of Geophysical &amp; Geoscientific Investigations</b>	<b>73</b>
4.1 Ejina Basin .....	74
4.1.1 General Overview of Satellite Data.....	74
4.1.2 Satellite Image Interpretation.....	76
4.2 Jingsutu Structure & Pluton.....	80
4.2.1 Satellite Image Interpretation & Geology .....	81
4.2.2 Petrology.....	84
4.2.3 Geophysics .....	95
4.2.4 Interpretation.....	102
4.3 Gurinai Structure .....	111
4.3.1 Geophysics .....	112

4.3.2 Interpretation .....	116
4.4 Conclusion.....	117
<b>Acknowledgement</b>	<b>119</b>
<b>References</b>	<b>121</b>
<b>Appendix A</b>	
<b>LAPTEM - Specifications &amp; Modifications</b>	<b>133</b>
A.1 General Mode of Operation .....	133
A.1.1 Control Software.....	134
A.1.2 Port Logic .....	136
A.2 Specification Receiver .....	138
A.2.1 Offset.....	138
A.2.2 Precision of Time Scale.....	139
A.2.3 Frequency Response .....	140
A.3 Specification Transmitter .....	142
A.3.1 Current Measurement .....	142
A.3.2 Ramp Time.....	144
A.3.3 Turn-On Time .....	145
A.4 Calibration Measurements in Århus, Denmark.....	146
A.5 Summary - LAPTEM.....	147
A.6 List of Laboratory Instruments for Calibration.....	148
<b>Appendix B</b>	
<b>Coefficient Bands in the Wavelet Domain</b>	<b>149</b>
<b>Appendix C</b>	
<b>Data Fits &amp; Additional Inversion Results</b>	<b>163</b>
C.1 Jingsutu Structure.....	163
C.2 Gurinai Structure .....	166
<b>Curriculum Vitae &amp; List of Publications</b>	<b>171</b>



## Abstract

This dissertation deals with the processing and interpretation of TEM data, which was measured in a basin structure in NW China. The work was conducted within a DFG-project in collaboration with other geoscientific work groups. Besides the analysis of geophysical data within a conductivity model of the subsurface, other important goals were the classification of results in a broader geological framework as well as the classification of results in the subgoal of the DFG-project, i.e. examination of the tectonics of the basin structure. For this, in addition to the geophysical work, petrological and remote sensing related investigations were conducted.

In the course of data preparation, theoretical considerations regarding the characterization of TEM signals in the wavelet domain were made. They led to the design of a novel noise prediction filter in the wavelet domain. With this filter, a simultaneous elimination of several harmonic noise frequencies from a signal can be achieved. It was demonstrated, that this filter has a certain tolerance to non-stationarity in the harmonic noise.

With the newly developed approaches, an improvement of processed data could be achieved for some data-sets from NW China, but since the geophysical work areas are located in non-populated regions with a generally very low noise level, the processing did not lead to significant improvements for most of the data-sets when compared to the common processing techniques.

Since the analysis of TEM-data should not be restricted to 1D Inversion only, the 3D modeling program TEMDDD was tested within a model study. It could be demonstrated that the program is suitable for the computation of transient data for the coincident loop configuration. In the course of this model study, the creation of input models for the program turned out to be a time-consuming factor, just as well as the still relatively high time need for the 3D modeling itself. Therefore, a tool for the rapid generation of TEMDDD input files for arbitrary 2D block models and a parallelization in terms of the automatic distribution of computations over networks were developed to facilitate the 2.5D modeling of data from NW China.

In the analysis of remote sensing data prior to fieldwork a hypothetical, about 130 km long, NS-striking, tectonical axis was identified along the eastern margin of the Ejina Basin. The two work areas, where geophysical investigations were carried out, are situated at the northern (Jingsutu Structure) and southern (Gurinaï Structure) end of this axis.

In the northern part, the axis is ending in the basement, where the Jingsutu Structure is developed as a NNE-striking, sediment-filled depression. Apart from the geophysical investigations, additional petrological investigations were carried out. In the interpretation of TEM data, the 1D inversion models as well as the model from 2.5D modeling show highly conductive units with thicknesses of at least 350 m in the central part of the structure. These units are interpreted in conjunction with geological maps as Late Jurassic and Quaternary sediments.

Because of the distinct conductivity contrasts at the eastern and particularly at the western margin of the structure, normal faults were interpreted there and the structure was referred to as a graben. On the basis of Ka/Ar-datings of samples from the nearby Jingsutu Pluton, it is assumed, that the structure's main formation phase can be attributed to Early Jurassic extensional movements, which can be traced all over NW China.

The central and southern part of the postulated tectonic axis are formed by the Gurinai Structure. At the southern margin of this structure, the second work area is located. It is largely covered by Quaternary and Holocene sediments. In addition to conclusions about the hydrology of the work area, which can be drawn from 1D inversion models of the TEM, special interest was put on the outcome of the 1D joint inversion of MT-, TEM- and DC-data. The associated section of 1D models shows a pronounced trough-like increase of thicknesses of Holocene and Prequaternary sediments in the western part of the structure. By means of a strike analysis of MT data, which is not in the scope of this thesis, a NS-striking of this trough-like structure was interpreted. On the basis of these results, the interpretation of SRTM data and because of the similar geometric forming, it is seen in direct connection with the Jingsutu Structure and thus, counts as evidence for the actual existence of the postulated NS-striking tectonic axis, which links the western margin of the Gurinai Structure with the western margin of the Jingsutu Structure. The fact, that the tectonic axis in the range of the Gurinai Structure is morphologically evident in the Quaternary/Holocene sediments - visible in the SRTM data - is considered as an evidence for neotectonic activity.

In the central array of the Ejina Basin, other lineaments were analyzed by means of SRTM data. These additionally indicate, that parts of the basin were tectonically influenced in Late Quaternary times.

## Zusammenfassung

Die vorliegende Arbeit beschäftigt sich mit der Aufbereitung und Interpretation von TEM-Daten, die in einer Beckenstruktur in NW China gemessen wurden. Die Arbeiten wurden im Rahmen eines DFG-Bündelprojektes in Zusammenarbeit mit anderen geowissenschaftlichen Fachrichtungen durchgeführt. Neben der reinen Analyse der geophysikalischen Daten im Rahmen eines Leitfähigkeitsmodells des Untergrundes, war auch die Einordnung der erzielten Ergebnisse in den größeren geologischen Rahmen sowie die Einordnung in das übergeordnete Teilziel des DFG-Bündelprojektes (tektonischer Aufbau der Beckenstruktur) von Bedeutung. Hierzu wurden neben den geophysikalischen Messungen auch petrologische sowie fernerkundliche Untersuchungen durchgeführt.

Im Zuge der Datenaufbereitung wurden theoretische Überlegungen zur Charakterisierung von TEM-Signalen im Waveletbereich angestellt. Diese ergaben u.a. ein neuartiges "noise prediction filter" im Waveletbereich, das die gleichzeitige Eliminierung mehrerer harmonischer Störfrequenzen ermöglicht. Es konnte gezeigt werden, daß dieses Filter eine gewisse Toleranz gegenüber nicht-stationären Einflüssen im harmonischen Rauschen hat.

Mit den neu entwickelten Ansätzen konnten während der Bearbeitung der Meßdaten aus NW China in einigen Fällen Verbesserungen erzielt werden. Da die geophysikalischen Arbeitsgebiete aber in nicht besiedeltem Raum lagen, wurden aufgrund des hier generell sehr geringen Rauschpegels für die meisten Datensätze keine signifikanten Änderungen gegenüber der bisherigen Prozessierung festgestellt.

Da die Datenauswertung nicht nur auf die reine 1D Modellierung von TEM Daten und die 1D-Joint Inversion von TEM-, MT-, und DC-Daten beschränkt werden sollte, wurde das 3D Modellierungsprogramm TEMDDD im Rahmen einer Modellstudie getestet. Es konnte gezeigt werden, daß das Programm zur Berechnung transienter Daten für die koinzidente Spulenordnung geeignet ist. Hierbei erwies sich - neben dem immer noch grossen Zeitbedarf für die Berechnung eines 3D Untergrundmodells - die Erstellung von Eingabemodellen für das Programm als zeitintensiver Faktor. Darum wurden zur Vorbereitung der Datenmodellierung der Meßdaten aus NW China mit dem Programm TEMDDD Werkzeuge entwickelt, die eine einfache Generierung von 2D Untergrundmodellen und die Verteilung von Berechnungen über Computernetzwerke erlauben.

Aufgrund fernerkundlicher Analysen im Vorfeld der Geländearbeiten, wurde entlang des östlichen Randes des Ejina Beckens eine hypothetische, ca. 130 km lange, NS-streichende tektonische Achse ausgewiesen. Die beiden Arbeitsgebiete befinden sich im nördlichen (Jingsutu Struktur), bzw. südlichen (Gurinaï Struktur) Endbereich der Achse.

Im nördlichen Bereich endet diese Achse im Basement, wo die Jingsutu Struktur eine NNE-streichende, sedimentgefüllte Depression ausbildet. Diese Struktur wurde außer mit geophysikalischen Methoden zudem petrologisch untersucht. Die 1D Inversionsmodelle sowie das Modell der 2.5D Modellierung weisen im Zentralbereich der Struktur niederohmige Einheiten mit einer Mächtigkeit von mind. 350 m aus, die in Verbindung mit geologischen Karten als spätjurassische und quartäre Sedimente interpretiert wurden. Aufgrund der scharfen Leitfähigkeitskontraste am östlichen und insbesondere am westlichen Rand der Struktur wurden dort Abschiebungen interpretiert und die Struktur als Graben angesehen. Anhand von Ka/Ar-Datierungen im nahegelegenen Jingsutu-Pluton wird vermutet, daß die Hauptbildungsphase der Struktur auf frühjurassische Extensionsbewegungen zurückzuführen ist, die in Gesamt - NW China nachgewiesen sind.

Der zentrale und südliche Bereich der postulierten tektonischen Achse wird durch die Gurinaï Struktur gebildet. An deren südlichem Ende liegt das zweite Arbeitsgebiet, das im wesentlichen durch quartäre und holozäne Sedimente geprägt ist. Neben Rückschlüssen auf die Hydrologie des Arbeitsgebietes, die aus den 1D Inversionsmodellen der TEM gezogen werden können, ist im Rahmen dieser Arbeit insbesondere das Ergebnis der 1D Joint Inversion von MT-, TEM- und DC-Daten von Interesse. Die zugehörige Sektion von 1D Modellen zeigt zum westlichen Bereich der Struktur hin einen starken trogförmigen Mächtigkeitsanstieg der holozänen und präquartären Sedimente. Anhand der Streichwinkelanalyse von MT-Daten, die nicht Bestandteil dieser Arbeit ist, wurde ein NS-Streichen dieser trogförmigen Struktur interpretiert. Aufgrund dieser Ergebnisse, der Interpretation von SRTM-Daten sowie der ähnlichen geometrischen Ausprägung, wird sie im direkten Zusammenhang mit der Jingsutu Struktur gesehen und gilt demnach als Beleg für die Existenz der postulierten NS-streichenden tektonischen Achse, die den westlichen Rand der Gurinaï Struktur mit dem westlichen Rand der Jingsutu Struktur verbindet. Die Tatsache, daß sich die tektonische Achse im Bereich der Gurinaï Struktur durch die quartären und holozänen Sedimente hindurch morphologisch ausprägt (sichtbar in den SRTM-Höhendaten), wird als Beleg für eine hier mögliche neotektonische Aktivität gesehen.

Im Zentralbereich des Beckens wurden weitere lineamentartige Strukturen mit Hilfe von SRTM-Daten untersucht. Auch diese deuten darauf hin, daß Teilbereiche des Ejina Beckens spätquartär tektonisch beeinflusst worden sind.

# 1 Introduction

In the years 2000-2004 a multidisciplinary geoscientific investigation was carried out in the Ejina Basin, Inner Mongolia, NW China. The project's general geoscientific objective was focused on the study of basin sediments, which are composed of lacustrine alluvial fan deposits from the drainage system of the river Ruoshui, in order to reconstruct the paleoclimatic environmental changes. The endorheic, intracontinental basin was chosen as the target for investigations, because it contains a substantial Quaternary sedimentary record and, as part of the Alashan Plateau, was assumed to be tectonically stable (e.g. WANG ET AL., 1997; WÜNNEMANN & HARTMANN, 2002). Although tectonic stability of the basin was originally assumed, recent publications demonstrate an influence of neotectonic deformation processes on the sedimentation within the basin (e.g. HARTMANN, 2003; WANG ET AL., 2004). Therefore, it was important to get a basic understanding of the tectonic setting of the basin to be able to distinguish between changes in the sedimentation environment induced by climatic changes and those caused by the tectonic activity within the basin.

To contribute to the general geoscientific objective, the specific task of the geophysical workgroup was the characterization of the physical properties, distribution, and thicknesses of sediments and the underlying crystalline basement in the basin. A combination of three electromagnetic methods (transient electromagnetics, magnetotellurics, geoelectrics) was used to gain information about the distribution of the subsurface electric resistivity.

Work areas for the geophysical investigation were chosen following the visual inspection of satellite images. They are located in the eastern part of the Ejina Basin, NW China, where several distinct geomorphological features together form an approximately 130 km long, hypothetical, N-S striking tectonical axis. In the scope of this thesis, results from the evaluation of transient electromagnetic (TEM) data from two of these work areas are presented. These are the work area in the Jingsutu Structure (chap. 4.2) and the work area in the Gurinai Structure (chap. 4.3). They are located at the northern end southern end of the hypothetical tectonical axis, respectively.

TEM measurements, which were conducted along several profile lines in the two work areas, were carried out in the coincident loop configuration with a loop size of 100x100 m<sup>2</sup>, which - under ideal conditions - allows an interpretation of the data in terms of the subsurface

resistivity structure down to a depth of at maximum 400 m. In comparison to the extension of the hypothetical tectonical axis it was therefore necessary to obtain additional information to achieve more than local interpretations of TEM data.

From a geophysical viewpoint this is achieved by the joint interpretation and 1D joint inversion (chap. 4.3.2) of TEM data and magnetotelluric (MT) data, which was acquired in the same work areas (BECKEN, 2005). In terms of the geoscientific objective, additional petrological investigations (chap. 4.2.2) and the evaluation of remote sensing data (chap. 4.1.2 & chap. 4.1.2) were needed to integrate the results of the TEM investigations into the general geological framework.

All TEM measurements in China were carried out with the LAPTEM acquisition system. Since little information about this device was available and the quality of the measuring apparatus was put into question in the course of a discussion between Panaitov and Spies (chap. 2.2.1), it was necessary to go further into this matter. These questions are dealt with in the appendix. Furthermore in terms of data quality and -processing, theoretical considerations regarding attributes of TEM signals in the wavelet domain were made (chap. 2.4.2).

In the course of the project, K. Árnason granted permission to use his 3D modeling code TEMDDD. Prior to the analysis of the measured TEM data, the question of numeric stability of the program was raised, which is dealt with in chap. 2.3.2 and chap. 2.3.5. During the performed modeling, the creation of input files for TEMDDD at more complicated underground models turned out to be a time-consuming factor in addition to the relatively high time need for the computations. Therefore, it was indispensable for the analysis of real data to speed up these processes. This was achieved by programming a model generator with an appropriate user interface (chap. 2.3.3) and the parallelization of computations over a message passing interface (chap. 2.3.4).

## 2 Theory & Methods

In this chapter, bold type small and bold type capital characters in formulas refer to vectors and matrices, respectively. All regular type characters in formulas refer to scalar quantities.

### 2.1 TEM - General Introduction

The transient electromagnetic (TEM) method is a well established geophysical method, which is used to investigate the distribution of the electrical conductivity in the underground. Since the method measures the secondary fields of actively induced current systems, it is inherently sensitive to good conductors<sup>1</sup>. Therefore, the method is frequently applied in situations, where the investigated geological target is associated with spatial variations of the conductivity. Amongst others, examples from literature for the application of TEM can be found for mineral exploration (e.g. WEBB & ROWSTON, 1995), where e.g. sulfides or ore bodies contrast with the surrounding basement, or for hydrogeological studies (e.g. DANIELSEN ET AL., 2003), where groundwater and the confining aquifers are the target of investigation.

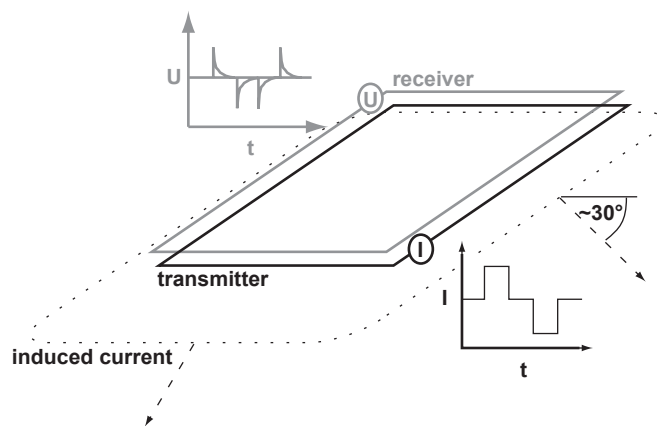


Fig. 2-1: TEM coincident loop configuration. Transmitter- and receiver-signals are further explained in Fig. 2-6.

Various measurement configurations exist for the TEM method, which can roughly be distinguished with respect to the deployment of the measurement system (ground-based or airborne), the coupling of the transmitter to the ground (inductive or galvanic), the type of receiver (coil, SQUID<sup>2</sup> or electrodes) and the positioning of the receiver with respect to the transmitter (coincident, separate, inloop, bore-hole). This thesis focuses on an inductively coupled, ground-based system,

where transmitter and receiver are realized by coincident loops (Fig. 2-1).

1. In the following terms like "conductor", "resistor" and alike always refer to "electrical conductor" and "electrical resistor", respectively.

2. Superconductive Quantum Interference Device.

Such TEM systems usually use a bipolar waveform to generate a current in the transmitter loop (Fig. 2-1, lower right), which excites a quasi static primary magnetic field while being turned on. Based on Faraday's law of induction, the current switch-off in the transmitter and, thus, the breakdown of the associated primary magnetic field, induces eddy-currents in the conductive underground. The strength and geometry of these eddy-currents depends on the spatial distribution of the conductivity in the underground. Thus, the secondary magnetic field associated with the eddy-currents carries information about the underground and is the measured quantity<sup>1</sup> (Fig. 2-1, upper left).

Due to the quasi infinite contrast in conductivity between the air and the underground, the induced electric fields only have horizontal components (NABIGHIAN & MACNAE, 1991), i.e. the induced electric field is tangential to the surface of the underground. Therefore, the induction due to the coupling of a magnetic source to the underground is often referred to as tangential electric<sup>2</sup> or TE-mode (e.g. WARD & HOHMANN, 1987).

In the instant of the current shut-off in the transmitter loop, the induced current system in the underground is mostly confined to the position of the transmitter loop (WEIDELT, 2000). With progressing time, the current system quickly diffuses down and outward with respect to the transmitter loop. Consequently, the measured signal in the TEM receiver coil drops rapidly in amplitude (Fig. 2-1, upper left). NABIGHIAN (1979) introduced the illustrative concept of "smoke rings" to describe the diffusion of the current systems in a homogeneous half-space. In Fig. 2-2 slices of these "smoke rings" (only right half) are depicted for progressing times as contour plots. It can be seen that the maximum of the current density travels down and outward at an angle of  $\sim 30^\circ$  with respect to the transmitter at the surface (Fig. 2-1 & Fig. 2-2).

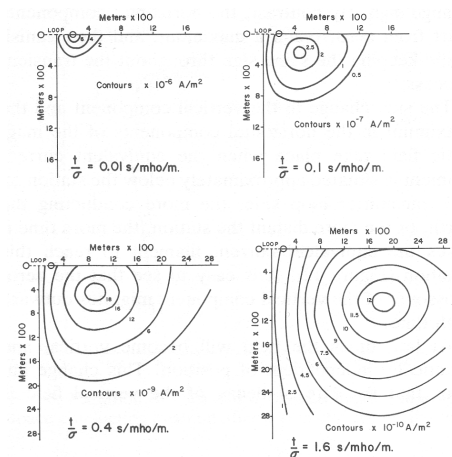


*Fig. 2-2: Current densities in a homogeneous halfspace for progressing times after the current shut-off (from NABIGHIAN & MACNAE, 1991).*

The operating expense for the deployment of a coincident loop system strongly depends on the size of the loop. For 100x100m<sup>2</sup> loops - like the ones which were used for measurements in China - the time need for the assembly or moving of loops from one measurement station to the next is considerable. Therefore, measurements under such conditions are frequently carried out along profile lines, which cross the geological target under investigation perpendicular to

1. Note that in common TEM systems, where a coil is used as receiver, the actually measured physical quantity is the time derivative of the magnetic field. The direct measurement of the magnetic field can be achieved by using a SQUID.
2. Alternatively, the term "transverse electric", which relates the fields to the surface normal, is also used.



the assumed geoelectric strike direction. Due to logistical considerations, a further consolidation of measurements, which would yield an areal coverage, can usually only be achieved selectively. Consequently, TEM measurements, which were conducted during field work in China, were carried out almost exclusively along profile lines perpendicular to the strike of the investigated geological structures.

## 2.2 1D Modeling & Inversion

The general theory for the TEM response of a layered halfspace is well established and can be found e.g. in WARD & HOHMANN (1987). For the coincident loop configuration the induced, normalized voltage  $V_{norm}$  into a circular loop (radius  $r$ , Area  $A$ , transmitter current  $I$ ) on the surface ( $z=0$ ) over a layered halfspace with the reflection coefficient  $r_{TE}$  (TE-mode) is given by:

$$V_{norm}(\omega, r) = \frac{V(\omega, r)}{IA} = -i\omega\mu_0 \int_0^\infty \lambda(1 + r_{TE}(\lambda))J_1^2(\lambda r)d\lambda \quad 2-1$$

In the above formula,  $\mu_0$  and  $J_1$  are the magnetic permeability of free space and a Bessel-function of the first kind, respectively. The normalization of the induced voltage to the magnetic moment of the transmitter ( $IA$ ) facilitates the comparability of measurements with different loop sizes. In the following, voltages are implicitly assumed to be normalized to the magnetic moment, if not stated otherwise, and the respective subscript will be dropped.

Generally, integrals of the form

$$g(r) = \int_0^\infty \lambda f(\lambda) J_\nu(\lambda r) d\lambda \quad 2-2$$

can be evaluated efficiently using Hankel transform filters (JOHANSEN & SØRENSEN, 1979; CHRISTENSEN, 1990). To calculate 2-1, WEIDELT (1984) used a generalized Hankel transform filter in the modeling code *TEMIDmod* and in the inversion code *TEMIDinv*. Additionally, he showed that the transformation of 2-1 from the frequency into the time domain can also be formulated in terms of a Fast Hankel Transformation. Thus, the transformation of 2-1 from the frequency-wavenumber domain into the time-space domain involves two Hankel transforms with suitable transform filters.

Generally, no analytical solutions exist for the calculation of transient signals for a coincident loop. However, at sufficiently late times the coincident loop response converges towards the response of the inloop configuration<sup>1</sup>, for which analytical solutions exist for homogeneous

---

1. In the inloop configuration the receiver is realized by a small coil, which is located at the center of the transmitter loop.

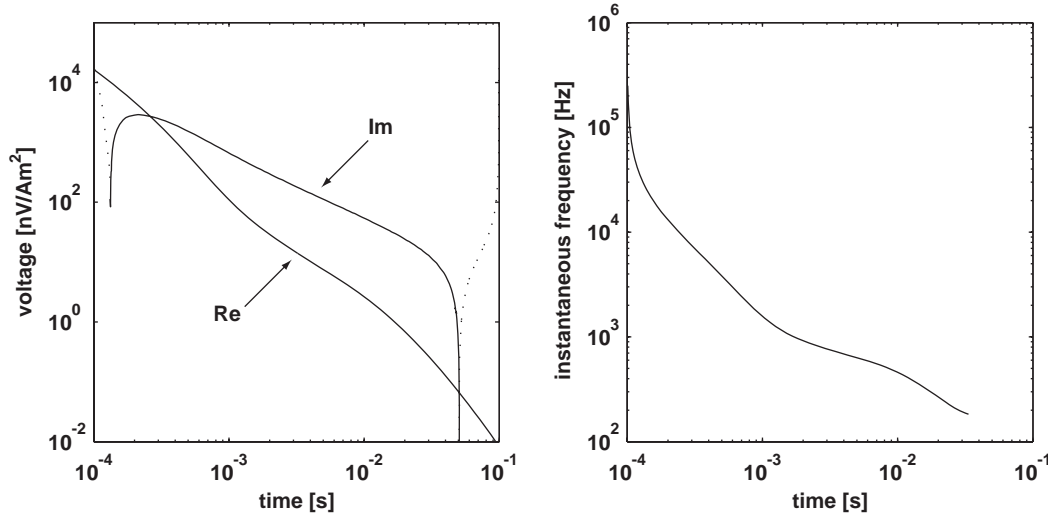


Fig. 2-3: Analytical signal constructed by the Hilbert transformation of an arbitrary transient (left, dotted line = negative values). The analytical signal is used to define an instantaneous frequency (right) as time derivative of the phase (HANSTEIN, 1996).

halfspaces (WARD & HOHMANN, 1987). Consequently, the transient response measured with a coincident loop system - i.e. the time derivative of the vertical magnetic field - over a homogeneous halfspace exhibits a decay  $\sim t^{-5/2}$  at late times.

Certain aspects of such transient signals can be investigated by an approach described by HANSTEIN (1996). To estimate the frequency contents of a transient signal in the time domain, he uses the Hilbert transformation to construct a complex valued (analytical) signal in the time domain (Fig. 2-3, left). The real part of this function ("Re" in Fig. 2-3) is defined by the transient, here modeled for an arbitrary 1D underground model and the coincident loop configuration. The imaginary part ("Im" in Fig. 2-3), which is calculated by the Hilbert transformation, has the same amplitude characteristic as the transient, but a phase shifted by  $\pi/2$ . The so constructed analytical signal defines an instantaneous phase, which can be used to calculate an instantaneous frequency as its time derivative (Fig. 2-3, right, comp. 2-3). The instantaneous frequency calculated from the transient signal clarifies that early times in a transient are dominated by high frequencies, whereas at late times low frequencies prevail.

The original modeling code *TEMIDmod* was extended to account for receiver- and transmitter-effects (chap. 2.2.1), which may significantly influence TEM measurements. Due to the complicated program structure, the forward code within *TEMIDinv* was not changed and work on this inversion code was not pursued. Instead, the extended modeling code *TEMIDmod* was combined with the external optimization routine *lsqnonlin* of the MATLAB Optimization Toolbox (MATHWORKS, 2006). Using this combination, receiver- and transmitter effects may now be considered in the inversion of data and several sets of data with distinct receiver- or transmitter-configurations can be inverted simultaneously (chap. 2.2.2).

Furthermore, the use of an external optimization routine also greatly facilitated the creation of a smooth inversion algorithm and the coding of an 1D joint inversion algorithm, which can be used to jointly invert any combination of TEM-, MT- and DC-data (chap. 2.2.2). The new inversion algorithm will be referred to as *EMIDinv*.

### 2.2.1 Extension of 1D Modeling Code

#### Influence of Lowpass-Filters on TEM-Signals

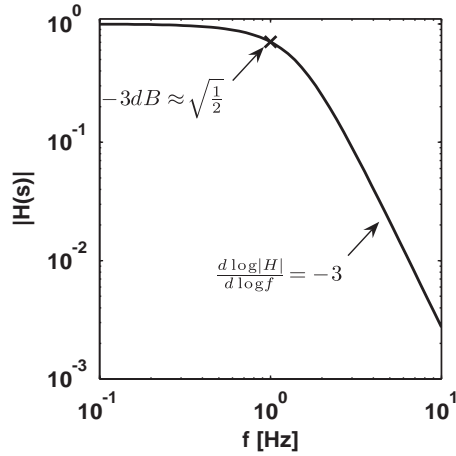


Fig. 2-4: Magnitude response of a Bessel filter (3<sup>rd</sup> order,  $f_c=1\text{Hz}$ ), calculated with 2-6.

To avoid aliasing effects, the bandwidth of most TEM-systems is limited by analog lowpass-filters, which have a corner frequency adjusted to the Nyquist-frequency, i.e. half the sampling frequency. Depending on the type of filter, this band-limitation may lead to significant distortions of transients at early times, especially for measurements over undergrounds with high resistivities at shallow depths (EFFERSØ ET AL., 1999; AUKEN ET AL., 2000).

In the LAPTEM device, two different Nyquist-filters are implemented. They are designed as Bessel lowpass-filters with cutoff frequencies of about 10kHz and 50kHz for the old and new configuration, respectively (s. Appendix, p. 140). Generally, on a logarithmic

scale Bessel filters exhibit a decay proportional to the filter order in the attenuation band and a nearly constant amplification and linear phase in the pass band (Fig. 2-4). Because of the phase-linearity for frequencies below the corner frequency, they are characterized by a constant group delay across the passband, which leads to a constant time delay for frequencies below the corner frequency (BUTTKUS, 1991). Generally, the group delay of filters with phase characteristic  $\phi(\omega)$  is given by:

$$dt = -\frac{d\phi}{d\omega} \quad 2-3$$

Therefore, the constant delay for frequencies in the pass band of a Bessel filter can simply be calculated by evaluating 2-3 as finite difference for two arbitrary frequencies well below the corner frequency. Thus, the influence of a Bessel filter on TEM-measurements can be approximated by simply shifting the time base of a transient:

$$t \rightarrow t + dt \quad 2-4$$

Alternatively, the influence of the filter can also be evaluated directly by multiplication of the transfer functions of filter and underground (2-1 & 2-6) in the frequency domain (multiplication theorem) prior to the transformation into the time domain (EFFERSØ ET AL., 1999):

$$V_{\text{flt}}(\omega) = H(\omega) V(\omega) \quad 2-5$$

The complex transfer function of Bessel filters up to the order  $N=10$  (excluding gain) can be calculated according to a second-order sections representation by TIETZE & SCHENK (1985):

$$H\left(i\frac{\omega}{\omega_c}\right) = H(s_c) = \prod_{i=1}^{\lceil N/2 \rceil} \frac{1}{1 + a_i s_c + b_i s_c^2} \quad 2-6$$

Using their coefficients (s. Appendix, p. 140), the attenuation for a gainless filter is -3dB at the corner frequency for all filter orders (Fig. 2-4).

An exemplary calculation is used to clarify the influence of a Bessel filter for the model transient of a homogeneous halfspace (Fig. 2-5, black). According to 2-3, the group delay of a 6<sup>th</sup> order Bessel filter with a corner frequency of 13kHz, similar to the one used in the LAPTEM, is calculated to be about 30 $\mu$ s, consequently shifting the time base by the same amount (Fig. 2-5, dashed).

Due to the constant group delay or synonymous constant time shift for frequencies in the pass band, the distortion of the transient is especially significant at early times. The estimation of the filter's influence in the frequency domain (Fig. 2-5, dotted) according to 2-5 & 2-6 leads to a similar time shift and for times sufficiently larger than  $1/f_c$  the two methods are essentially equal. For times around  $1/f_c$  the two methods to estimate the filter's influence do not compare well and the second formulation has to be preferred, since it is directly incorporated in the frequency domain.

In conclusion, the effect of Bessel filters in TEM-devices is especially significant at early times and can lead to significant distortions of the measured signal. For times sufficiently larger than  $1/f_c$ , the distortion is determined by a constant time delay and may thus be considered by simply shifting the time base of the measurement. For times around  $1/f_c$  the influence should be modeled by directly including the filter response in the frequency domain.

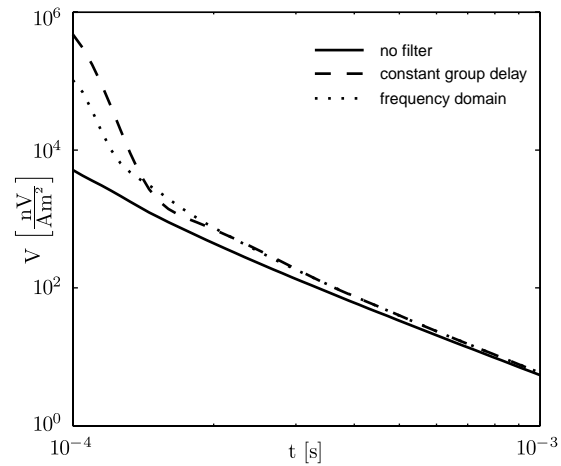


Fig. 2-5: Influence of Bessel filter ( $f_c=13\text{kHz}$ , 6<sup>th</sup> ord.) on TEM-measurement.

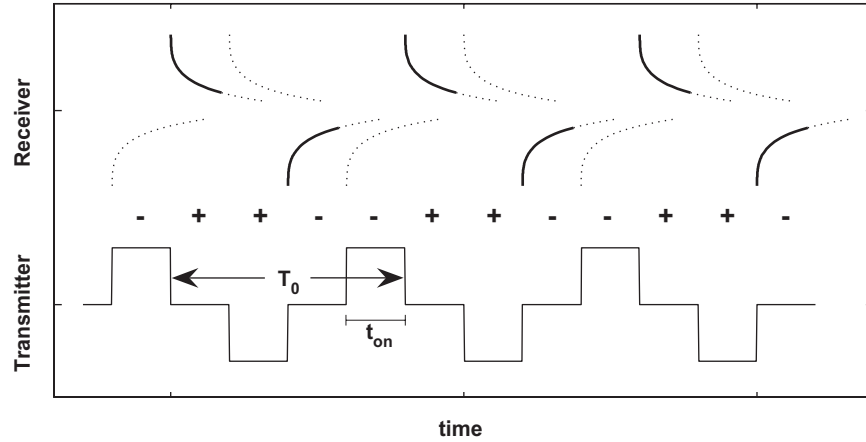


Fig. 2-6: Schematic diagram showing the transmitter current (bottom) with a repetition frequency of  $1/T_0$ . For the depicted bipolar waveform with 50% duty-cycle, which is used in many TEM-devices, the pulse duration is  $t_{on} = 1/4 T_0$ . Measurements are performed, while the transmitter is turned off (top, solid lines). They are superpositions of all previously excited transients as in 2-7.

The Bessel filter was integrated into the modeling code *TEMIDmod* according to the formulation of TIETZE & SCHENK (1985) and was taken into account for the modeling and inversion process of data measured in China.

### Influence of Pulse Duration on TEM-Signals

In real TEM-measurements, the exciting transmitter waveform deviates from the step-function assumed in the formulation of 2-1, thus, leading to distortions of the measured transients. The most pronounced influence of the transmitter waveform on measurements is caused by the finite time (ramp-time), which is needed to shut-off the transmitter current (WEIDELT, 1984). The influence of the ramp-time is especially significant at early times in the transient and needs to be determined precisely for a correct interpretation of data (s. Appendix, p. 144).

In addition to the ramp-time, which was already incorporated in the modeling code and is therefore not considered further in this chapter, the repetitive transmitter waveform can also influence the measured signal (ASTEN, 1987). In a recent controversial discussion, PANAITOV ET AL. (2002, 2004) and KRAUSE ET AL. (2005) see the repetitive transmitter signal as possible cause for sign reversals at late times in their TEM inloop measurements using a SQUID receiver. SPIES (2004) negates their explanation and concludes that the measured sign reversals may be caused by the electronic of the measurement device, external noise sources or by induced polarization. The discussion is of special interest for this thesis, because Panaitov, Krause and colleagues used a LAPTEM device in their measurements. Since measurements in China sometimes exhibited peculiarities comparable to the ones described by Panaitov and colleagues, it will be investigated if these effects are due to the transmitter waveform or are merely caused by the device's electronic.

Generally, the influence of the transmitter's pulse duration on TEM-signals is explained in Fig. 2-6, which clarifies that every switching operation of the transmitter excites a new transient. Consequently, the measured signal is the superposition of all previously excited signals and, according to Fig. 2-6, the true voltage of a transient during the  $n^{\text{th}}$  measurement cycle is calculated by:

$$|V(t)| = \left| \sum_{i=1}^n \{V_{i-1} - V_{i-3/4} - V_{i-1/2} + V_{i-1/4}\} \right|$$

$$V_k = V(t + k \cdot T_0)$$

2-7

$$V_{n-1/2} = V_{n-1/4} = 0, \quad \text{positive transients only}$$

Voltages for coincident or inloop measurements exhibit a monotonic decay, which at late time is proportional to  $\sim t^{-5/2}$  over a homogeneous halfspace. Therefore, the sum in 2-7 quickly converges. For the following calculations, five cycles ( $n=5$ ) are generally sufficient to reach convergence.

KRAUSE ET AL. (2005) show that the influence of the transmitter signal on measurements is especially strong for short pulse durations over underground models with decreasing resistivity towards larger depths. The effect is exemplarily depicted for a homogeneous halfspace and a 2-layer model in Fig. 2-7 for the shortest pulse duration of the LAPTEM ( $t_{\text{on}}=10\text{ms}$ ).

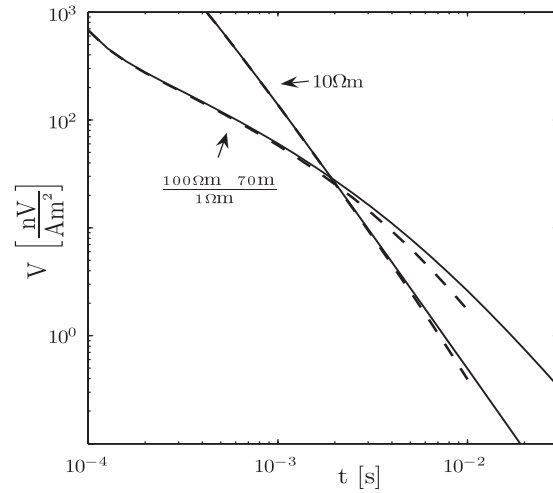


Fig. 2-7: Two exemplary model responses with (dashed) and without (solid) influence of finite duration of transmitter pulses ( $t_{\text{on}}=10\text{ms}$ ).

To estimate the importance of the effect, the deviation between the pure step response  $\mathbf{v}_0$  and the response including the influence of the transmitter's pulse duration  $\mathbf{v}_{\text{ton}}$  is calculated as weighted root mean square (RMS), where only the  $n_d$  samples with detectable voltages ( $>10^{-1}\text{nV/Am}^2$ ) are considered:

$$\text{RMS}_{\delta V} = \left\| \frac{\mathbf{v}_{\text{ton}} - \mathbf{v}_0}{\mathbf{v}_0} \right\| / \sqrt{n_d}$$

2-8

Fig. 2-8 depicts the calculated deviations for various pulse durations and underground models. For homogeneous halfspaces (Fig. 2-8, left) the generally small deviation (s.a. Fig. 2-7) is well below 10% for all pulse durations relevant for the LAPTEM (arrows in

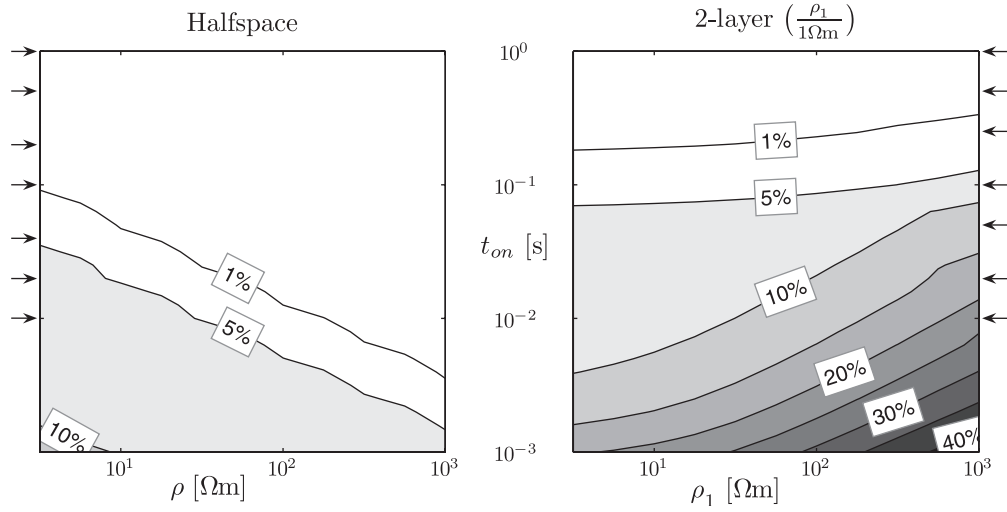


Fig. 2-8: Influence of the finite duration of transmitter pulses (compare Fig. 2-6). Possible pulse durations of the LAPTEM are indicated by arrows. The deviation, calculated according to 2-8, is depicted for homogeneous halfspaces (left) and for 2-layer models (right). For the latter, a maximum deviation was achieved in an optimization by varying the thickness of the resistive top layer ( $\rho_1$ ).

Fig. 2-8). For layered models with a resistive top layer over a conductive halfspace the deviation is generally more pronounced. In the calculations for Fig. 2-8 (right) the deviation is maximized by varying the thickness of the top layer. For pulse durations of 100ms or lower, which were frequently used during field measurements in China, the maximized deviations exceed 5% and may reach values above 20% for models with highly resistive top layers.

In conclusion, the influence of the finite pulse duration of the transmitter signal may be significant, especially for measurements with short pulse durations on undergrounds with a shallow resistive layer. Generally, it can be reduced by increasing the pulse duration, which also leads to an increase for the total acquisition time. The pulse duration was integrated as selectable parameter into the modeling code *TEMIDmod* and was taken into account for the modeling and inversion process of data measured in China.

In terms of the presented results it seems unlikely that the sign reversals described by Panaitov and colleagues are solely due to the transmitter waveform. They see the sign reversals for transmitter pulse durations of 50ms (according to Fig. 4 & 5 in PANAITOV ET AL., 2002), where the maximized error ( $\rightarrow$  Fig. 2-8) is around 10% for a highly resistive top layer. This maximum deviation is far below the deviation needed to cause a sign reversal. Following the argumentation of Spies, it seems more likely that the sign reversals are primarily caused by the devices electronic, external harmonic noise or effects due to induced polarization.

### 2.2.2 1D Inversion

#### 1D Block- & Smooth-Inversion

Generally, a 1D inversion of TEM-data minimizes the misfit between measured data  $\mathbf{d}_{\text{meas}}$  and the calculated model response  $\mathbf{d}_{\text{calc}}$ . The data vector  $\mathbf{d}_{\text{meas}}$  contains the normalized voltages measured at the time gates  $t_i$  ( $i=1, \dots, n_d$ ). Several sets of measured data with different acquisition parameters - e.g. varying ramp times or differing Bessel-filters - may be concatenated to form a single data vector. The model response  $\mathbf{d}_{\text{calc}}$  is calculated using the extended modeling code *TEM1Dmod* (chap. 2.2) for a horizontally layered earth model with the parameter vector  $\mathbf{p}$  containing the logarithm of layer resistivities and layer thicknesses. The usage of logarithmic parameters in  $\mathbf{p}$  offers the advantage that negative model parameters are implicitly barred from the inversion. Additionally, the time gates and acquisition parameters (ramp time, loop size, pulse duration, Bessel filter, etc.) as determined by  $\mathbf{d}_{\text{meas}}$  enter the calculation of  $\mathbf{d}_{\text{calc}}$ . The misfit, aka objective function, to be minimized by the variation of  $\mathbf{p}$  is expressed in terms of the squared sum of residuals:

$$\min_{\mathbf{p}} \|\mathbf{d}_{\text{meas}} - \mathbf{d}_{\text{calc}}\|_2^2 \quad 2-9$$

The above objective function is dominated by residuals belonging to the largest measurement values, i.e. measurements during the earliest time gates in  $\mathbf{d}_{\text{meas}}$ , which can be several decades larger than those during the latest time gates (e.g. Fig. 2-7). Additionally, 2-9 does not account for the quality of data. Therefore, it is necessary to introduce a weighting into the objective function prior to the optimization. The weighting is denoted by the square weighting matrix  $\mathbf{W}$ , which has non-zero elements along the main diagonal only:

$$\min_{\mathbf{p}} \|\mathbf{W} \cdot (\mathbf{d}_{\text{meas}} - \mathbf{d}_{\text{calc}})\|_2^2 \quad 2-10$$

For TEM measurements, it is usually not appropriate to choose the inverse of the measurements' standard deviations as elements for  $\mathbf{W}$ , since they are either not known exactly or, if specified, also exhibit a large dynamic range spanning several decades between early and late time gates (e.g. Fig. 2-19, p. 39). Instead, WEIDELT (1984) suggests the following weighting to account for the large dynamic range:

$$W_{ii} = (d_i)^{-q} \quad q \in [0; 1] \quad 2-11$$

The choice for the exponent  $q$  in 2-11 determines the relative weighting of early to late time gates (or large to small measured values): If  $q$  equals 1, the weighting by the inverse of the measured value at each time gate essentially equals a constant relative error floor. With a choice of  $q < 1$ , the emphasis of the objective function is shifted towards early time gates or



large amplitudes by assigning a higher relative precision. Either way, the actual quality of data does not enter the weighting scheme and care has to be taken to avoid the influence of outliers onto the objective function.

In this thesis the weighting in the objective function is chosen according to **2-11** with an exponent  $q=1$ , implicitly already used in **2-8**. Because of limitations in the precision of the LAPTEM (s. Appendix A, p. 133ff), which can introduce systematic errors especially significant at early times, an increased importance of early time gates in the objective function is undesirable. To avoid a possible influence of outliers or bad data values, all measured data with a relative error above  $\sim 20\%$  are rejected. It should be noted that, due the large dynamic in the relative errors, the transition from accepted and rejected data values is abrupt and the value chosen for the threshold will only have a minor influence on the amount of data which is accepted or rejected.

Various algorithms exist for the minimization of the objective function. The original inversion code *TEMIDinv* and the new inversion code *EMIDinv*, which is based on the optimization routine *lsqnonlin* (MathWorks, 2006), both use the Levenberg-Marquardt optimization algorithm (LEVENBERG, 1944; MARQUARDT, 1963). This standard algorithm is based on a stabilized linearization of the least squares formulation and is suitable for the minimization of nonlinear, continuous objective functions. Since it was used as is and not extended or altered in the scope of this thesis, a detailed description of the algorithm has not been included here and can instead be found in e.g. WEIDELT (1984) or COMMER (2003).

Two different inversion strategies may be distinguished with respect to the number of model parameters  $n_p$  in  $\mathbf{p}$  with respect to the number of measurements  $n_d$  in  $\mathbf{d}_{\text{meas}}$ :

In a block inversion the number of model parameters is much smaller than the number of measurements ( $n_p < n_d$ ). Typically, such a block inversion will use a 1D-model with 5 layers or less  $\Leftrightarrow n_p \leq 9$ . In such an overdetermined problem, all model parameters can be left unconstrained in the optimization. Additional external information about the underground's resistivity or layering, e.g. from boreholes or other geophysical methods, may be incorporated easily by fixing the respective model parameters within the inversion. The final result of a block inversion will to some extent depend on the number of free parameters and the starting model. The resolution of model parameters in the final result of the block inversion can be estimated by analysis of the singular values of the Jacobi matrix (e.g. WEIDELT, 1984; HÖRDT ET AL., 1992). The block inversion is implemented in both inversion codes. The new inversion code offers the advantage that several measurements with different acquisition parameters, e.g. different ramp times or loop sizes, may be inverted simultaneously.

In a smooth inversion the 1D-model consists of many layers and only the layer resistivities are free parameters, whereas the layer thicknesses remain fixed. The number of free model parameters exceeds the number of measurements ( $n_p > n_d$ ) leading to an underdetermined

inversion problem. In such an ill posed inversion problem, small perturbations of the data vector  $\mathbf{d}_{\text{meas}}$  will lead to arbitrary large perturbations of the resulting model vector  $\mathbf{p}$ , thus, yielding the inversion result useless. To overcome the ill posed problem, the optimized objective function needs to be regularized by imposing additional constraints on the norm of the free model parameters or a similar measure (HANSEN, 1994):

$$\min_{\mathbf{p}} \left\{ \|\mathbf{W}(\mathbf{d}_{\text{meas}} - \mathbf{d}_{\text{calc}})\|_2^2 + \lambda^2 \|\mathbf{L}\mathbf{p}\|_2^2 \right\} \quad \mathbf{2-12}$$

In this so called *Tikhonov regularization*,  $\mathbf{L}$  may be the identity matrix or the discrete approximation of a derivative operator and the regularization parameter  $\lambda^2$  is a non-negative number controlling the relative weighting of the constraint on  $\mathbf{p}$  and the residual norm in the objective function. A simple choice for  $\mathbf{L}$ , which is used in *EMIDinv*, was suggested by CONSTABLE ET AL. (1987):

$$L_{i,i} = -1 \quad L_{i,i+1} = 1, \quad i = 1, \dots, n_p - 1 \quad \mathbf{2-13}$$

Here,  $\mathbf{L}$  is a  $(n_p-1 \times n_p)$ -matrix, where  $n_p$  is the number of free model parameters. A calculation of the model constraint in **2-12** with **2-13** leads to a sum with squared differences of the free model parameters:

$$\lambda^2 \|\mathbf{L}\mathbf{p}\|_2^2 = \lambda^2 \sum_{i=1}^{n_p-1} (p_{i+1} - p_i)^2 \quad \mathbf{2-14}$$

For large values of  $\lambda^2$ , the objective function in **2-12** is dominated by the constraint on  $\mathbf{p}$  and the norm of the data residual is suppressed. This will lead to an increasing smoothness of the inverted model parameters. In the limit  $\lambda^2 \rightarrow \infty$ , all free model parameters, i.e. the layer resistivities, will be equalized in the inversion and the resulting model will be a homogeneous halfspace. For small values of  $\lambda^2$ , the objective function is dominated by the data residual. In the limit  $\lambda^2 \rightarrow 0$ , the inverted parameter vector may be arbitrarily rough, thus, representing a completely unrealistic underground model.

Since the inversion result is greatly influenced by the value of  $\lambda^2$ , a proper choice of the regularization parameter is needed to arrive at a good compromise between data fit and model smoothness. HANSEN (1994) uses an L-curve analysis to determine the proper choice for the regularization parameter: in his analysis the two summands in **2-12** are plotted into an axis for varying values of  $\lambda^2$ . The resulting curve is L-shaped and the proper value for the regularization parameter is located in the vicinity of the turning point. Fig. 2-9 depicts a similar approach, but plots the normalized RMS ( $\rightarrow$  **2-9**) against the regularization parameter. According to turning points of curves in Fig. 2-9,  $\lambda^2$  was chosen to be between 0.05-0.2 for the smooth inversion of data.

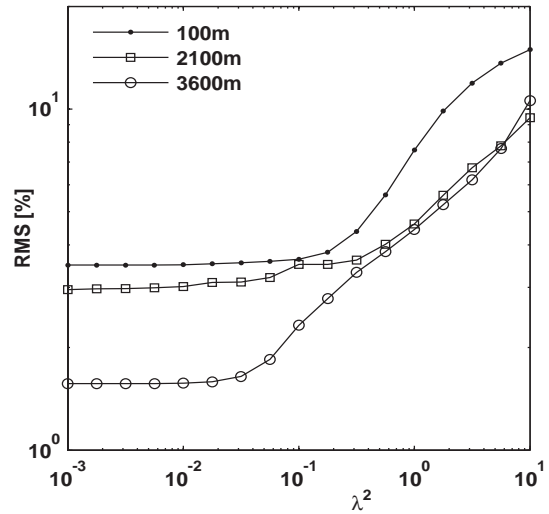


Fig. 2-9: Influence of regularization parameter  $\lambda^2$  in the optimization of **2-12** (results from three exemplary stations of the N-profile in the Jingsutu Structure (s. chap. 4.2.3, p. 95ff)).

### 1D Joint Inversion

A joint inversion, originally presented for electromagnetic methods by VOZOFF & JUPP (1975), is used to simultaneously invert the data of different geophysical methods at one location. In the scope of this thesis the joint inversion is used for a combination of TEM-, DC- and MT-data (s. chap. 4.3.1, p. 112ff). The advantage of a joint inversion is generally seen in the improvement of model resolution, because different geophysical methods have different sensitivities to the distribution of physical parameters in the underground. Thus, a joint inversion can help to reduce the ambiguity in the parameters of an inverted underground model, e.g. demonstrated by HÖRDT ET AL. (1992) for a combination of MT- and LOTEM-data. Additionally, the joint inversion can be used to estimate the magnitude of static shift in MT- and DC-data (e.g. STERNBERG ET AL., 1988; MEJU, 2005). Static shift, caused by near surface inhomogeneities of the conductivity distribution, can lead to a frequency independent distortion of the electric field, consequently shifting the apparent resistivities of MT- and DC-data by constant factors. Since the inductively coupled TEM method measures the time derivative of the magnetic field, it is inherently unaffected by distortions of the electric field and can be used for the estimation and correction of static shift. Finally, the simultaneous inversion of data from different methods also serves as additional cross-check for the validity and quality of measured data.

The implementation of a joint inversion extends the formulations for the 1D block- and smooth-inversion to simultaneously invert the data of different geophysical methods. The

objective function needs to include the residuals of all relevant methods and for a block inversion the minimization problem can, similar to **2-10**, be formulated as:

$$\min_{\mathbf{p}} \left\{ \sum_m \lambda_m^2 \|\mathbf{W}_m(\mathbf{d}_{\text{meas},m} - \mathbf{d}_{\text{calc},m})\|_2^2 \right\} \quad \mathbf{2-15}$$

Here, the subscript  $m$  is simply used to distinguish different methods included in the joint inversion - e.g.  $m = \{\text{TEM}, \text{MT}, \text{DC}\}$  - in which case the weighting matrices, measured data and calculated model responses are chosen or calculated accordingly. Since the residuals of different methods are calculated based on different quantities - e.g. normalized voltages (TEM), phases (MT) or apparent resistivities (MT & DC) - additional, non-negative weighting factors  $\lambda_m^2$  are specified in **2-15** to balance the residuals of different methods. If the joint inversion is performed with a 1D-model with many layers, the objective function in **2-15** needs to be extended with a smoothness constrain on the model parameters  $\mathbf{p}$  as in **2-12**:

$$\min_{\mathbf{p}} \left\{ \lambda^2 \|\mathbf{L} \mathbf{p}\|_2^2 + \sum_m \lambda_m^2 \|\mathbf{W}_m(\mathbf{d}_{\text{meas},m} - \mathbf{d}_{\text{calc},m})\|_2^2 \right\} \quad \mathbf{2-16}$$

In the joint inversion, a possible static shift in the apparent resistivities of MT- or DC-data is included in the associated summands of the objective functions (**2-15**, **2-16**):

$$\|\mathbf{W}_m(\mathbf{d}_{\text{meas},m} - \mathbf{d}_{\text{calc},m})\|_2^2 \longrightarrow \|\mathbf{W}_m(\mathbf{d}_{\text{meas},m} - s_m \cdot \mathbf{d}_{\text{calc},m})\|_2^2 \quad \mathbf{2-17}$$

Within the joint inversion, the static shift factors  $s_m$  ( $m = \{\text{MT}, \text{DC}\}$ , apparent resistivity only) are free parameters and constrained to positive values only. Since the static shift factors are linear parameters in the inversion, a partitioned least square optimization (SMYTH, 2002) is used, in which the linear parameters - i.e. the static shifts - are determined using a linear regression in every optimization step.

## 2.3 2.5D Modeling - TEMDDD

Several 3D modeling codes for the TEM method were introduced in the past years (e.g. WANG & HOHMANN, 1993; DRUSKIN & KNIZHNERMAN, 1994; TABAROVSKY ET AL., 1995; ÁRNASON, 1999; COMMER & NEWMAN, 2004). In several model studies these 3D codes were used to investigate the effects of 2D/3D structures on TEM measurements (e.g. GOLDMAN ET AL., 1994; RABINOVICH, 1995; TOFT, 2001). Furthermore, the possibilities of applying 3D inversion techniques to sets of TEM model-data were also started to be investigated in recent studies (e.g. HABER ET AL., 2004; NEWMAN & COMMER, 2005). However, at present the interpretation of TEM field-data almost exclusively relies on 1D inverse modeling (e.g. DANIELSEN ET AL., 2003; PAGANO ET AL., 2003; YOUNG ET AL., 2004; BARRETTA ET AL.,

2005; KAFRI & GOLDMAN, 2005) and only very few publications exist, where field-data was modeled or inverted in 2D or 3D, e.g. for the LOTEM-method in MITSUHATA ET AL. (2002) and COMMER ET AL., (2006), or for the TEM-method in SCHAUMANN (2001). For the application of 3D codes to real field-data, flexible tools are required to facilitate the rapid generation and adaption of underground models and according input-models for the 3D code. In the scope of this thesis, such tools were developed (chap. 2.3.3) for the 3D modeling code TEMDDD, which was made available for research purposes by Knútur Árnason (The National Energy Authority of Iceland, Reykjavík, Iceland). Since there was only little experience to revert to prior to the investigations, a numerical testing was first carried out to check the feasibility and possible limitations of the program (chap. 2.3.2). Subsequently, the code was used for a model study over basic 2D models (chap. 2.3.5). Generally, 2D models are constructed by keeping the resistivity of input-models to TEMDDD constant perpendicular to the profile direction. Since the modeled source field and the geometry of bodies are both 3D, but the represented resistivity distribution is only 2D, such a modeling is frequently referred to as 2.5D modeling (HOHMANN, 1988). The model study was aimed to further test the numerical stability of the code, to assess the approximate time need for computations, to develop tools for the generation of 2D models, and to get a deeper insight into possible misinterpretations when using a 1D inversion code on an inherently 2D data set.

The restriction on 2D models was imposed, because field measurements in China were almost exclusively carried out along approximately straight profile lines and measurements of horizontal field components were not conducted. Such data sets do not contain enough information to put useful constraints on the interpretation of a true 3D model. Therefore, in this case a 3D modeling would be an over-parametrization of the model space and would only be appropriate, if external information about the resistivity structure were available.

The model study, as summarized in chap. 2.3.2 and chap. 2.3.5, was initiated in cooperation with HILLER (2005), final results are from HÖLZ ET AL. (2006). It was inspired by a model study of TOFT (2001), who also tested the feasibility of TEMDDD. When comparing our model study to the one of TOFT (2001), main differences can be seen in the investigated loop configuration (coincident loop  $\leftrightarrow$  inloop- and separate-loop), loop size ( $100 \times 100 \text{ m}^2 \leftrightarrow 40 \times 40 \text{ m}^2$ ), maximum considered time ( $t_{max}$  determined by resolution of the measurement system  $\leftrightarrow$  fixed time range), and general 2D model type (dipping layer  $\leftrightarrow$  buried valley).

### 2.3.1 TEMDDD - General Description

The program TEMDDD (ÁRNASON, 1999) formulates the transient electromagnetic problem for a step-current excitation in the time-domain by a finite difference formulation of Maxwell's equations on a staggered grid (YUE, 1966). In this formulation, a 3D model is represented by a rectilinear grid (Fig. 2-10), i.e. a tessellation of the 3D space by parallelepipeds, which are not necessarily congruent to each other. Within each parallelepiped, hereafter referred to as cell, the discretized physical quantity ( $\rightarrow$  conductivity) of the underlying 3D model has a constant value.

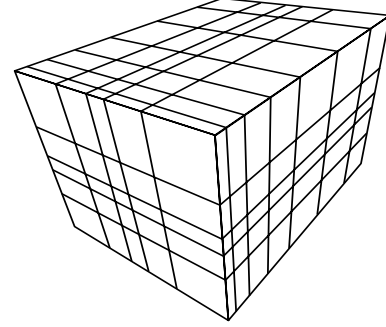


Fig. 2-10: Rectilinear grid.

In the formulation, Maxwell's equations are used in their quasistatic approximation:

$$\nabla \times \mathbf{e} = -\dot{\mathbf{b}}$$

$$\nabla \times \mathbf{b} = \mu_0 (\sigma \mathbf{e} + \mathbf{j}_e)$$

2-18

Here,  $\mathbf{e}$  and  $\mathbf{b}$  are the electric and magnetic field, respectively,  $\mu_0$  is the free space permeability,  $\sigma$  is the conductivity and  $\mathbf{j}_e$  is the source current density of the transmitter, which is shut-off at  $t=0$  (WEIDELT, 2000).

The vectorial electric and magnetic fields in Maxwell's differential equations are evaluated on the rectilinear grid by approximating the according spatial differential operators in 2-18 with appropriate linear finite difference forms. In Fig. 2-11 one cell of the rectilinear grid (white parallelepiped) exemplarily shows, how the electric and magnetic field are localized in the middle of the edges and faces of cells, respectively. Each node, where the magnetic field is evaluated, is surrounded by an elementary electric loop and similarly on the "staggered" grid cell (gray parallelepiped), each node where the electric field is evaluated, is surrounded by an elementary magnetic loop. These elementary loops are used to cast the spatial vector differential operators in 2-18 into finite difference forms. As consequence of the spatial formulation of the finite difference approximation (comp. Fig. 2-11), transmitters in TEMDDD need to be aligned with cell edges of the rectilinear grid and can either be grounded dipoles or inductively coupled loops of rectangular shape (ÁRNASON, 2000). Similar to Fig. 2-11, receivers for the vertical magnetic field are represented in TEMDDD by the z-component of the magnetic field (or its time derivative) in the center of according cell faces.

Since electric fields are localized on cell edges and, thus, are bounded by the conductivities of adjacent cells, the discretization of the second equation in 2-18 requires some sort of material averaging scheme. A common approach is to assign an average conductivity, which is

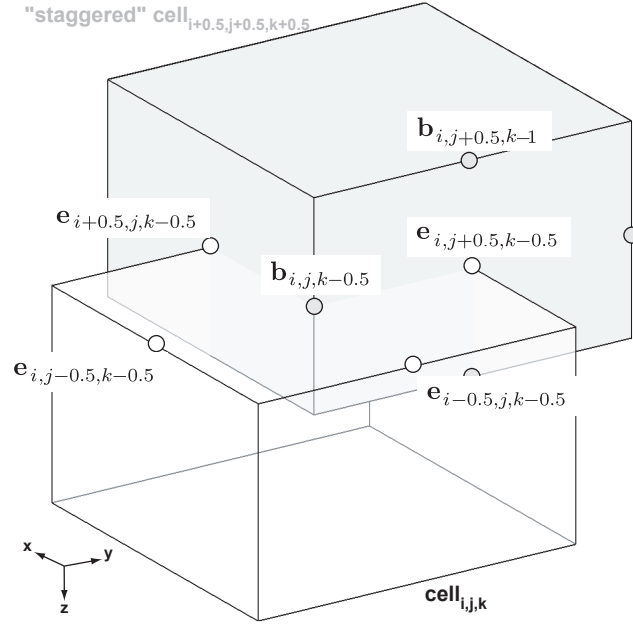


Fig. 2-11: Staggered grid scheme after YEE (1966). Within each cell (white parallelepiped) of the rectilinear grid (s. Fig. 2-10) the discretized physical quantity ( $\rightarrow$  conductivity) is constant. The electric and magnetic fields are evaluated in the middle of the edges and faces of cells, respectively.

calculated as arithmetic average of the adjacent cells weighted by the associated volumina or cross sectional area of involved cells (e.g. WANG & HOHMANN, 1993; WEIDELT, 2000). For the electric field at the node  $(i, j-0.5, k-0.5)$  in Fig. 2-11 the material averaging for the conductivity is:

$$\bar{\sigma}_{i,j-0.5,k-0.5} = \frac{\sum_{I_j, I_k} (\sigma V)_{i, I_j, I_k}}{\sum_{I_j, I_k} V_{i, I_j, I_k}} \quad 2-19$$

$$I_j = j - 1, j; \quad I_k = k - 1, k$$

Advanced material averaging schemes exist (e.g. MOSKOW ET AL., 1999), but are not considered in this thesis. Further elaborations on the formulation of the finite difference scheme on a staggered grid can be found e.g. in WANG & HOHMANN (1993) or COMMER (2003).

The time dependency of the differential vector equations can either be solved by explicit time-stepping as in WANG & HOHMANN (1993), where the time dependency in 2-18 is replaced by a finite difference approximation, or by the reformulation of the problem as eigenvalue problem, which is the case for TEMDDD. The latter formulation is solved by the Spectral Lanczos Decomposition Method (SLDM) as proposed by DRUSKIN & KNIZHNERMAN (1988). A concise description for both methods and suggestions for the discretization of spatial and time parameters can be found in WEIDELT (2000) and further references therein.

### 2.3.2 Numerical Testing

The dependency of accuracy and speed of TEMDDD on the choice of input parameters, e.g. number of cells and spacing of cells within the discretization grid, was evaluated for layered 1D models. For these elementary models, transients were calculated with TEMDDD and compared to reference 1D transients calculated with *TEM1Dmod*. Input parameters for TEMDDD were chosen with respect to the generally applied measurement geometry and device specifics of the LAPTEM:

- coincident-loop configuration, 100x100m<sup>2</sup>
- earliest time in transient: 30μs
- minimum voltage of transient: 10<sup>-2</sup>nV/Am<sup>2</sup>
- resistivity range of models: 1-1000Ωm
- maximum error with respect to reference transient: <1%
- grid spacing in xy-direction (Δxy) ...  
... constant for cells inside the loop  
... increasing outside the loop

$$\Delta xy_{i+1} = f_{xy} \cdot \Delta xy_i \quad f_{xy} > 1 \quad 2-20$$

- grid spacing in z-direction (Δz) increasing downward

$$\Delta z_{i+1} = f_z \cdot \Delta z_i \quad f_z > 1 \quad 2-21$$

Since TEMDDD calculates the vertical magnetic field (or its time derivative) at the center of cell faces only (s. Fig. 2-11), the transient response for the coincident-loop configuration was calculated by numerical integration of the inloop-responses for all cells located inside the loop. The minimum time for testing was chosen in correspondence to the earliest analyzable time for the LAPTEM measurement system, which is determined by the minimum achievable ramp time of ~30μs for a 100x100m<sup>2</sup> loop (s. chap. A.3.2, p. 144ff). The maximum time limit ( $t_{max}$ ) was chosen variable. It was determined by the point in time, where normalized voltage of the reference 1D transients dropped below the resolution of the measurement system. The minimum normalized voltage resolved by the measurement system depends on the maximum available gain, the effective resolution of the AD-converter, the used loop size and the maximum transmitter current:

$$V_{min} \approx \frac{10}{1000_{gain} \cdot 2^{13}_{AD} \cdot 10^4_{loop} \cdot 10_{I_{max}}} \cdot \frac{V}{Am^2} \approx 10^{-2} \frac{nV}{Am^2} \quad 2-22$$



Even though the time dependency in **2-18** is approximated with different approaches in time-stepping codes (e.g. WANG & HOHMANN, 1993) or codes based on the SLDM (ÁRNASON, 1999), the accuracy of the solution is ultimately coupled to the Courant-Friedrichs-Lewy criterion or a similar form (WANG & HOHMANN, 1993; WEIDELT, 2000). This criterion relates the minimum number of required time steps  $N_t$  (or dimension of the generalized derivative matrix for the SLDM) to the parameters of the discretization:

$$N_t \simeq \frac{f}{\Delta_{min}} \sqrt{\frac{t_{max}}{\mu_0 \sigma_{min}}} \quad \mathbf{2-23}$$

Here,  $t_{max}$  is the latest time channel of the calculated transient, and  $\Delta_{min}$  and  $\sigma_{min}$  are the minimum grid spacing and conductivity, respectively.  $N_t$  greatly influences the computational time and has to be chosen with respect to the required accuracy of solution. Estimates as found in several publications are summarized in Tab. 2-1.

Resistivity of Halfspace	$t_{max}$ [ms]	ORISTAGLIO & HOHMANN (1984)	ADHIDJAJA & HOHMANN (1989)	WANG & HOHMANN (1993)	WEIDELT (2000)
		$f = 2$	$f = \sqrt{6}$	$f = \frac{\sqrt{6}}{\alpha}$ $\alpha = 0.1 - 0.2$	$f = \frac{1}{\alpha}$ $\alpha = 0.05 - 0.1$
1 $\Omega\text{m}$	191	156	190	953-1905	778-1555
10 $\Omega\text{m}$	48	247	302	1512-3025	1235-2470
100 $\Omega\text{m}$	12	391	479	2394-4787	1954-3909
1000 $\Omega\text{m}$	3	618	757	3785-7569	3090-6180

*Tab. 2-1:* Number of required time steps ( $N_t$ ) according to **2-23** with factors  $f$  as specified by different authors. A minimum grid spacing of 5m is assumed. The maximum time  $t_{max}$  is determined by the resolution of the measurements system ( $V_{min} \sim 10^{-2}\text{nV}/\text{Am}^2$ ).

Transients were first calculated with TEMDDD for homogeneous halfspaces (1-1000 $\Omega\text{m}$ ) and compared to the 1D reference transients. The input parameters to TEMDDD were successively adjusted to find an appropriate discretization for each halfspace. After some testing, the factors controlling the outward ( $f_{xy} \rightarrow \mathbf{2-20}$ ) and downward ( $f_z \rightarrow \mathbf{2-21}$ ) increasing grid dimensions were fixed to 1.15 and 1.17, respectively. The 100x100m<sup>2</sup>-loop was discretized with 14x14 cells to stabilize the integration for the calculation of the coincident-loop response. To keep model discretizations for input models of different half spaces comparable,

Halfspace	$N_{xy}$	$f_{xy}$	$N_z$	$f_z$	$N_t$	Dim [m]
1 $\Omega\text{m}$	42	1.17	24	1.15	1000	3112x980
10 $\Omega\text{m}$	48	1.17	27	1.15	1500	5137x1504
100 $\Omega\text{m}$	52	1.17	29	1.15	1800	7184x2000
1000 $\Omega\text{m}$	56	1.17	32	1.15	3000	9900x3055

*Tab. 2-2:* Final optimized parameters of input models to TEMDDD for homogeneous halfspaces.  $N_{xy}$  and  $N_z$  refer to the number of grid cells in xy- or z-direction.  $N_t$  approximately falls in the ranges specified by WEIDELT (2000) (s. Tab. 2-2).

larger grids were constructed by simply adding additional cells to the outer bounds of the model. The dimensions of the added cells were chosen according to **2-20** and **2-21**.

Calculations with the final grids (Tab. 2-2) yielded deviations between the 1D and 3D code below 1% for all relevant times ( $t_{max}$  in Tab. 2-1). Only for the lowest resistivity of 1  $\Omega\text{m}$  and times  $< 300\mu\text{s}$  the relative error exceeded 1% and reached values of up to 12% for the earliest times. According to ÁRNASON (2000), this behavior for low resistivities and early times is due to the high frequency cut-off caused by the discretization and can only be circumvented by introducing a refined grid. However, further numerical testings with refined grids did not lead to any significant changes in the calculations and, therefore, yielded the same deviations. Alternatively, following the argumentation of SMITH & PAINE (1999), a plausible explanation for the deviations could be seen in the fact that the 1D code and the 3D code inherently use different loop geometries: while the 1D code calculates the transient response for a circular loop, the discretization of the 3D code describes the transmitter as a rectangular loop. Ultimately, the described deviations are negligible in the scope of this thesis, because they relate to a model type which was not encountered during 2.5D modeling (s. chap. 4.2.3, p. 98ff).

In a second test, the calculated responses of TEMDDD were compared with reference transients for layered halfspaces (100  $\Omega\text{m}$  | 10  $\Omega\text{m}$  | 100  $\Omega\text{m}$  and 10  $\Omega\text{m}$  | 100  $\Omega\text{m}$  | 10  $\Omega\text{m}$ ) with varying interface depths. The discretization grids were constructed with respect to the discretization parameters found for the 100  $\Omega\text{m}$  halfspace (Tab. 2-2). Generally, the comparison yielded deviations  $< 1\%$ . Only for very early and very late times the relative error exceeded 1% and reached values of up to 5% for a few time steps.

The numerical tests demonstrate the general applicability of TEMDDD for simple 1D model geometries. In chap. 2.3.5 (p. 34ff) the plausibility of results is further investigated for calculations with TEMDDD for basic 2D models. Additional comparisons of TEMDDD with other 3D TEM-codes were not performed in the scope of this thesis, but can be found in TOFT (2001) and in ÁRNASON (1999).



Fig. 2-12: Example for the application of the *General Polygon Clipper Library*, which is used to calculate the intersection between a rectangular cell and an arbitrarily shaped polygon. The model geometry is displayed on the left, the resulting intersection on the right.

### 2.3.3 2D - Model Generator

Generally, the generation of input-files for TEMDDD poses the problem that an arbitrary 2D resistivity model and the discretization grid for TEMDDD (s. chap. 2.3.2) are usually non-conforming. Furthermore, a new input file needs to be generated for every station along a profile, because the 2D resistivity model and the discretization grid are shifted with respect to each other. In the scope of the model study, which was described in the previous chapters, a first model generator for the automated generation of input-files for TEMDDD was developed in cooperation with T. Hiller (HILLER, 2005). This first model generator allows the generation of input-files for the basic model of a dipping layer by specifying the loop position, the angle of inclination, and the resistivities of the top and bottom layer. However, to allow TEMDDD to be used for the 2.5D modeling of real field-data, a much more flexible approach was needed to account for general model geometries.

The new model generator developed in the scope of this thesis is based on the *General Polygon Clipper Library* (GPCL by MURTA, 2007), which uses an algorithm by VATTI (1992) to calculate the union ( $A \cup B$ ), intersection ( $A \cap B$ ), difference ( $A - B$ ), or exclusive disjunction (= XOR;  $A \oplus B$ ) of two arbitrary 2D -polygons. A gateway function was programmed to make the GPCL available within Matlab (HÖLZ, 2007). An example for the calculation of the intersection of two polygons is depicted in Fig. 2-12. The GPCL is very flexible, because each polygon ...

- may be composed of a single face or several faces,
- may have self-intersecting edges, and
- may contain an arbitrary number of holes.

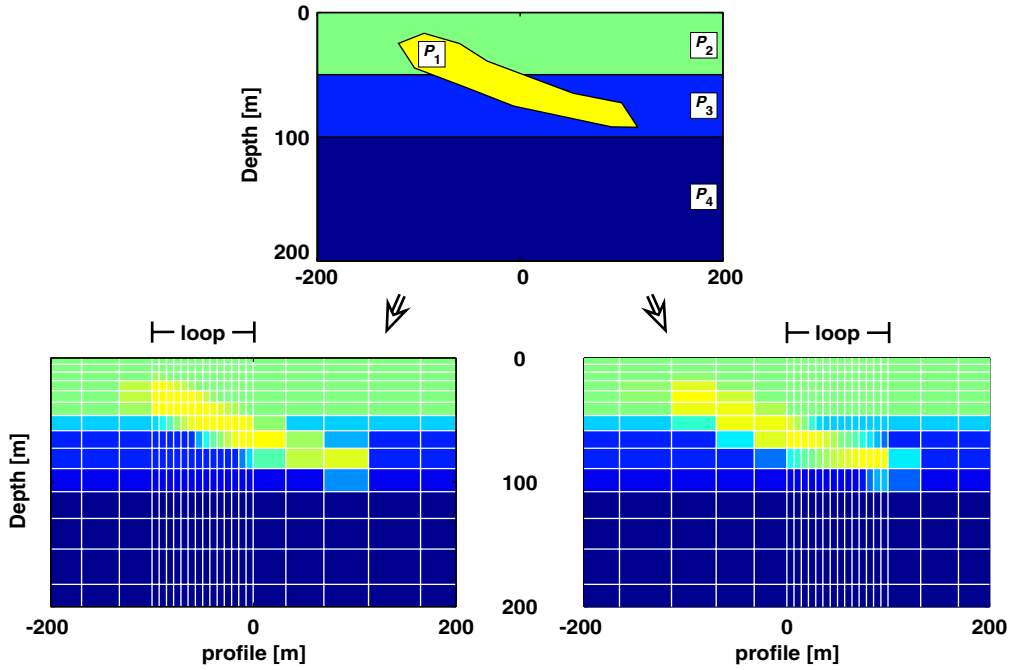


Fig. 2-13: Illustration of TEMDDD input models (bottom) for an arbitrary 1D-model with three layers and one 2D body (top), which are represented by polygons ( $P_1$ - $P_4$ ) with fixed resistivities. The center of the  $100 \times 100 \text{ m}^2$  loop is located at -50m (lower left) and at +50m (lower right), thus, shifting the discretization grid along the profile. Resistivities of cells are calculated according to 2-26.

Fig. 2-13 exemplarily depicts the application of the new model generator for a 1D-model with 3-layers and one 2D body. In the following, the first subscript  $i$  of a polygon  $p_i$  not only distinguishes different polygons, but also refers to the stacking order of polygons: polygons with smaller first subscript can possibly overlap polygons with larger subindices, e.g. in the example in Fig. 2-13, the polygon of the 2D body ( $=P_1$ ) is stacked on top of the polygons representing the 1D model ( $=P_{2-4}$ ). For a general 2D model, which consists of a 1D background-model with  $n$ -layers and  $m$  2D bodies, the generation of input models involves three main steps.

1. Calculate the difference of each polygon with all polygons, which are higher in the stack order. This assures that polygons are pairwise disjoint:

$$p_i = P_i - P_j \quad i = m + n, \dots, 2 \quad j = i - 1, \dots, 1 \quad 2-24$$

2. Calculate the intersection between the disjoint polygons ( $p_i$ ) from 2-24 and all cells ( $c_j$ ) of the discretization grid (sim. Fig. 2-12):

$$\tilde{p}_{i,j} = p_i \cap c_j \quad i = 1, \dots, m + n \quad j = 1, \dots, n_{\text{cells}} \quad 2-25$$

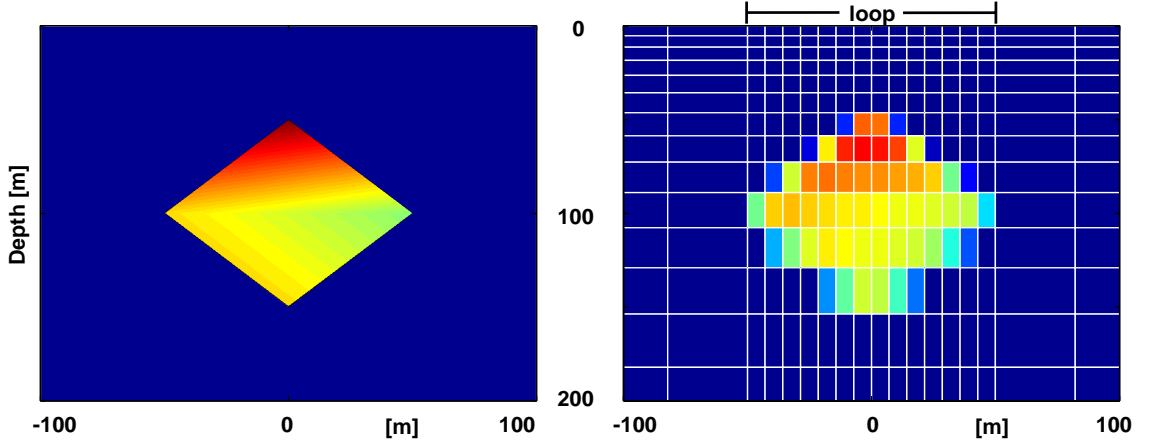


Fig. 2-14: Exemplary 2D body with a gradient resistivity structure in a homogeneous halfspace (left) and resulting TEMDDD input-model (right). The calculation of resistivities for the input-model involves a bilinear interpolation of resistivities inside the 2D body.

3. Similar to **2-19**, calculate an average conductivity ( $\bar{\sigma}_j$ ) for each cell ( $c_j$ ) with respect to the area and conductivity ( $\sigma$ ,  $A$ ) of the intersected and disjoint polygons ( $\tilde{p}_{i,j}$ ) from **2-25**:

$$\bar{\sigma}_j = \frac{1}{A_{c_j}} \sum_{i=1}^{n+m} (\sigma A)_{\tilde{p}_{i,j}} \quad \mathbf{2-26}$$

For a correct calculation of areas, the intersected and disjoint polygons currently may not have any self intersecting edges. Since this is - under normal circumstances - always the case, this special case poses no relevant restriction on the applicability of the model generator. The calculation of average cell resistivities in **2-26** resembles the parallel connection of resistors. The weighted average of conductivities is equal to the material averaging scheme in the finite difference formulation of TEMDDD and can similarly be found in WANG & HOHMANN (1993). It should be clarified that in the new model generator the averaging is purely applied to solve the problem of projecting an arbitrary 2D resistivity distribution as represented by polygons onto a predefined grid to define input models for the 3D code.

To add more flexibility for the modeling of field-data, the restriction of limiting a 2D body's resistivity to a unique value is lifted. Local variations within a body can be accounted for by assigning a resistivity value to each vertex of the body, exemplarily depicted in Fig. 2-14. Accordingly, an adjustment for the calculation of a cell's average conductivity in **2-26** is needed, where the local conductivity of a 2D body ( $\sigma(\tilde{p}_{i,j})$ ) is estimated using a bilinear interpolation.

A similar approach for the projection of 2D structures with locally varying resistivities onto a non-conforming discretization grid of a finite difference code (geoelectrics) was recently

published by CHRISTIANSEN & AUKEN (2004). They use a weighting scheme similar to 2-26 for the averaging of cell resistivities, but limit the possible model space to arbitrary layered models.

To facilitate work with the model generator, the graphical user interface (GUI) *ModelCreatorGUI* was designed, which greatly simplifies the creation of 2D models (Fig. 2-15). Similar to common graphic-programs, a 2D body is simply created by defining the vertices of a polygon using either file import, keyboard, or an interactive pointing device. A polygon or single vertices can be dragged around with the mouse to change the polygons's position or shape. Vertices may be added or removed at any point to refine or simplify the polygons's structure. Each polygon may represent a homogeneous resistivity distribution, in which case a unique resistivity value is assigned to the representing polygon (s. Fig. 2-13), or it may have locally varying resistivities, in which case a single resistivity value is assigned to each vertex of the representing polygon (s. Fig. 2-14). Additionally to the 2D bodies, the 1D background-model and the position of TEM-stations need to be defined prior to the generation of input-files for TEMDDD. The position of stations determines the positioning of the discretization grid relative to the 2D model.

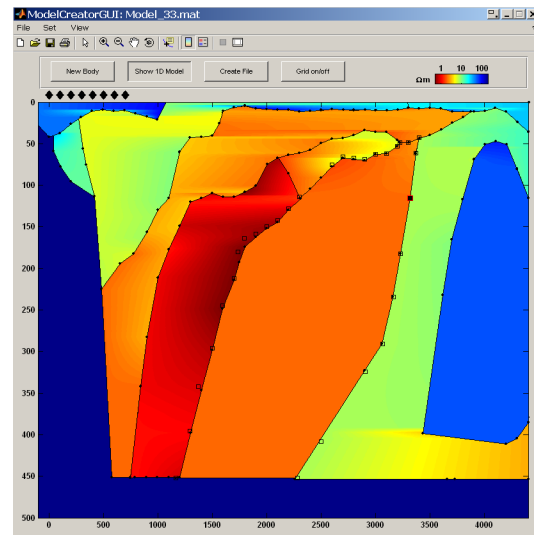


Fig. 2-15: *ModelCreatorGUI* - graphical user interface for the creation of 2D models.

Model creator and *ModelCreatorGUI* offer a great flexibility in the creation of 2D models. Both are platform independent, but require Matlab to be installed on the operating system. The model creator is not restricted to the projection of 2D models onto a rectangular grid, but can also be used for projections onto triangular or other irregular grids.

### 2.3.4 Parallelization

The time need for the calculation of TEMDDD for a single input model with the discretization grid derived in chap. 2.3.2 is in the order of 30min on current computer systems, e.g. 25min on an Intel Centrino, 2GHz, 2Gb RAM. For calculations along a profile line, the computational time increases proportional to the number of stations along the profile. To reduce the total time need and to make optimal use of available resources, the computational process is parallelized by means of a job based message passing interface, which was implemented in Matlab based on the TCP/UDP/IP-toolbox by RYDESÄTER (2003).

The parallelization involves an arbitrary number of MatlabClients and one central MatlabServer, which can reside on one computer utilizing several processors or be distributed on different computers, which are connected over a local network or the internet. New jobs - i.e. input files for TEMDDD - are deposited in a specific directory on the MatlabServer. Upon request of a MatlabClient, the server distributes available input-files over the TCP/IP connection to the client. Thus, server and client don't need to share a common file system. Calculations are then performed on the client with a local copy of TEMDDD. Finished or erroneous calculations are signaled from the client to the server and transferred into the appropriate directories on the server.

The approach taken here is flexible regarding the possibility to add or remove clients from the calculation network "on the fly": if a computer is free for calculations, the client simply needs to be started and will seamlessly integrate into an existing network. Also, the server may be interrupted and started later without affecting the calculations on the clients.

Both, MatlabServer and MatlabClient, can be used on any operating system with installed Matlab. Additionally, the client possibly needs a recompiled version of TEMDDD, which is compatible to the operating system. Other than that, the parallelization can run on a completely heterogeneous network. Both, MatlabServer and MatlabClient, were also implemented as system-services under the Windows operating system. The implementation as service offers the advantage that it is automatically started in the background after the operating system has booted i.e. the service does not require a logged-on user. Furthermore, a service can be protected from any user interaction, thus, preventing unwanted interferences of a user with the server or client. The implementation of MatlabServer and MatlabClient as services into operating systems like Linux is straightforward, but has not been tested, yet.

The parallelization approach described here, differs greatly from the one described by COMMER (2003), who parallelized the internal calculations of his finite difference code by dividing the 3D model into submeshes and distributing the calculations to individual processors. His approach offers the advantage that - depending on the number of available processors - the computational time needed for the calculations of an individual station, i.e. for a single input-file of a 3D model, may be greatly reduced. However, this approach greatly depends on the available hardware and is harder to be generalized to a heterogeneous infrastructure. In contrast, the approach taken here is easily scalable and can flexibly be adjusted to the available computational resources. In a network with as many computer nodes as stations to be calculated, the reduction for the time need is only limited by the slowest computer in the network, since the time for communication between the MatlabServer and MatlabClients is negligible with respect to the time need for the calculation with TEMDDD.

### 2.3.5 2.5D Model Study

In this chapter, the results of a 2.5D model study by HÖLZ ET AL. (2006) are summarized. The study was aimed to test the plausibility of results calculated with TEMDDD for a more complicated model type as compared to the layered halfspaces used in chap. 2.3.2. Furthermore, it was investigated what sort of effects are introduced by the 1D inversion of inherently 2.5D data and how possible misinterpretations may be avoided.

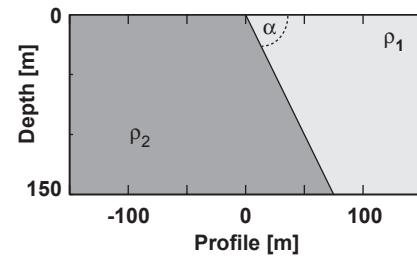


Fig. 2-16: Model with dipping layer.

Input-models for TEMDDD for the basic model of a dipping layer (Fig. 2-16) were constructed using the discretization parameters for the  $100\Omega\text{m}$  halfspace (Tab. 2-2). A basic model generator was implemented (chap. 2.3.3) to facilitate the generation of input-models for calculations along the profile, where the discretization grid is shifted with respect to the 2D model. For cells of the discretization grid intersected by the dipping layer of the 2D model, an average conductivity value was calculated ( $\rightarrow$  2-26). The angle of inclination was varied between  $10^\circ$ - $90^\circ$  and resistivities for the upper and lower layer were chosen pairwise different from a set of resistivities (10, 17.8, 31.6, 56.2,  $100\Omega\text{m}$ ). "2.5D transients" were calculated according to the model parameters along a profile across the dipping layer using TEMDDD. In 1D block inversions of these "2D transients" the number of layers was varied with respect to the resulting RMS ( $\rightarrow$  2-8). A maximum of three layers was sufficient to achieve a nearly perfect data fit ( $\text{RMS} < 1.5\%$ ) at all stations along the profile.

Model sections of the 1D inversion models yielded similar results for all calculated resistivity contrasts. They are, exemplarily, depicted for the resistivity contrast of  $10\Omega\text{m}:100\Omega\text{m}$  in Fig. 2-17:

With the resistor as top layer and small to moderate angles of inclination (left column,  $\alpha \leq 30^\circ$ ), the sections of 1D inversion models closely resemble the associated 2D model. A fictitious second layer of intermediate resistivity is introduced by the 1D inversion above the dipping layer of the true model (solid white lines). For larger angles of inclination ( $\alpha \geq 45^\circ$ ) additional fictitious anomalies can be seen in the homogeneous parts of the true models (i.e. for  $x > 0\text{m}$ , left column). The anomalous regions have a pyramidal wedge shape. With the conductor as top layer (right column) the anomalous pyramidal wedge is visible for all inclinations, less pronounced for small angles of inclination. Below the dipping layer the resistivity of the second layer is overestimated. A sensitivity analysis for the 1D inversion results shows that this parameter is poorly resolved. In all 1D sections, the first layer interface above the dipping layer underestimates the true angle of inclination. When comparing model calculations for 2D models with the same angle of inclination but swapped resistivity contrast,



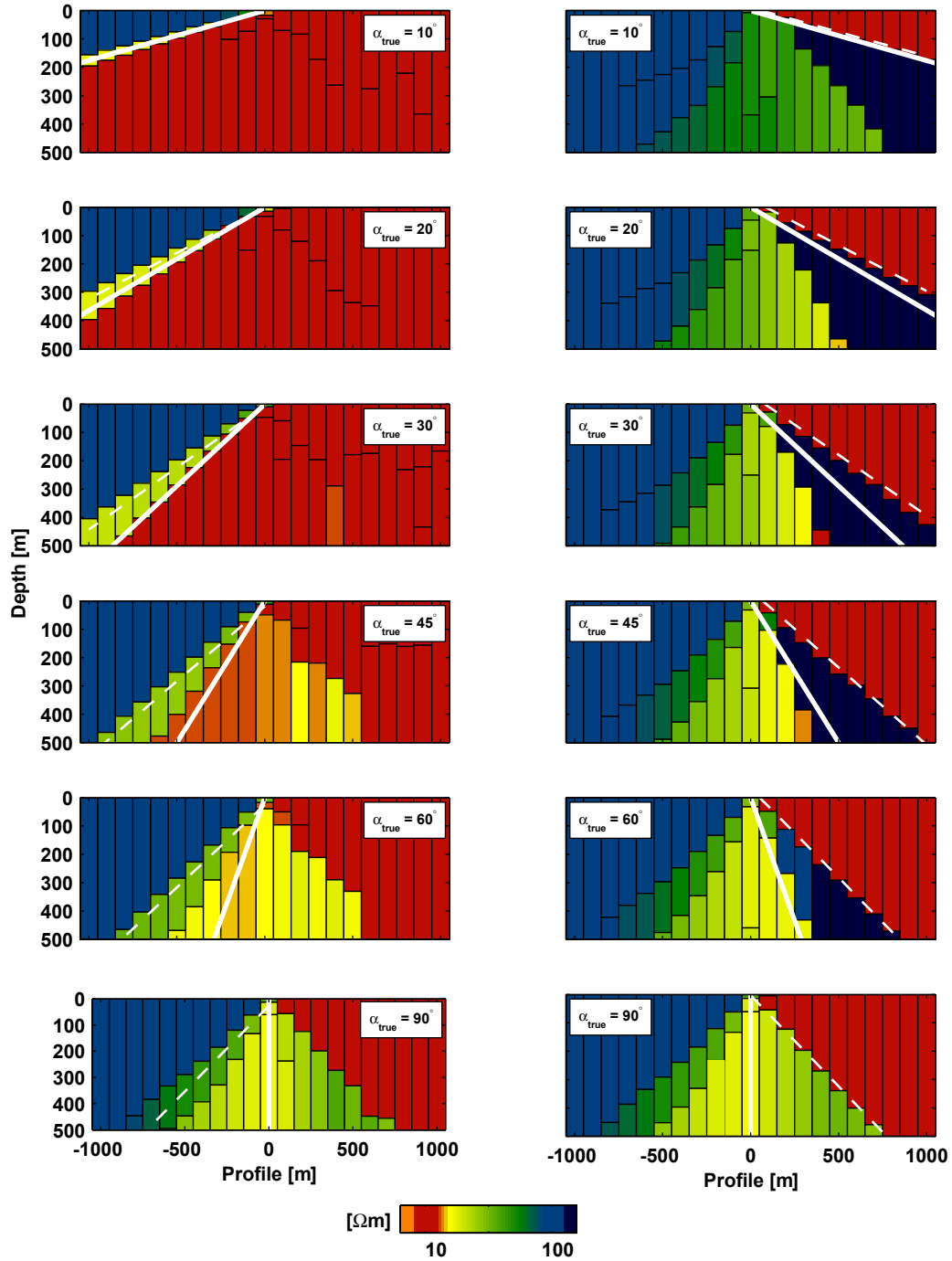


Fig. 2-17: 1D block inversions of 2.5D transients calculated with TEMDDD. The true inclination of the dipping layer in the 2D model (comp. Fig. 2-16) is indicated by a white solid line, the inferred apparent inclination by a white dashed line. All resistivities within 10% of the true resistivity are colored alike. Calculations with changed resistivity contrasts essentially lead to the same geometrical relationships (modified from HÖLZ ET AL., 2006).

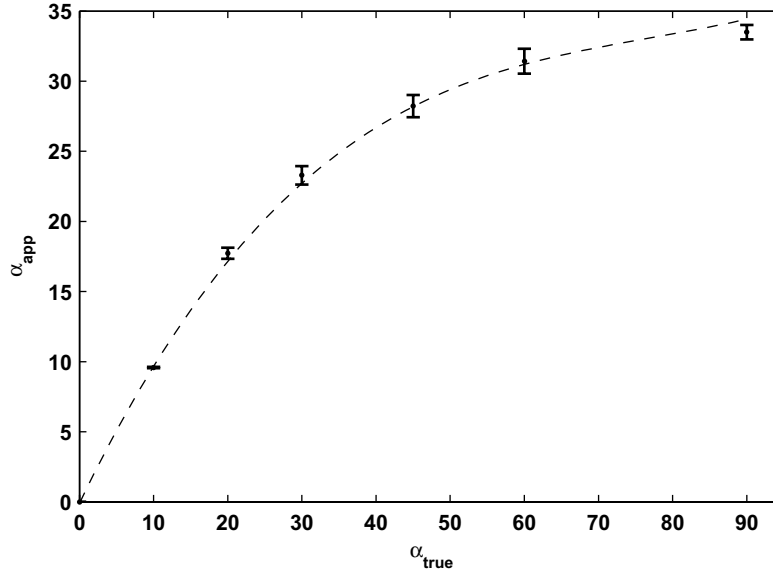


Fig. 2-18: Relationship between apparent and true angle of inclination (→ Fig. 2-17). Error bars represent the standard deviation of the apparent inclination for all eight calculated resistivity contrasts. A cubic polynomial fit (dashed line) is given in 2-26. (from HÖLZ ET AL., 2006; mod.)

it can be seen that the depth of this first layer interface for both model types is essentially equal (e.g.  $\alpha=20^\circ \leftrightarrow$  Fig. 2-17, 2<sup>nd</sup> row). Additional tests with different resistivity contrasts yielded the same general relation between the true angle of inclination in the 2D model and the "apparent inclination", which was derived from the depth of the first layer interface in the 1D sections.

In Fig. 2-18 the relationship between true and apparent angle of inclination is averaged for all calculated resistivity contrasts. The small error bars demonstrate that the apparent inclinations for all resistivity contrasts referring to the same true inclination are similar. Cubic polynomial fits to the averaged inclinations yield:

$$\begin{aligned}\alpha_{\text{true}} &\approx 2.7 \cdot 10^{-3} \alpha_{\text{app}}^3 - 7.5 \cdot 10^{-2} \alpha_{\text{app}}^2 + 1.6 \alpha_{\text{app}} \\ \alpha_{\text{app}} &\approx 5.6 \cdot 10^{-5} \alpha_{\text{true}}^3 - 1.3 \cdot 10^{-2} \alpha_{\text{true}}^2 + 1.1 \alpha_{\text{true}}\end{aligned}\tag{2-27}$$

For steep angles of inclination ( $\alpha_{\text{true}} > 60^\circ$ ) the apparent inclination does not change significantly anymore and the errors of the estimates increase. Therefore, use of 2-27 should be restricted to inclinations of  $\alpha_{\text{true}} \leq 60^\circ$  or  $\alpha_{\text{app}} \leq 30^\circ$ .

Results for the 1D block inversions of 2.5D transients are explained by the concept of "smoke rings" (NABIGHIAN, 1979), which are an illustrative description of the outward and downward diffusing induced current system (s. Fig. 2-2, p. 10). For a loop positioned above a dipping layer (Fig. 2-17,  $x < 0\text{m}$  for left column or  $x > 0\text{m}$  for right column) the current system

will, due to its outward propagation, always be influenced by the conductivity change, even for steep inclinations of the dipping layer. The same holds true for steep inclinations ( $\alpha \geq 45^\circ$ ) above the homogeneous part of models (Fig. 2-17,  $x > 0$ m for left column or  $x < 0$ m for right column). For small inclinations ( $\alpha \leq 30^\circ$ ) and high resistivities in the homogeneous part of models (Fig. 2-17, right column,  $x < 0$ m), the maximum of the current system is shifted into the conductive top layer, which causes the 1D inversion to introduce fictitious layers. For small inclinations ( $\alpha \leq 30^\circ$ ) and high conductivities in the homogeneous part of models (Fig. 2-17, left column,  $x > 0$ m) the propagation of the current system is not significantly influenced by the resistive top layer. Thus, the 1D inversions reflect the homogeneous structure in this part of the model.

Summarizing, the calculations with TEMDDD yielded physically meaningful results for 2D models, which concur with results of similar model studies by GOLDMAN ET AL (1994), RABINOVICH (1995), and TOFT (2001)<sup>1</sup>. The dependency between true and apparent inclination can be helpful for the interpretation of real data sets. However, for true measurements the identification of apparent inclinations as in Fig. 2-17 may be difficult due to lateral variations of the conductivity, more complex geometries of the underground, measurement errors and the resulting ambiguities in the interpretation of TEM data. Therefore, a strict application of 2-27 for real data sets will not be appropriate in most cases, but general tendencies may be derived in terms of possible magnitudes for inclinations.

An interesting aspect can be seen in the fact that even for models with a strong 2D character, here realized by dipping layers with steep inclination, the modeled "2D transients" can be explained with the model of a 1D inversion. Consequently, a single measured data set by itself will usually not contain enough information to distinguish between a 1D or a 2/3D underground. The other way around one can also conclude that a set of TEM data, which is completely explainable by a 1D inversion, may still be misinterpreted, if 2D effects are present and not recognized.

---

1. Toft also used TEMDDD in his model study.

## 2.4 Processing of TEM Signals in the Wavelet Domain

In the last 15-20 years the wavelet transformation (WT) has become an important tool for the analysis, compression and processing of signals. The WT was especially developed to work with signals, which are not purely periodic, but also contain aspects which are mainly localized in time. Since this is the case for many true signals the application range for the WT is very broad. Before looking at general aspects of the WT (chap. 2.4.2) and its application to TEM signals (chap. 2.4.3-2.4.5) a brief review of common processing techniques and existing advanced filtering concepts is given in the following chapter.

### 2.4.1 Common Processing Techniques for TEM Signals

For TEM measurements with a bipolar waveform as depicted in Fig. 2-6 there are common processing steps, which can be summarized as follows:

1. During each cycle of the bipolar waveform, two transients of alternating polarity are measured (Fig. 2-6). They are averaged to a single transient, which automatically cancels out any sufficiently stable offset. Furthermore, the application of the bipolar waveform limits the noise acceptance to frequency bands centered on the odd harmonics of the repetition frequency ( $1/T_0$  in Fig. 2-6), while even harmonics of the repetition frequency are efficiently suppressed (MACNAE ET AL., 1984).
2. During log-gating the samples of the mean transient calculated above are averaged on time windows (aka channels), which have an exponentially increasing width with time. This means that in early channels ( $\Leftrightarrow$  early times in transient) only few samples are averaged while late channels ( $\Leftrightarrow$  late times in transient) comprise the average of many samples. Since the integration inherently resembles a lowpass filter, the process of log-gating can be considered as a low-pass with variable corner frequency (EFFERSØ ET AL., 1999).
3. In the last step all log-gated transients are averaged. To reduce the possible influence of outliers, the averaging should be performed in a robust manner by selective stacking (e.g. BUSELLI & CAMERON, 1996; MACNAE ET AL., 1984).

The effect of the common processing is exemplarily depicted in Fig. 2-19, where transients of a simulated measurement (128 stacks, transmitter repetition frequency  $f_0=2.5\text{Hz} \rightarrow$  comp. Fig. 2-6) with added noise are processed. For white noise (Fig. 2-19, left) the noise reduction is  $\sim t^{1/2}$ , which is in accordance with MUNKHOLM & AUKEN (1996). Due to the fast decay of the transient signal ( $\sim t^{-5/2}$ ) the transition from a practically noise free signal at early times to very low signal-to-noise ratios at late times is rather abrupt.

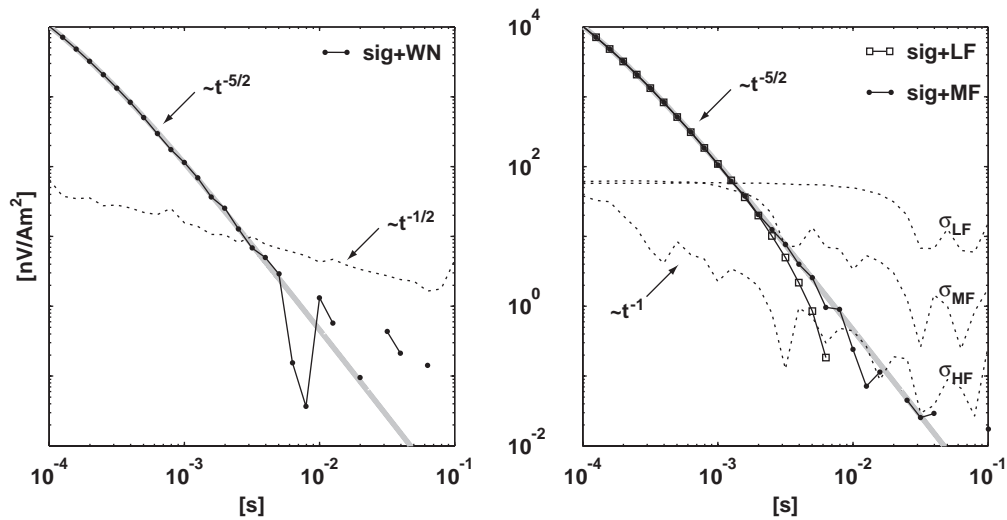


Fig. 2-19: Noise reduction using the common processing scheme for simulated measurement with reference transients (gray line) and added white noise (left) or harmonic noise (right; LF=123.21Hz; MF=1232.1Hz; HF=12321Hz). Standard deviations are displayed as dashed lines.

For harmonic noise (Fig. 2-19, right) it is assumed that its frequency is not an even multiple of the transmitter's repetition frequency, otherwise it would already be completely canceled out by the common processing as mentioned above. The processing characteristics depend on the frequency of the harmonic noise with respect to the repetition frequency of the transmitter. For harmonics with a much higher frequency ( $HF \sim 5000 \cdot f_0$ ; Fig. 2-19, right) the processing leads to a noise reduction  $\sim t^{-1}$ , which is in accordance with EFFERSØ ET AL. (1999). This means that high frequency noise will only pose a problem if it has a significant magnitude.

The processing of harmonic noise with comparatively low frequency ( $LF \sim 50 \cdot f_0$ ) results in an almost constant or gently dropping error level ( $< \sim t^{-1/3}$ ). Even though the processed transient still looks smooth at intermediate times, its deviation from the true transient (gray line in Fig. 2-19) is considerable. For harmonics with frequencies close to odd multiples of the transmitter's repetition frequency, the processing may even leave sign reversals in the processed transient, while indicating small standard deviations at the same time. Without going further into details it can be stated that harmonics with comparatively low frequencies may pose problems and, if not accounted for, may lead to misinterpretations.

Several additional techniques have been proposed for a further noise reduction, which can complement the above processing steps. All techniques require that the rawdata is available, i.e. the linearly sampled data of each measurement cycle of the bipolar waveform before any stacking or log-gating is performed. With the LAPTEM device it is possible to record rawdata for each transient during the transmitter off-time, but an acquisition of any pre-trigger data, i.e. during the transmitter on-time, is not possible in the current configurations.

Additional information about the noise can be obtained by simultaneous measurements at the actual measurement station and a remote station, which is placed at a sufficiently large

distance (e.g. STEPHAN & STRACK, 1991; OLSEN & HOHMANN, 1992). After the estimation of a horizontal transfer function the noise from the remote station can be used to estimate and subtract the noise at the measurement station. The method can lead to a great noise reduction, but requires two precisely synchronized acquisition systems. It is logistically and technically complex and consequently not relevant in the scope of this thesis.

SPIES (1988) proposed to reconstruct the noise in the vertical magnetic component by simultaneous measurement of the horizontal components via the "TEM-tipper". His approach is based on the fact that for 1D models the response of the layered earth in the horizontal components is zero (WARD & HOHMANN, 1987). Therefore, under the assumption of a 1D layered earth, any potentially measured signal in the horizontal components must relate to noise and can be used to reconstruct the noise in the vertical component ( $\rightarrow$  TEM-tipper). Apart from the strong restriction to 1D models, this approach is problematic because it requires the simultaneous measurement of the horizontal field components, which usually have small magnitudes. Due to the device specifics of the LAPTEM, a simultaneous measurement of all components is impossible for the old configuration and problematic for the new configuration (s. Appendix A, p. 133ff).

Apart from the above processing schemes, which require the measurement of additional signals, several techniques have been proposed which directly work with the measured data to improve the signal-to-noise ratio. All methods have to deal with the fact that transient signals are inherently broadband, since they resemble delta spikes in the time domain. Advanced filtering concepts like recursive filters (notch & delay) and lockin filters, which can lead to a significant reduction of noise while leaving the amplitude of the true transient intact, have been proposed by the LOTEM<sup>1</sup>-workgroup at the University of Cologne (e.g. STRACK ET AL., 1989; HANSTEIN, 1996; SYLVESTER, 1996; THERN, 1996). In the scope of this thesis the concept of lockin filtering is integrated into the processing scheme in the wavelet domain (chap. 2.4.4).

Lockin filters try to approximate noise in the signal free part of a measurement - i.e. during late times of the transient measurement, where no or only little signal energy is left - by a harmonic noise series  $S_{HN}$ :

$$S_{HN}(t) = \sum_i A_i \cdot \cos(2\pi f_i \cdot t + \varphi_i) \quad \mathbf{2-28}$$

The noise series is then extended into the signal part - i.e. to early times of the transient measurement - and subtracted. This offers the advantage that noise at certain frequencies can be greatly reduced without altering the signal shape of the transient, provided that the frequencies **2-28** are determined with great accuracy. Small inaccuracies in the determined

---

1. *Long-offset transient electromagnetics*

frequencies can lead to a dephasing between the true noise and the estimated noise series, when the noise series is extended into the signal part, rendering the lockin filter useless.

HANSTEIN (1996) assumes a single harmonic of a known frequency and solves a least squares approximation to determine its amplitude and phase. To avoid a dephasing of the lockin filter and to account for local variations of the noise frequency, he splits up the measured signal into segments and performs the parameter estimation and the noise cancellation segment-wise. An extension of the noise series from segments into the signal part is only performed for times close to zero, where the transient is dominant in the measured signal. For segments where the transient and the harmonic noise roughly have amplitudes of the same order, an additional polynomial of 3<sup>rd</sup> degree, which represents the transient signal, is integrated in 2-28. This is done to avoid systematic errors in the estimation of amplitude and phase. BUTLER & RUSSELL (2003) show that lockin filters can also be constructed for a whole set of frequencies at once. They simultaneously determine all parameters in 2-28 in their processing of seismic and seismoelectric signals.

### 2.4.2 Wavelet Transformation - General Concept

Basic concepts of the wavelet transformation (WT) as presented in this chapter are taken from DAUBECHIES (1994), FRAZIER (1999), VALENS (2004), and MATHWORKS (2005). Further references cited in this chapter are secondary references found therein.

Without restricting the generality of the WT, a time dependency of the analyzed signal will be assumed hereafter. It is also assumed that the analyzed signal has finite energy. Complex wavelets will not be considered in this basic summary of the wavelet transformation. In this thesis the Matlab Wavelet Toolbox is used for calculations.

#### Continuous Wavelet Transformation

Similar to the Fourier transformation and the inverse Fourier transformation (FT & IFT), the continuous wavelet transformation and its inverse (CWT & ICWT) are defined as integral transformation pair, which allow the transformation of a function  $f(t)$  from the time domain to the transform domain and a perfect reconstruction by the inverse transformation:

$$f_{WT}(a, b) = \int_{-\infty}^{\infty} f(t) \cdot \psi_{a,b}(t) dt$$

$$f(t) = \frac{1}{C_{\psi}} \iint_{-\infty}^{\infty} f_{WT}(a, b) \cdot \psi_{a,b}(t) \frac{da db}{a^2}$$
2-29

Contrary to the FT, the basic basis function  $\psi$  of the WT is not specified explicitly in the general formulation of the transformation. SHENG (1996) showed that for a perfect reconstruction of the original signal, the admissibility constant  $C_{\psi}$  in 2-29 must be finite and greater zero:

$$C_\psi = \int_{-\infty}^{\infty} \frac{|\psi_{FT}(\omega)|^2}{|\omega|} d\omega \quad 0 < C_\psi < +\infty \quad \mathbf{2-30}$$

This admissibility condition has important implications for the yet unspecified basis function in **2-29**. First of all it excludes the trivial solution  $\psi=0$ . Additionally, if the admissibility condition in **2-30** is met, it follows that:

$$\Rightarrow \quad |\psi_{FT}(\omega)|^2 \Big|_{\omega=0} = |\psi_{FT}(\omega)|^2 \Big|_{\omega \rightarrow \infty} = 0 \quad \Rightarrow \quad \int_{-\infty}^{\infty} \psi(t) dt = 0 \quad \mathbf{2-31}$$

Since the amplitude spectrum of the basis function vanishes towards zero and large frequencies in the frequency domain, it must have the spectrum of a bandpass. Furthermore, the average of the basis function in the time domain must be zero, because of the vanishing amplitude spectrum at zero frequency.

Apart from the admissibility condition in **2-30** the basis function needs to meet regularity conditions, which will not be discussed in detail here. They basically state that the basis function should be sufficiently smooth and compact in the frequency and time domain. Combining the admissibility and regularity conditions, they require  $\psi$  to be an oscillatory, i.e. wave-like function with a limited duration in time. Thus, functions, which fulfill these conditions are generally called "wavelets".

The most important relationships established in the basic formulation in **2-29** are the scaling and translation of a "mother-wavelet"  $\psi$ . The scaling and translation parameters  $(a,b)$  define a "wavelet-family" with wavelets of equal shape, but variable dilatation and position:

$$\psi_{a,b}(t) = \frac{1}{\sqrt{a}} \cdot \psi\left(\frac{t-b}{a}\right) \quad a, b \in \mathbb{R}; \quad a > 0 \quad \mathbf{2-32}$$

Fig. 2-20 exemplarily depicts the connection between a "mother-wavelet" (upper left) and its scaled and translated versions as in **2-32**. From a visual comparison it is clear that the scaling of the wavelet influences its frequency contents, which may also be expressed in terms of the scaling theorem of the FT. The general scaling theorem states that for a signal the dilatation in the time domain will lead to an inversely proportional compression in the frequency domain and vice versa:

$$f(t) \leftrightarrow f_{FT}(\omega) \quad \Leftrightarrow \quad f(at) \leftrightarrow \frac{1}{|a|} f_{FT}\left(\frac{\omega}{a}\right) \quad \mathbf{2-33}$$



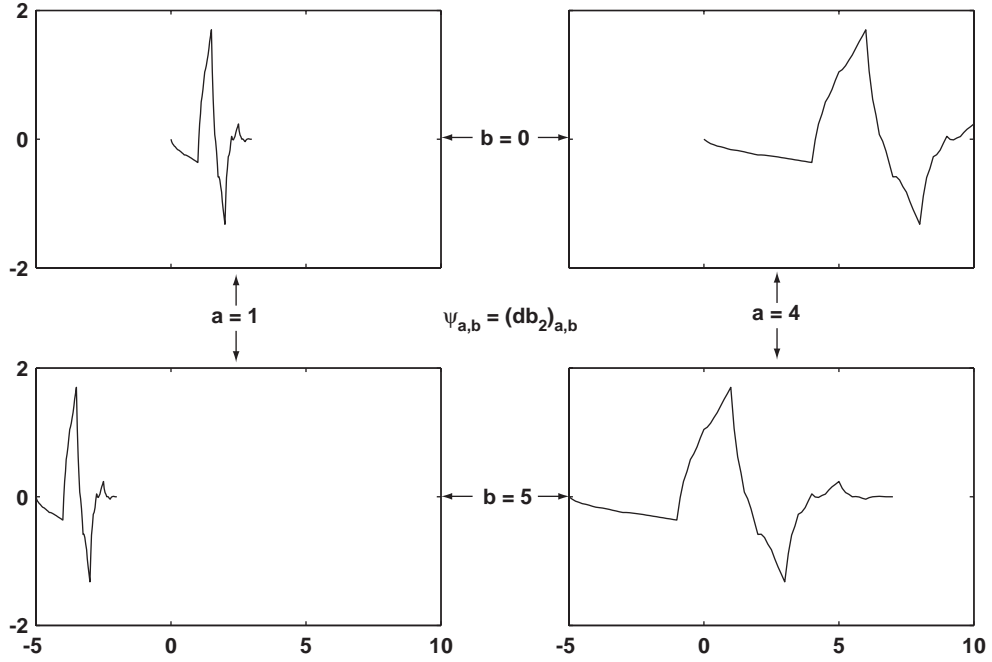


Fig. 2-20: Scaling and translation of the db2 wavelet function (Daubechies wavelet, order 2).

The application of the general scaling theorem to the scaling relationship of wavelets (2-33), neglecting the translation  $b$  for the moment, yields:

$$\psi(t) \leftrightarrow \psi_{FT}(\omega) \Leftrightarrow \psi_a(t) = \frac{1}{\sqrt{a}} \psi\left(\frac{t}{a}\right) \leftrightarrow \psi_{WT}(a\omega) \quad 2-34$$

This means that, due to the choice of the scaling relationship, all wavelets of a family share the same amplitude characteristic in the frequency domain, which is only shifted and scaled along the frequency axis. In other words, the ratio between the center frequency and the bandwidth of wavelet spectrums is invariant to the scaling of the wavelets.

### Multi Resolution Analysis

Because of the continuous choice for scale and translation, the information in the CWT is highly redundant. The CWT is computationally inefficient and mostly used for analytic and illustrative purposes. To reduce the redundancy of the CWT, the scaling and translation parameter can be restricted to dyadic values, i.e. powers of two:

$$a = 2^j; b = k \cdot 2^j = k \cdot a \quad j, k \in \mathbb{Z} \quad 2-35$$

In this equation,  $j$  is called the level (of scaling). The given formulation greatly reduces the redundancy of the CWT, because the members of the wavelet family are now only scaled and transformed in discrete steps:

$$\psi_{j,k}(t) = \frac{1}{\sqrt{2^j}} \cdot \psi\left(\frac{t - k \cdot 2^j}{2^j}\right) \quad j, k \in \mathbb{Z} \quad 2-36$$

Note that in this formulation the wavelet functions are still continuous.

Daubechies (1994) showed that under certain conditions the dyadic wavelet family in **2-36** forms an orthonormal basis and allows the perfect reconstruction of a decomposed signal ( $\rightarrow$  **2-29**, top). Since the wavelets of such an orthonormal basis only allow discrete scaling and translation, the ICWT (**2-29**, bottom) needs to be reformulated:

$$f(t) = \sum_{j,k \in \mathbb{Z}} f_{WT}(j, k) \cdot \psi_{j,k}(t) \quad 2-37$$

With this formulation, the detail  $D$  and the approximation  $A$  of a signal for a fixed level  $J$  are defined as follows:

$$\begin{aligned} D_J &\stackrel{\text{def}}{=} \sum_{k \in \mathbb{Z}} f_{WT}(J, k) \cdot \psi_{J,k}(t) \\ A_J &\stackrel{\text{def}}{=} \sum_{j > J} D_j \end{aligned} \quad 2-38$$

It can be shown that for certain types of wavelets the approximations  $A_j$  can be expressed in terms of a scaling function  $\Phi$ , which is uniquely defined by the mother wavelet. The concept of scaling functions was first introduced by MALAT (1989). Using the same dyadic scaling and translation scheme as for the mother wavelet ( $\rightarrow$  **2-35**), the scaling function is related to the approximations at level  $J$  as follows:

$$A_J = \sum_{k \in \mathbb{Z}} f_{WT}(J, k) \cdot \phi_{J,k}(t) \quad 2-39$$

Some general statements about details and approximations can be derived in short to explain their significance:

- A detail  $D_J$  represents a bandpass filtered version of the analyzed signal, because all wavelets involved in **2-38** refer to the same scale and, thus, the same amplitude spectrum.
- If a dyadic wavelet family forms an orthonormal base and a perfect reconstruction is possible using **2-37**, the spectra of wavelets belonging to adjacent levels must overlap, i.e. there can be no gap between adjacent wavelet spectra.

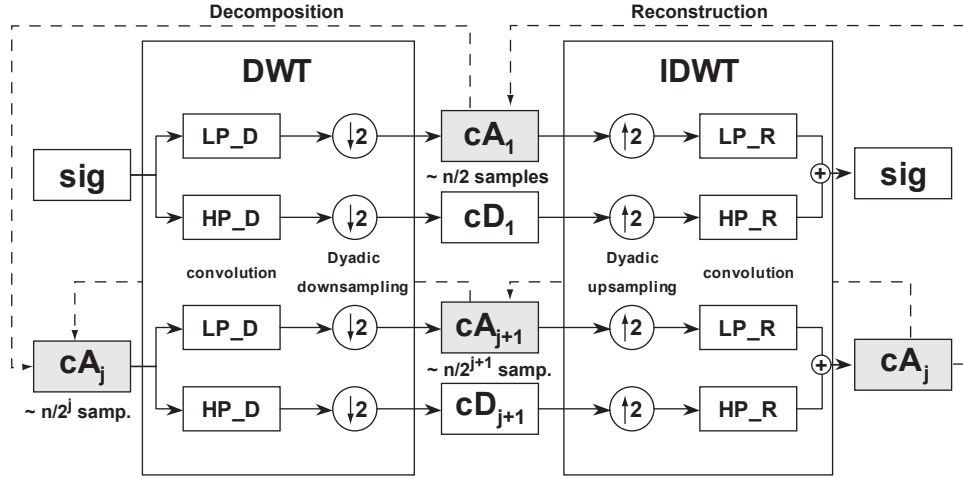


Fig. 2-21: Principle of the discrete wavelet transformation (DWT), its inverse (IDWT) and of the multi resolution analysis. See text for explanations.

- By increasing the scale-level, the wavelet spectrum is scaled to lower frequencies ( $\rightarrow$  2-34). Consequently, detail levels at higher scales represent lower frequency aspects of the analyzed signal. Similarly, detail levels at lower scales represent high frequency aspects of the analyzed signal.
- The approximation  $A_J$  is constructed from all details with levels  $j > J$ . Since higher detail levels refer to successively lower frequencies, the approximation  $A_J$  comprises a lowpass filtered version of the analyzed signal.
- Due to the orthogonality of the wavelet base, details at different levels are orthogonal to each other.
- For the same reason, the approximation  $A_J$  is orthogonal to all details  $D_j$ , where  $j \leq J$ .

With the above definitions and the formulation of the ICWT for an orthonormal, dyadic base as in 2-29, the following relations hold:

$$f = \sum_{j \in \mathbb{Z}} D_j = \sum_{j > J} D_j + \sum_{j \leq J} D_j = A_J + \sum_{j \leq J} D_j \quad 2-40$$

This shows how - in terms of the WT - a signal can be completely decomposed into details, which together contain the high frequency content in bandpass filtered versions of the original signal, and into an approximation, which carries the remaining low frequency content.

### Discrete Wavelet Transformation

In the discrete wavelet transformation (DWT) the analyzed signal, wavelet and scaling functions are all discrete. The DWT is efficiently implemented by using digital lowpass and

highpass filters, which are uniquely determined by the scaling function and wavelet function, respectively.

Fig. 2-21 illustrates how the decomposition of a signal (top, left) is initiated by convolving the input signal (sig) with the appropriate low- and highpass decomposition filters (LP\_D, HP\_D). After dyadic downsampling, which is a consequence of the dyadic scaling ( $\rightarrow$  2-35), the combined number of approximation- and detail-coefficients ( $cA_1$ ,  $cD_1$ ) approximately equals the number of samples in the original signal. The original signal can be reconstructed (top, right) by performing the inverse DWT (IDWT), which involves the dyadic upsampling of the coefficients ( $cA_1$ ,  $cD_1$ ) and convolution with the appropriate reconstruction filters (LP\_R, HP\_R).

After the first decomposition step (top, left) a second decomposition can be initiated by reusing the approximation coefficients in the decomposition scheme ( $cA_1 \rightarrow$  lower left). The decomposition of approximations can be applied iteratively ( $cA_{j+1} \rightarrow$  lower left). Since each decomposition step approximately halves the number of coefficients in the associated approximation, it is appropriate to stop the iteration, if the number of coefficients in  $cA_{j+1}$  approximately equals the number of coefficients in the decomposition filters (LP\_D, HP\_D). It should be noted that all decomposition steps use the same set of decomposition filters.

This iterative process, which is called multiresolution analysis (MRA), creates a succession of detail- and approximation coefficients ( $cD_1$ ,  $cD_2$ , ...,  $cD_J$ ,  $cA_J$ ). It can be reversed for a perfect reconstruction of the original signal by iteratively applying the IDWT to the appropriate details and approximations as depicted on the right hand side of Fig. 2-21 (i.e.  $cD_J$  &  $cA_J \rightarrow cA_{J-1}$  |  $cD_{J-1}$  &  $cA_{J-1} \rightarrow cA_{J-2}$  | ... |  $cD_1$  &  $cA_1 \rightarrow$  sig).

By the manipulation of coefficients ( $cA_j$ ,  $cD_j$ ), certain aspects of the original signal may be extracted, suppressed or enhanced. Specific detail- or approximation levels as in 2-38 (e.g.  $D_3$ ) can be constructed by first performing the MRA ( $\Rightarrow cD_1$ ,  $cD_2$ ,  $cD_3$ ,  $cA_3$ ), then setting all unwanted coefficients to zero ( $\Rightarrow cD_1=cD_2=cA_3=0$ ) and reversing the MRA by iterative application of the IDWT as described.

## Examples

The first example in Fig. 2-22 demonstrates the bandpass and lowpass characteristics for two different wavelets and the associated scaling functions (top panels). Using the MRA, details and approximations ( $D_2$ ,  $D_3$ ,  $D_4$ ,  $A_4$ ) are calculated for input signals, which contain white noise ( $\rightarrow$  random numbers, 20kHz sampling frequency assumed). Because white noise in the time domain transforms to white noise in the frequency domain, details and approximations contain band limited white noise which resembles the filter characteristics of the wavelet or scaling function, respectively. The average of many amplitude spectra reduces the scatter of the band limited white noise and reveals the filter characteristics:

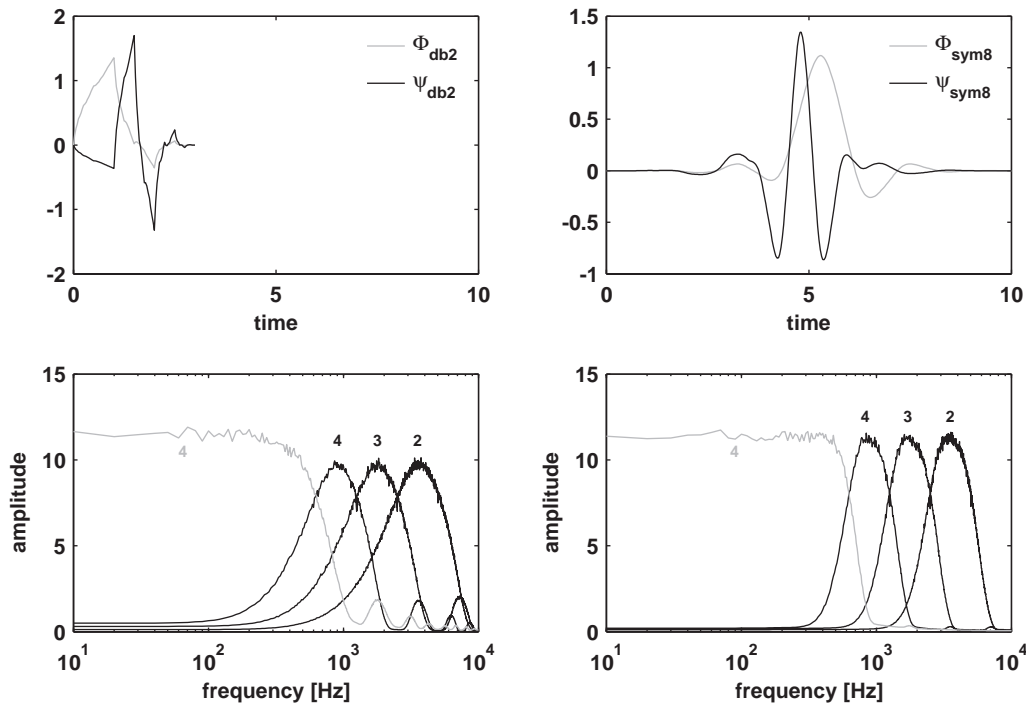


*Fig. 2-22:* The top panels show two exemplary wavelet and scaling functions (black and gray, resp.). Wavelets with small orders have a short support length (i.e. width) and tend to be irregular in shape (top left), whereas wavelets of higher orders have a long support length and generally smoother shapes (top right). For white noise as input signal, the averaged amplitude spectra are shown in the lower panels for details (black, scale-level 2,3,4) and approximations (gray, scale-level 4). See text for explanations.

- Details contain bandpass filtered versions of the analyzed signal, approximations contain the remaining signal informations at low frequencies.
- Due to the dyadic transformation of wavelets in the MRA, the bandwidth and centerfrequency of details are exactly halved when going to the next higher level (note that the frequency axis is logarithmic!). This demonstrates that the ratio between the center frequency and the bandwidth of a wavelet spectrum is invariant to the scaling of wavelets.
- Wavelets with a short support width (top, left) are connected to bandpass filters with a greater bandwidth as compared to wavelets with a longer support width (top, right). The support width is defined as the time range on which the amplitude of a wavelet differs from zero.
- Wavelets with a "smooth" shape will also have a "smooth" frequency spectrum (right panels). The amplitude spectra of the wavelet db2 and of the associated scaling function, which both have irregular shapes, contain several side-lobes (left panels).

In Fig. 2-23 the localization of wavelets in time and frequency is demonstrated by the decomposition of a signal (top) with assumed sampling frequency of 1 kHz, which contains a harmonic (50Hz) and a single spike in the first and second half, respectively. In the detail-coefficients (bottom) the harmonic is mainly captured in the coefficients at scale levels 3 and 4, which is in agreement with the previous example in Fig. 2-22. From the displayed coefficients alone it is immediately clear that the harmonic is confined to the first half of the original signal, i.e. the signal energy of the harmonic part of the transformed signal is well localized in the detail coefficients. The same holds true for the spike in the second half of the signal, which is also clearly identified by only a few coefficients. This is in contrast to the FT, where the energy of such a delta impulse would be spread to all

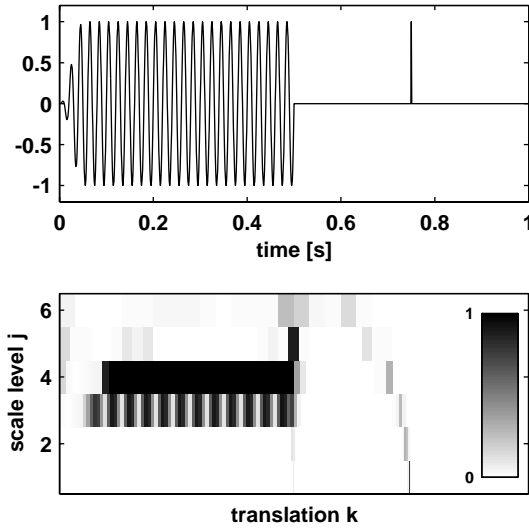


Fig. 2-23: Absolute value for detail coefficients (bottom) after the MRA (sym8, s. Fig. 2-22) of an exemplary signal (top). The harmonic is damped at times close to zero for illustrative purposes. Please note that details at small scale levels contain more coefficients as compared to large scales, which is due to the dyadic downsampling (s. Fig. 2-21).

Fourier coefficients. It should be noted that most coefficients are colored white, meaning that they (nearly) have zero amplitude. As suggested by Fig. 2-22, the resulting distribution of signal energy in the coefficients in this example strongly depends on the type of wavelet used in the MRA.

### Extension to 2D

In the 2D extension of the WT, mother wavelets and scaling functions can be defined by tensorial products of their 1D counterparts. In the 2D case the MRA takes a slightly different form as compared to Fig. 2-21, because the dyadic downsampling has to be applied to both, rows and columns. As in the 1D case the details and approximations ( $D_j, A_j$ ) contain bandpass- and lowpass filtered versions of the original signal. The 2D MRA will be used in chap. 4.1.2 to investigate details of a satellite image.

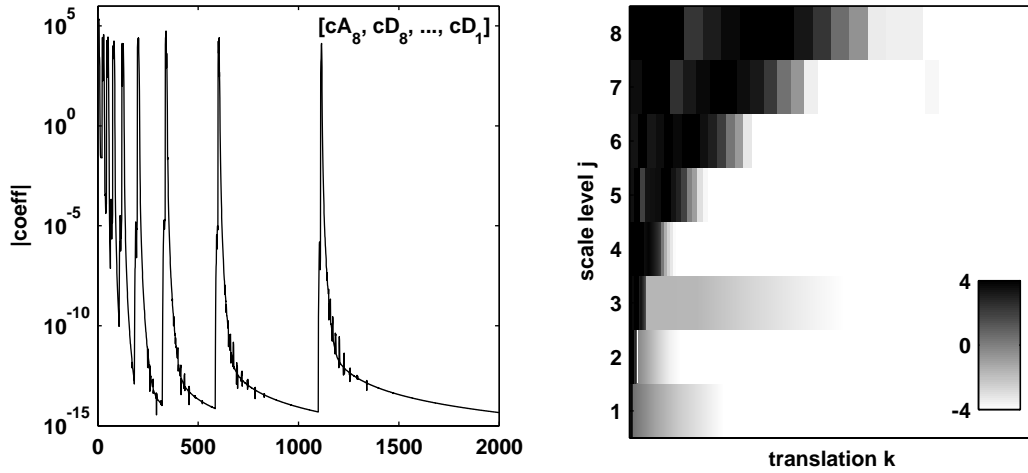


Fig. 2-24: MRA using the sym8 wavelet of an arbitrary transient with 2000 samples. The left panel shows the absolute value of all coefficients in the indicated order. In the right panel only the detail coefficients are displayed with respect to their level and translation. The color bar is adjusted to the logarithmized absolute values to account for the large dynamic range of coefficients.

### 2.4.3 TEM Signals in the Wavelet Domain

Fig. 2-24 gives a first impression of the energy localization in the wavelet domain for the transformed transient of an arbitrary 1D model. While the original signal spans a dynamic range of about 7 decades with its 2000 samples (not depicted), there are only very few coefficients in the wavelet domain with significant amplitudes and most coefficients are more than 10 decades below the maximum amplitude. It is trivial to show that the original transient can be recovered almost perfectly when setting the smallest  $\sim 85\%$  of coefficients exactly to zero, since they have vanishing amplitudes anyway. In the right panel the colorbar is chosen accordingly to highlight detail coefficients, which have a relevant amplitude not smaller than 8 decades below the maximum amplitude. The relevant detail coefficients form well-defined bands, which successively widen when going from small to large scales levels. It should again be pointed out that the number of detail coefficients decreases in successively higher levels, which is due to the downsampling in the MRA. Therefore, the widening of coefficient bands as depicted in the right panel does not necessarily signify that the total number of relevant coefficients increases with successively higher levels, but rather that they cover successively larger ranges on the translation axis. Because the translation  $k$  is related to the time axis, this is a mere consequence of the fact that high frequencies dominate early times in transients, whereas at late times low frequencies prevail (comp. Fig. 2-3, p. 12).

#### Coefficient Bands in the Wavelet Domain

A systematic analysis was conducted to further investigate the characteristics and stability of coefficient bands in the wavelet domain for different wavelet types and measurement

configurations in dependence to differing transient TEM signals. Generally, the measurement configuration (sampling rate; first time channel; loop area; transmitter current; gain; resolution of AD-converter) needs to be specified to define the discrete sampling times and to constrain the relevant time range for the analysis. The relevant time range is simply defined as the time range, for which the true voltage ( $\rightarrow$  2-1) of a model transient is within the resolution limits of the specified measurement configuration.

For a given wavelet type and measurement configuration, the analysis was performed by creating a set of transient TEM-signals, which was calculated from randomly selected 1D models using the sampling times as defined by the measurement configuration. The random models were constructed by randomly choosing a number of layers (1-6) with arbitrary resistivities (1-1000  $\Omega$ m) and layer thicknesses. In the set all transients were supposed to be noise-free at this stage.

One may argue that it would have been necessary to include transient responses from 2D or 3D models into this analysis. However, in the 2.5D model study in chap. 2.3.5 (p. 34ff) it was demonstrated that the transient responses of 2D models may readily be explained by 1D transients. Consequently, it is concluded that the above set of random transients forms a representative subset for a wide range of possible transient shapes in the specified resistivity range, which also includes large subset of possible transients related to 2D or 3D models.

For each transient of the set it was tested, which coefficients in the wavelet domain are needed for an acceptable reconstruction. If  $C_{j,k}$  is one of the detail or approximation coefficients of the decomposed transient, this was basically done with the following scheme:

1. Set coefficient  $C_{j,k}$  to zero.
2. Reconstruct transient from all coefficients.
3. Calculate deviation between original and reconstructed transient ( $\rightarrow$  2-41).
4. If the deviation is greater than a certain threshold,  $C_{j,k}$  must be relevant and is consequently reset to its original value. The according scale level and translations ( $j,k$ ) are stored.

The calculation of the tolerated maximum deviation ( $\Delta_{\max}$ ) between the original transient ( $\mathbf{v}_0$ ) and the reconstructed transient ( $\mathbf{v}_{WT}$ ) was restricted to the relevant time range, where the modeled true voltage of  $\mathbf{v}_0$  was within the resolution limits of the specified measurement configuration. The number of samples contained in this time range will be referred to as  $n^{\text{sig}}$ . It was also stored for each measurement configuration and wavelet in the analysis and will be used in the next section. The following formula and threshold were applied in the calculation of the deviation:

$$\Delta_{\max} = \max \left( \left| \frac{\mathbf{v}_0 - \mathbf{v}_{WT}}{\mathbf{v}_0} \right| \right) < 1\% \quad 2-41$$



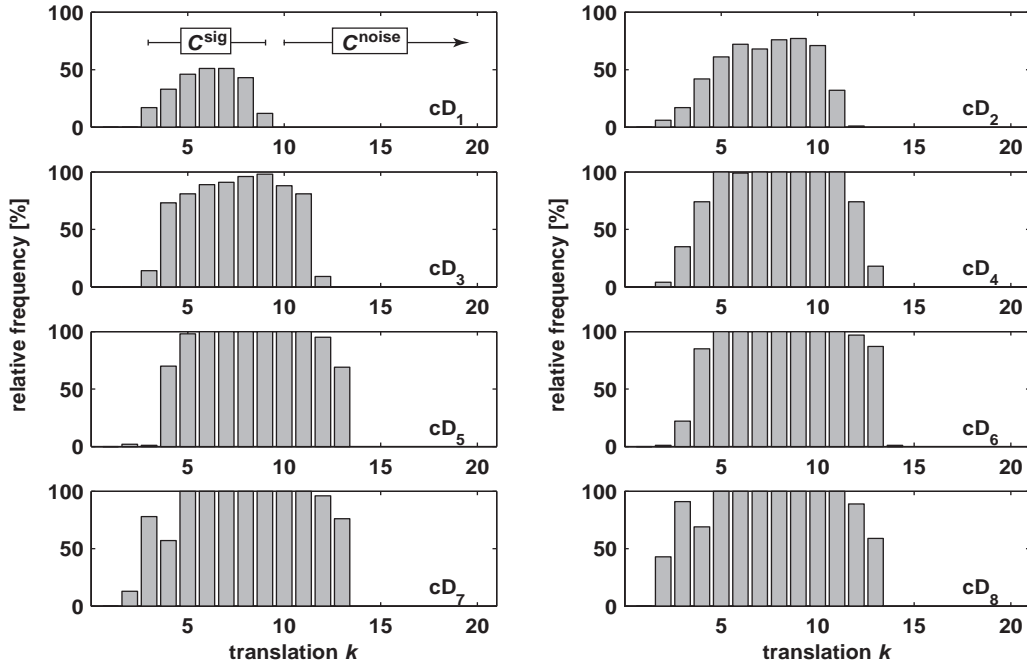


Fig. 2-25: Exemplary result for the analysis of coefficient bands using the sym8 wavelet. The histograms show to which detail coefficients the signal energy of random transients is transferred by the MRA. In this example, coefficients at translations  $k > 15$  never contain any relevant energy (comp. Fig. 2-24, right). The axis limits are chosen accordingly.

The above scheme (1.-4.) was systematically applied to all detail and approximation coefficients and subsequently to all transients in the set. The result of the analysis is a frequency distribution for the  $C_{j,k}$  in the wavelet domain, which depends on the chosen wavelet and measurement configuration.

Fig. 2-25 exemplarily depicts this frequency distribution for the analysis with the sym8 wavelet. The histograms show, which and how frequently coefficients are needed for an acceptable reconstruction of a transient signal and clarify that the signal energy of arbitrary transients is confined to well defined coefficient bands in the wavelet domain. In the following, all coefficients inside or outside these coefficient bands will be called signal coefficients or noise coefficients, respectively ( $C^{\text{sig}}$  and  $C^{\text{noise}}$  in Fig. 2-25). The total number of coefficients in these bands will be denoted by  $nC^{\text{sig}}$  and  $nC^{\text{noise}}$ .

### Comparison of Wavelets by Family and Order

The above analysis was performed for 50 different wavelets - including various orders of the following wavelet types: Daubechies  $\Leftrightarrow$  db; Symlets  $\Leftrightarrow$  sym; Coiflets  $\Leftrightarrow$  coif; Biorthogonal  $\Leftrightarrow$  bior; reverse Biorthogonal  $\Leftrightarrow$  rbio - and for 12 different measurement configurations, which resemble the ones used for measurements in China. The resulting coefficient bands are summarized as tabulated values in Appendix B (p. 149ff).

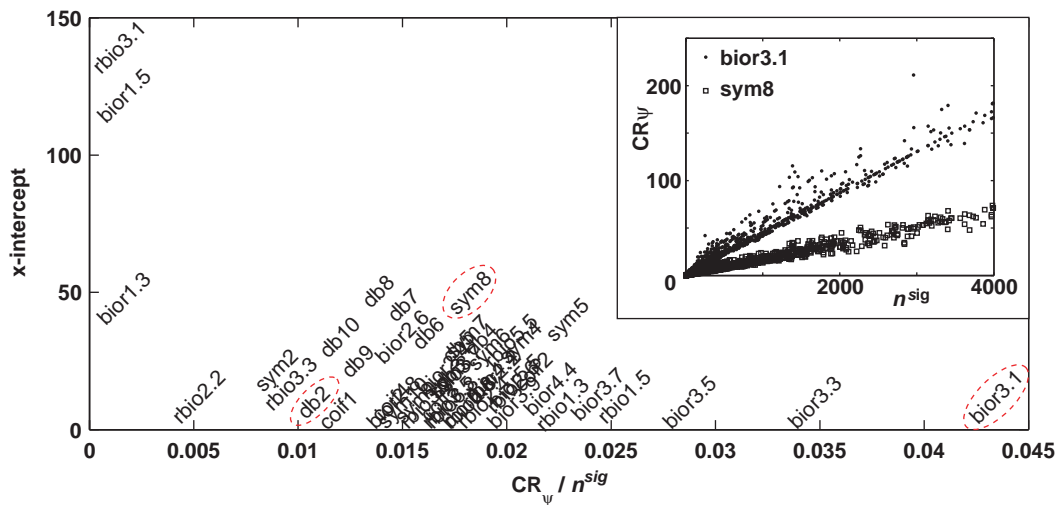


*Fig. 2-26:* Characterization of coefficient bands for all wavelets with respect to the compression rate  $\text{CR}\psi$ . *Inlet:* Quasi linear relationship between compression rate  $\text{CR}\psi$  and number of relevant samples  $n^{\text{sig}}$ , here depicted for all analyzed random transients and measurement configurations for two exemplary wavelets. *Main plot:* A linear regression yields the slope (x-axis) and the x-intercept for the linear relationship. Wavelets which plot further to the right have a higher compression rate and need fewer coefficients to represent arbitrary transients.

Due to the large number of wavelets and measurement configurations analyzed only general trends can be derived:

- For wavelets of low orders (e.g. db1, sym1, bior1.1, and rbio1.1), i.e. wavelets with the shortest support lengths, the coefficient bands are very wide. Consequently, the application of these wavelets in a MRA of transient signals does not lead to a localization of the signal energy in the wavelet domain.
- For the remainder of wavelets, the coefficient bands are well defined, which signifies a better localization of signal energy in the wavelet domain. The exact position and width of coefficient bands depends on the wavelet. For many wavelets the relative frequency distribution resembles the one for the sym8 wavelet in Fig. 2-25.

In the analysis of random transients, the compression rate  $\text{CR}_\psi$  for a specific wavelet  $\psi$  can be defined as

$$\text{CR}_{\psi} = \frac{n^{\text{sig}}}{nC^{\text{sig}}} \quad \mathbf{2-42}$$

It turns out that the so defined compression rate is a good parameter to summarize and characterize the analysis of random transients for all wavelets. In the inset in Fig. 2-26 the compression rate is plotted against the number of resolvable samples in the transient for all

analyzed random transients and all measurement configurations. A linear relationship between the two parameters is evident, exemplarily depicted for two wavelets in the inlet. A large positive slope signifies a high compression rate, meaning that only few coefficients are needed to represent an arbitrary transient in the wavelet domain. A linear regression was used to determine the slope for all wavelets. In the main plot of Fig. 2-26 all wavelets are plotted with respect to the determined slope on the x-axis. Wavelets to the right have high compression rates and wavelets to the left have relatively low compression rates. For the majority of wavelets the slope is in the interval [0.015-0.025]. A better performance is only indicated for wavelets of the types bior3.x, where slopes with values up to 0.045 can be achieved for the wavelet bior3.1. Wavelets with slopes below 0.05 generally offer a poor localization of transient signals in the wavelet domain and are not considered further.

With respect to Fig. 2-26, the absolute number of signal and noise coefficients can exemplarily be estimated for a transient with 1000 samples as follows:

$$\text{slope} = 0.045 \Rightarrow CR_{\psi} = 45x \Rightarrow nC^{\text{sig}} \sim 22; nC^{\text{noise}} \sim 978$$

$$\text{slope} = 0.030 \Rightarrow CR_{\psi} = 30x \Rightarrow nC^{\text{sig}} \sim 33; nC^{\text{noise}} \sim 967$$

$$\text{slope} = 0.010 \Rightarrow CR_{\psi} = 10x \Rightarrow nC^{\text{sig}} \sim 100; nC^{\text{noise}} \sim 900$$

#### 2.4.4 Filtering in the Wavelet Domain

In the following chapter all analyzed signals have a sampling frequency of 20kHz, since most measurements in China were conducted with this sampling frequency.

##### Basic Filtering

For a noisy transient signal the most basic filter in terms of the results in the previous chapter consists of simply discarding, i.e. setting to zero, all noise coefficients  $C^{\text{noise}}$  of a decomposed signal. This assumes that the coefficient bands for the measurement configuration under consideration are known. If not, they have to be constructed by an analysis similar to the one demonstrated in the previous chapter, which however needs to be performed just once for each measurement configuration.

Fig. 2-27 depicts the effect of discarding the noise coefficients of transient signals with added noise for three wavelets, which are representative for the distribution of compression rates in Fig. 2-26. White noise (top row) is efficiently suppressed by all wavelets. For harmonic noise (middle row) the wavelets db2 and bior3.1 lead to almost no enhancement in the filtered signal. For the sym8 wavelet a suppression is evident at late times in the transients. Generally, the application of the sym8 wavelet leads to better noise suppression in both cases.

The effect of the basic filtering scheme resembles that of a lowpass with variable corner frequency. Therefore, it basically has the same effect as the log-gating in the common processing of transient signals (s. chap. 2.4.1, p. 38). Consequently, the log-gating of a noisy

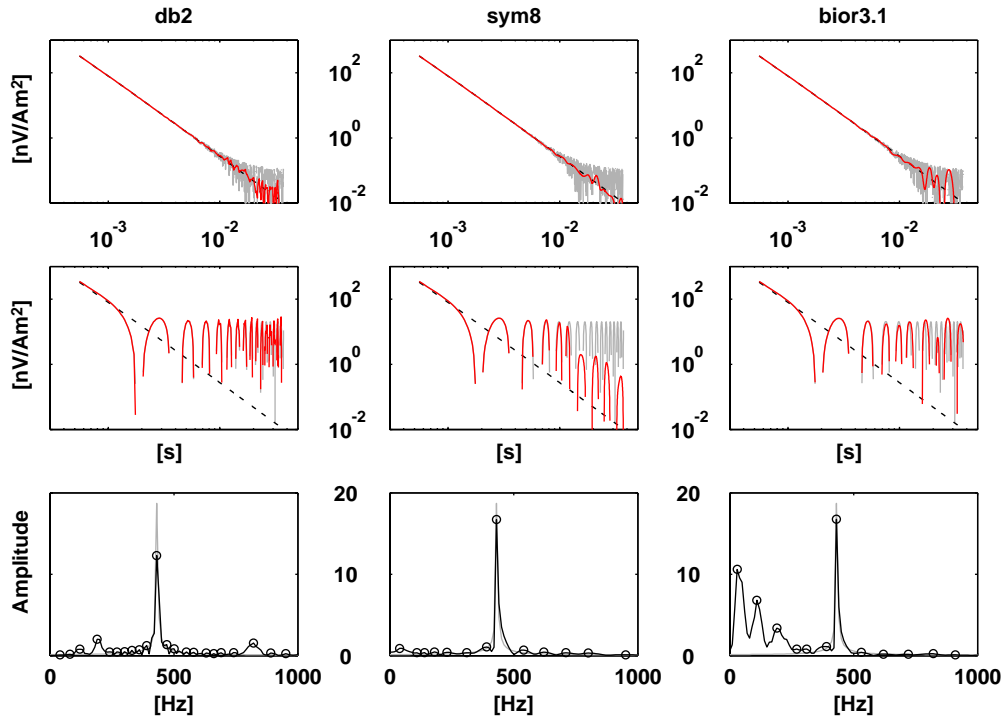


Fig. 2-27: Basic filtering (measurement configuration 10; Appendix B) by rejection of all noise coefficients for three wavelets (columns). The filtering is applied to a transient (15Ωm halfspace, dashed lines) with added noise (gray lines; top row: white noise; middle row: harmonic noise, 432Hz). All noise amplitudes are chosen with 20nV/Am<sup>2</sup>. The filtered signals are depicted with red lines. The bottom row displays amplitude spectra constructed from the noise coefficients (black lines). The true amplitude spectra are depicted by gray lines.

transient, which is preprocessed with the basic filtering scheme in the wavelet domain, leads to the same or only slightly better result as compared to the log-gating without preprocessing. Therefore, the main advantages of the basic filtering arise when working with the pre-logged data.

In the bottom row of Fig. 2-27 the true noise amplitude spectrum (gray lines), which contains just one peak at 432Hz, is estimated from the noise coefficients. This is done by discarding, i.e. setting to zero, the signal coefficients  $C^{\text{sig}}$ . By using only the noise coefficients, an approximation of the true noise signal is reconstructed in the time domain and subsequently transformed into the frequency domain. It is worthwhile to note that this reconstruction of the noise signal and the subsequent approximation of the amplitude spectrum is completely decoupled from the shape of the transient signal, as long as the associated underground model does not exceed the resistivity limits (1-1000Ωm) assumed in chap. 2.4.3. It does however depend on the length of the transient signal. With the definition of the unit decibel as

$$\text{dB}_{A_0} \stackrel{\text{def}}{=} 20 \cdot \log_{10} \left( \frac{A}{A_0} \right) \quad 2-43$$

the quality of the approximations can shortly be quantified: the true amplitude is equally well approximated by the sym8 and bior3.1 wavelets (-1.5dB) and with less precision by the db2 wavelet (-4.3dB). The distances between the approximated amplitudes and the side-lobes are 25dB, 14.5dB and 2.7dB for the sym8, db2 and bior3.1, respectively. For the db2 and bior3.1 wavelet the side-lobes are due to the irregular shapes of the wavelets and their inherent irregular bandpass characteristics (exemplarily for db2 in Fig. 2-22, p. 47).

It can be concluded that smooth wavelets (e.g. sym8) have the best filter characteristics for the analysis of TEM transients. Wavelets with highly irregular shapes (i.e. bior 3.x) have a great potential for compressing TEM-signal, but exhibit undesirable filter characteristics.

### Selection According to Noise Energy

Instead of just discarding the noise coefficients as demonstrated in the previous section, one may also choose to analyze the noise coefficients in terms of their energy. To take advantage of the properties of the wavelet transformation, the noise energy should be calculated separately for each scale level. If chosen this way, the noise coefficients at a given level  $j$  can directly be related to a certain frequency band (comp. Fig. 2-22; p. 47). Additionally, it makes sense to only include a few noise coefficients, which are located directly behind the signal coefficient band (sim. Fig. 2-25, p. 51, top left). This automatically assures that the energy of high and low frequency noise is estimated at early times and late times, respectively. Consequently, the noise energy at a certain scale level  $j$  is defined by:

$$E_j^{\text{noise}} = \sum_{k'=1}^{\min(15, nC_j^{\text{noise}})} |C_{j,k'}^{\text{noise}}|^2 \quad 2-44$$

In the chap. 2.4.5 the noise energy is used as selection criterion for the rejection of bad data.

### Noise Prediction Filtering

Fig. 2-27 demonstrates that wavelets with regular shapes ( $\rightarrow$  sym8) are suitable for the approximation of a noise spectrum, which only contains a single harmonic. In a similar manner, Fig. 2-28 depicts the results for the reconstruction of a whole noise series, which contains the first 10 odd multiples of 50Hz. The analyzed noise signals contain 2000 (top) or 3000 (bottom) samples, which equals a signal duration of 100ms and 150ms, respectively. It can be seen that for sufficiently high frequencies, the true and reconstructed spectra are similar and the parameters of the noise series - i.e. amplitudes, frequencies, and phases - can be estimated from the reconstructed noise spectrum.

The noise coefficients of the shorter signal ( $n=2000$ ) obviously do not contain any information of the lowest frequency (50Hz) and, hence, this frequency can not be recovered from the approximated noise spectrum. For the longer signal ( $n=3000$ ), the total number of coefficients in the wavelet domain increases and some of the noise coefficients now contain energy of the 50Hz noise, which can therefore be partially recovered in the approximated noise spectrum. With the given durations of signals it can be estimated that a frequency can only be recovered in the approximated noise spectrum, if the analyzed signal contains a sufficient amount of cycles, in the investigated case here 7.5 cycles ( $=150\text{ms} * 50\text{Hz}$ ).

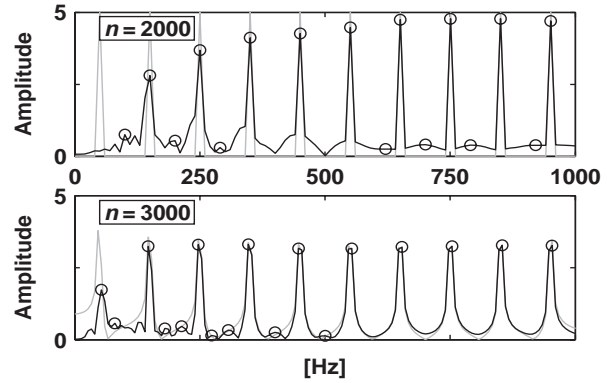


Fig. 2-28: Noise spectra (black lines) from reconstructed noise coefficients ( $\rightarrow$  sym8, sim. Fig. 2-27) for a harmonic noise series (odd multiples of 50Hz) with  $n$  samples. The true amplitude spectra are depicted by gray lines.

The fact that the true noise frequency spectrum can be approximated from the noise coefficients can be used to construct a novel type of noise prediction filter (s. chap. 2.4.1, 2-28), which is designed to remove a harmonic noise series from a transient signals. For a given transient signal which contains an unknown number of noise frequencies, the filter is constructed as follows:

1. By detecting the peaks in the approximated noise spectrum (circles in Fig. 2-27 & Fig. 2-28), the frequencies, amplitudes and phases of the true harmonic noise are approximated for a certain number of harmonics. Peaks belonging to small side lobes are rejected. The resulting harmonic noise series and its coefficients in the wavelet domain are termed  $HN_0$  and  $C(HN_0)$ .
2. For the so determined set of harmonics an associated set of reference noise coefficients is selected from those coefficients, which best represent the noise directly adjacent to the signal coefficients (red shaded area in Fig. 2-29). This set is termed  $C_{\text{ref}}^{\text{noise}}$ .
3. A least squares problem can now be formulated, in which the deviation between the reference coefficients  $C_{\text{ref}}^{\text{noise}}$  and the associated coefficients in  $C(HN_0)$  is minimized. Basically speaking, this means that only coefficients of  $C(HN_0)$  are used, which fall into the red shaded area in Fig. 2-29. The least squares problem is solved using a Levenberg-Marquardt inversion.

If the inversion converges, the resulting harmonic noise model will fit the subset of noise coefficients directly adjacent to the signal bands. The final noise model is then propagated into the signal range and subtracted.

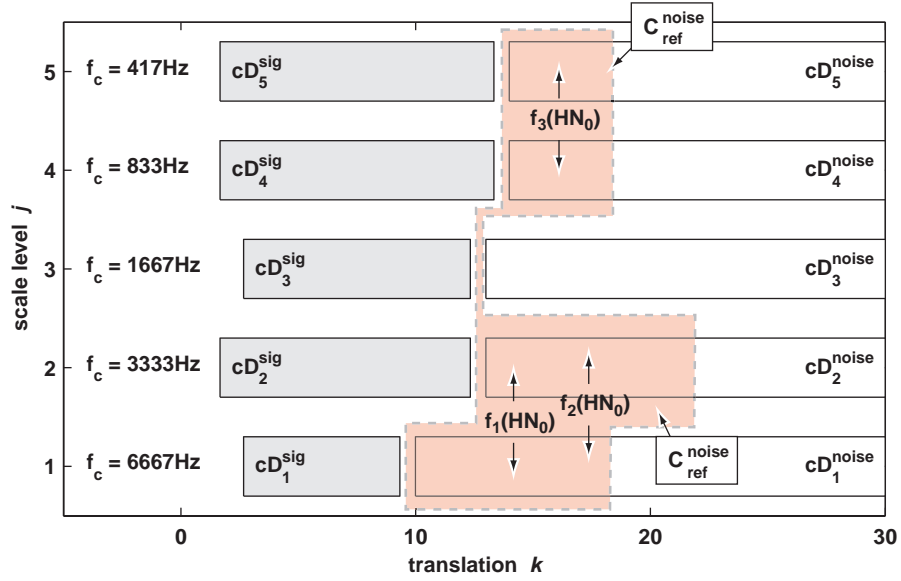


Fig. 2-29: Basic scheme for the selection of reference noise coefficients (red shaded area). The number of coefficients, which is picked from each scale level is determined by the frequencies contained in the approximated harmonic noise series and their location with respect to the scale level.

The optimized parameters in step 3 are the amplitudes, frequencies and phases of the harmonic noise series. In each step of the optimization a harmonic noise series is calculated for these parameters and subsequently transformed into the wavelet domain.

This approach is novel in the sense that it does not fit the harmonic noise series to a segment of the measured signal in the time domain (e.g. HANSTEIN, 1996) but rather to a selected set of noise coefficients in the wavelet domain.

To test the so defined noise prediction filtering, random harmonic noise and white noise are added to arbitrary transients. In the construction of such random harmonic noise the number of harmonics and their frequencies, amplitudes and phases are chosen randomly with only a few restrictions:

- The minimum amplitude needs to be above the amplitude of the white noise.
- A minimum frequency was defined with respect to the analyzed signal length.
- The minimum spacing between two adjacent frequencies must be above 20Hz.

This essentially assures that no beat will occur.

Fig. 2-30 depicts the result of the noise prediction for such a random harmonic noise model, which contains seven randomly picked harmonics. The transient signal is modeled for a 3-layer model and contains 2000 samples. Consequently, the minimum allowed noise frequency is 100Hz. The recovery of the original signal by the noise prediction filtering is extremely good, since all parameters of the harmonic noise are identified correctly. It is

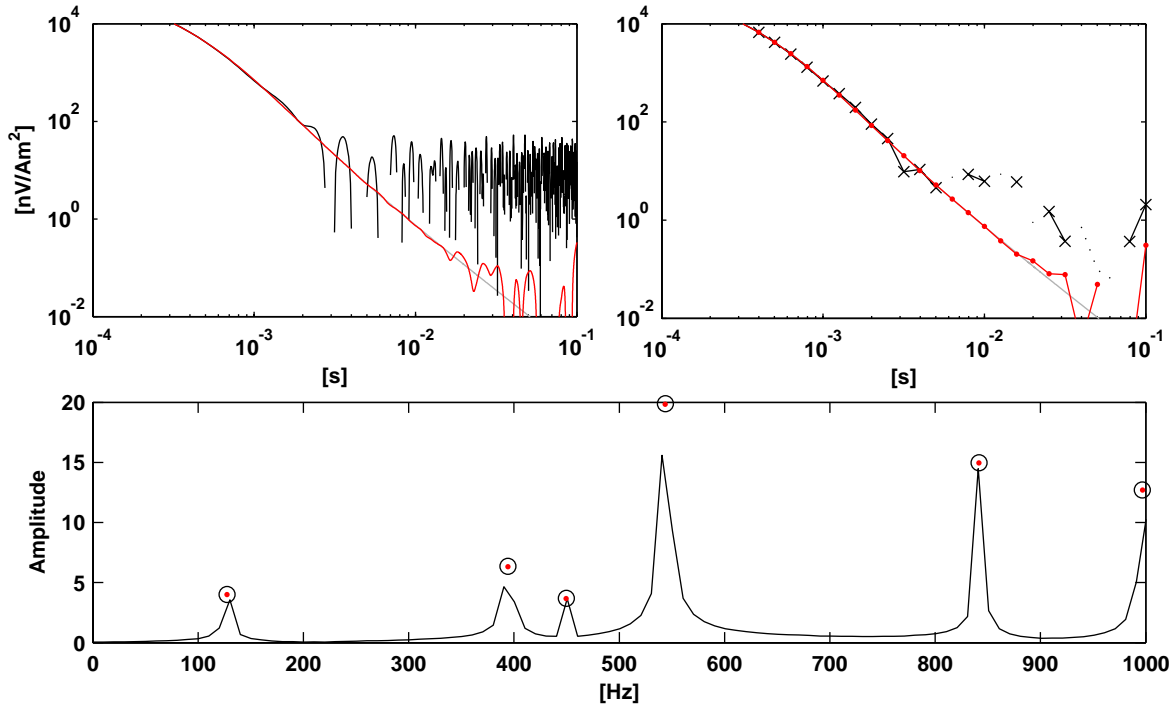


Fig. 2-30: Application of the noise prediction filtering in the wavelet domain to an arbitrary transient (gray lines in top panels) with added random harmonic noise and white noise (black lines in top panels). The red lines show the filtered result. The top left and right panels display the signals prior to and after log-gating, respectively. The lower panel shows the frequency spectrum of the random harmonic noise (line), the random frequencies and amplitudes (circles) and the noise prediction (red points).

interesting to note that in this specific case, only 33 reference coefficients ( $C_{\text{ref}}^{\text{noise}}$ ) are used to recover the 21 parameters of the random model.

Further tests have shown that the noise prediction filtering usually converges to the correct harmonic noise model, if the restrictions for the signal length and the minimum spacing between frequencies are met. Problems can arise, if too many frequencies fall within a narrow frequency band.

In the construction of the noise prediction filtering, the stationarity of the harmonic noise is assumed. A linear chirp signal is used to exemplarily test the stability of filtering in the presence of non-stationary noise. In the plots in Fig. 2-31 the amplitude of chirps is fixed to  $200\text{nV/Am}^2$  and the magnitude of non-stationarity of chirps changes from low to high for plots to the left and right, respectively. Each chirp signal has an instantaneous frequency of  $f_0=200\text{Hz}$  at  $t_0=10^{-4}\text{s}$ , which is linearly increased to  $f_1=f_0*(1+\delta f)$  at  $t_1=10^{-1}\text{s}$ . A comparison of the log-gated transients after the noise prediction filtering (red lines) with the simply log-gated transients (black lines) shows a significant improvement in the recovery of the noise free transient signals (gray lines), if the relative change of the chirp frequency is below 1%.



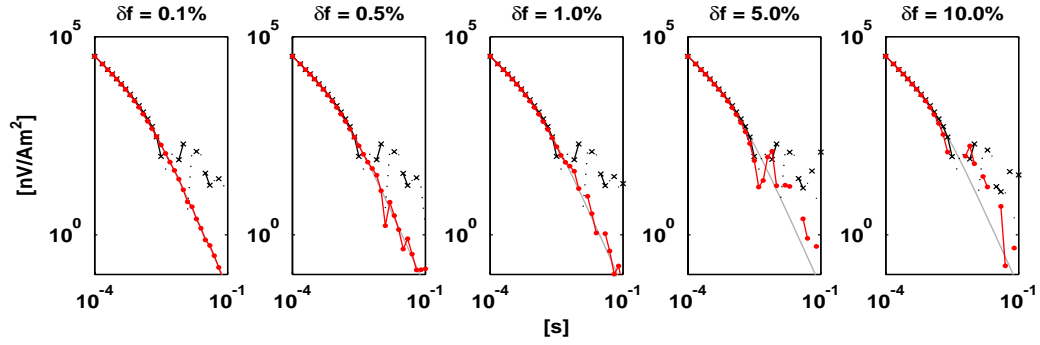


Fig. 2-31: Noise prediction filtering for a transient signal with non-stationary noise (chirp + white noise). In the examples, the base frequency of chirps increases linearly from 100Hz at early times to  $100\text{Hz} \cdot (1 + \delta f)$  at late times. Plots show the log-gated results for the noise prediction filtering (red) and the common processing (black). The transient without noise is displayed as gray line.

This demonstrates that the presented implementation of a noise prediction filtering in the wavelet domain can deal with a certain amount of non-stationarity in the analyzed signal. Further analyses with chirp signals show that the exhibited tolerance to non-stationarity depends on the magnitude and frequency of noise. Generally speaking, it can be stated that the tolerance increases for smaller noise amplitudes and higher frequencies.

### 2.4.5 Examples

In the following, short examples will be given to demonstrate the application of the wavelet based processing schemes to field data measured in China.

#### Basic Filtering

The application of the basic filtering scheme as derived in the previous section was routinely applied in the preprocessing of data from China (Fig. 2-32). Please note that in the adjacent plot the transient data is displayed prior to log-gating.

It can lead to a great reduction of high frequency noise in the pre-loggated data. Due to the lowpass filter characteristics of the log-gating process, which is routinely performed in the common processing, the basic filtering scheme does not lead to a significant improvement in the logged transient.

Therefore, its benefits are mainly in previewing the data prior to logging.

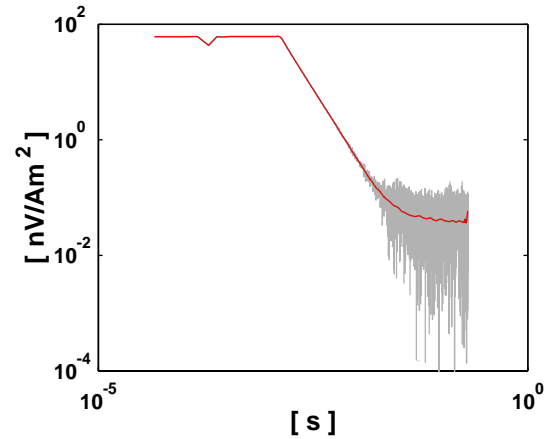


Fig. 2-32: Application of basic filtering scheme to real data set (gray: unfiltered, red: filtered). At early times the receiver is saturated.

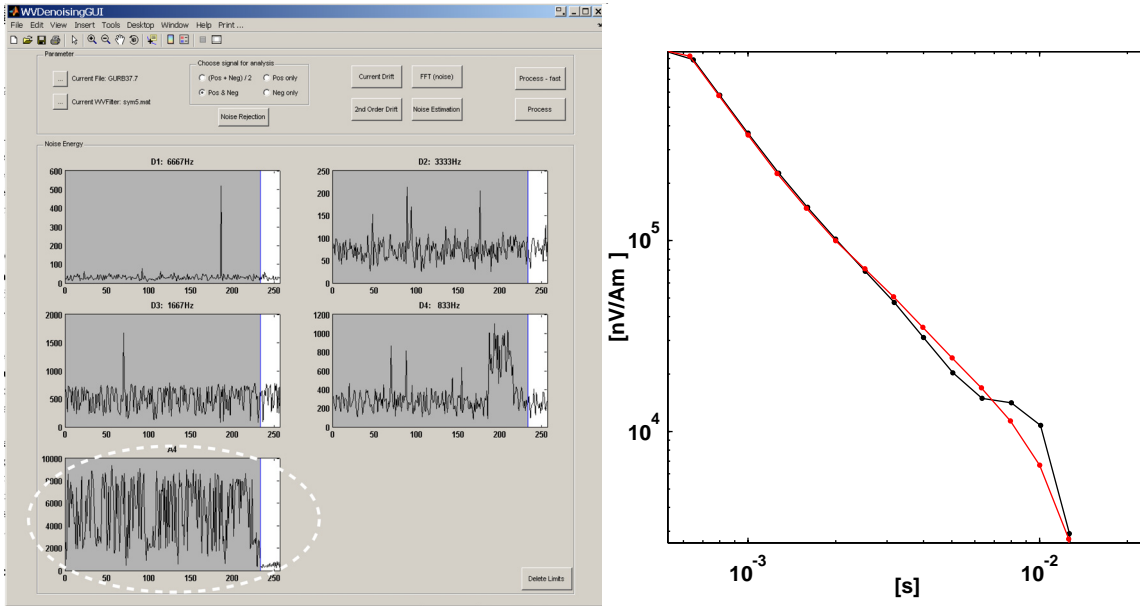


Fig. 2-33: Example for the selection of data with respect to the energy of the noise coefficients. Graphical user interface for the selection of data (left). In the given example the first ~230 stacks of the measured data are rejected (shaded area, left) and only the last ~30 stacks are accepted. The difference in the loggated transients (right) is evident (black: without selection; red: selected with respect to noise energy).

### Selection According to Noise Energy

Fig. 2-33 depicts the selection of data with respect to noise energy. A graphical user interface (left panel) was designed to facilitate this process. In the given example the noise energy ( $\rightarrow$  2-44) was calculated for each scale level  $j$  of the 256 stacks of a real measurement. In the user interface, the noise energy is displayed for each scale-level. The noise energy of the approximation coefficients (marked plot) indicates that low frequency noise was present during the measurement of the first ~230 stacks. By selecting only the remaining ~30 stacks for further processing, the data quality of the processed transient is greatly enhanced.

### Noise Prediction Filtering

Fig. 2-34 provides an example for the application of the noise prediction filtering to real TEM data, which was measured in China. The left panel displays an amplitude spectrum of the approximated noise. Three harmonics between 1000 - 2300Hz can be identified. The displayed spectrum is representative for many data sets acquired with the LAPTEM device. Frequently, high frequencies ( $>500$ Hz) were identified in subsets of the data, i.e. the occurrence of the harmonic noise temporarily limited and therefore only occurred in certain stacks of the whole measurement (similar to Fig. 2-33). The source of the noise is unknown, but might be internal to the LAPTEM.

The result after the noise prediction filtering (right panel), demonstrate that the harmonic noise was removed. It leads to a certain smoothing of the log-gated transient at late times and

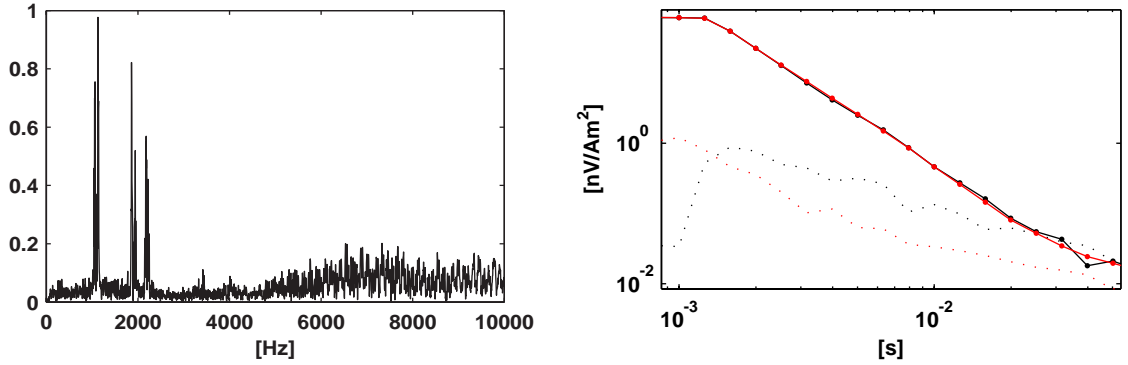


Fig. 2-34: Spectrum of noise approximation derived from TEM measurement (left) and result of noise prediction filtering (right). The logged transient after common processing is displayed as black line. The transient, which was enhanced by noise prediction filtering prior to the common processing, is displayed as red line. Resulting standard deviations are displayed as dashed lines.

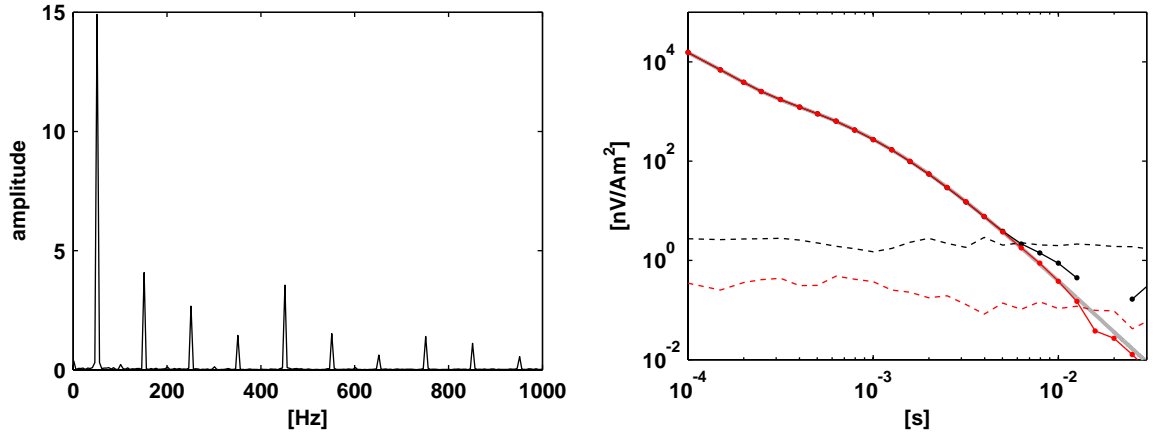


Fig. 2-35: Noise prediction filtering for arbitrary transient (right, gray line) with added real noise measured in Berlin, Germany. The noise spectrum (left) mainly shows 50Hz and odd multiples. The logged result after noise prediction filtering (right, red) is stable at later times when compared to the commonly processed transient. See text for further explanations.

the calculated standard deviation is substantially smaller. For the general application of the noise prediction to measurements in China it turned out that in most cases no substantial improvement of the final processing results were achieved by the noise prediction filtering. This is due to the fact that the harmonic noise usually only occurred in a limited number of stacks of the whole measurement. Therefore, the small effects of the noise prediction filtering as depicted in Fig. 2-34, could usually also be achieved by selective stacking.

To conclude the examination of transient signals in the wavelet domain, a last example is given in Fig. 2-35, where a noise measurement was conducted with the LAPTEM device at a location in Berlin, Germany. The amplitude spectrum of the measured noise (left) is dominated by harmonics of 50Hz and odd multiples. The measured noise was cut into appropriate segments and added to a modeled transient to simulate a real measurement as in Fig. 2-6 (p. 15). For the sake of demonstration, the pulse duration ( $\Leftrightarrow$  segment length) was deliberately not

chosen as multiple of 0.02s and long enough to assure that the lowest frequency could be derived from the approximated noise, as described in the previous chapter. The result of processing after the noise prediction filtering shows a great improvement of data quality at late times in the transient.

### **3 Regional Geology & Tectonical Framework**

This chapter will introduce major aspects of the regional geology of Central Asia by describing the evolution of its major tectonic units and by outlining the zones of structural weakness between these units (chap. 3.1). The geological framework is needed to present valid interpretations for the geoscientific results. An overview of the Ejina Basin will then show, how the target of geoscientific investigations fits into the regional geology (chap. 3.2). The specific locations, where geoscientific work was carried out, will be introduced in the next chapter (chap. 4).

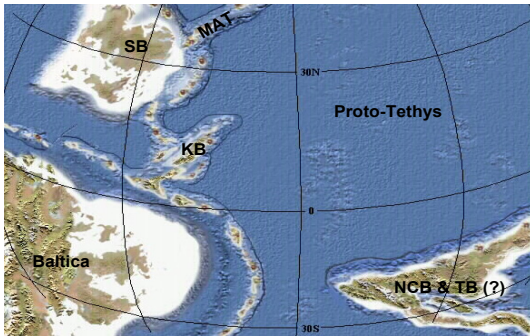
Generally, in publications the naming and spelling - e.g. of tectonic units or faults - may differ from author to author. This is frequently due to the transcription from Chinese or Mongolian into English. Furthermore, many authors tend to assign names of local villages or landmarks to their targets of investigations, if a proper naming has not been established previously. This often hampers the comparison between publications. In this thesis, the apparently most common used terms are used. Differing naming conventions will be pointed at where appropriate.

#### **3.1 Regional Geology of Central Asia**

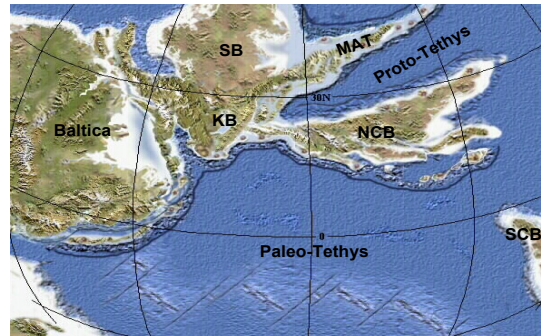
China and the surrounding landmass of Central Asia consist of several main blocks, which joined together with the megacontinent of Laurasia (aka Eurasia) at different times throughout earth history (Fig. 3-1). The suture zones between these blocks are often marked by ophiolites (e.g. NOZAKA & LIU, 2002) and constitute zones of crustal weakness, where magmatic intrusions were massively generated (e.g. JAHN ET AL., 2000). Due to the inherent crustal weakness, major fault systems developed along these zones, which were reactivated repeatedly since the Late Paleozoic. Even though the exact extension, evolution, and interrelation between the main blocks are still a matter of debate, it is evident from literature that the geoscientific work area in the Ejina Basin is located in the junction region between some of the main blocks (e.g. HUANG ET AL., 2002). Therefore, it is reasonable to assume that the formation of the Ejina Basin and its present structure are to a considerable extent influenced by the regional tectonic evolution.



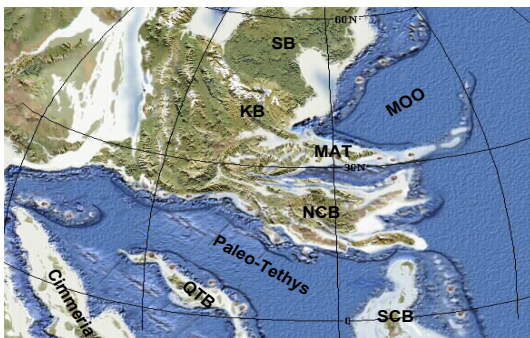
**Late Devonian**



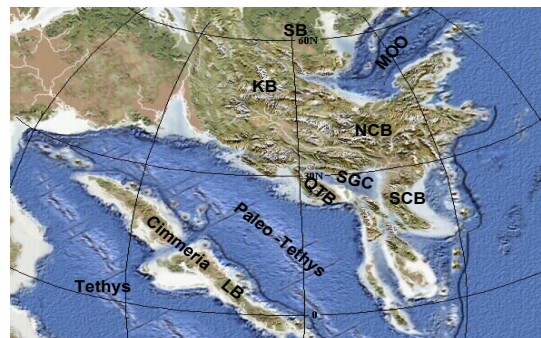
**Late Carboniferous**



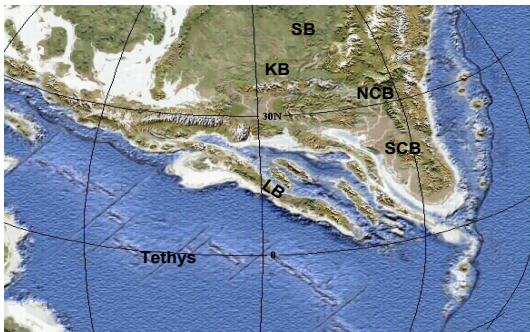
**Middle Permian**



**Late Triassic**



**Late Jurassic**



**Tertiary (Eocene)**

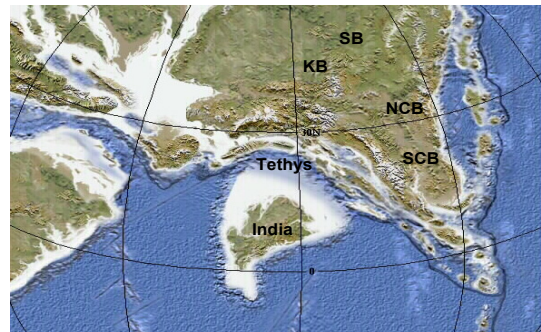


*Fig. 3-1:* Modified reconstruction of plate motions in the formation of Asia (BLAKEY, 2006; based on SENGÖR & NATAL'IN, 1996 and YIN & NIE, 1996). See text for explanations.  
Major units: Lhasa Block (LB); Kazakhstan Block (KB); Mongolian Arc Terranes (MAT); Mongol-Okhotsk Ocean (MOO); North China Block (NCB); Qaidam-Qilian Block (QTB); Qiangtang Block (QTB); Siberian Block (SB); South China Block (SCB); Songpan - Ganzi Complex (SGC).

### 3.1.1 Tectonic Evolution

Generally, the development of Central Asia in terms of earth history is characterized by the rifting of terranes, island arcs and microcontinents from the southerly Gondwanaland to the north, and their accretion to Laurasia. A reconstruction of plate motions by BLAKEY (2006) illustrates the tectonic evolution (Fig. 3-1):

### **Devonian**

Major blocks - i.e. the North China Block (NCB), Siberian Block (SB), South China Block (SCB, not depicted) - were rifted from Gondwanaland (not depicted) and formed distinct units within the Proto-Tethys Ocean. While BLAKEY (2006) interprets the NCB and Tarim Block (TB) as a single block, other authors still see them separated during the Devonian (e.g. METCALFE, 1998). Studies on paleomagnetic, geochemical, and geochronological data give strong evidence that the Alashan Plateau, the Ordos Plateau, and the Qaidam-Qilian Block (AP, OP, QQB; all in Fig. 3-2) were already part of the NCB (HUANG ET AL., 2001; SONG ET AL., 2006). At present the Alashan Plateau comprises parts of the geophysical work area. Between the converging SB and Baltica, the Kazakhstan Block (KB) was forming by the consolidation of islands, small terranes and small microcontinents belonging to the Kipchak Island Arc (e.g. TORSVIK & COCKS, 2003). In the area of the Mongolian island arc terranes (MAT) similar conditions prevailed (e.g. BADARCH ET AL., 2002).

### **Carboniferous**

In the formation process of Pangea, the KB and SB collided (comp. Fig. 4-14), and were moved and rotated towards Laurasia. The continuing closure of the Proto-Tethys moved the NCB towards the southern margin of Laurasia (e.g. XIAO ET AL., 2003). Paleomagnetic data indicates that the NCB was still separated from the SCB, the TB, and Inner & Outer Mongolia (HUANG ET AL., 2001). The subduction of the Proto-Tethys, e.g. on the northern margin of the NCB (COPE ET AL., 2005), occurred contemporary to the rift-related growing of the Paleo-Tethys. The W to E progressing closure of the Proto-Tethys and subsequent phases of accretion of the NCB and the MAT to Laurasia occurred until the Early-Middle Triassic and is documented in the petrological results of the work area (s. chap. 4.2.2, p. 84ff). Orogenic phases were frequently followed by extensional phases, where large amounts of juvenile magmatic intrusions were emplaced into the crust.

### **Permian**

In the north, remnants of the Proto-Tethys were subducted between the converging margins of the NCB the MAT, the KB and SB. It should be noted that in the context of this thesis the Junggar Block is seen as part of the KB, while some authors (e.g. LAURENT-CHARVET ET AL., 2003) treat the Junggar Block as separate unit. In the south, rifting along the northern margin of Gondwanaland separated the Qiangtang Block (QTB) and the Cimmerian Block, of which the Lhasa Block (LB) is a part, from Gondwanaland. Along the southern margin of Laurasia and the northern margin of the QTB, portions of the Paleo-Tethys were subducted. In the reconstruction of BLAKEY (2006), a considerable oceanic basin exists between the QTB and Cimmeria (s.a. KAPP ET AL., 2003), which is challenged by results of the INDEPTH III seismological study (HAINES ET AL., 2003), where only a small forearc- or backarc-basin is interpreted between these two blocks.

### ***Triassic***

During the Early-Middle Triassic, the NCB and the MAT were completely accreted and incorporated into the easternmost section of Laurasia. With this orogenic cycle the main land-masses around our present working area were consolidated and the resulting orogens are frequently referred to as the Central Asian Orogenic Belt (CAOB in Fig. 3-2). During the Late Triassic-Early Jurassic the Qiangtang Block (QTB) was accreted to the southern margin of Laurasia (e.g. HAINES ET AL., 2003; YIN & HARRISON, 2000), and the NCB and the SCB collided (KAPP ET AL., 2003). Between these blocks large amounts of Triassic sediments - flysch & oceanic lithosphere of the Paleo-Tethys - were accumulated, folded, and uplifted. Parts of these series constitute the SGC and comprise the largest volume of Triassic sedimentary rocks on earth (KAPP ET AL., 2003). Between the southern margin of Laurasia and Cimmeria, the Paleo-Tethys was closing and to the south of Cimmeria, where extensional tectonics prevailed, the Tethys Ocean was opening.

### ***Jurassic-Cretaceous***

During the Late Jurassic-Early Cretaceous the Paleo-Tethys ocean closed due to the accretion of Cimmeria, including the LB, to the southerly margin of Laurasia (e.g. YIN & HARRISON, 2000). Coeval, during the Late Jurassic-Early Cretaceous, the Mongol-Okhotsk Ocean (MOO), which BLAKEY (2006) calls "Solonker Ocean", closed in the north (GRAHAM ET AL., 2001). The stress fields of these tectonic processes on the margins of Laurasia reached into the already consolidated landmasses, including the geophysical work area. They are identified by many authors to be a likely cause for the widespread and substantial formation and growing of continental basins, e.g. for the East Gobi Basin (GRAHAM ET AL., 2001; JOHNSON, 2004), the Minle and Chaoshui Basin (VINCENT & ALLEN, 1999), and the Sichuan Basin (MENG ET AL., 2005).

### ***Eocene-Present***

The Tethys closed between the northward rifting India and Asia. The continental collision with an estimated crustal shortening of at least 1400km (YIN & HARRISON, 2000) led to the Himalayan orogeny, the uplifting of the Tibetan Plateau, and to overthrusting, faulting and folding in the Qilian Shan on the northern rim of the Tibetan Plateau. The vertical movements of the continental crust is clearly outlined in the present topography (Fig. 3-2). At greater distance the continental blocks reacted to the collisional stress field by escape tectonics, which led to the reactivation of old fault systems and the rotation of crustal blocks.

### ***Current State***

FOURNIER ET AL. (2005) use analog sandbox experiments to simulate the crustal deformations in Central Asia (Fig. 3-3). Their experiments give an illustrative account, how the continental crust in Central Asia reacts to the stressfield induced by its collision with the Indian



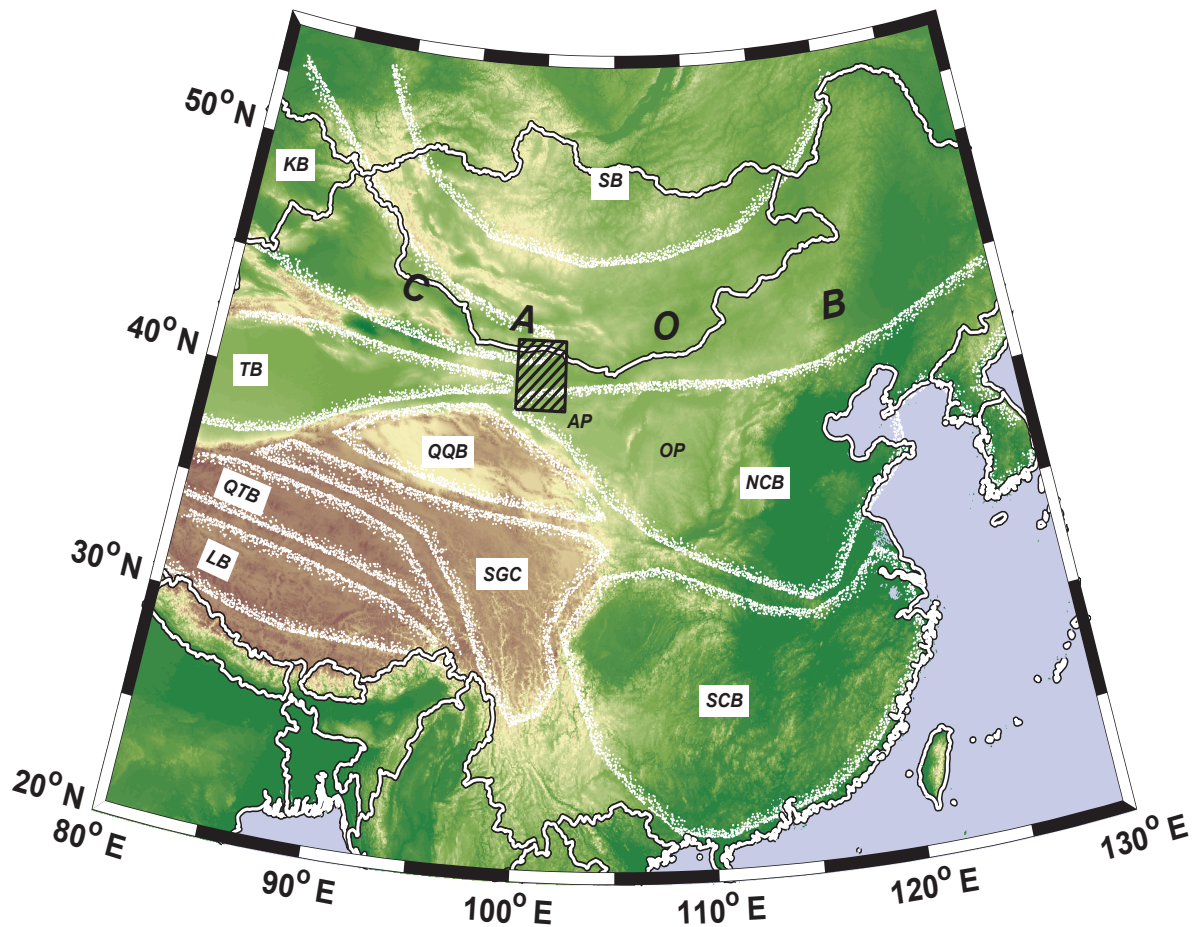


*Fig. 3-2:* Outline map (based on SRTM30 elevation data) of Central and SE Asia with the approximate present constellation of main blocks (s. Fig. 3-1 and text), the Alashan Plateau (AP) and the Ordos Plateau (OP). The study area (hatched rectangle) is located in the border region between China and Mongolia.

plate. They use a homogeneously layered substratum - i.e. without horizontal zones of structural weakness - to represent the lithosphere and asthenosphere of Central Asia and the adjacent Pacific Ocean. The Indian plate is represented by a rigid indenter (Fig. 3-3, left), which penetrates the sandbox models with varying speeds and durations. An analysis of the deformed reference grid is then used to estimate the deformations (Fig. 3-3, right). A close-up of deformations in the northeastern part of the model (Fig. 3-3, top) shows a first order, northeast striking, left-lateral, strike-slip fault system. Between the faults of this system, blocks are rotating counterclockwise. Along the edges of these rotating blocks, extensional faults are observed. The interpreted dynamics are in good general agreement with the current velocity field of Central Asia as deduced from long-term GPS measurements (e.g. HOLT ET AL., 2000).

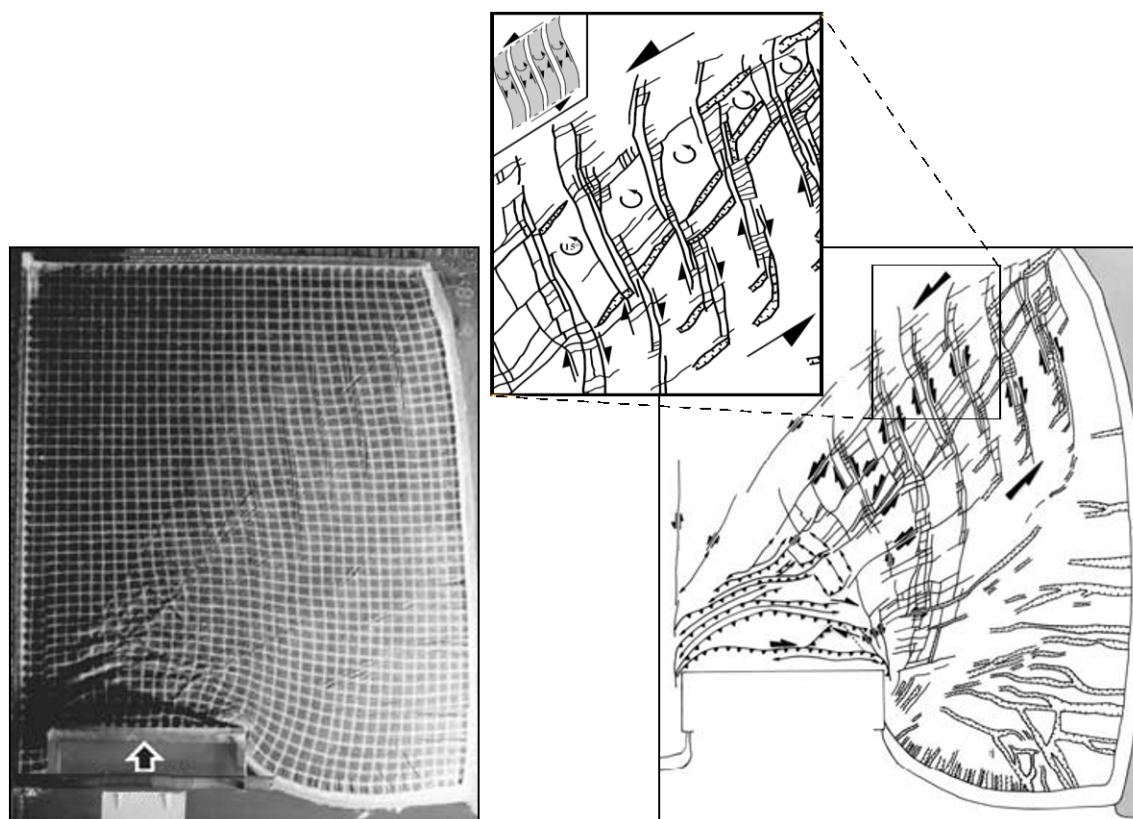


*Fig. 3-3:* Analog sandbox experiment for the simulation of crustal deformations in Central Asia by FOURNIER ET AL. (2005). The figure shows a snapshot of their experiment "E2" (left), the associated analysis of deformations (right), and a close-up of the northeastern part (top). North is oriented to the top.

### 3.1.2 Stratigraphy & Plutonism

The accretionary history along the southern margin of Laurasia is preserved in sedimentary sections in Central Asia, which frequently show the following pattern:

- Phanerozoic-Late Paleozoic marine sedimentary and submarine volcanic rocks in the lower sections
- Early-Middle Triassic hiatus of sediments or distinct change in type of sedimentary facies
- Late Triassic-Early Tertiary onset of terrigene sedimentation. The Mesozoic sediments usually overly the underlying sequences unconformably and are usually explained by intervals of intense rifting (e.g. GRAHAM ET AL., 2001; MENG ET AL., 2003).

Exemplary sedimentary sections fitting into this pattern can be found in the Tarim and Qaidam Basin (MENG ET AL., 2001), the Beishan and South Gobi area (ZHENG ET AL., 1996), the Yingen and the Minle Basin (VINCENT & ALLEN, 1999), the East Gobi Basin (GRAHAM ET

AL., 2001; JOHNSON, 2004; MENG ET AL., 2003), and in the Sichuan Basin (MENG ET AL., 2005). For the interpretations in the Ejina Basin the publications from VINCENT & ALLEN (1999) and MENG ET AL. (2003) are of interest, because they contain deep sections in the proximity of the work area, i.e. at distances of less than 500km. Within the Ejina Basin, Late Quaternary sediments were recovered and analyzed down to a depth of ~230m in the borehole D100 by the geographical workgroup (WÜNNEMANN ET AL., 2006).

The formation processes of Central Asia were accompanied by widespread emplacement of intrusions (e.g. JAHN ET AL., 2000) and some extrusive volcanism. Of special interest for the interpretation of petrological fieldwork in the vicinity of the Jingsutu Structure (chap. 4.2.2) are investigations, which describe the plutonism related to the formation and evolution of the CAOBS (Fig. 3-2). Even though this belt comprises a huge area with an E-W extension of several thousands of kilometers and a N-S extension of several hundreds of kilometers, some general trends for the plutonism connected to the CAOBS can be concluded from literature:

- Intrusions are almost exclusively classified as I-Type (e.g. WU ET AL., 2003A,B) or A-Type (e.g. WU ET AL., 2002; ZHOU ET AL., 2004).
- Three main episodes for the emplacement of intrusions are identified:
  - (1) Late Paleozoic (Permian),
  - (2) Early Mesozoic (Triassic),
  - (3) Late Mesozoic (Late Jurassic - Early Cretaceous).
- Common isotopic characteristics<sup>1</sup> are usually interpreted as evidence for a juvenile, mantle-dominated origin of the protoliths. Consequently, many authors consider the granitic magmatism in CAOBS and Central Asia to be the most important formation of juvenile crust in the Phanerozoic (e.g. JAHN ET AL., 2000; HAN ET AL., 1997).

## 3.2 The Ejina Basin

The term "Ejina Basin" is used to describe the geomorphological unit of a basin structure in NW China, which at shallow depth is filled by Quaternary and Holocene sediments of the river "Ruoshui". Here the term "Ruoshui" refers to - in sensu lato - the present river and its branches as well as to no longer active paleo-channels within the basin. The "Ejina Basin" is congruent with the "Gaxun-Nur Basin" of BECKEN (2004), the "Ejin Banner" (WANG ET AL., 2004), and probably with the "Yingen Basin" (MENG ET AL., 2003).

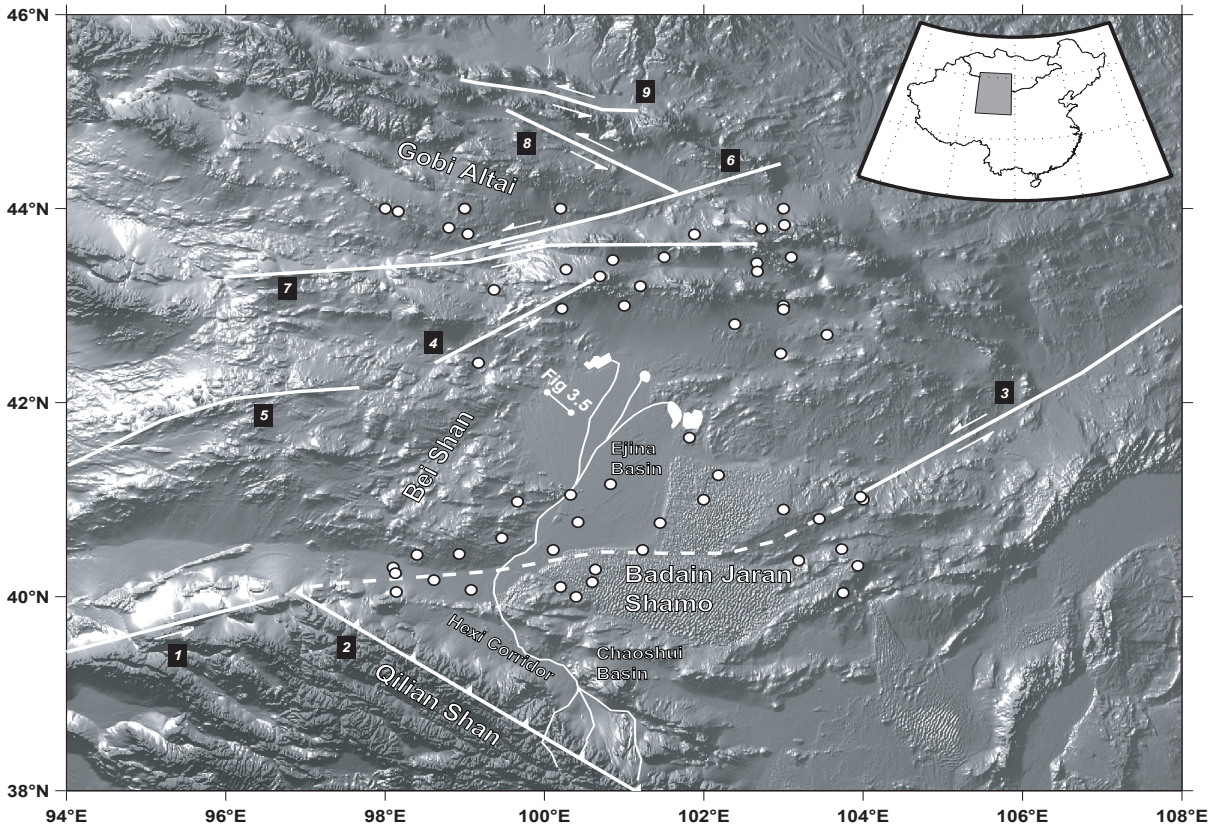
### 3.2.1 Tectonical Framework, Topography and Seismicity

Fig. 3-4 shows the position of the Ejina Basin in terms of the general tectonic framework of Central Asia, which is presently driven by the approximately N-trending stress induced by the collision of the Indian and Eurasian plates. The Ejina Basin, located in the northern foreland of

---

1. Indicators are: low initial Sr isotopic ratios, positive  $\epsilon_{Nd}(T)$  - values, young Sm - Nd model ages ( $T_{DM}$ ).





*Fig. 3-4:* Shaded relief image (SRTM) of the Ejina Basin, the Badain Jaran Shamo desert, and main mountain ranges around the basin. The main fault systems are: Altyn Tagh Fault (1), fault systems in the northern Qilian Shan (2), East Gobi Fault System (3), Tost Fault (4), Ruoqiang Fault (5), Gobi Onon Fault (6), Gobi Tien Shan Fault System (7), Gobi Altay Fault System (8), Gurvan Bogd Fault System (9). Earthquake events around the Ejina Basin (points) are marked in a rectangle between 98° - 104°E and 40° - 44°N for the years 1975-2005 (ISC, 2001). A seismic section in the NW part of the Ejina Basin is depicted in Fig. 3-5.

the Tibetan plateau, is embedded in the stress field of some of the major active fault zones in Central Asia (lines in Fig. 3-4):

- the Gobi Altay Fault System (8 in Fig. 3-4; CUNNINGHAM ET AL., 1996) and the Gurvan Bogd Fault System (9 in Fig. 3-4; BAYASGALAN ET AL., 1999) to the N,
- the Gobi Tien Shan Fault System (7 in Fig. 3-4; CUNNINGHAM ET AL., 1996) to the NW
- the Altyn Tagh Fault to the SW (1 in Fig. 3-4; e.g. MEYER ET AL., 1996; MENG ET AL., 2001),
- several fault systems in the northern Qilian Shan to the S, where both left-lateral and reverse faulting is observed (2 in Fig. 3-4; e.g. MEYER ET AL., 1998; DING ET AL., 2004).

While recent tectonic activity of these faults is clearly indicated by seismicity, other prominent faults like the Ruoqiang Fault<sup>1</sup> (5 in Fig. 3-4) to the W, the Tost Fault (4 in Fig. 3-4) and

the Gobi-Onon Fault (6 in Fig. 3-4) to the NW, and the Zuunbayan Fault (3 in Fig. 3-4), which is part of the East Gobi Fault Zone (EGFZ), to the NE of the Ejina Basin, are considered to be Late Mesozoic (LAMB ET AL., 1999). A Cenozoic reactivation of faults in the EGFZ is interpreted from seismic sections by JOHNSON (2004) and several authors propose an interconnection between the East Gobi Fault System and the Altyn Tagh Fault (e.g. WEBB & JOHNSON, 2006; YUE & LIOU, 1999), which probably runs along the southern margin of the Ejina Basin (dashed line in Fig. 3-4). The amount of left-lateral displacement and the identification of active periods for this hypothetical connection are a matter of debate in the current literature (e.g. LAMB ET AL., 1999; DARBY ET AL., 2005; WEBB & JOHNSON, 2006).

The Ejina Basin (Fig. 3-4) covers an area of approximately 28000km<sup>2</sup> and is bordered by the Bei Shan (*chin.*: *Shan* → mountain range) to the west, the Gobi Altay to the north, and the dune fields of the Badain Jaran Shamo to the east and south. The Ruoshui (*chin.*: *Shui*, *He* → river) originates in the Qilian Shan, where it is called Heihe, and enters the basin from the southwest through a depression between the Bei Shan and the Heli Shan. It separates into the two main branches Xihe and Donghe and terminates in the end lakes Gaxun Nur, Sogo Nur and Juyanze (s. Fig. 4-1, p. 73 for details). Within the basin, the primarily Quaternary sediments show very little relief and gently dip northwards with a gradient of about 0.9‰ along the Ruoshui (comp. Fig. 4-4, p. 77).

A map of seismicity (points in Fig. 3-4) shows locations of earthquakes in the Ejina Basin and the surrounding area as determined from local seismic stations in NW China (source: BJI, Chinese Earthquake Administration in ISC, 2001). Since one of these local stations is situated in Gaotai (GTA, 99°49'E, 39°25'N), which is located directly to the SW of the Ejina Basin, the locations of epicenters are considered to be representative. However, since the relevant data was not available, no thorough examination of focal mechanisms was implemented and error estimates for the locations can not be given. The map of seismicity can be divided into two clusters: one cluster of events in the vicinity of the southern, and a second cluster in the vicinity of the northern margin of the basin. All earthquakes are crustal with a maximum depth of 30km and magnitudes between 3-5 (where specified). Comparing the two clusters, there is a slight tendency of earthquakes in the northern cluster to be more shallow (7-30km) as compared to the southern cluster (15-30km). In addition, magnitudes in the northern cluster are slightly larger. Events in the southern cluster as well as events in the center of the northern cluster are aligned along several NE striking bands. The central section of the Ejina Basin shows no activity.

---

1. The Ruoqiang Fault seems to be part of the Shibanjing - Xiaohuangshan Fault in WANG ET AL. (1997).

### 3.2.2 Previous Geophysical Studies

Only very little unclassified geophysical data from the Ejina Basin has been published and is publicly available for reference purposes:

The last segment of the global geoscientific transect "Golmud - Ejina Transect, China" crosses the basin from SW to NE. The interpretation of geophysical data (gravimetry, magnetics, magnetotellurics (MT), seismics, geothermics) along the transect depicts crustal and upper mantle features in a depth range between 1-200km (WANG ET AL., 1997; MT in ZHU & HU, 1995).

Towards the NW margin of the Ejina Basin three seismic profiles are published by MENG ET AL. (2003). The profiles are interpreted in terms of the Mesozoic extensional evolution of the Ejina Basin. The according seismic sections (exemplarily in Fig. 3-5) do not resolve the uppermost Quaternary sequences, but show that Mesozoic

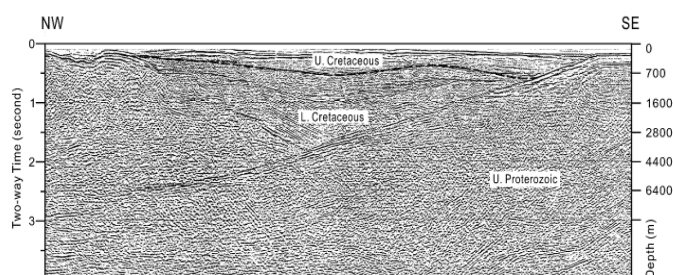


Fig. 3-5: Seismic section in the NW part of the Ejina Basin (from MENG ET AL., 2003; s. Fig. 3-4 for profile location).

sequences, which are interpreted as Cretaceous, unconformably overly the pre-Mesozoic basement. The sections clarify that the pre-Mesozoic structures beneath the Mesozoic and Cenozoic sedimentary cover of the Ejina Basin are strongly undulating and exhibit fault bound horst and graben structures.

The results along the transect and the seismic profiles have little direct implications for the interpretation of geophysical data presented in this thesis, because they are at large distance to the geophysical work areas (>50km for the transect; >80km for the seismic sections) and generally consider larger horizontal and vertical scales. One interesting fact from the interpretation of MT data along the transect (ZHU & HU, 1995) is that the basin fill of the Ejina Basin is interpreted with a low resistivity of  $10\Omega\text{m}$  and a thickness of 1-2km above crystalline basement. However, some broader aspects of the published geophysical results are picked up again in the interpretations in the following chapters.

## 4 Results of Geophysical & Geoscientific Investigations

In this chapter the results of the geophysical and additional geoscientific investigations are presented. The geoscientific investigations comprise the interpretation of satellite data and images, and the presentation and interpretation of petrological data (chap. 4.2.2). Since both, remote sensing and petrology, are not introduced in the methodical part of this thesis, brief introductions are given in the according sections (chap. 4.1.1 & chap. 4.2.2).

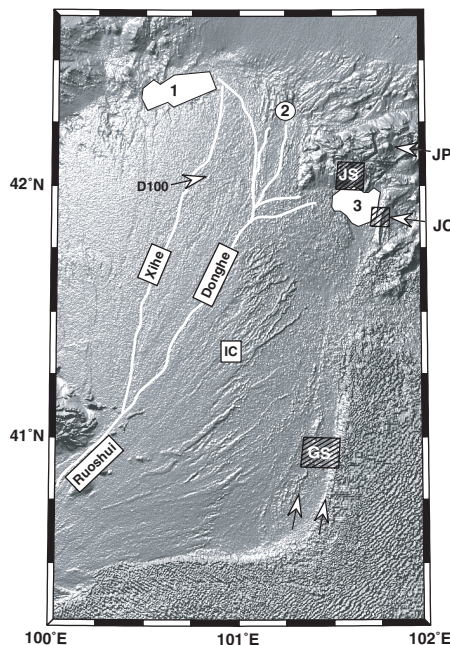


*Fig. 4-1:* Work areas in the Ejina Basin with the terminal lakes Gaxun Nur (1), Sogo Nur (2) and Juyanze (3). The NW part of the Juyanze is also called Jingsutu. A 232m deep drilling (D100) of the geographical workgroup is located in the central section of the basin.

The following sections are concentrating on the locations of geophysical field measurements. All work areas have been giving working titles connected to nearby lakes or settlements. They are from north to south (Fig. 4-1): Jingsutu Pluton (JP) and Jingsutu Structure (JS) (chap. 4.2), Juyanze Cliff (JC), and the Gurina Structure (GS) (chap. 4.3). In each section the location is first introduced according to information from geological maps and satellite images, then the results of geoscientific and of geophysical investigations are presented.

Generally, the structures under investigation in each work area are striking approximately N-S. Together they form a NNE-SSW striking axis, which marks the eastern margin of the Ejina Basin. The axis connects areas covered with Pleistocene-Holocene sediments in the S with areas composed of Paleozoic basement rocks in the N. In a satellite image interpretations prior to the start of the project, this was interpreted as tectonical axis with possible neotectonic activity and the work areas

were chosen accordingly. However, in terms of the regional geology, similar N-S striking tectonical lineaments are almost completely missing in adjacent areas (s. Fig. 3-4, p. 70), which at first sight contradicts the working hypothesis. The results of geophysical and geoscientific

investigations in this chapter show, how the structures under investigation link together and give clues about the possibly involved tectonical processes. In the following discussion (chap. 5) the results are then interpreted together in the regional context.

## 4.1 Ejina Basin

This section covers large scale aspects relevant for the whole basin, which are exclusively deduced from the interpretation of satellite data (Landsat TM, SRTM, Corona). They provide the framework or the interpretation of geophysical data acquired in selected key locations of the Ejina basin.

### 4.1.1 General Overview of Satellite Data

#### Landsat TM

Georeferenced subsets of the Landsat TM data, which comprise three (7=mid-infrared / 4=near-infrared / 2=visible green) of the original seven bands, are available in the compressed MrSID-format (NASA, 2006). The data is spatially and spectrally unenhanced, and specified with a horizontal resolution / absolute positional accuracy of 28.5 m /  $\pm 50$  m or 14.25 m /  $\pm 75$  m for the Landsat 4/5 missions (ESC, 2002) and the Landsat 7 mission (ESC, 2004), respectively. In this thesis, only the high resolution data sets are used. The absolute positional accuracy was checked and verified by the correlation of GPS field-measurements at characteristic locations, e.g. on the northern edge of the Juyanze Cliff, which can be identified with the same coordinates, within the specified error, on the satellite image.

#### Corona

The Corona Program was named after a series of US military reconnaissance satellites (KH 1 - KH 4b) used between 1959 - 1972 in spying missions. The program was declassified in 1995 and the films were made available to the public. The panchromatic films of the second generation satellites (KH-4a/b) offer a horizontal resolution better than 3 m.

20 negatives film strips<sup>1</sup> were purchased by the geographical workgroup for detailed structural investigations. Due to their size, digitizing of the negatives was problematic. HARTMANN (2003) digitized and georeferenced a small subset of the negatives for his thesis, but reported considerable spatial distortions for the digitized images. To overcome these problems and to achieve a better coverage, 14 film strips were digitized at 5400dpi using a flat bed scanner with transmitted light unit. Since each strip was too long to be scanned in one piece, several scans were needed for each strip. The digitized partial-scans were then assembled and a contrast stretch was selectively performed. Subsequent georeferencing with respect to the Landsat TM images was carried out using ArcMap. In the final version, the digitized Corona images generally show little distortion in the central section and sometimes considerable distortions

---

1. Strips have a size of 700x80mm, cover ~250 x 20 km each, and were recorded 1964 & 1968 by the KH 4a satellite.



close to the edge. For exemplary ground control points in the work areas, the deviation between the Corona image and the Landsat TM image lies between 50-200m (~4-15 Landsat TM pixel).

### SRTM

In February 2000 the Shuttle Radar Topography Mission (SRTM) was carried out in cooperation between the space agencies of the USA (NASA, NIMA), Germany (DLR), and Italy (ASI) to produce a new, high quality, global digital elevation model (DEM). During a shuttle mission an active radar system with two sensors (C- and X-band) was used to collect data between 55°S and 60°N. In the following only the freely available C-band data is used. Details of the mission can be found in WERNER (2001). The global SRTM-DEM has a horizontal resolution of 3" (~90m), in some regions, e.g. in the continental USA or Italy, an increased horizontal resolution of 1" (~30m) is available. The absolute vertical accuracy for the elevation data is specified to be better than 16m (e.g. SMITH & SANDWELL, 2003).

Voids in the SRTM-DEM exist over areas with steep topography or low signal-to-noise ratio, where the interferometric phase unwrapping algorithm failed or returned questionable results. In the vicinity of the Ejina Basin data-voids can especially be observed in the area of the Badain Jaran Shamo, where the regular dune pattern seemingly scattered the radar signals (Fig. 4-2). The data voids are clustered along SW-NE striking bands, parallel to the ground path of the space shuttle (Paetzold, DLR, pers. comm.).

With a 10-fold increase in horizontal resolution and a 6-10-fold increase in vertical accuracy, the SRTM-DEM comprises a great improvement over the previously best available global data set GTOPO30 (USGS, 2006). Two versions of global SRTM-DEMs based on the C-band data were released (USGS, 2007), of which the final release is used in this thesis. A comparison of the two releases showed that both versions are essentially identical within the work area (100-102°N, 40-42°E): 92.51% of elevation values remained unchanged between version 1 and version 2, 7.46% were changed by just  $\pm 1$  m, and only 0.3% by  $\pm 2$  m or more.

An import routine was programmed to make the SRTM-DEM available within Matlab (HÖLZ, 2007B). It can be used to extract arbitrary sections of the data to be displayed e.g. in profiles, contour plots, color coded images or shaded relief maps. The routine can also be used to patch data voids as in Fig. 4-2 by interpolation or by using the GTOPO30 or SRTM30 (USGS, 2007B) data sets.

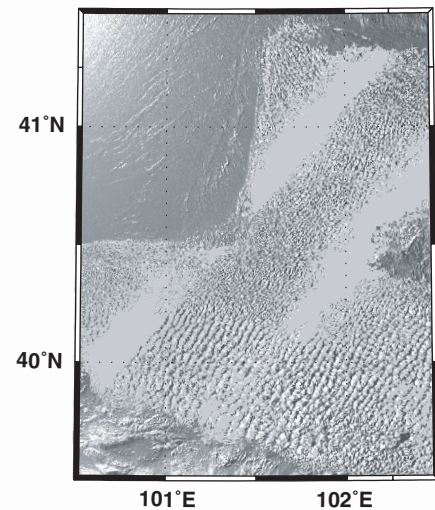


Fig. 4-2: Example of voids in the SRTM-DEM in the area of the Badain Jaran Shamo.

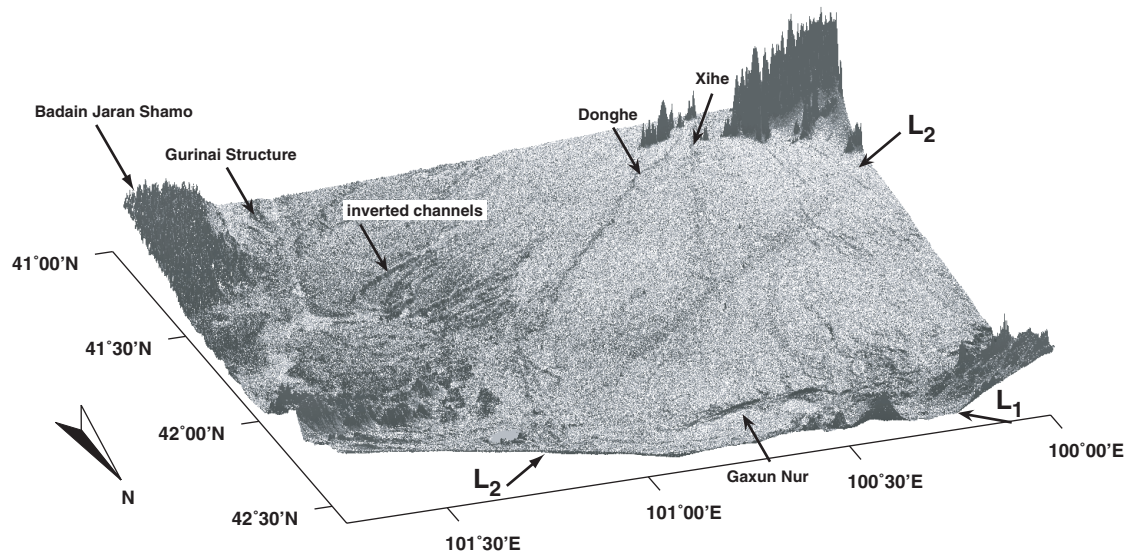


Fig. 4-3: Shaded relief image of the Ejina Basin based on SRTM-data, view from the NE. Apart from the known geomorphological features (Fig. 4-4), two lineaments  $L_1$  and  $L_2$  are visible.

The accuracy of the SRTM-DEM can be checked by comparison to ground based differential GPS measurements (DGPS). A ground check in central Siberia by SUN ET AL. (2003) yielded an absolute vertical accuracy of 10m for areas with no substantial vegetation cover. To test the accuracy of the SRTM-DEM within the Ejina Basin, DGPS measurements of HARTMANN (2003) were used as reference points and compared to the according elevations of the SRTM data set. When comparing the two data sets one has to bear in mind that DGPS measurements refer to a localized point in space, whereas SRTM-DEM elevations represent an averaged elevation over an area of  $\sim 90 \times 90 \text{ m}^2$ . The DGPS stations of HARTMANN (2003) were located in the northern portion of the Ejina Basin, most of them in the vicinity of Lake Gaxun Nur and Lake Juyanze. The standard deviation ( $1\sigma$ ) between the two data sets is 5.1 m, which equals 8.4m at a 90% confidence interval. The absolute difference exceeded 10m at only three stations, which were identified to be close to vertical edges, e.g. on the edge of the Juyanze Cliff. If these three stations are excluded, the standard deviation ( $1\sigma$ ) between the two data sets is reduced to 4.1 m, which equals 6.8m at a 90% confidence interval.

In conclusion the vertical accuracy of the SRTM-DEM in the area of the Ejina Basin surpasses the NASA mission specification by a factor 2-2.4.

#### 4.1.2 Satellite Image Interpretation

In Fig. 4-3 the dominant features in terms of elevation are the basement units to the NW and the SW and the dunes of the Badain Jaran Shamo in the SE. Within the basin the alluvial fan of the Ruoshui forms a leveled plain with only a few marked features. Most of these features are known geomorphological units, e.g. the barrier beach of the Gaxun Nur, the two branches of the Ruoshui (Donghe and Xihe) and several old riverbeds, which HARTMANN

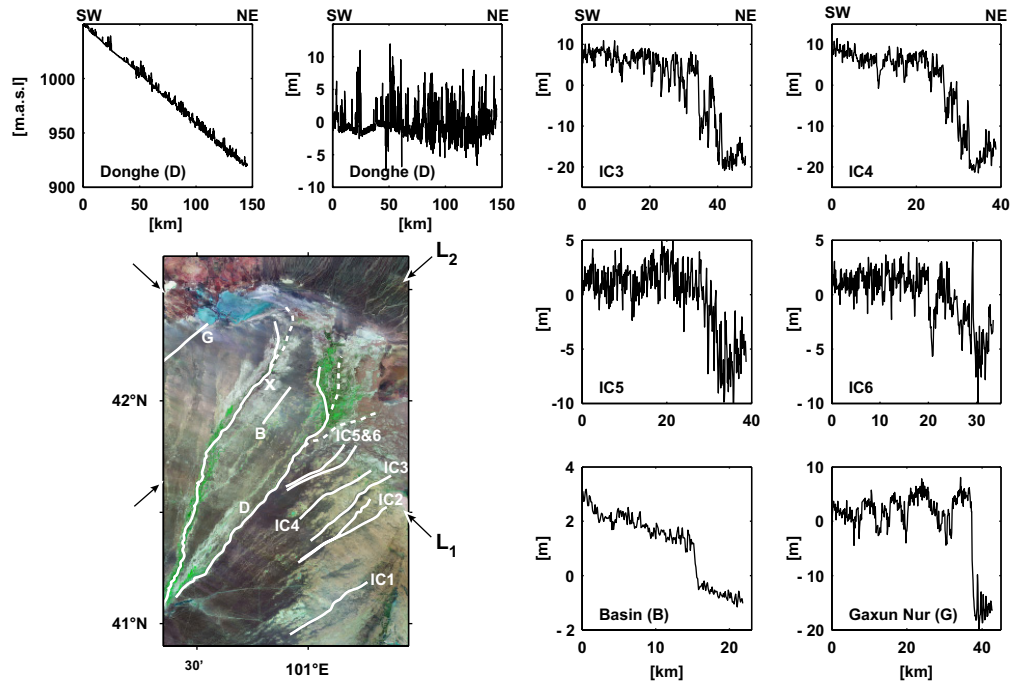


Fig. 4-4: Landsat TM image (lower left) with lineaments ( $L_1$ ,  $L_2$  → Fig. 4-3), the drilling D100 (x), and locations of digitized elevation profiles (solid lines). All profiles run from the SW to the NE. The top left plot shows the true elevation along the Donghe (D). The remaining plots show residual elevations along the indicated profiles with a gradient of 0.9‰ removed.

(2003) describes as "inverted channels" (for locations compare Fig. 4-4). The inverted channels are all located to the east of the currently active river system and mark a system of paleo-channels. They are preserved from deflation related erosional processes by partially consolidated gravels and top the surrounding topographic level by up to 25m. Apart from the known geomorphological units, two straight lineaments ( $L_1$ ,  $L_2$ ) can be seen in Fig. 4-3, which strike SE-NW resp. SW-NE and approximately intersect at  $100^{\circ}49' \text{ E} / 42^{\circ}1' \text{ N}$ .

The SE-NW striking lineament ( $L_1$ ) can be traced for about 130km from the northern end of the Gurinai Structure (chap. 4.3) across the basin into the basement to the NW. The inverted channels terminate at  $L_1$  and the main branches of the Donghe and the Xihe change their flow-direction from NE to N in the vicinity of the lineament (Fig. 4-4, lower left).

Several profiles along the active river streams and the paleo-drainage system ("inverted channels") were digitized to investigate elevations in relation to this lineament. Along the Donghe (Fig. 4-4, upper left), i.e. the eastern branch of the Ruoshui, the elevation profile shows a nearly linear decline and linear fitting yields a gradient of  $\sim 0.9\text{‰}$ . After removing the linear trend from the elevation profile, the residual elevation of the Donghe shows no further indications for a tectonic deformation along the digitized profile of the river, i.e. south of  $L_1$  ( $\sim 42^{\circ}10' \text{ N}$ ). The same holds true for the Xihe, the western branch of the Ruoshui, where the same gradient of  $\sim 0.9\text{‰}$  can be observed (not depicted) and no indications for a tectonic

deformation along the river can be found along the digitized profile of the river, i.e. south of  $L_1$  ( $\sim 42^\circ 25'N$ ). Additional elevation profiles along the inverted channels, which extend into the basin of the Juyanze, again show a gradient of  $\sim 0.9\%$  south of  $L_1$ . Hence, this linear trend has been removed to depict the residual elevations (Fig. 4-4, profiles "IC3-6").

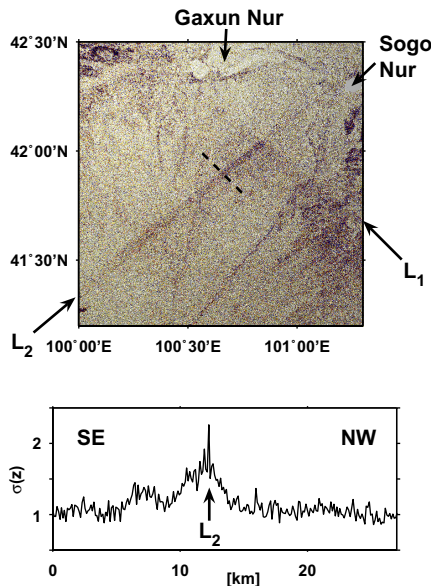


Fig. 4-5: Highpass filtered SRTM-data (top) with profile line (dashed line) of average elevation across lineament  $L_2$  and standard deviation of average elevation (bottom).

seen in the residual elevation of the Donghe (Fig. 4-4), the SRTM-data is further investigated by averaging the elevations along several adjacent, parallel profiles across  $L_1$  to reduce the scatter in the data. This basic approach is justified, because the lineament is subparallel to the contour lines and the relief is very flat. The resulting residual elevation averaged from 50 parallel profiles (Fig. 4-4, profile "Basin") reveals a step of  $\sim 2m$  across the lineament. Similar steps in the order of 1-2m can be derived, if the average profile is shifted along lineament  $L_1$ .

The second lineament  $L_2$  strikes SW-NE and can be traced for about 95km from the SW margin of the Ejina Basin to the intersection with lineament  $L_1$  (Fig. 4-3 & Fig. 4-5, top). Further to the NE the lineament is less pronounced, but can still be identified for another 40km to the Sogo Nur. The only distinctive feature of a geomorphological unit in connection with the lineament is a change in the flow direction of the Xihe from NE to NNE (Fig. 4-4).

A wavelet based filtering scheme (s. chap. 2.4.2, p. 41ff) is used to investigate the nature of the  $L_2$ , in which the elevation data is decomposed by a 2D wavelet transformation (WT) and only the coefficients of the first two detail-levels are used in the reconstruction, i.e. in the 2D inverse WT. This is essentially equal to a localized 2D highpass filtering, where only

All profiles show a characteristic drop in elevation when crossing  $L_1$ . The profiles along the inverted channels IC3 and IC4 show a step of 20-25m and farther to the west steps of  $\sim 7m$  and  $\sim 6m$  can be observed along the inverted channels IC5 and IC6. The profile directions of inverted channels located further to the SE (e.g. IC1 & IC2) are not pointing towards the basin of the Juyanze anymore and are therefore not considered further. However, it should be noted that these channels are much less pronounced in the elevation data and, hence, a considerably stronger erosion and older age of these channels has to be assumed. To the NW an additional profile across  $L_1$  into the Gaxun Nur (Fig. 4-4, profile "Gaxun Nur") shows a step of  $\sim 20m$ , which is comparable to the step along the profiles IC3 and IC4. Since the SE-NW striking lineament  $L_1$  is clearly visible across the whole basin in the shaded relief image (Fig. 4-3), but can not be

wavelengths below  $\sim 1$  km are considered. Average elevation profiles of the filtered data across the lineament reveal no distinctive features, instead the standard deviation of the average elevations exhibits a clear peak at the lineament (Fig. 4-5, bottom). Consequently, the lineament can not be connected to a small downstep or a very shallow depression, but rather to an increased "roughness" in the data.

### Interpretation

The nearly linear gradients of the Donghe (Fig. 4-4, upper left) and Xihe reflect an equilibrium state along the rivers and demonstrate that no considerable vertical tectonic movements have influenced the rivers south of  $42^{\circ}10'N$  resp. south of  $42^{\circ}25'N$  in the recent past. This contradicts the findings of MISCHKE (1996), who - based on Soviet topographic maps - interpreted an increased gradient along the river north of  $\sim 41.5^{\circ}N$  and deduced a recent neotectonic influence on the Holocene river profile. Since the differences in the analyzed elevations are small, the conflicting results may be attributed to the precision of the analyzed data sets.

Along the lineament  $L_1$  the total vertical displacement is estimated to be at least 25m according to the displacements visible at the inverted channels and at the Gaxun Nur (Fig. 4-4). Smaller displacements along the profiles IC5, IC6, and "Basin" are well explainable by increased sedimentation in the vicinity of the active riverbeds. In addition to the assumed normal faulting, a certain amount of tilt or horizontal displacement of the block north of  $L_1$  is required to account for the changes in flow directions and drainage characteristics of the Xihe and Donghe. Due to the generally flat topography, the magnitude of these changes may be small compared to the magnitude of normal faulting and have not been identified directly. Since the sedimentation processes in the vicinity of the current rivers have leveled much of the displacement, the minimum age of the normal faulting along the lineament is restricted by the assumption of reasonable sedimentation rates. HARTMANN (2003) already recognized that the inverted channels terminate at a SE-NW striking lineament and proposed a connection of this lineament to the southwestern margin of the Gaxun Nur<sup>1</sup>. In his tectonic analysis he concluded that normal faulting has to be assumed. The analysis of the SRTM-data in the vicinity of lineament  $L_1$  supports his findings, localizes the lineament with respect to the residual elevations (Fig. 4-4, right), clarifies that the lineament can be traced across the whole basin, and shows that normal faulting is evident across its whole length. It is of special interest to note that the drilling D100 is located within 3 km distance of the lineament  $L_1$ . WÜNNEMANN ET AL. (2006) show that AMS dates in the D100 drilling core do not increase with depth, but scatter in a wide range between  $\sim 14$ -40ka up to 90m depth<sup>2</sup>. They explain these temporal unconformities within the stratigraphic sequence by repeated reworking processes, which they explain by tectonically induced subsidence. Due to the close spatial relationship between the lineament  $L_1$

1. Compare Fig. 4-7 and 4-10 in HARTMANN (2003).

2. Compare Table 1 in WÜNNEMANN ET AL. (2006). The first datable material was found at a depth of 11m (21ka & 14ka), the oldest material feasible for radiocarbon dating was found at a depth of 90m ( $> 42$ ka).



and the drilling D100, the described unconformities can be connected to phases of normal faulting along  $L_1$ . Thus, the available datings constrain possible times of fault activity. Further constraints can be deduced from findings at the inverted channels: At the NE end of IC4 ( $101^{\circ}15'E$ ,  $41^{\circ}39'N$ ), fragments of ostrich-eggshells were found in the fine-grained strata below the gravels of the inverted channel (HARTMANN, 2003). In radiocarbon datings these fragments were dated at 37-42ka BP (BERGMAN ET AL., 1980). Since the normal faulting along  $L_1$  has cut the inverted channels, it must postdate the active river phase as documented by the gravels of IC4. Therefore, the datings of the ostrich-eggshells can be considered an upper age limit for the normal faulting and a minimum displacement of 20m past 40ka can be deduced.

The lineament  $L_2$  is hitherto unknown and can be seen in connection to a known geological or tectonical feature. Its changing characteristic across the lineament  $L_1$  in the elevation data (Fig. 4-5) as well as some small scale aspects - only visible e.g. in a curvature analysis (no figure) - are indicators that the lineament is indeed related to real geology (Theilen-Willige, pers. comm.). However, it has to be stated that it may also result from small inconsistencies in the SRTM-dataset. Fig. 4-2 demonstrates that errors in the DEM may be aligned along the flight track and that the acquisition of SRTM-data was carried out subparallel to  $L_2$ . Since the groundtrack data of the mission is not readily available for research purposes (Pätzold, DLR, pers. comm.), the quality and possible artefacts of the SRTM-rawdata in the close vicinity of lineament  $L_2$  can not be investigated further. Ultimately, a more exhaustive investigation of the SRTM-rawdata would be needed to resolve the conflict, which is beyond the scope of this thesis.

## 4.2 Jingsutu Structure & Pluton

The Jingsutu Structure and Jingsutu Pluton (both working titles) are located within the crystalline and metamorphic basement to the N of lake Jingsutu<sup>1</sup>. They terminate the postulated N-S striking tectonical axis to the N (s. Fig. 4-1). Since this is the only work area, where outcropping basement can be found, additional geoscientific investigations were carried out in addition to the geophysical field work to better integrate results into the regional context. While geophysical field work was limited to the area of the Jingsutu Structure, geoscientific investigations were concentrated on basement structures in both work areas.

The analysis of the magnetotelluric (MT) measurements in the Jingsutu Structure are published in BECKEN & BURKHARDT (2004) and BECKEN (2005). Additionally, 1D inversions of TEM measurements are discussed together with results from MT measurements in BECKEN ET AL. (2007).

---

1. The Jingsutu ist the NW-most section of the western subbasin of lake Juyanze.

According to a geological map (GPGB, 1981, white boxes in Fig. 4-6), the basement shows a general subdivision of the work area along  $\sim 42^{\circ}6'N$ :

- The border separating the areas north and south of  $\sim 42^{\circ}6'N$  - hereafter referred to as northern and southern basement, respectively - is marked by a "Middle Variscan"<sup>1</sup> quartz diorite ( $\delta o_4^2$  in Fig. 4-6).
- In the northern basement the Jingsutu Pluton is classified as "Middle Variscan" acidic intrusion of granitic to granodioritic composition ( $\gamma_4^2$  in Fig. 4-6), which has intruded Ordovician sequences ("O" in Fig. 4-6). The sequences are classified as low grade metamorphized volcanics with clastics, silicolite and limestone/marbles (GPGB, 1981). They are related to metamorphized marine sequences, which is in accordance with the general picture of the regional geology (s. chap. 3.1). The Ordovician sequences are roughly striking WSW-ENE with the oldest sequences in the NNW ( $O^c$  in Fig. 4-6) and the youngest

1. *In the Chinese geological maps used in the scope of this thesis, specific orogenic cycles are classified in their English translation as "Caledonian Period" or "Variscan Period", whereas a direct translation of the original Chinese terms should actually refer to "Western Period" and "Eastern Period" (X. Chen, pers. comm.). It is not quite clear, if the English translations directly reflect the geochronological classification in western literature or have to be understood in a broader sense. In the following orogenic cycles as derived from Chinese maps will be quoted to underline this possible difference.*

sequences in the SSE ( $O^a$  in Fig. 4-6). According to the geological map, patches of Ordovician sequences are preserved on top of the pluton (SW edge and in the central section).

- The southern basement mainly consists of "Late Caledonian" plagiogranitic intrusions ( $\gamma_3^3$  in Fig. 4-6). In the W of the Jingsutu Structure, some small scale "Late Variscan" monzogranitic intrusions ( $\eta_4^3$ , not depicted in Fig. 4-6) are embedded into the "Late Caledonian" units. Within this crystalline basement, the Jingsutu Structure forms a shallow depression, which is bounded by basement units towards the N, E and W. Towards the S, basement and Jingsutu Structure plunge below the Quaternary sediments of lake Jingsutu ("LJ" in Fig. 4-6). In the Jingsutu Structure Quaternary (Pleistocene) and Late Jurassic sedimentary units ("Q+J" in Fig. 4-6) are preserved. The Jurassic units are described as marly, partially brecciated sandstones. Towards the W margin of the depression the sediments of the Jingsutu Structure are in contact with a rhyolitic extrusion, which was mapped during field work ("R", hatched area in Fig. 4-8). From the geological map it is not clear, if the rhyolitic extrusion is related to the "Late Variscan" units mentioned above. East of the Jingsutu Structure a ridge of Proterozoic sequences is preserved (P in Fig. 4-6)<sup>1</sup>. The Jingsutu Structure and the Proterozoic sequences are both striking NNE-SSW. In the geological map (GPGB, 1981), the contact between the Proterozoic sequences and the "Late Caledonian" intrusions is depicted as fault related, while no fault-related contact is indicated between the Jingsutu Structure and the crystalline basement.
- Additional information is available from two drillings, which are both located in the Eastern Juyanze. About 20km to the E of the Jingsutu Structure, 96m of Jurassic sandstones were drilled in the drilling "D3" in Fig. 4-6 (GPGB, 1983). The Jurassic units are described as sandstones with a graded, downward coarsening bedding. In the shallow drilling "G36"<sup>2</sup> of the geographical workgroup, the groundwater level was found just 3.25m below top ground surface at 904m.a.s.l. (HARTMANN, 2003), which is remarkable for a region with a mean annual precipitation of just 40mm/a (FENG ET AL., 2001) and a potential evaporation rate of 2600mm/a (WÜNNEMANN, 1999).

According to elevation data, the Jingsutu Pluton is clearly visible in the northern basement as an slightly ellipsoidal-shaped depression with the elongated axis striking NW and an average diameter of ~14km (Fig. 4-6). The surrounding units of the less erodible metamorphic basement top the pluton by 60-100m. Both, basement and pluton, are dipping to the SSE with a gradient of ~1%, which indicates a tilt in this direction. The erosional surface of the pluton is

---

1. According to Hucai (pers. communication), the ridge is the "Hongshishan klippe" described by ZHANG ET AL. (1996).

2. G36 is located just outside Fig. 4-6 at 101°50'E, 41°53.4'N (Hartmann, 2003).



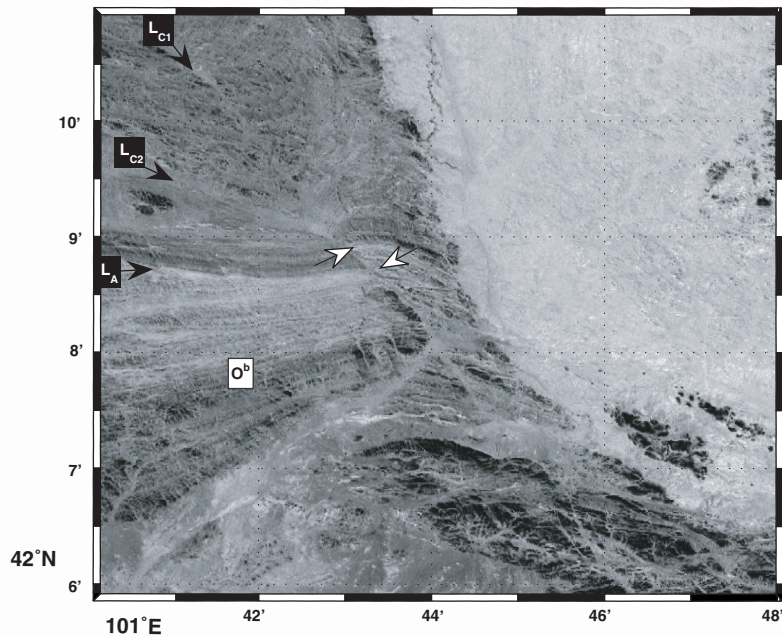


Fig. 4-7: Corona image with the SW edge of the Jingsutu Pluton and adjacent basement, lineaments as in Fig. 4-6. The sinistral offset of the Ordovician sequences is indicated by white arrows.

generally flat, except for a dome-shaped structure in its center and some ridges at its SW margin, which clearly correlate with the patches of Ordovician metasediments in the geological map (GPGB, 1981). Three prominent directions of lineaments are identified in the elevation data (black boxes in Fig. 4-6) and are illustrated and interpreted in combination with Corona images:

- The W-E striking lineament direction L<sub>A</sub> is only visible in the northern basement. It is clearly correlated with the Ordovician sequences (O<sup>b</sup> in Fig. 4-6 & Fig. 4-7). Therefore, it may not primarily be related to tectonical, but rather to stratigraphical features. Along the edge of the pluton the contact between the lineament direction L<sub>A</sub>, i.e. the Ordovician sequences, and the pluton is clearly discordant (Fig. 4-7), which indicates a Post Ordovician age for the emplacement of the pluton.
- The approximately SSW-NNE striking direction L<sub>B</sub> is visible at several locations in the southern basement (Fig. 4-8), but can not be traced into the northern basement. Therefore, no direct connection to the Jingsutu Pluton is evident. The geophysical work group considers L<sub>B</sub> to represent a major tectonical direction, because similar strike can be observed at the Juyanze Cliff and in the Gurinai Structure (chap. 4.3). However, the geological map (GPGB, 1981) does not unambiguously support this interpretation (s.a.).
- The approximately WNW-ESE striking directions L<sub>C</sub> are related to sinistral tectonical movements. In the northern basement they can be identified as

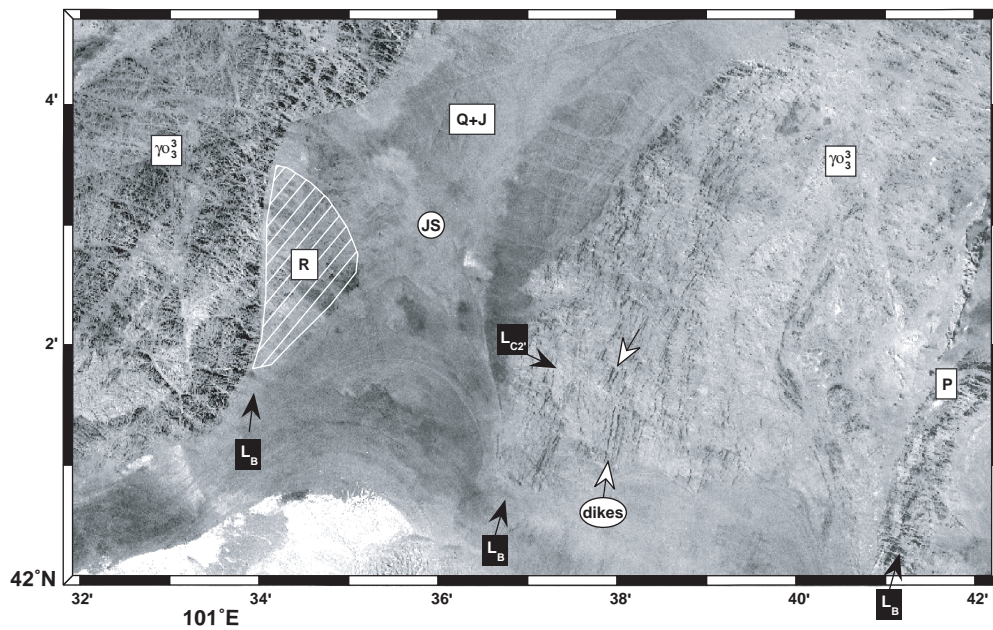
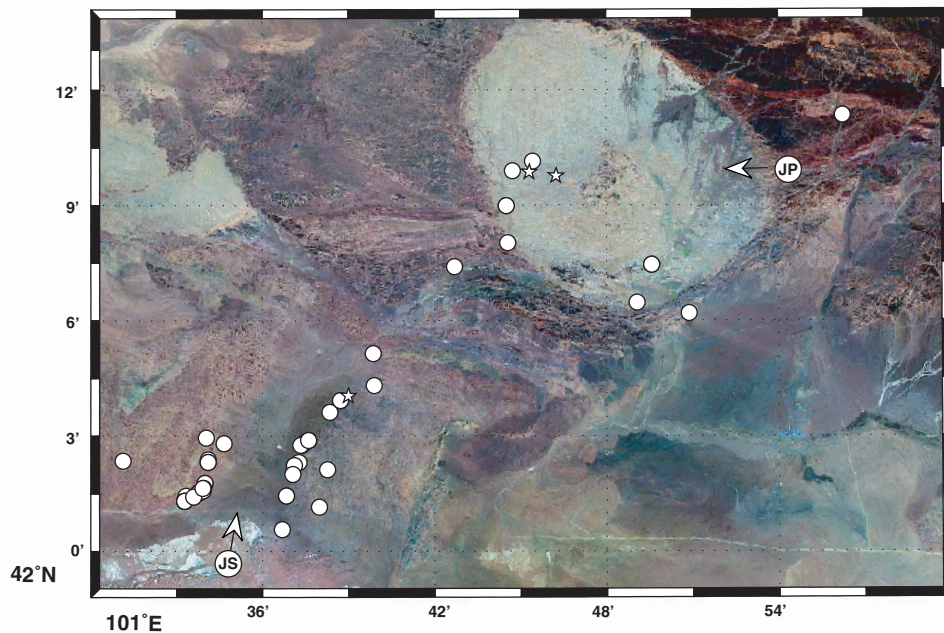


Fig. 4-8: Composite of Corona images showing the Jingsutu Structure (JS) and basement ~13 km SW of Fig. 4-7. The SSW-NNE striking direction  $L_B$  is especially pronounced along the western margin of the JS. Dikes in the basement to the E of the JS experienced sinistral shearing (white arrows) subparallel to the direction  $L_{C2}$ . Structural and spectral differences between the basement to the W and E of the JS are evident.

transpressional sinistral shearing with an offset of about 1-2 km in the Ordovician sequences (Fig. 4-7). In the southern basement a comparable sinistral offset of 1-2 km is evident at sheared dikes on the eastern shoulder of the Jingsutu Structure (Fig. 4-8). Because of the close spatial relationship of the two locations, it is reasonable to assume that sinistral shearing is related to the same tectonical phase.

#### 4.2.2 Petrology

Petrological investigations of the basement in the vicinity of the Jingsutu Structure and the Jingsutu Pluton (Fig. 4-9) were carried out complementary to the geophysical investigations. The petrological investigations were aimed to classify basement units in terms of the regional geology, to look for significant compositional differences, and to put constraints on the timing of formation. It should be noted that the general petrogenetical and tectonical implications of granitoid intrusions in Central Asia are still a matter of controversy in the current literature. Therefore, this chapter will reflect and interpret results of the petrological investigations in terms of the current literature. However, a profound contribution to this controversy is beyond the scope of this thesis.



*Fig. 4-9:* Landsat TM - image with the Jingsutu Structure (JS) and the Jingsutu Pluton (JP). Rock samples for petrological analysis were collected on the eastern and western shoulder of the Jingsutu Structure and in the vicinity of the pluton. Note that the basement on the eastern and western shoulder of the JS exhibits distinct spectral characteristics, which was confirmed by field observations. Three of the samples (stars) were further used for isotopic age determinations.

Field work and laboratory investigations were performed by several colleagues from the TU Berlin - namely Dr. Fiedler-Volmer, Prof. Dr. Franz, T. Hiller, and Dr. Mattheis - and included the following steps:

- Collection of samples during field work. Rocks were collected directly from outcropping basement blocks. Any strongly weathered rocks were removed with a sledge hammer prior to the sampling to obtain fresh material.
- Macroscopic inspection of samples prior to laboratory investigations.
- Preparation and analysis of thin sections.
- Preparation of powder- and melting-pellets of selected samples and following geochemical analysis by X-ray fluorescence spectroscopy (XRF).
- Manual separation of biotites from selected samples and following age determinations.

Age determinations were performed at the Geochemical Center, University of Göttingen.

### Geochemical Analysis

A general classification of the samples (s. Appendix D, p. 165ff) with respect to major elements (MgO vs. SiO<sub>2</sub>) is shown in Harker diagrams in Fig. 4-10. The majority of samples from the Jingsutu Pluton (Fig. 4-10, right) are characterized as intermediate to granitic. The



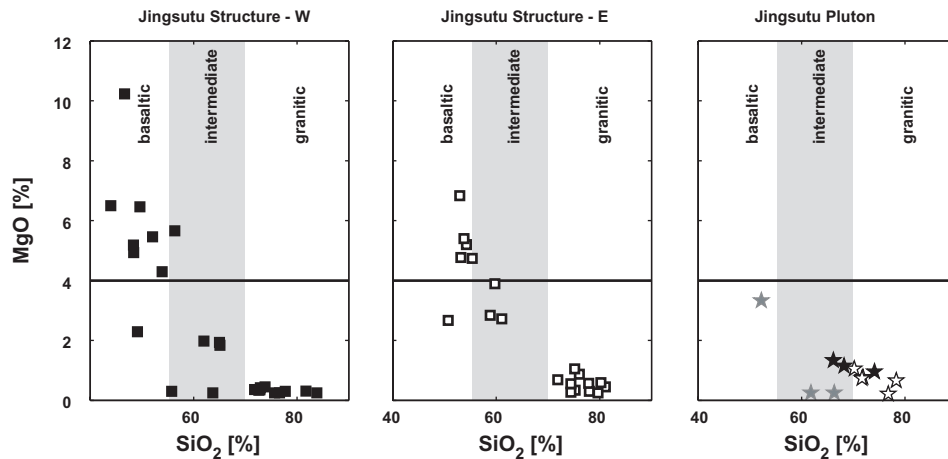


Fig. 4-10: General classification of rock samples with respect to major elements. In the analyses of the Jingsutu Pluton (right), samples from the edge resp. center of the pluton are depicted with white resp. black stars. Three xenolithic samples are depicted by gray stars.

samples from the southern basement generally show a greater compositional variability and span the whole range from basaltic to granitic. A comparison of rock samples from the western (Fig. 4-10, left) and eastern shoulder (Fig. 4-10, middle) of the Jingsutu Structure reveals differences within the southern basement: samples from the W show a generally greater variability in  $\text{SiO}_2$  and MgO, while samples from the E generally cluster in two regions, because samples with an intermediate  $\text{SiO}_2$ -content (61-71%) are missing.

Fig. 4-11 summarizes the analyses of rock samples from the Jingsutu Pluton in the form of a spidergram (SUN & McDONOUGH, 1989). This form of data-representation is frequently used to characterize and compare rock samples with respect to the content of trace elements, which is less affected by weathering. The absolute abundances of elements are normalized to predefined values, which reflect the typical melt composition of the assumed protolith. The elements are sorted in terms of their compatibility to the protolith with the compatibility of elements increasing from left to right (e.g. WU ET AL., 2002). Therefore, the slope in a spidergram reflects, how far evolved a melt has developed from the assumed protolith by fractional crystallization. Deviations in the spidergram from the general trend can be related to the crystallization of specific phases.

A general comparison of samples from the Jingsutu Pluton (Fig. 4-11, bottom) shows that most samples have matching signatures and demonstrates that no significant deviation exists between samples from the center (black stars) and the edge (white stars) of the pluton. The general slope of the spidergram demonstrates that advanced fractional crystallization has taken place during the formation of the granite. The signatures are generally characterized by several negative anomalies (Ba, Nb, Sr, P, Ti). Three samples from the center of the pluton (4P4, 4P6, 4P7; gray lines in Fig. 4-11) show deviating geochemical patterns as compared to the first group. In thin sections it can be seen, that samples 4P6 and 4P7 contain sillimanite, which is an

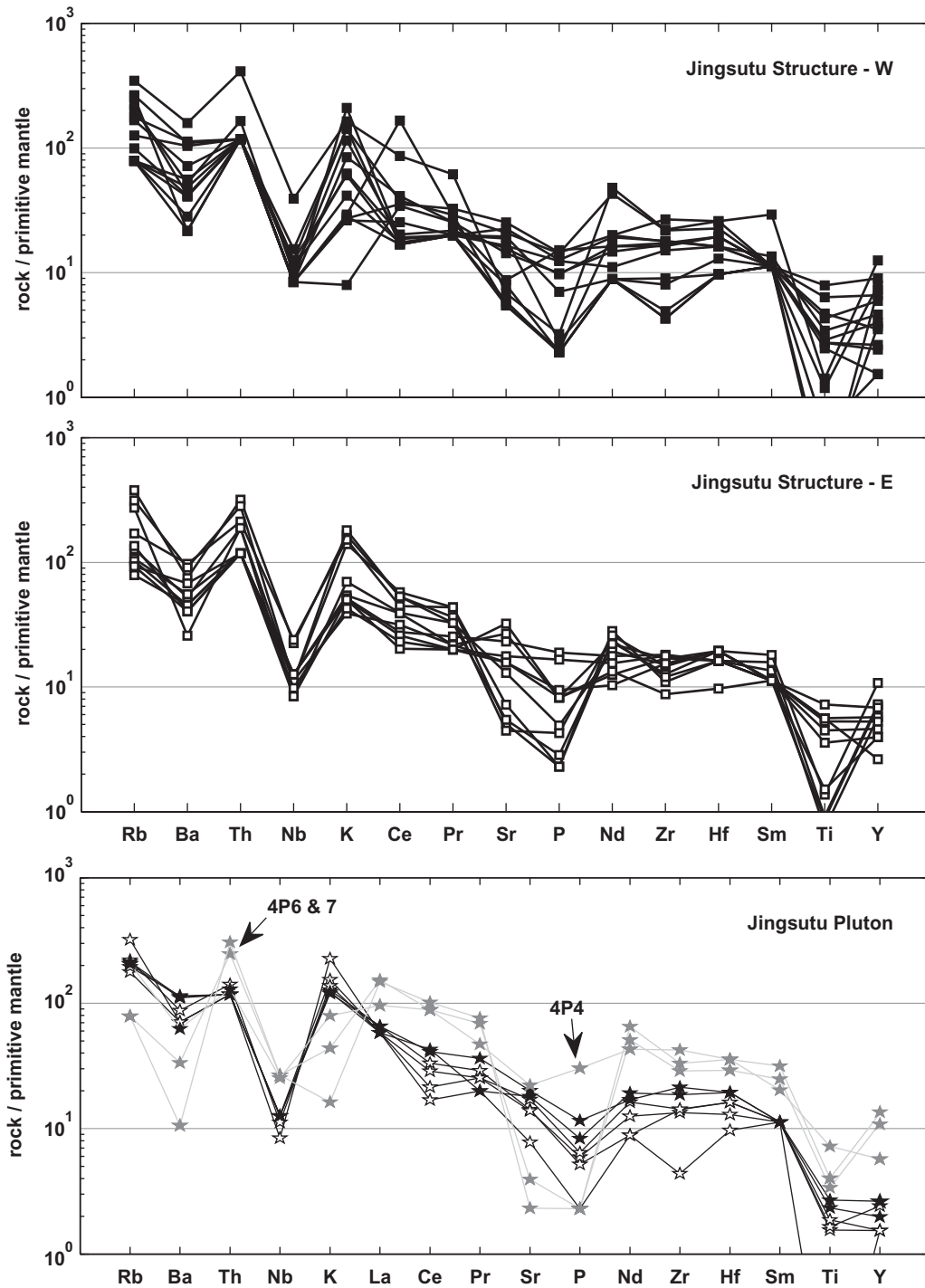


Fig. 4-11: Analyses of trace elements in spidergrams normalized to primitive mantle values (SUN & McDONOUGH, 1989). Three samples from the Jingsutu Pluton (bottom) show differing signatures and are identified as xenolithic (s. Fig. 4-10).

indicator mineral for contact-metamorphism. Therefore, they are considered to be xenolithic. Sample 4P4, which was also used for isotopic age determination, exhibits some characteristics of both groups and may comprise a mixture of xenolithic material with the main melt. Samples

from the eastern (Fig. 4-11, middle) and western shoulder (Fig. 4-11, top) of the Jingsutu Structure show the same general trend and depletions, when compared to the samples from the Jingsutu Pluton. However, differences within the samples from the southern basement are again visible, especially for certain trace elements (K, Nd, Zr, Hf, Ti, Y), where the samples from the W again show a much greater variability and samples from the E again cluster for some elements (only K, Hf, Ti), like in the analysis of major elements (Fig. 4-10).

### **Tectonic Implications**

Granites are frequently classified as fractionation products of materials either derived from the lower crust, from the remelting of upper crustal units (I- resp. S-type in CHAPPELL & WHITE, 1974), from selective fractionation of mantle diapirs (M-type in WHITE, 1979), or as anorogenically emplaced units (A-type in LOISELLE & WONES, 1979). While the (I,S,M)-classification was at first based on the geochemical composition only, the introduction of the anorogenic A-type also related the generation of melts to a certain tectonical setting. Consequently, the first group of granites (I,S,M) are related to the generation of melts in active or post-orogenic tectonical settings (e.g. volcanic arc, continental collision, post-orogenic gravitational collapse of orogenic belts), while the A-type is related to an anorogenic setting, namely to rift zones as a result of plume or hot spot activity and within stable continental blocks (EBY, 1992).

Whalen-diagrams are used to correlate the geochemical composition of granitic rocks to their petrogenesis by giving a rough discrimination between intrusions of the A-type on the one hand, and (I,S,M)-type on the other hand. The representative samples of the Jingsutu Pluton (stars in Fig. 4-12), i.e. excluding samples 4P4, 4P6, and 4P7, again do not show a great variability between samples from the center (black stars) and the edge (white stars) of the pluton. All samples, i.e. from the southern and the northern basement, are classified as transitional between (I,S,M)-type and A-type and a clear classification to a specific type is not possible in the diagrams. Samples from the southern basement, especially from the western shoulder of the Jingsutu Structure, generally show a greater variability (Fig. 4-12, upper right), which was already evident in the spidergrams (Fig. 4-11).

In tectonical discrimination diagrams, samples generally fall in the "syncollisional & volcanic arc"-field (Fig. 4-13, left) or in the "postcollisional"- or "volcanic arc"-fields (Fig. 4-13, right). Due to their more variable and generally greater Y- and Nb-content, samples from the southern basement roughly fall in the same fields in the diagrams, but form distinct clusters when compared to samples from the Jingsutu Pluton. The Pearce Diagrams are not in favor to a classification of granites as A-type, because A-type granites should generally fall in the "within plate"-fields (EBY, 1992). Instead, the geochemical analysis, the textural characteris-

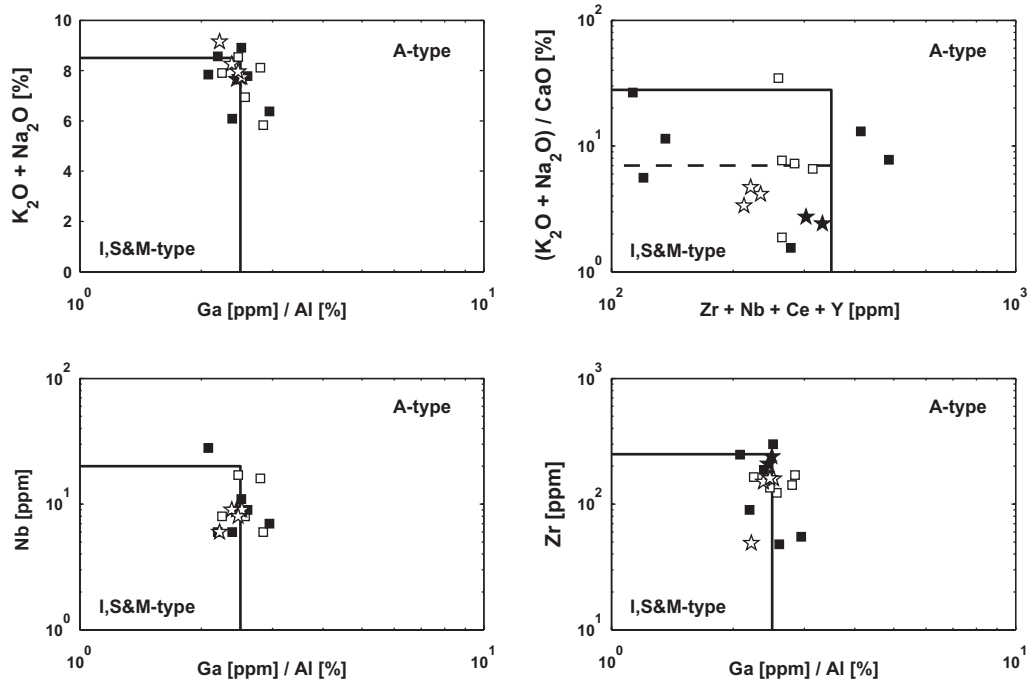


Fig. 4-12: Petrogenetic diagrams after WHALEN ET AL. (1987) with samples ( $\text{SiO}_2 > 68\%$ ) from the Jingsutu Pluton (stars) and the Jingsutu Structure (W: black squares, E: white squares).

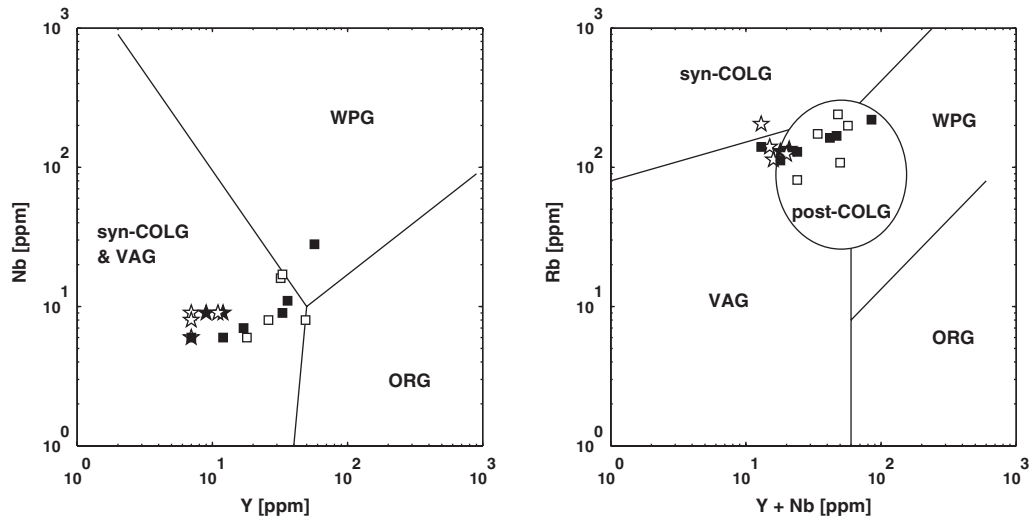


Fig. 4-13: Tectonical discrimination diagrams for granites (PEARCE ET AL., 1984; PEARCE, 1996). Symbols as in previous plot. Granites are: VAG = volcanic arc; syn-COLG = syncollisional; post-COLG = postcollisional; WPG = within-plate; ORG = ocean-ridge.

tics of rock samples, the approximately round shape of the Jingsutu Pluton with its clear spatial delineation from the surrounding units and the overall geodynamic setting (s. discussion) favor the classification of analyzed samples as I-type granites (Matheis, pers. comm.)

## Geochronology

Sample	Location	Description (Thin Section)	Age [Ma]
4E3	southern basement - east of Jingsutu Structure	pyroxene, amphibole, biotite (mostly fresh), amphibole and pyroxene intergrowth	270.2 ( $\pm 4.6$ )
4P3a	Jingsutu Pluton	granitoid, biotite (slightly chloritized), feldspar (slightly sericitized), some titanite, some amphibole	219.3 ( $\pm 3.4$ )
4P4b	Jingsutu Pluton	dioritic, increased mafic content, biotite (slightly chloritized), titanite $\rightarrow$ xenolithic	218.0 ( $\pm 3.4$ )

*Tab. 4-1:* Results of K/Ar-datings on biotites of three rock samples.

The collected rock samples contained only little Zircon. Therefore, the originally planned U/Pb-datings could not be realized. Instead, biotites were separated from three rock samples and used for K/Ar-analyses (Tab. 4-1).

For the two samples from the pluton (4P3, 4P4), which are classified as "Middle Variscan" in the geological map (GPGB, 1981), the analyses yield - within error bounds - conforming ages of  $\sim 219$  Ma, i.e. Late Triassic. Since 4P3, according to the geochemical analysis, represents the main pluton population and 4P4 has been identified to be xenolithic, the conforming ages of the two samples indicate a rather rapid cooling of the pluton, which was most likely emplaced at a subvolcanic level (Matheis, pers. comm.) A third sample taken from the eastern shoulder of the Jingsutu Structure, which is classified as "Late Caledonian" in the geological map (GPGB, 1981), yields an age of  $\sim 270$  Ma (Early Permian). Thus, this sample is considerably older than the analyzed samples from the Jingsutu Pluton. The age determinations are in accordance with the general classifications in the geological map and underline that southern and northern basement are genetically distinct basement units.

## Interpretation of Geoscientific Investigations

Generally, many authors (e.g. LIU ET AL. (2005), WU ET. AL. (2003A), WANG ET AL. (2004)) favor the generation of Late Paleozoic and Early Mesozoic granitoids along the CAOBS in a tectonical setting, where a post-collisional or post-orogenic extensional collapse and crustal thinning provide the heat to generate melts, which are derived from previously underplated material. Some I-type intrusions with geochemical compositions comparable to the analyzed samples from the Jingsutu Pluton and the Jingsutu Structure are described by:

- CHEN & JAHN (2004), who describe the Late Carboniferous ( $\sim 294$  Ma), post-collisional I-type magmatism in the Junggar Terrane to the NW of the Ejina Basin,



- CHEN ET AL. (2000), who describe the Halatu Granite. The intrusion is located about 1000km to the ENE of the Ejina Basin and is dated as Late Triassic (~228Ma).
- WU ET AL. (2003A & 2003B), who describe highly fractionated I-type granites in the Xing'an Range to the NE of the Ejina Basin, which are dated as Late Jurassic (~140Ma, Yiershi Pluton, see Appendix). They explain negative anomalies in their spidergrams (sim. Fig. 4-11) by the fractionation of Ti-bearing phases (ilmenite, titanite → Nb–Ti), apatite (→ P), plagioclase (→ Sr), and K-feldspar (→ Ba), which is hence considered to be a possible interpretation for our analyzed samples.

The given references emphasize that comparable intrusions were emplaced along the CAOBS throughout the Late Paleozoic and Mesozoic.

When comparing our age determinations to published values, one has to bear in mind that depending on the method, ages correspond to the crystallization of certain mineral phases at specific closing temperatures. WU ET AL. (2003A) estimate rapid cooling rates between 25-45°C/Ma for I-type granites in NE-China. Accordingly, datings on biotites (K/Ar, closing temperature ~400°C) may post-date datings on Zircon (U/Pb, cooling temperature ~850°C) by approximately 10-20Ma. Considering this, a regional overview of age determinations from literature and maps (different isotopic dating methods) in Fig. 4-14 facilitates the interpretation of the geochronological results and tectonical implications:

To the NW of the Ejina Basin, the oldest datings are associated with granitic intrusions of Early Carboniferous - Late Permian age, i.e. >300Ma (HAN ET AL., 1997; KOZLOVSKY ET AL., 2005<sup>1</sup>). The intrusions are roughly aligned on a NW-SE striking line along the Chinese - Mongolian border and mark the suture corridor between the Siberian Block (SB) to the N and Kazakhstan Block (KB) to the S. In the publications the Early Carboniferous - Late Permian intrusions are related to post-orogenic extension. Additionally, datings on aluminous granites (HAN ET AL., 1997) and various mineralizations further to the NW<sup>2</sup> (CHIARADIA ET AL., 2006) indicate a second, post-tectonical phase of activity during the Early Permian (~265-280Ma). Along the suture corridor between the SB and the KB, the Early Permian phase of activity is seemingly restricted to the NW section, which may be due to the lack of data available along the international border.

Our age determination of the Permian intrusion in the southern basement can be seen on an E-W striking line of consistent datings approximately along 42°N to the W of the Ejina Basin (Fig. 4-14, dark gray boxes): Ore deposits (ZHANG ET AL., 2005; MAO ET AL., 2005), mafic intrusions (ZHOU ET AL., 2004), a monzogranitic intrusion (GPGB, 1981), and basement to the

---

1. The bimodal volcano-plutonic association in the Tost Range, which was investigated by Kozlovsky et al. (2005), is located N of the Ejina Basin, ca. 135 km NW of the Jingsutu Pluton.  
 2. Not depicted in Fig. 4-14.

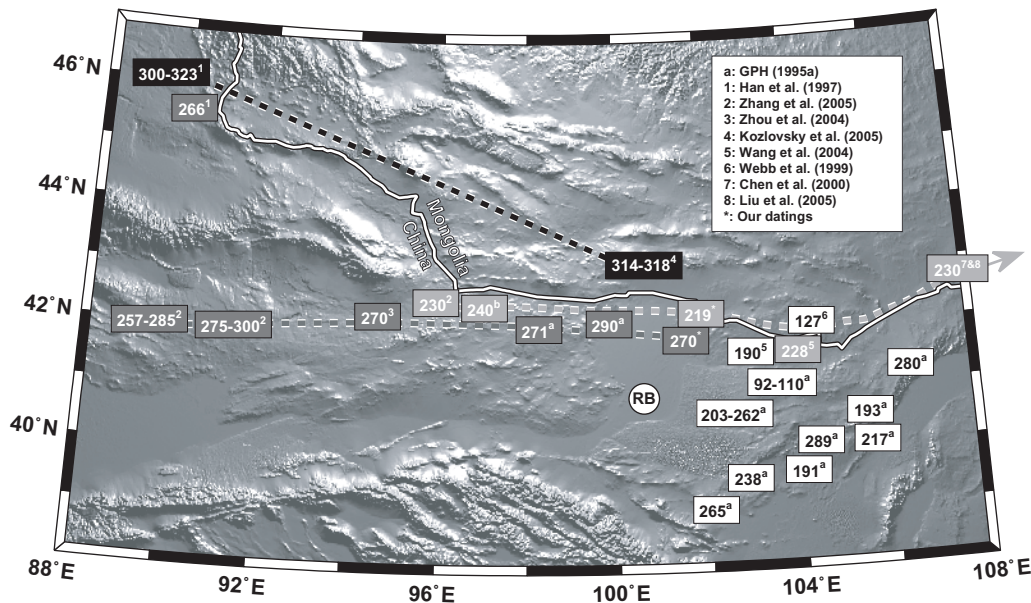


Fig. 4-14: Overview of age determinations (<400Ma) in NW China. Post-collisional resp. post-orogenic intrusions are reported along the international border (Carboniferous, black), along ~42°N towards the W (Early Permian, dark gray) and towards the E (Late Triassic, light gray) of the Eji-na Basin (RB). Additional age determinations (various ages, white) show, that post Triassic activity is exclusively reported to the E of the RB. For block boundaries refer to Fig. 3-2 (p. 67).

E of the Jingsutu Structure are all dated as Early Permian (~270Ma). All intrusions are related to post-collisional resp. post-orogenic extension. Authors describe the line along 42°N as part of the suture corridor between the KB or MAT to the N and the Tarim Block (TB) to the S. The line is supposed to extend into the Ejina Basin below Quaternary sediments as the Ebinur-Juyan Fault (WÜNNEMANN, 1999). This interpretation is supported by geophysical investigations (WANG ET AL., 1997), where the suture between the KB and the TB is interpreted ~40km to the S of the Ebinur-Juyan Fault (Hongshishan Fault in WANG ET AL., 1997) along the Shibanjing-Xiaohuangshan Fault.

Subparallel, just to the N of the previously described line of Early Permian intrusions, a second E-W striking line with Middle-Late Triassic (219-240Ma) datings can be seen along ~42.5°N (Fig. 4-14, light gray boxes). Along this line, ore deposits (ZHANG ET AL., 2005), the Jingsutu Pluton, granitic intrusions in the Yagan Metamorphic Core Complex (YMCC; WANG ET AL., 2004), the Halatu Granite (CHEN ET AL., 2000), and the Longtoushan 1 Granite (LIU ET AL., 2005) are related to a Late Triassic phase of post-collisional resp. post-orogenic extension. According to the authors, the YMCC, which is located 160km to the ESE of the Jingsutu Pluton, and the Halatu Granite are both located N of the Solonker Suture, which separates the southerly NCB from the northerly SB resp. MAT.

Our age determinations are consistent with age determinations along the approximately E-W striking suture zones between the southerly blocks (TB, NCB) and the northerly blocks (KB, SB, MAT). They reflect the W to E progressing closure of the Proto-Tethys with subsequent phases of accretion (p. 65) and extension. This trend of decreasing intrusion ages towards the E is further underlined by additional ages determinations from literature and maps in Fig. 4-14: while the W of the Ejina Basin was stabilized after the Triassic, younger phases of Jurassic-Cretaceous magmatic activity are solely concentrated to the E of the Ejina Basin. The cited references give possible leads for extended petrological investigations and interpretation of our data, which will however not be pursued further in the scope of this thesis.

The evaluation of satellite data yields two distinct strike directions of lineaments ( $L_B$  and  $L_C$  in Fig. 4-6), which are possibly connected to phases of tectonical deformation:

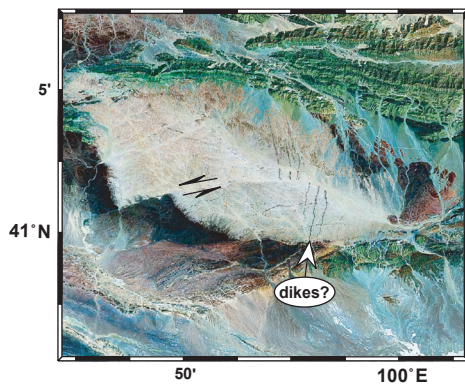


Fig. 4-15: Sinistral shearing in "Late Caledonian" intrusion (GPH, 1990) within the basement units to the SW of the Ejina Basin.

For the WNW-ESE striking direction  $L_C$  sinistral shearing is obvious and an upper age limit can be derived from our datings on the eastern shoulder of the Jingsutu Structure: since  $L_C$  cuts the dikes associated with the intrusion (Fig. 4-8), the sinistral shearing postdates the Early Permian (~270Ma, sample 4E3, Tab. 4-1). No further direct constraints for the timing of sinistral shearing can be deduced from the isotopic age determinations in the northern basement, because the relationship between the sinistral shearing and the Jingsutu Pluton is not clear from the satellite images (Fig. 4-7). However, additional evidence pointing to a regional occurrence of sinistral shearing can be

found in satellite images ~185km to the SW of the Jingsutu Structure (Fig. 4-15), where similar sinistral shearing with an offset of ~2-3km is evident at a "Late Caledonian" intrusion (GPH, 1990) in the basement to the SW of the Ejina Basin. Under the assumption of a coeval regional occurrence, two possible phases of regional tectonical activity with predominant sinistral shearing can be identified in the current literature:

A Late Paleozoic phase is identified by LAURENT-CHAVRET ET AL. (2003). Based on structural studies and isotopic age determinations, they report several sinistral events in the spurs of the Altay mountains along the Erqishi-Irtysh shear zone to the NW of the Ejina Basin, which they date as Late Paleozoic (Permian). They relate these events to post-orogenic processes along the suture zone between the KB and the SB. However, most of their described indicators for sinistral shearing are dated as Early Permian (~280-290Ma), which predates our age determinations.

Cenozoic activity with sinistral offsets related to the Himalayan orogeny is reported at several locations around the Ejina Basin, e.g. in the easternmost Gobi Altay to the N of the Ejina Basin (CUNNINGHAM ET AL., 1997), to the W of the Ejina Basin (CUNNINGHAM ET AL., 1996), in the Hexi Corridor to the S of the Ejina Basin (DING ET AL., 2004; DARBY ET AL., 2005), and in the South Gobi Basin along the EGFZ (s. Fig. 3-4, p. 70) to the NE of the Ejina Basin (WEBB & JOHNSON, 2006).

According to the widespread spatial occurrence of sinistral shearing during the Cenozoic, a connection of  $L_C$  to this phase of activity is the preferred interpretation. However, the connection of  $L_C$  to the Late Paleozoic or a yet undefined phase of activity can generally not be ruled out, since no direct datings of kinematic markers are available.

The interpretation of the SSW-NNE striking lineament  $L_B$  in connection to the Jingsutu Structure as a tectonical feature is at first sight less obvious. Geological maps indicate no fault related context of the Jingsutu Structure. However, the petrological investigations reveal distinct differences in the geochemical compositions of basement rocks on the eastern and western shoulder of the Jingsutu Structure (Fig. 4-10 and Fig. 4-11). This spatial distinction of the southern basement is also evident in spectral (Fig. 4-9) and structural differences (Fig. 4-7) visible in satellite images. Thus, the geoscientific investigations give first evidence that the Jingsutu Structure may separate different basement units or different basement levels.

The interpretations of the geoscientific investigations in the vicinity of the Jingsutu Structure are summarized as follows:

- In accordance with the current literature the basement around the Jingsutu Structure and the basement around the Jingsutu Pluton are related to two distinct phases of post-collisional resp. post-orogenic extension.
- The classifications of our age determinations in terms of the current literature concurrently show that the basement units around the Jingsutu Structure and Jingsutu Pluton are located N of suture zones, which separate the southerly (NCB, TB) from the northerly blocks (KB, SB, MAT) (s. Fig. 3-2, p. 67).
- The distribution of intrusion ages in Fig. 4-14 shows that the Ejina Basin separates a region with predominantly Late Paleozoic activity to the W and a region with predominantly Mesozoic activity to the E.
- According to differences in the geochemical composition as well as structural and spectral characteristics, the SSW-NNE striking Jingsutu Structure separates distinct basement units. These differences may be explained by vertical or horizontal offset of basement units. However, a fault related contact is not indicated in geological maps. In connection to the Jingsutu Structure, the SSW-NNE striking direction  $L_B$ , may be related to Late Jurassic-Early Cretaceous normal faulting with the same strike direction, which is reported

from seismic sections in the Chaoshui Basin to the S of the Ejina Basin (VINCENT & ALLEN, 1999).

- NW-SE striking lineaments ( $L_C$ ), along which sinistral shearing is evident in satellite images, are classified in terms of the regional occurrence of sinistral strike-slip faulting in NW China during the Cenozoic.

### 4.2.3 Geophysics

#### TEM Measurements

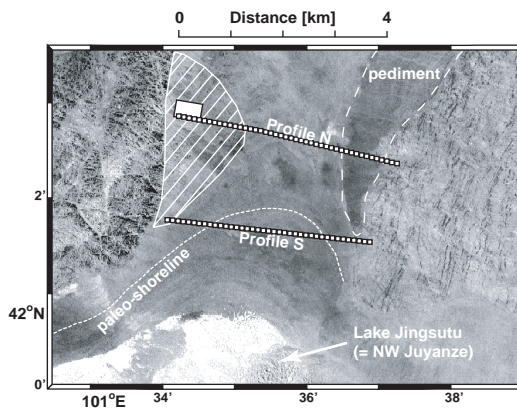


Fig. 4-16: Location of TEM-measurements in the Jingsutu Structure.

Measurements in the Jingsutu Structure were conducted along two subparallel, ~4km long profiles, which cross the structure perpendicular to the assumed geological strike from E-W (small squares in Fig. 4-16). Basement units on either side of the structure exhibited a rather rough topography and were not suitable for the placement of a large TEM coil. Thus, measurements were restricted to the central section of the structure. The only minor obstacles for measurements were occurrences of a rhyolite (hatched area in Fig. 4-16), which in places reached relative elevations of up to approximately ten meters

with respect to the surrounding. The remainder of the profiles was located on flat terrain in the central sections of the profiles or on gently sloping uphill terrain towards the E margin of the structure (marked pediment surface in Fig. 4-16). The northern profile (Profile N), which coincides with the central section of the AMT profile (BECKEN ET AL., 2007), comprises a total of 44 stations. Along the southern profile (Profile S), which is located about 3km to the S, measurements were taken at a total of 40 stations. With respect to the N-S extension of the structure, Profile N is located in the center and Profile S is located on the southern margin of the structure. Profile S crossed several paleo-shorelines (exemplarily depicted in Fig. 4-16), which mark holocene phases of higher water levels of the adjacent lake (HARTMANN, 2003). Along both profiles, loops at neighboring stations were placed edge to edge, thus, resulting in a constant station-spacing of 100m. While the dense spacing of stations along each profile guarantees that measurements partially share the same induction volume, the distance between the profiles is too large for any significant sensitivity overlap. In the following, stations along these two profiles will be referred to with respect to the position, e.g.  $S_N0m$  is the westernmost station at 0m on Profile N.

Additionally, measurements were taken on a small array (6x3 stations) on the W margin of the structure (large rectangle in Fig. 4-16). The southern stations of the array coincide with the westernmost stations of Profile N (Fig. 4-20). The main purpose of measurements on the array was to identify possible 3D effects in the data, thus, checking the validity for the assumption of a 2D distribution of resistivities.

All measurements were carried out in the coincident-loop configurations (100x100m<sup>2</sup>) using the old LAPTEM configuration (s. Appendix A, p. 133ff). Measured transients yielded evaluable data between ~170µs up to at maximum 200ms. At eleven stations on Profile N and one station on Profile S the switching to high gains was accidentally not performed during measurements. Therefore, measured transients at these stations cover a time range of only up to ~8ms, which causes a decreased depth of investigation. Consequently, the new control software for the LAPTEM was designed with the possibility to perform measurements with a pre-set script (Appendix A.1.1, p. 134), which reduces the chances of such operational mistakes. In the following 1D inversion of measurements (Fig. 4-17) these stations are easily recognizable by the decreased depth of investigation. For the 2.5D modeling the missing data at late times is less critical, if it is available at adjacent stations. In this case the partially overlapping induction volume of neighboring stations guarantees a sufficient sensitivity of the underground model to the measured data. Therefore, the only critical section to be considered in the 2.5D modeling of data is located between S<sub>N</sub>2300m-S<sub>N</sub>2800m.

### 1D Inversion

The processed data was used in constrained 1D smooth inversions. At each station, all measured runs were inverted simultaneously with a starting model chosen as homogeneous half-space. According to the example analysis (s. Fig. 2-9, p. 21) the regularization parameter for the smooth inversion (→ 2-12, p. 20) was first fixed to a value of 0.18. After visual inspection of the inversion results it was lowered to values of 0.056-0.1 at some stations, which improved data fits without significant changes to the resulting inversion models.

Along the profiles the 1D smooth inversion yield average RMS misfits (→ 2-8, p. 16) between 3.3(±0.8)% on Profile N and 3(±1)% on Profile S. Three stations with larger RMS errors (~10%), located directly on the western edge of the Jingsutu Structure (S<sub>N</sub>0m, S<sub>S</sub>0m, S<sub>S</sub>200m), were excluded from the calculation of the average RMS. Measured data and results of the 1D smooth inversions are summarized in Appendix C (p. 164ff).

In Fig. 4-17 the resulting sections of 1D models show a general trisection of the subsurface resistivity distribution into a highly conductive central section (1-5Ωm) and resistive units towards the E and W (>30Ωm). Since this trisection is evident along Profile N and Profile S (Fig. 4-17, top and bottom, resp.), the general similarity of sections implies that the overall structure in the considered depth range is 2D. The station map (Fig. 4-16) shows that Profile S is close to the southern edge of the Jingsutu Structure. It crosses several paleo-shorelines and

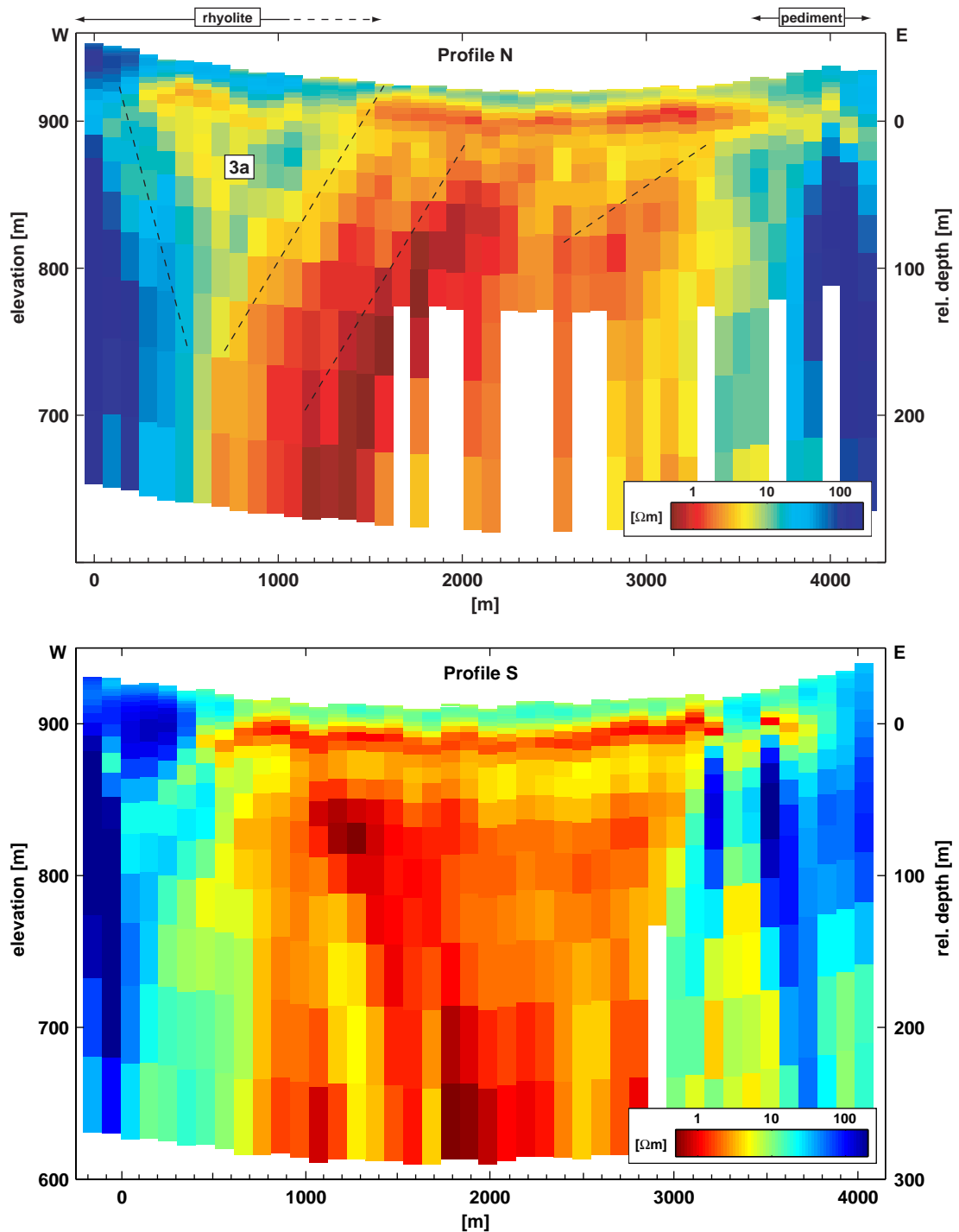


Fig. 4-17: Models of 1D smooth inversions displayed as sections for the two profiles across the Jingsutu Structure (Fig. 4-16). At each station the associated 1D model is plotted with respect to the true elevation. The vertical exaggeration for both profiles is about 7:1. A section displaying the results of the 1D block inversions along Profile N can be found in the Appendix (Fig. C-3, p. 166).



is possibly already in the sphere of influence of the southerly adjacent lake Jingsutu, but does not connect to marked surface features like the rhyolite or the pediment surface (Fig. 4-16). Thus, it can be expected that the two profiles to some extent represent distinct geological settings and direct comparisons should be restricted to the general features. The interpretation of structural details on Profile S is problematic, because additional information and confirmation from the AMT is not available. A distinction between 2D- and 3D effects in the data of Profile S is not possible and in the following, structural details are only further discussed for Profile N.

Between  $S_N200$ - $S_N1500$ m a wedge shaped structure (**3a** in Fig. 4-17) of intermediate resistivities (5-10 $\Omega$ m) can be seen down to a relative depth of  $\sim 150$ m on Profile N. This structure coincides well with the E-W extension of the rhyolite and has no counterpart on Profile S. Thus, a comparison of the areal distribution (Fig. 4-16) further suggests that the wedge shaped structure is associated with the rhyolite.

The resistivity section along Profile N indicates a general westward dipping of structures in the highly conductive part of the section between  $S_N700$ - $S_N3000$ m (dashed lines). At a different scale this general westward inclination is also evident in the AMT section (s. following chapter). Because structural details are difficult to interpret in the smooth section, an additional 1D block inversion was performed for measurements on Profile N (s. Appendix C, Fig. C-3, p. 166). The section of 1D block models yields essentially the same structural westward dip and angles of inclination in the range between 3-22°. Since the placement of the depicted layer interfaces depends on the interpreters choice and is ultimately also influenced by the selected coloring, the given inclinations have to be considered rough estimates. Consequently, a strict application of formula **2-27** (p. 36) for the estimation of the true inclinations from the apparent inclinations with respect to the 1D section is not appropriate. However, a rather general application of the theoretical results suggests that the true inclinations may be somewhat steeper than the interpreted angles of inclination, but not excessively (comp. Fig. 2-18, p. 36).

A 1D joint inversion together with AMT data along Profile N was not conducted, since an analysis of AMT data indicates 2D/3D conditions at most stations and for most frequencies in the recorded frequency bands (Becken, pers. comm.).

## 2.5D Modeling

As shown in chap. 2.3.5, the 1D inversion of 2D or 3D data introduces bias in the 1D inversion models. Therefore, a 2.5D modeling is applied to the measurements along profile. Since fitting data with trial-and-error forward modeling is a time consuming process, it is concentrated on profile N. This also has the advantage that the modeling results can be compared with the 2D inversion model obtained from the MT data along the same profile.



According to the number of stations on Profile N, each iterated 2D model required 44 forward calculations with TEMDDD, which were performed on a small cluster at the department with, depending on availability, between 1-10 parallel computer nodes (s. chap. 2.3.4, p. 32ff). The 2D models were created and adjusted using the *ModelCreatorGUI* and input models to TEMDDD were generated using the associated model generator (s. chap. 2.3.3, p. 29ff). A look at the elevations along the profile (comp. Fig. 4-17) shows that measurements were conducted on generally flat terrain. Therefore, any effects due to the topography can only have a marginal importance and all 2D models consequently were created with a flat topography.

The 2.5D modeling was performed by comparison of late time apparent resistivities of modeled and 1D reference transients. Reference transients were calculated by using the models of the 1D inversion for forward calculations with *TEMIDmod*. In these forward calculations any parameters purely related to the acquisition - i.e. ramp time, internal lowpass filter and repetition frequency of the transmitter - were excluded or set to zero. This approach was taken to avoid the necessity to include these parameters into the calculated 2.5D transients. It is justified, because the models of the 1D smooth inversion represent the measured data well without significant deviations (e.g. Fig. C-1, p. 164).

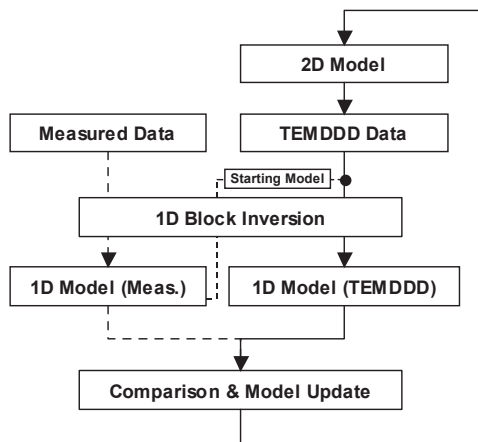


Fig. 4-18: Schematic diagram explaining the model update in the 2.5D modeling.

The starting model (not depicted) was chosen with respect to the result of the 1D section (Fig. 4-17, Fig. C-3) and included seven 2D bodies, each with a homogeneous resistivity. The 2D bodies were embedded into a homogeneous halfspace of  $200\Omega\text{m}$ . During the first iterations, only the structure and bulk resistivity of bodies were altered and some additional bodies were included into the model. In this phase of modeling, model updates were constructed in a "trial-and-error" manner by visual inspection of the data fit. Once the apparent resistivities of the modeled transients started to exhibit similar characteristics when compared to the reference transients, model updates were constructed as illustrated in Fig. 4-18. In this approach

the calculated 2.5D transients were subjected to a 1D block inversion (right branch in Fig. 4-18). The starting model for this 1D inversions was taken from the according result of the already existing 1D block inversion of the measured data (left branch in Fig. 4-18). A comparison of the resulting block models was then used to adjust the 2D model. This approximation strategy for the 2D sensitivity is similar to the approach for a 2D block inversion of DC

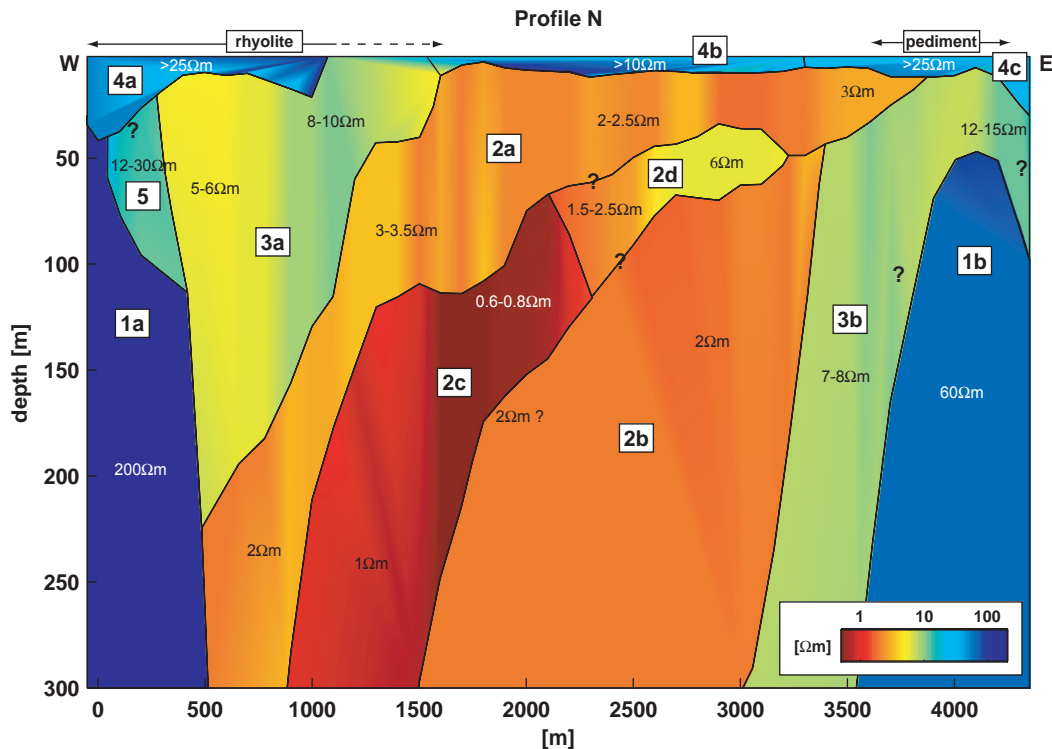


Fig. 4-19: Final result of the 2D block-modeling along Profile N. Within the model bodies, resistivities are locally varying as indicated. Sectors of the model with poor model resolution or poor data fit are indicated by question marks.

data described by CHRISTIANSEN & AUKEN (2004). During the last phases of modeling, resistivities were also adjusted locally within 2D bodies to further improve the data fit (comp. Fig. 2-14, p. 31).

The final result of the 2.5D modeling is displayed in Fig. 4-19. The resulting model curves are summarized in terms of apparent resistivities together with the associated data fits in Appendix C.1 (p. 163ff). Except for the four westernmost stations, which show a poor data fit with RMS errors between 20-80%, all measured data is explained well by the 2D model with an average RMS of  $8(\pm 4)\%$ . Generally, the 2D model consists of 11 bodies with internally varying resistivities, which are combined into 5 groups in Fig. 4-19.

The most prominent features of the 2D model are represented by the resistive bodies **1a-b** in the W and E, and the highly conductive bodies **2a-d** in the center of the model (bold characters refer to Fig. 4-19). In the course of the modeling, bodies **2a** and **2b** were handled as distinct units, but are represented by similar resistivities between 2-3.5Ωm in the final model. Thus, they could also be considered as single entity with respect to the resistivities. Between  $S_N 2100$ - $S_N 2600$ m, body **2d** shows increasing conductivities and could also be attributed to the bodies **2a,b** or to body **2d**. Since the position roughly coincides with the section of the profile where - due to an operational mistake - several stations with decreased depth of

investigation exist, the exact mapping of resistivities to bodies and, thus, the connection of bodies **2c** and **2d** as depicted in the final 2D model is an arguable feature as indicated, which will be further discussed in the following chapter. Since the TEM method is inherently sensitive to good conductors, body **2c** is the best resolved feature of the 2D model. With resistivities well below  $1\Omega\text{m}$  in some sectors, this unit exhibits extremely high conductivities. The increase in resistivity beneath **2c** between  $S_N1500\text{m}$ - $S_N2000\text{m}$  is indicated by the measurements and is connected to body **2b** in the 2D model. However, the exact amount of increase is a poorly resolved parameter and the modeled value of  $2\Omega\text{m}$  has to be considered a lower bound (comp. A-type model in FITTERMAN, 1988).

The resistive units **1a-b** are separated from the conductive units **2a-d** by units **3a-b**, which are modeled with intermediate resistivities between  $5\text{-}15\Omega\text{m}$ . The westerly body **3a** exhibits a rather heterogeneous resistivity structure. It coincides with the wedge shaped structure, which was already indicated in the 1D section (Fig. 4-17, top) and is likely connected to the occurrence of the rhyolite. To achieve a better data fit it would generally be possible to split this body up into several smaller bodies, but for reasons outlined in the following chapter it was left as single unit to avoid a possible over-parametrization of the 2D model. The easterly body **3b** marks a subparallel transition zone between the highly conductive unit **2b** and the resistive unit **1b**. It shows continuously increasing resistivities from W to E and is a relevant feature needed to explain the measured data. However, with respect to the measured data between  $S_N3300\text{m}$ - $S_N3900\text{m}$  (s. Fig. C-1, p. 164), the gradually increasing resistivities with depth connected to unit **2b** constitute a model type, which is generally not well resolved by the TEM method (A-type model in FITTERMAN, 1988). Therefore, the overall structure at intermediate depths in terms of a layered model is inherently bound to equivalence in this part of the model.

Bodies **4a-c** indicate generally higher resistivities at shallow depth along most of Profile N. Again, the increase in resistivity is indicated by the measured data, but the displayed resistivity values have to be considered lower bounds, i.e. similar data fits could also be achieved with arbitrarily increased resistivities (Ka-type models in FITTERMAN, 1988). Finally, body **5** represents a part of the 2D model, which does not explain the measured data well. As outlined below, 3D effects in the data are likely to be relevant in this part of the model and the structure of this unit should not be over-interpreted.

To estimate the depth of investigation, the final 2D model in Fig. 4-19 was cut below fixed depth levels by including homogeneous halfspaces of  $1\Omega\text{m}$  or  $30\Omega\text{m}$  (not depicted). The according 2.5D modeling shows that, depending on the considered station, sensitivity in the time range covered by measurement is usually given down to depths between 300-400m. Hence, the 2D model in Fig. 4-19 is displayed down to a depth of 300m.

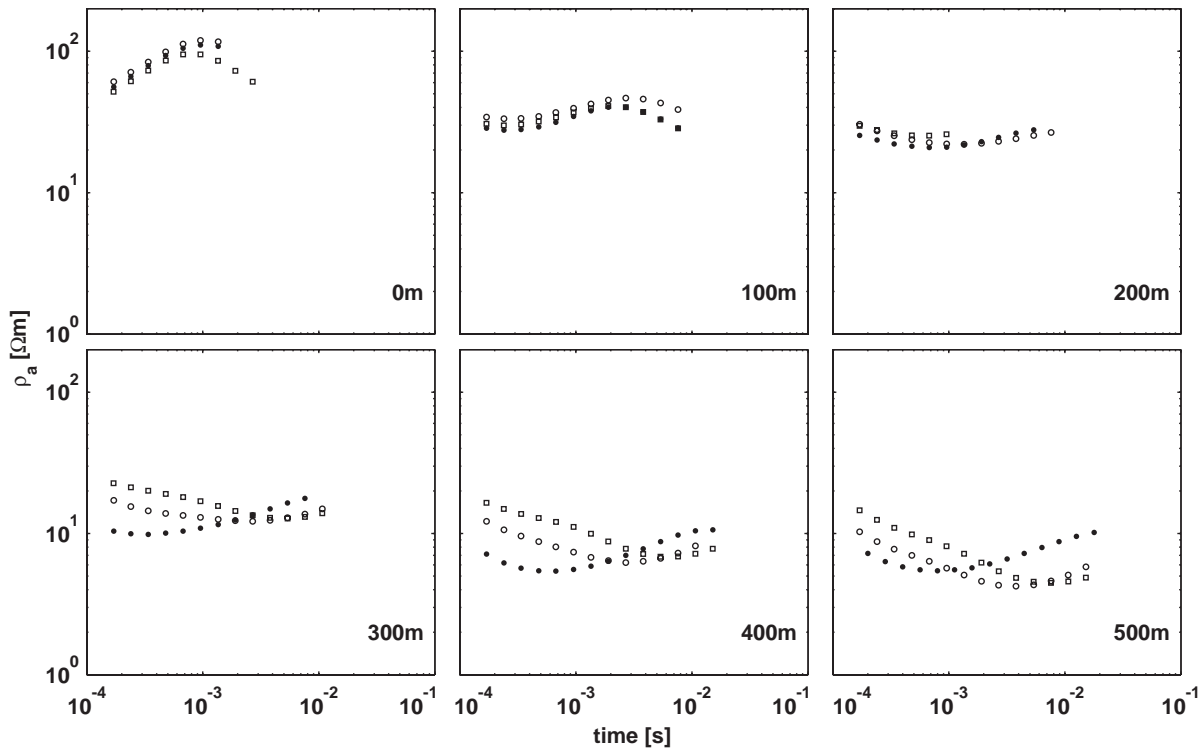


Fig. 4-21: Late time apparent resistivity of 1D smooth inversion models for stations on the array in the Jingsutu Structure, symbols as in Fig. 4-20.

#### 4.2.4 Interpretation

The general similarity of the 1D sections along the two profiles (Fig. 4-17) shows that the resistivity distribution within the Jingsutu Structure is aligned with the geological strike of the structure and, thus, 2.5D modeling is generally feasible. Furthermore, the general 2D characteristic of the Jingsutu Structure in the depth range relevant for the interpretation of TEM data is also inferred from the strike- and dimensionality-analysis of AMT data in BECKEN & BURKHARDT (2004), which was performed for AMT measurements on Profile N.

However, a detailed look at local variations of the resistivity structure perpendicular to the profiles shows that 3D effects may also play a significant role in some parts of the profiles. Exemplarily, Fig. 4-21 displays the 1D smooth inversion results of measurements on a small array (Fig. 4-16, Fig. 4-20) on the W margin of the Jingsutu Structure. For a better comparability of measurements, the data is represented as apparent resistivity, which was calculated from the 1D inversion models with acquisition-specific parameters (e.g. ramp time) set to zero. While stations in the W of the array (0m-200m in Fig. 4-21) show

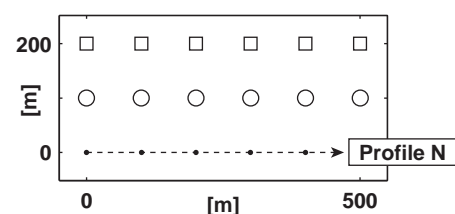


Fig. 4-20: Schematic station map for array (comp. Fig. 4-16 and Fig. 4-21).

strong variations in the E-W direction, but a relatively homogeneous distribution in the N-S direction ( $\rightarrow$  2D conditions), the stations in the E of the array (300-500m) show variations in E-W and N-S direction, thus, indicating significant 3D effects in this part of the array. Ultimately, a clear identification of 3D effects purely based on the TEM measurements is only possible for the westernmost stations depicted in Fig. 4-21, i.e. where areal measurements are available. Otherwise, a distinction of 2D- and 3D-effects in the TEM measurements is not possible, because no horizontal components of the electrical or magnetical fields were performed in the TEM measurements. The 3D effects in Fig. 4-21 are most likely connected to local variations due to the rhyolite or the transition zone from westerly basement into the central, more conductive sediments of the Jingsutu Structure. For the remainder of the profile, it is inferred from the general similarity of the 1D sections and the analysis of AMT data in BECKEN & BURKHARDT (2004) that the assumption of a general 2D characteristic of the structure is valid and, thus, 2.5D modeling is feasible.

To facilitate the interpretation, the final result of the 2.5D modeling is combined with a 3D topographic view of the Jingsutu Structure and a satellite image in Fig. 4-22. Please note the vertical exaggeration of 8:1. Just like the 1D sections, the 2D model shows a general trisection of the Jingsutu Structure into an easterly and westerly basement and a central part with highly conductive sediments of presumably Late Jurassic and Quaternary age (GPGB, 1981).

The basement units to either side of the Jingsutu Structure are distinct in their resistivity characteristic. The westerly basement (**1a**, bold characters refer to Fig. 4-22 or Fig. 4-19) is modeled with a value of  $200\Omega\text{m}$  or higher, which can be considered a typical value for a basement unit. The easterly basement (**1b**) exhibits a much lower resistivity of around  $60\Omega\text{m}$  (comp.  $S_N0\text{m}$  and  $S_N4300\text{m}$  in Fig. C-1, p. 164), which was measured directly on top of outcropping metamorphic units by both TEM and AMT. A possible explanation for such an exceptional low value for a metamorphic basement unit should require a considerable jointing of the basement rocks and substantial amounts of associated fissure water. Since the upper edge of the easterly basement is modeled at 890m.a.s.l., a possible source for the fissure water are floodings of the Jingsutu Structure from the S, which will be discussed in detail below. The significant differences of the westerly and easterly basement in the 2D model is concurrent with results of the AMT (BECKEN ET AL., 2007), the geochemical analysis (s. chap. 4.2.2, p. 84), and the results of remote sensing data (s. chap. 4.2.1, p. 81).

Even though the TEM 2D model is not adequate in detail for the westernmost stations on Profile N, it is evident from the measurements (s. Fig. C-1, p. 164), the 2.5D modeling of TEM data and the interpretation of AMT data (BECKEN ET AL., 2007) that the transition from high resistivities, which represent the westerly basement (**1a**), toward the low resistive units in the center of the Jingsutu Structure (**2a** & **3a**) is rather abrupt. According to the modeling, a steeply inclined interface with an angle of inclination probably above  $45^\circ$  is indicated, which is

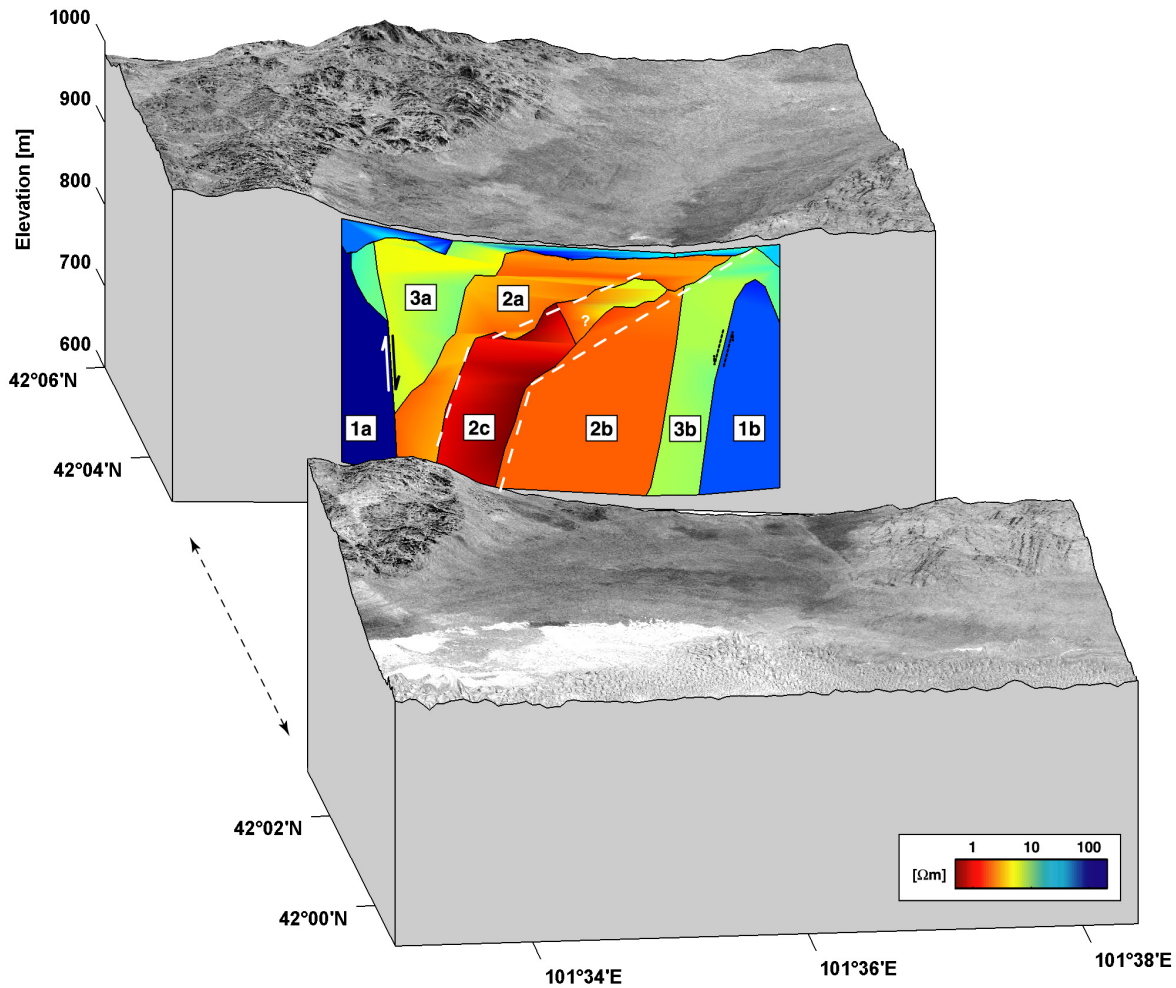


Fig. 4-22: 3D view of the Jingsutu Structure (Corona- & SRTM-data) together with the TEM section displaying the final result of 2.5D modeling along Profile N ( $\rightarrow$  Fig. 4-19). The underground blocks are sliced along the geophysical profile line and shifted with respect to each other. Please note that the underground model is displayed with a vertical exaggeration of 8:1.

located somewhere between  $S_N300$ - $S_N500$ . Consequently, normal faulting with substantial vertical displacement is interpreted along the western margin of the Jingsutu Structure. Similarly, the eastern margin of the Jingsutu Structure also shows a steeply inclined transition in the 2D model, but no direct contact between the basement unit (**1b**) and the highly conductive units (**2a-d**). Generally, sounding curves between  $S_N3300$ m- $S_N3900$ m (s. Fig. C-1, p. 164) show gradually and smoothly increasing apparent resistivities, a model type, which for the TEM method is inherently affected by model equivalences (FITTERMAN, 1988). Thus, the structural significance of the 2D model is limited in this part of the profile and the interface between basement and sediments is only approximate. Therefore, the indicated normal faulting along the eastern margin of the Jingsutu Structure (Fig. 4-22) is possible with respect to the 2D model, but less evident if compared to the interpreted normal faulting along the western margin.

In the central part of Profile N sedimentary units with very low resistivities prevail (**2a-d**). The maximum depth of investigation for the TEM data suggests that these sediments reach a considerable maximum thickness of at least 350m in the central part of the Jingsutu Structure between S<sub>N</sub>1000m-S<sub>N</sub>2000m. According to AMT measurements the maximum thickness is even larger and amounts up to at least 500m (BECKEN ET AL., 2007). However, due to the limitations of both applied electromagnetic methods, the good conductors' exact lower bound (**2c-d**) remains a poorly determined parameter.

Considering the geology and climate of the work area, resistivities below 3.5Ωm can be attributed to saline groundwater, which can generally be generated under arid conditions - due to high evaporation rates - by the enrichment of minerals in shallow standing water bodies or in shallow groundwater (KIRSCH, 2006). High concentrations of clay may further contribute, but by themselves would not suffice to explain the encountered high conductivities. The large volume of saline groundwater interpreted in the Jingsutu Structure requires a long duration of the underlying geological process, thus, ruling out a purely modern generation of the saline waters. Since low resistivities of sediments are mainly attributed to the pore-fluids, a basic form of Archie's law for water-saturated, clay-free material (e.g. KIRSCH, 2006B) may be applied:

$$\rho_{\text{bulk}} = \rho_{\text{pf}} \cdot F = \rho_{\text{pf}} \cdot a\Phi^{-m} \quad 4-1$$

In this empirical formula the bulk resistivity ( $\rho_{\text{bulk}}$ ) of a material is attributed to the resistivity of the pore-fluid ( $\rho_{\text{pf}}$ ) and the formation factor (F), which depends on the porosity of the material ( $\Phi$ ) and material constants. Typical values for the material constants are e.g. [a=1.0; m=1.3] for loose sands or [a=0.7, m=1.9] for sandstones (KIRSCH, 2006B). Because neither the material constants nor the pore-fluid resistivities of the sedimentary units are known from direct measurements, only very general conclusions may be drawn.

The application of Archie's law suggests that the sedimentary units should have a substantial porosity and are probably not consolidated at depth: a consolidated sandstone with small porosity and a large formation factor (e.g.  $\Phi=10\% \rightarrow F \sim 56$ ) would require abnormally low pore-fluid resistivities to explain the encountered low bulk resistivities. The observed spread of resistivities in bodies **2a-d** (0.6-3.5Ωm) can either be explained by a change in lithology, by local variations of the pore-fluid resistivities, or a combination of both. From the drilling "D3" (s. Fig. 4-6, p. 81) it is known that Jurassic units show a graded, downward coarsening bedding. It is reasonable to assume that such an lithologic change will also be connected to a change of porosities, thus, changing the formation factor F ( $\rightarrow 4-1$ ) and the resulting bulk resistivity. Examples from literature show that variations of the formation factor in the order 2-4 are frequently observed due to changing porosities in geological units (e.g. KIRSCH,

2006B, SCHÖNE, 1998), which is in the same order as the observed variations of resistivities in bodies **2a-d**. Consequently, without further information from drillings it is not possible to determine, which of the two described effects might dominate.

With the reservation that neither direct hydrogeological investigations were carried out within the Jingsutu Structure nor information from drillings is available, some additional preliminary conclusions are derived as follows:

In the Jingsutu Structure, the highly conductive groundwater presumably has a depth to watertable of about 10m from top ground surface, which equals a true elevation of about 910m.a.s.l.<sup>1</sup> This presumed groundwater level approximately concurs to the level of 904m.a.s.l. found in the drilling G36 in the eastern Juyanze (HARTMANN, 2003), which however is attributed to a distinct hydrological system. In a hyper-arid region with current mean annual precipitation rates of just 40mm/a (FENG ET AL., 2001) the replenishment or buildup of an aquifer by local rainfall events is an unlikely cause and would also conflict with the low resistivities encountered in the 2D model. An alternative explanation would be the influx of surface- or groundwater from the N, which is generally possible with respect to the topography of the Jingsutu Structure and the concealing basement units to the N, E, and W. However, the involved catchment area of the landscape at present, which can be estimated by visual inspection of the elevation data in Fig. 4-6, is obviously too small to assume a significant contribution from the N. Instead, an influx from the area of the southerly adjacent lake Jingsutu could be the dominant cause for the buildup and accumulation of saline groundwater. Investigations of the geographical workgroup (e.g. WÜNNEMANN, 1999; HARTMANN, 2003) have identified several stable lake phases with lake levels between 910-926m.a.s.l. between the Late Pleistocene - Late Holocene. Paleo-shorelines (s. Fig. 4-16, p. 95) are remnants of these higher lake levels and indicate that the Jingsutu Structure was frequently partially flooded from the S. Since stable lake phases altered with periods of drought, the massive precipitation of salts during phases of drought and their subsequent redepositioning during wet phases into the Jingsutu Structure possibly explains the high conductivities encountered in the 2D model for bodies **2a-d** and **1b** in Fig. 4-19 and Fig. 4-22. Alternatively it can not be excluded that the formation of saline groundwater is related to a much older period, where the assumptions about the present landscape possibly do not apply. Ultimately, a thorough hydrogeological investigation would be needed to further substantiate the given hydrogeological interpretations for the Jingsutu Structure, but the sketched scenario gives a plausible explanation according to the available facts.

---

1. Please note that all elevations related to the geophysical measurements are extracted from the SRTM data set, which may deviate from elevations from DGPS measurements (s. chap. 4.1.1, p. 75ff).



The examination of the hydrogeological situation concludes with an observation made during field excursion in the spring of the year 2004, where the work group passed by the old measurement area in the Jingsutu Structure and found that an enormous portion - i.e. at least several square kilometers - of lake Jingsutu was filled with water. According to informations from the local government the influx of surface water was seemingly initiated by the opening of dams in the upper reaches of the Ruoshui river just to the S of the Ejina Basin. The encountered lake level was not measured directly with DGPS, but can be estimated at  $\sim 900(\pm 5)$  m from SRTM data. The observation shows that in this hyper-arid area, relevant lake levels of the Jingsutu are episodically possible at present from the drainage system of the Ruoshui (comp. Fig. 4-1, p. 73).

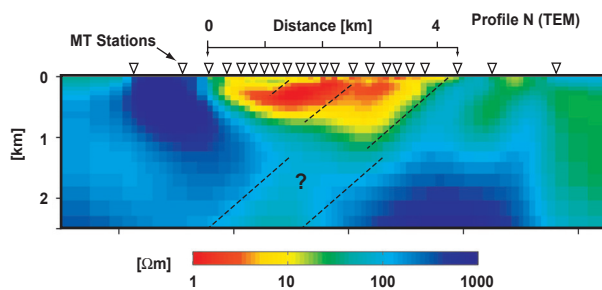


Fig. 4-23: 2D inversion result of AMT data in the Jingsutu Structure (Becken et al., 2007, modified). Note the different depth- and color scale when comparing to the TEM 2D section (Fig. 4-22). Below the good conductor in the center of the profile, the resolution of model parameters is poor and the indicated westward dipping is questionable.

Apart from possible hydrogeological aspects, the structural details of the final 2D model probably give clues about lithological boundaries in the center of the Jingsutu Structure, which may hint at the tectonic evolution. As already indicated in the 1D section (s. Fig. 4-17, Fig. C-3) a general dip of units towards the W can be observed (dashed lines in Fig. 4-22). At a larger scale this westward dip is also indicated by the 2D section of AMT data (Fig. 4-23), which was collected at stations located on Profile N and further to the E and W (s. Fig. 4-16, p. 95). The 2D section of AMT data displays the dipping

interfaces with steep inclinations of  $\sim 35\text{--}45^\circ$ , but due to the different depth scale under consideration a comparison to the TEM section is generally difficult.

In the TEM 2D model the westward dip is connected to several bodies and is characterized by shallow inclination of  $\sim 5^\circ$  between  $S_N1700\text{--}S_N3900$  (**2a-d**, **3b**, **4c**) and a steep inclination of  $\sim 25^\circ$  between  $S_N700\text{--}S_N1700$  (**2a-b**, **3a**). Thus, the inclinations in the 2D model are in general agreement with the values, which can be estimated from the apparent inclinations of the 1D models ( $\rightarrow$  **2-27**, p. 36). Even though the 2D model is not well resolved in some sections ( $\rightarrow S_N2300\text{m--}S_N2800\text{m}$ ) the good alignment of several body interfaces in the well resolved parts of the model suggests that they may connect to form a single unit (dashed lines in Fig. 4-22). The extrapolation of the unit with the shallow inclination to the surface connects it to the pediment surface at the eastern margin of the Jingsutu Structure. This implies that the sediments encountered on the pediment surface along the eastern margin of the Jingsutu Structure continue below Late Jurassic and Quaternary sediments in the center of the structure. Whether or not they continue across most of the structure and coincide with the steeply

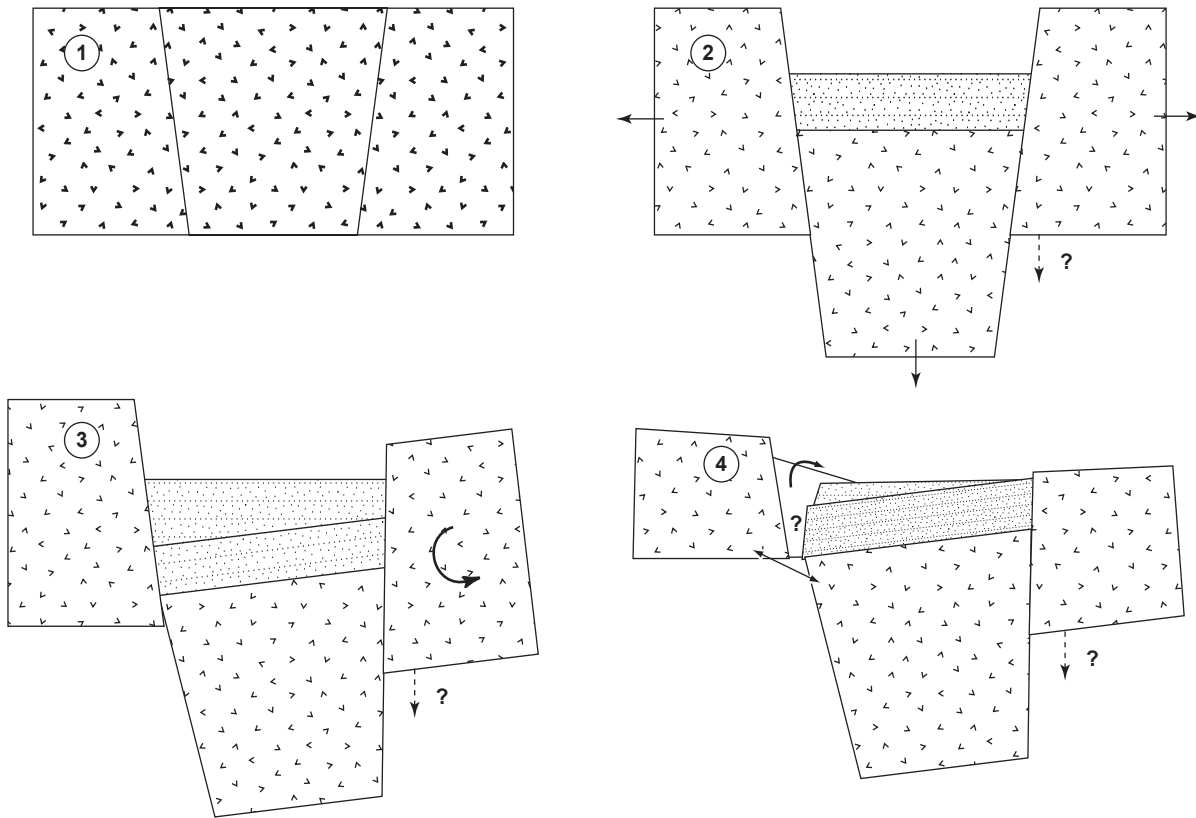


Fig. 4-24: Schematic diagram for the interpreted tectonical evolution of the Jingsutu Structure. In details, this reconstruction has to be considered hypothetical, but general aspects concur to the results of the geophysical and geoscientific investigations (s. text for further discussion and explanations).

inclined unit (western section of **2c**) can only be assumed speculatively. Even though the classification is not clear, it is evident from the 2D model that the westernmost sections of the highly conductive units (**2a,b**) continue below the mapped surface occurrences of the rhyolite. The extrusion of the rhyolite should therefore post-date the deposition of these sediments. It remains unclear, if unit **3a** coincides with the rhyolite, i.e. really marks its' occurrence at depth or rather represents a block of sediments, which is influenced by the superficial distribution of the rhyolite. The fairly low resistivities of unit **3a** (comp. PALACKY, 1987) favor the latter, which would mean that the rhyolite has only a minor thickness ( $\rightarrow$  **4a**).

The interpretation of the geophysical and geoscientific investigations in the Jingsutu Structure concludes with a - in parts hypothetical - schematic sketch of the tectonic evolution in Fig. 4-24, which also summarizes most results of the geophysical and geoscientific investigations:

1. According to an age determination of a sample collected on the eastern shoulder of the Jingsutu Structure, the formation of the basement units around the structure occurred during the Early Permian ( $\sim 270$ Ma, s. Tab. 4-1, p. 90). This age fits into the regional concept (s. Fig. 4-14, p. 92) and relates the formation

of the basement to the post-collisional or post-orogenic collapse along the suture zone between the Kazakhstan Block or Mongolian Arc Terranes to the N and the Tarim Block to the S (s. chap. 3.1.1).

2. Subsequent to the formation of the basement, extensional movements led to the creation of a graben structure. The direct relationship between the Jingsutu Structure and the Jingsutu Pluton is not quite clear from the interpretation of satellite images and it seems possible that the present day constellation might differ from the original configuration during formation. However, it is evident that the Early Jurassic Jingsutu Pluton (comp. datings, Tab. 4-1, p. 90) marks an extensional event, which integrates well into the regional context (s. Fig. 4-14, p. 92). In a regional context this extensional event is usually attributed to the accretion of Cimmeria to the southern margin of Laurasia (s. chap. 3.1.1). Consequently, it is assumed that the main phase for the formation of the Jingsutu Structure coincides with the emplacement of the Jingsutu Pluton. It is worthwhile to note that the creation of an approximately N-S striking extensional graben structure in a regional stressfield due to compressional forces from the SW is in agreement with sand box experiments, which are depicted in Fig. 3-3 (s. p. 68). Furthermore, an Early Jurassic formation of the graben structure would also concur to the geological maps, which depict the filling of the Jingsutu Structure as Jurassic.
3. The westward dip of bodies in the 2D model of TEM data, which is connected to the pediment surface on the eastern margin of the Jingsutu Structure (s. Fig. 4-22, p. 104), suggests that some rotation of the eastern block occurred, which post-dates a first phase of sedimentation into the structure. With respect to the AMT section (s. Fig. 4-23, p. 107) it is clear that the depicted model is rather crude.
4. Subsequent to the deposition of Late Jurassic sediments in the structure, an extensional phase caused the rhyolitic extrusion along the western margin of the Jingsutu Structure. This extensional event post-dates the Jurassic sedimentation, because in the 2D model (s. Fig. 4-22, p. 104) the highly conductive units, which likely represent the Jurassic sediments, clearly continue below the rhyolite. According to the geological map (s. Fig. 4-6, p. 81) the rhyolite could relate to a "Late Variscan" phase, which would probably mean a Latest Jurassic-Early Cretaceous age. Since the original formation of the Jingsutu Structure was related to a regional stressfield due to compressional forces from the SW (s.a.), it seems plausible that a similar regional tectonical setting with stress from the SW could also explain a reactivation of the structure. Therefore, the extension along the western margin of the Jingsutu Structure might alternatively also be explained in terms of an Early Mesozoic reactivation driven by the commencing Himalayan orogeny. Ultimately, direct

age determinations of rock samples would be needed to distinguish between the two possibilities.

A relative subsidence of the eastern shoulder with respect to the western shoulder of the Jingsutu Structure is likely according to the encountered geochemical, structural, and geophysical differences, but cannot be constrained to a certain time period. Long lasting phases of deflation, e.g. the Triassic period, obviously contributed to the current state of the structure, but have not been included in the schematic sketch (Fig. 4-24).

The results of the geophysical and geoscientific investigations in the Jingsutu Structure are further interpreted together with the results in the other working areas (s. following sections) in the discussion (p. 113ff)

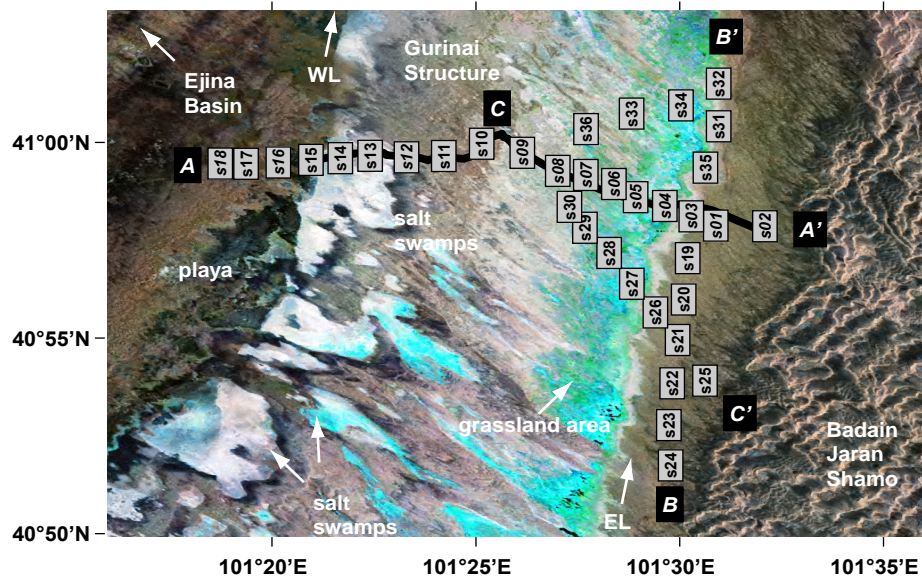


Fig. 4-25: Landsat TM image showing two lineaments (WL & EL, resp.) and the locations of geophysical profiles in the area of the Gurinai Structure. On the main profile (ACA'), TEM-, MT-, and DC-measurements were carried out (s1-s36: MT; black line: TEM). Results for the other profile lines can be found in BECKEN, 2005 (from HÖLZ ET AL., 2007, modified).

### 4.3 Gurinai Structure

In this chapter, the TEM investigations from the Gurinai Structure are presented in combination with MT- and DC-data as a brief summary from HÖLZ ET AL. (2007). An elaborate interpretation of MT-data can be found in BECKEN (2005).

The Gurinai Structure (working title) is named after a small village at the SE edge of the Ejina Basin. The structure, which is part of the postulated N-S striking tectonical axis (s. Fig. 4-1, p. 73), is defined by two almost 100km long, subparallel lineaments, which are separated by a distance of 12km. The geophysical work area was located on the southern termination of this axis.

In the location map of geophysical profiles (Fig. 4-25) the western and eastern lineament (WL, EL), which delineate the Gurinai Structure from the dune field of the Badain Jaran Shamo desert to the W and from the Ejina Basin to the E, are well defined. In contrast to the Jingsutu Structure, no outcropping basement units can be found in this part of the Ejina Basin and the sedimentary deposits within the structure are of late Quaternary respectively Holocene age (ZHANG, 1990).

In the eastern part of the structure, a flat grassland area with a number of small water holes, some containing fresh water, can be found. Water samples taken from wells in this grassland area indicate a general increase of water salinity towards the west, which coincides with a diminishing grass covering.

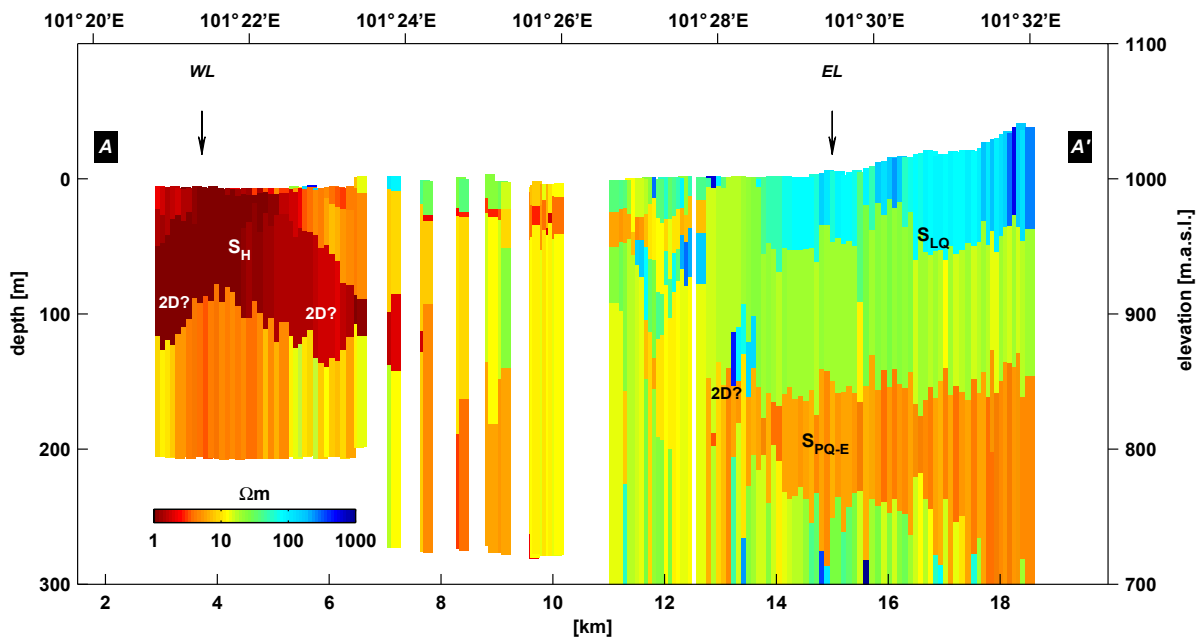


Fig. 4-26: Depth section composed of 1D models from the inversion of TEM data.

Salt swamps with stratifications of salt, silt and clay under a salterust are located to the W of the grassland. The salt swamps form the deepest depressions within the Gurinai Structure. They are usually 1-10 m deeper than the surrounding units.

Further to the W, playa units are clearly delineated from the salt swamps at the western lineament on the satellite image (WL in Fig. 4-25), but only showed a diffuse boundary with a small uplift (<1m) in the field investigations. The playa-like sediments are distinguishable from the salt swamps only by a seemingly smaller concentration of salts and an enrichment of silts and clays in the top soil.

Considering the results from geophysical measurements in the Jingsutu Wadi north of the Gurinai Structure as well as satellite image interpretation (s. a. HARTMANN, 2003; WANG ET AL., 2004), it was concluded that the lineaments in the Gurinai Structure might be a manifestation of neotectonic deformation processes affecting late Pleistocene and Holocene sediments.

### 4.3.1 Geophysics

#### 1D Inversion of TEM Data

The resistivity section based on the inversion of TEM data (Fig. 4-26) can be divided into two sections: In the eastern section of the main profile of geophysical investigations (AA' in Fig. 4-25), resistivities generally show values of 30  $\Omega\text{m}$  or higher, whereas towards the western section resistivities below 10  $\Omega\text{m}$  prevail.

In the eastern section of the profile (11-16 km in Fig. 4-26) the distribution of resistivities depicts a stable layering and 1D inversion is feasible. A shallow layer ( $S_{LQ}$ ) with an average thickness of 50 m can be traced from the first dunes of the Badain Jaran Shamo into the central portions of the grasslands. Resistivities within this layer decrease from 100  $\Omega m$  in the east to 50  $\Omega m$  in the west. The western boundary of the layer is linked to a distinct color change on the satellite image (turquoise to light gray Fig. 4-25), and its lateral extent correlates with the existence of fresh water in shallow wells and small water holes.

A second distinct feature in the eastern section of the main profile AA' can be found below the shallow resistive layer  $S_{LQ}$ . The wedge-shaped layer  $S_{PQ-E}$  with resistivities of about 5  $\Omega m$  is located below 150 m depth. While its top is subhorizontal, the lower boundary is gently declining towards the east. Below the wedge-shaped layer  $S_{PQ-E}$  resistivities increase ( $> 20 \Omega m$ ) but are not well resolved in the inversion of TEM data. Around the western margin of unit  $S_{PQ-E}$  (13-14 km) models of 1D inversions show a considerable lateral variation below 100 m depth, probably indicating artifacts caused by the 1D inversion of 2D/3D data. Unpublished internal reports of the local government based on ground water drillings depict Neogene (i.e. young Tertiary) sediments within the Gurinai Structure in the according depth range, without giving any further specifications. No significant vertical displacements are indicated at the eastern lineament in the resistivity section. Instead, lateral variations in the depth section of resistivities are indicated 2-3 km further west, where units  $S_{LQ}$  and  $S_{PQ-E}$  are discontinuous.

According to  $^{14}C$ -datings (MISCHKE, 1996; ZHANG ET AL., 2005), the resistive top layer is interpreted as a series of partially consolidated, Late Quaternary sandstones carrying a fresh water aquifer. The general elevation profile as well as the seemingly westward increasing salinity imply a westward direction of the assumed groundwater flow from the dunes into the grassland. Therefore, the dunes are considered to be an important source region for the groundwater refill in the Gurinai Structure. Below the presumed aquifer at depths between 50-150 m, resistivities around 30  $\Omega m$  still support the assumption of the existence of fresh groundwater. The decrease of resistivities with depth can be attributed to increased salinization or higher concentrations of clay. The existence of shallow groundwater and its connection to the dunes in the Badain Jaran Shamo, a desert environment with a mean precipitation of 50 mm/a (GEYH ET AL., 1996), is surprising but also supported by findings of JÄKEL (2002), who describes dunes in the Badain Jaran Shamo containing substantial amounts of groundwater. His findings coincide with observations of our workgroup at the foot of the westernmost dunes, where a considerable moisture penetration of dune sands was found at only a few decimeters depth.

In the central section of the profile (11-13 km) the distribution of resistivities generally shows a greater variability. Shallow variations of resistivities in the upper 70 m are linked to small geomorphological units of minor importance. Further to the west (7-11 km), the profile

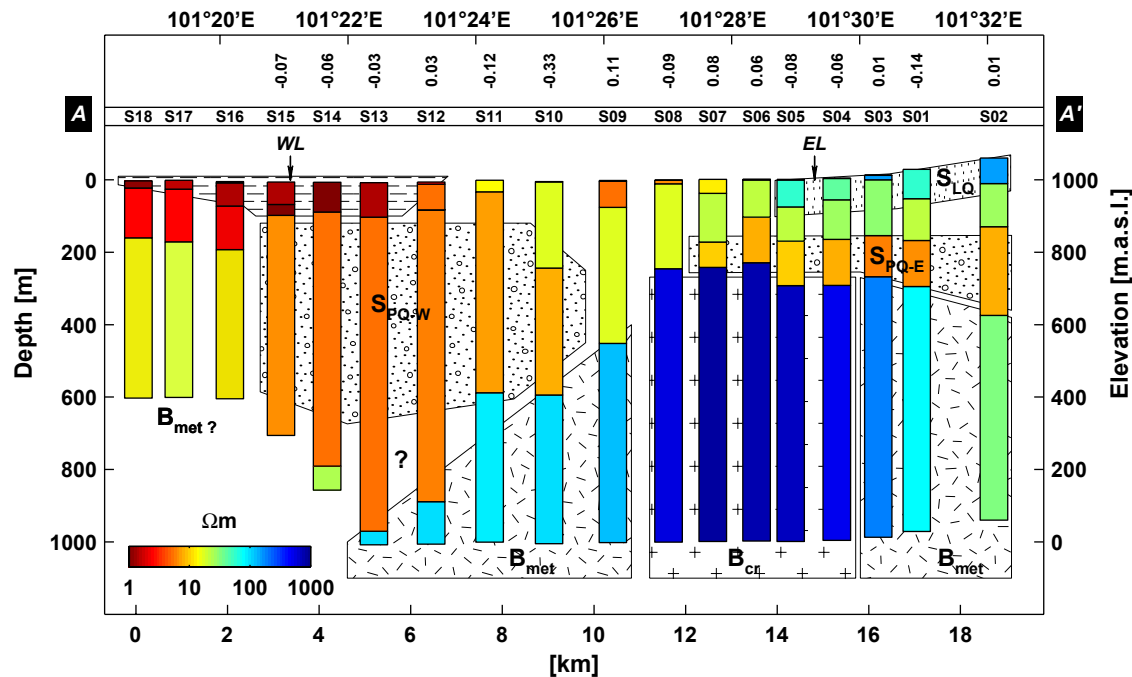


Fig. 4-27: Depth section of 1D joint inversion block models (locations in Fig. 4-25). Numbers above the station names (s1-s18) refer to the amount of static shift in decades between TEM- and MT-data. At all but one station static shift is smaller than 0.14 decades, equaling a maximum shift factor of  $10^{0.14} = 1.38$ . Units described in the text are identified by labels and signatures (from HÖLZ ET AL., 2007, modified)

line was not accessible at all locations due to sand dunes and vegetation. Resistivities show a general decrease but may not, due to the loose site spacing, be interpreted in terms of a consistent layering.

In the westernmost section of the TEM-profile (3-7 km) very low resistivities prevail, causing a decreased penetration depth. At shallow depths a highly conductive structure  $S_H$  with minimum resistivities well below 1  $\Omega\text{m}$  and a thickness of about 100 m is detected. They have to be interpreted as sediment packages containing substantial amounts of saline fluids as indicated at the surface by the existence of salt swamps (Fig. 4-26). Across the WL resistivities are discontinuous in the uppermost 40 m and show an increase from below 0.5  $\Omega\text{m}$  to 2.5  $\Omega\text{m}$ . Increasing resistivities below the good conductor  $S_H$  are evident from the TEM-measurements and will be interpreted in the following section.

### 1D Joint Inversion of MT, DC and TEM Data

BECKEN (2005) shows that 1D characteristics of MT data can be assumed in the shortest period range, typically for periods smaller than  $10^{-1}$  s. At stations along the main profile AA' (Fig. 4-25) a 1D joint inversion for these periods together with TEM- and DC-data is thus appropriate to construct sets of resistivity models, which cover the depth range down to about 1 km. A joint inversion can, due to the different sensitivities of methods to model parameters,



partially remove model equivalences and serves as additional cross-check for the validity and quality of measured data. Apart from the resistivity models, a joint inversion is used to estimate the magnitude of static shift in MT data. Static shift, caused by near surface inhomogeneities of the conductivity distribution, can lead to a frequency independent distortion of electric fields, consequently shifting the apparent resistivities of MT data by a constant factor. Since the TEM method measures the time derivative of magnetic fields and is therefore only inductively coupled to the ground, it is inherently unaffected by static shift and can be used for its correction (MEJU, 2005). For practical reasons, the MT determinant data is used in the joint inversion, which is, however, virtually equal to the off-diagonal elements. Following the suggestions of STERNBERG ET AL. (1988), TEM data is only used at times later than  $200\mu\text{s}$ . The resulting data fits of the 1D joint inversion are summarized in Appendix C.2 (p. 166ff). At all but one station the static shift for the MT apparent resistivity (Fig. 4-27, top) is smaller than 0.14 decades, which equals a maximum shift factor of  $10^{0.14} = 1.38$ . Assuming this result to be representative for the entire measurement area, it can be concluded that static shift is not causing any serious problems in the interpretation of MT data (compare distribution of static shifts in STERNBERG ET AL., 1988).

In the resistivity section derived from the joint inversion (Fig. 4-27), the shallow sedimentary units in the uppermost 200 m conform with the 1D inversion results of TEM data in the previous section. At greater depth, below the sedimentary strata  $S_{PQ-E}$ , a presumably crystalline basement block  $B_{cr}$  with high resistivities above  $500\ \Omega\text{m}$  between stations s04-s08, is laterally bounded by units  $B_{met}$  with moderate resistivities between  $30\text{-}100\ \Omega\text{m}$ . An interpretation of the units  $B_{met}$  as sediment packages, as suggested by the relatively low resistivities, poses a problem, because enormous vertical displacements along the eastern and western boundary of the crystalline block would have to be assumed. Similar to the results obtained from the results from the Jingsutu Structure (chap. 4.2.3), these units are therefore interpreted in terms of metamorphic basement. Like in the interpretation of TEM data in the previous section, no significant lateral variations of resistivities at greater depth can be observed at the EL. Instead, a lateral discontinuity in the basement is indicated 4 km further west at the western boundary of unit  $B_{cr}$ . A hypothetical connection between the discontinuities of the units  $B_{cr}$ ,  $S_{PQ-E}$  and  $S_{LQ}$  west of the EL can be proposed.

The top of the westerly unit  $B_{met}$  is declining towards the west and the overlying unit  $S_{PQ-W}$  with resistivities around  $5\ \Omega\text{m}$ , reaches a considerable thickness of at least 500 m below stations s12-s14. With the same reasoning applied to the easterly unit  $S_{PQ-E}$ , the westerly unit  $S_{PQ-W}$  is interpreted to consist of Prequaternary strata, which is mainly based on the conforming resistivities and the location of its top edge at a depth of about 100 m below stations s13-s15. At stations s12-s14, increasing resistivities with greater depth are indicated by MT data (apparent resistivity and phase), but the maximum thickness of  $S_{PQ-W}$  as well as the resistivity of the presumed metamorphic basement are not well resolved in the joint inversion. Note that

the resistivity of the basement in the joint inversion is largely determined by the MT responses, as the TEM- and DC-data will generally not penetrate as deep. If MT data starts to exhibit 2D effects at the periods under consideration, it is generally difficult to resolve basement resistivities within the joint inversion. The presumably Prequaternary strata  $S_{PQ-W}$  are discontinuous across the WL. At the westernmost stations s16-s18, 1D models show a consistent layering with increased resistivities ( $15 \Omega m$ ) below a depth of 200 m, probably indicating the presence of metamorphic basement.

### 4.3.2 Interpretation

In terms of the results obtained from the interpretation of TEM data in the Jingsutu Structure (chap. 4.2.4), the most important feature of the 1D joint inversion in the Gurinai Structure can be seen in the strong increase in the thickness of Prequaternary and Holocene sediments ( $S_{PQ-W}$  in Fig. 4-27) towards the western lineament. Even though the exact depth of this unit is not resolved in the vicinity of the westerly lineament, it seems to resemble a trough-shaped structure. The strike analysis of MT data (BECKEN, 2005) indicates a predominant geoelectric strike in the N-S direction ( $0^\circ$ ) in this part of the profile line, which is connected to the trough-shaped unit  $S_{PQ-W}$ . Thus, the geoelectric strike of the structure is consistent with the N-S strike of the western lineament as indicated by satellite images (Fig. 4-25).

Additionally local depressions like the salt swamps can be traced on elevation data along the western lineament of the Gurinai Structure for almost 100 km (Fig. 4-28).

In a hydrological study, GEYH ET AL. (1996) show that the isotope composition of shallow groundwater in the Gurinai Structure and the adjacent Badain Jaran Shamo is different from that of groundwater analyzed in the vicinity of the Ruoshui river, west of the geophysical array. They propose the existence of a groundwater divide between the Gurinai Structure and the Ruoshui basin (s.a. GEYH & GU, 1999). BOYADGIEV & VERHEYE (1996) state that the occurrence of gypsum is often connected to geological situations "... where faults and / or underground anticlinal folding structures are oriented perpendicularly to the natural flow of groundwater". In the introduction to this work area it was stated that the geomorphological change between the salt swamps and the

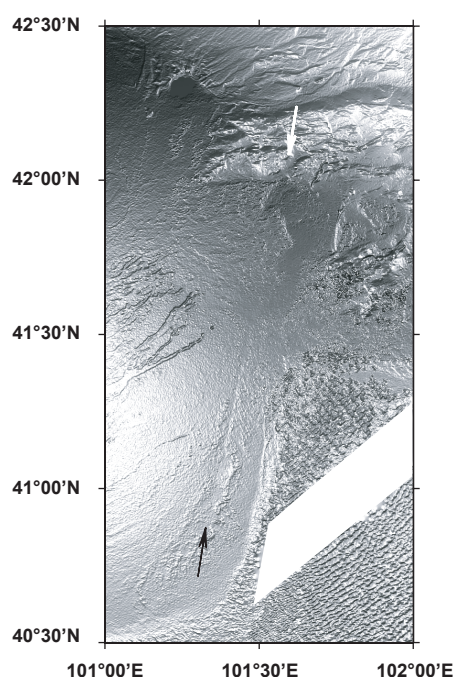


Fig. 4-28: Shaded relief image of SRTM Jingsutu Structuredata showing the connection between the western margin of the Jingsutu Structure (white arrow) and the western lineament of the Gurinai Structure (black arrow).

westerly adjacent playa (s. Fig. 4-25) is mainly indicated by the enrichment of silts and clays in the top soil. It is assumed that the westerly lineament coincides with the groundwater divide as proposed by GEYH & GU (1999), which would give further evidence to the interpretations of faulting.

According to the presented results from geophysical and geoscientific investigations it is concluded that extensional faulting is evident along the western lineament. Its connection to the westerly margin of the Jingsutu Structure is strongly suggested by satellite images (Fig. 4-28).

## 4.4 Conclusion

In the combined interpretation of geophysical data in the Jingsutu Structure and in the Gurinai Structure, similar trough-shaped sedimentary structures were identified, which have a depth of at least 500 m. For both structures under consideration, an extensional setting was concluded based upon the local findings of the geophysical and geoscientific interpretations. Remote sensing data gives strong evidence, that both structures are linked and have to be seen as part of a large N-S striking tectonical axis, along which extensional faulting occurred. Based on results from petrological fieldwork the main building phase is interpreted as Jurassic, which is in accordance with the generally assumed widespread occurrence of extensional faulting in NW China during that period. The fact, that the tectonical axis is morphologically (elevation data) and hydrologically (GEYH ET AL., 1996) apparent in the Quaternary sediments of the Gurinai Structure is seen as evidence of a certain amount of neotectonic activity in this area.

On a larger scale, sandbox experiments of FOURNIER ET AL. (2005) have shown that such pull-apart structures naturally arise in a tectonical setting similar to the present one, where tectonical stress is induced into NW China by the collision of India and Asia. However, according to an unpublished lineament analysis of NW China, which was conducted in the scope of the DFG-project, such N-S striking extensional pull-aparts are not evident outside the Ejina Basin (Ott, pers. comm.).

In an extended research of the current literature an important piece of evidence for a speculative tectonical interpretation was found in VINCENT & ALLEN (1999). They show SSW-NNE striking faults in the Chaoshui Basin, which is located to the SE of the Ejina Basin. In seismic sections, they identify normal faulting, which they interpret to be due to the accretion of the Lhasa Block to the southern margin of Laurasia during the Late Jurassic-Early Cretaceous. Fig. 4-29 depicts their seismic sections, which reveal extensional pull-apart basins concealed below Quaternary and Neogene sediments. According to their interpretation a NNE-SSW strike direction is indicated for these pull-aparts, which concurs with the orientation of the tectonical axis in the Ejina Basin. Furthermore, the lateral extent of one of the pull-aparts seems to coincide nicely with the extent of the Gurinai Structure. In the description of the work

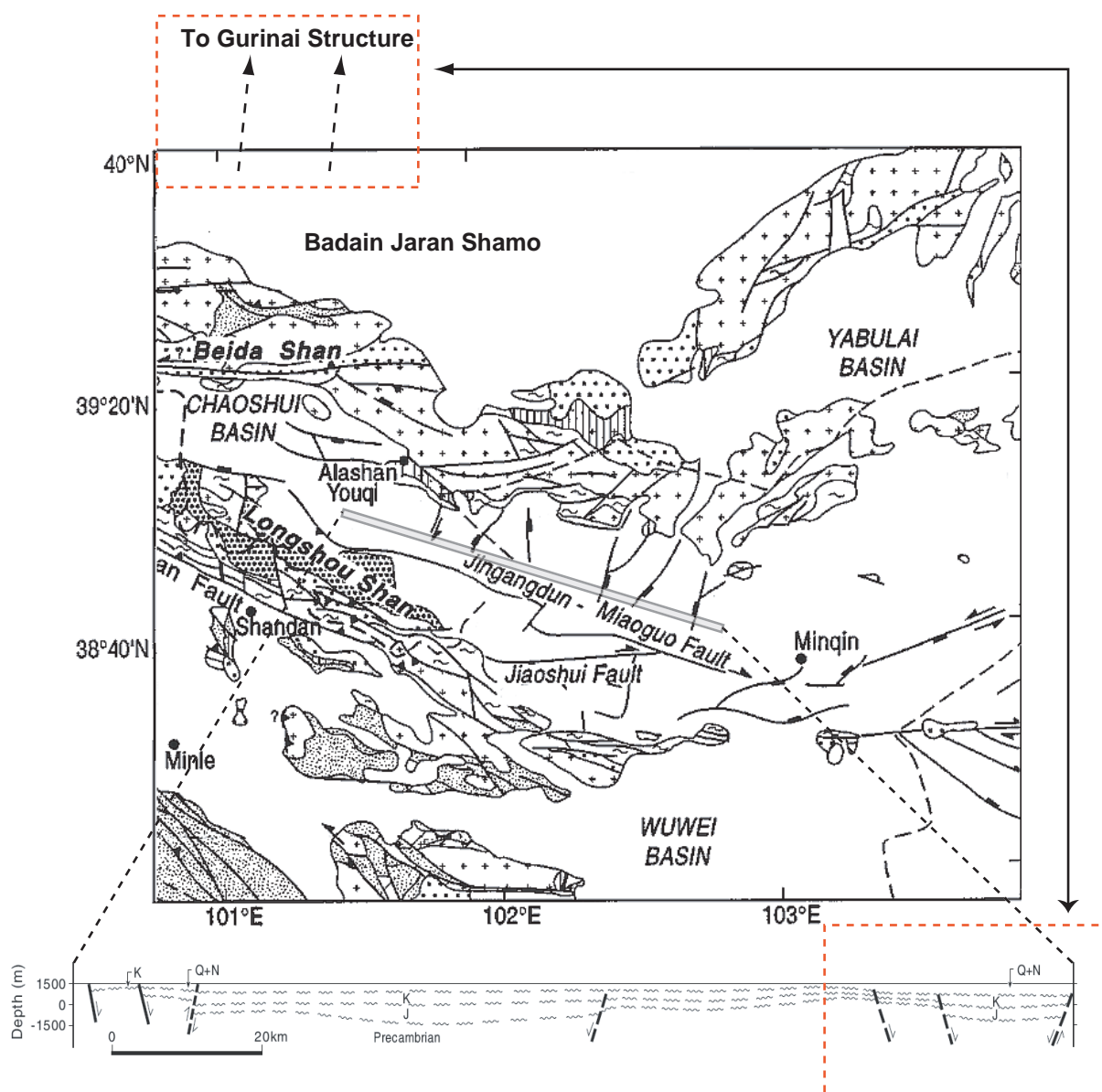


Fig. 4-29: Occurrence of NNE-striking normal faults in the Chaoshui Basin according to seismic sections (modified from VINCENT & ALLEN, 1999) and their hypothetical connection to the tectonical axis in the Ejina Basin.

area it was pointed out, that "several authors propose an interconnection between the East Gobi Fault System and the Altyn Tagh Fault (e.g. WEBB & JOHNSON, 2006; YUE & LIOU, 1999), which probably runs along the southern margin of the Ejina Basin." The hypothetical left lateral offset of about 80km between the two structures is therefore in accordance with the discussions in the current literature, and could, upon further substantiation, possibly add to the better understanding of the tectonical evolution in NW China.

## Acknowledgement

Many people, directly or indirectly, were involved in my work over the course of the past years and without their inspiration, contribution and help, I would not be able to write these final pages of my thesis at this moment.

Thanks to Prof. Burkhardt, who co-initiated the China-project, I received the opportunity to participate in an exciting project in one of the exceptional regions on this planet. Prof. Burkhardt patiently supervised my work in the past years and gave me the room to work on a broad range of topics and to develop my own ideas. I'm grateful for the given chance and I very much hope that this thesis is a good closure of his professional career as active professor at the TU Berlin.

I'm especially grateful to Prof. Weidelt, who - sacrificing his well deserved free time - agreed to be the external reviewer for this thesis. His articles, computer programs and numerous personal discussions during congresses and workshops, helped me to gain a deeper insight into the TEM method.

The funding of the project by the German Science Foundation (DFG) under the grant BU 298/15 is gratefully acknowledged.

Over the years the project-members of the TU Berlin were my main partners. They were involved in the preparation and realization of three field-campaigns in China and in the follow-up work in Berlin. Their contributions are too manifold to be enumerated in full and can only be acknowledged exemplarily: Dr. Fiedler-Volmer (aka FiVo) for discussions on the geological implications of geophysical results, Michael Becken for his friendly cooperation and organization in China and discussions about electromagnetics in Berlin, Daniela Polag for her endurance in finishing the article about the Gurinai Structure, Thomas Hiller for his hard work at about 200 TEM stations and the cooperation in exploring TEMDDD, Andreas Schenk for giving an introduction into the wavelet-method and Marcus Kroupa and Andreas Pfaffhuber for being patient.

The members of the TU Berlin would have been lost in China without the help of our partners from the geographical work group at the FU Berlin. Especially Kai Hartmann and Bernd Wünnemann gave valuable support during the first two field-campaigns and also participated in following discussions and interpretations.

## Acknowledgement

Obviously, successful work in China would also not have been possible without the help of our Chinese colleagues, most of them from the University in Lanzhou. They gave priceless help in organizing logistic matters (e.g. transport, permits, cars, trucks, food, customs) and participated in geophysical measurements. Just naming a few, a special thank goes to Prof. Zhang Hucai, Prof. Gu WeiZu, FanHong Fang, Ding Hu, and Dr. Ma.

The petrological field and laboratory work, which are part of this thesis, were carried out by colleagues from the TU Berlin, namely Dr. Fiedler-Volmer, Thomas Hiller, Prof. Franz and Dr. Matheis. They are thanked for letting me incorporate their data into this thesis. In the course of my literature research and the following interpretations, Dr. Matheis was an especially helpful and patient contact for all my questions.

Many people from the geophysical department of the TU Berlin and the MT working group were available for discussions and gave technical assistance. Special thanks go to Uwe Diefenbach-Moschick, who cooperated in the repair and improvement of the LAPTEM device prior to the field campaign 2004, and Xiaoming Chen, who was more than helpful in deciphering numerous Chinese maps and articles. Sincere thanks go to Knutur Árnason for making his 3D modeling code TEMDDD available for research purposes.

No acknowledgment would be complete without saying thank you to friends and family:

My friends Max, David, Clemens, and Ben gave useful comments, which helped me to improve this thesis, but are especially valuable to me, because they are there for me in good times - and in bad.

Anna entered my life in China and has been there for me ever since. Isn't it strange, how we travelled around the whole globe to meet at the other end of the world, while almost living next door in Berlin? I thank you for your love, enthusiasm, joy, patience and tolerance. I'm looking forward to our new family!

I hope that with our new family and this thesis I can hand something back to my dad and mom, who passed away too soon, for all the support I have received from them throughout the years.

## References

All references referring to internet resources reflect the status quo as of March 2007, but may change in the future. Dates of these internet resources refer to the date of creation or last update, if stated on the webpage. If not specified, they are dated as 2007.

### **ADHIDJAJA & HOHMANN, 1989**

Jl Adhidjaja & GW Hohmann: A finite-difference algorithm for the transient electromagnetic response of a three-dimensional body. *Geophysical Journal International*, 1989, vol. 98, pp. 233-242.

### **ÁRNASON, 1999**

K Árnason: Consistent discretization of electromagnetic fields and transient modeling. In: M Oristaglio, B Spies & MR Cooper (eds.): *Three-Dimensional Electromagnetics*, SEG, 1999, pp. 103-118.

### **ÁRNASON, 2000**

K Árnason: *A Short Manual For The Program TEMDDD*. 2000.

### **ASTEN, 1987**

MW Asten: Full transmitter waveform transient electromagnetic modeling and inversion for soundings over coal measures, *Geophysica*, 1987, vol. 52(3), pp. 279-288.

### **AUKEN ET AL., 2000**

E Auken, K Sørensen, P Thomsen & F Effersø: Optimized model resolution using low pass filters in TDEM soundings, *SAGEEP Proceedings*, 2000, pp. 477-484.

### **BADARCH ET AL., 2002**

G Badarch, W Cunningham & B Windley: A new subdivision for Mongolia: implications for Phanerozoic crustal growth in Central Asia. *Journal of Asian Earth Sciences*, 2002, vol. 21, pp. 87-110.

### **BARRETTA ET AL., 2005**

B Barretta, G Heinsona, M Hatchb & A Telferc: River sediment salt-load detection using a water-borne transient electromagnetic system. *Journal of Applied Geophysics*, 2005, vol. 58 (1), pp. 29-44.

### **BAYASGALAN ET AL., 1999**

A Bayasgalan, J Jackson, JF Ritz & S Carretier: 'Forebergs', flower structures, and the development of large intracontinental strike-slip faults: the Gurvan Bogd fault system in Mongolia. *JoSG*, 1999, vol. 21, pp. 1285-1302.

### **BECKEN & BURKHARDT, 2004**

M Becken & H Burkhardt: An ellipticity criterion in magnetotelluric tensor analysis. *GJI*, 2004, vol. 159, pp. 69-82.

### **BECKEN ET AL., 2007**

M Becken, S Hölz, R Fiedler-Volmer, K Hartmann, B Wünnemann & H Burkhardt: The electrical resistivity image of the Jingsutu Graben at the NE margin of the Ejina basin (NW China) and imp. for the basin development. *GJI*, 2007 (acc.).

### **BECKEN, 2005**

M Becken: Properties of magnetotelluric transfer functions - with a case study from the Gaxun-Nur basin, NW-China. Dissertation, TU Berlin, 2005.

### **BLAKEY, 2007**

R Blakey: *Sedimentation, Tectonics, and Paleogeography of Asia*. 2007.

[http://jan.ucc.nau.edu/~rcb7/paleogeographic\\_asia.html](http://jan.ucc.nau.edu/~rcb7/paleogeographic_asia.html)

### **BOYADGIEV & VERHEYE (1996)**

TG Boyadgiev & WH Verhey: Contribution to a utilitarian classification of gypsiferous soil. *Geoderma*, 1996, vol. 74, pp. 321-338.

**BUSELLI & CAMERON, 1996**

G Buselli & M Cameron: Robust statistical methods for reducing sferics noise contaminating transient electromagnetic measurements. *Geophysics*, 1996, vol. 61 (6), pp. 1633-1646.

**BUTLER & RUSSELL, 2003**

KE Butler & RD Russell: Cancellation of multiple harmonic noise series in geophysical records. *Geophysics*, 2003, vol. 68 (3), pp. 1083-1090.

**BUTTKUS, 1991**

B Buttkus: *Spektralanalyse und Filtertheorie*, Springer-Verlag, 1991.

**CHAPPELL & WHITE, 1974**

BW Chappell & AJR White: Two contrasting granite types. *Pacific Geology*, 1974, vol. 8, pp. 173-174.

**CHEN & JAHN, 2004**

B Chen & B Jahn: Genesis of post-collisional granitoids and basement nature of the Junggar Terrane, NW China: Nd-Sr isotope and trace element evidence. *Journal of Asian Earth Sciences*, 2004, vol. 23, pp. 691-703.

**CHEN ET AL., 2000**

B Chen, BM Jahn, S Wilde & B Xu: Two contrasting paleozoic magmatic belts in northern Inner Mongolia, China: Petrogenesis and tectonic implications. *Tectonophysics*, 2000, vol. 328, pp. 157-182.

**CHIARADIA ET AL., 2006**

M Chiaradia, D Konopelko, R Seltmann & RA Cliff: Lead isotope variations across terrane boundaries of the Tien Shan and Chinese Altay. *Mineralium Deposita*, 2006, vol. 41, pp. 411-428.

**CHRISTENSEN, 1990**

NB Christensen: Optimized Fast Hankel Transform Filters, *Geophysical Prospecting*, 1990, vol. 38, pp. 545-568.

**CHRISTIANSEN & AUKEN, 2004**

AV Christiansen & E Aukien: Optimizing a layered and laterally constrained 2D inversion of resistivity data using Broyden's update and 2D derivatives. *Journal of Applied Geophysics*, 2004, vol. 56, pp. 247-261.

**COMMER & NEWMAN, 2004**

M Commer & G Newman: A parallel finite-difference approach for 3D transient electromagnetic modeling with galvanic sources. *Geophysics*, 2004, vol. 69 (5), pp. 1192-1202.

**COMMER ET AL., 2006**

M Commer, SL Helwig, A Hördt, C Scholl & B Tezkan: New results on the resistivity structure of Merapi Volcano (Indonesia), derived from 3D restricted inversion of LOTEM data. *GJI*, 2006, vol. 167 (3), pp. 1172-1187.

**COMMER, 2003**

M Commer: Three-dimensional inversion of transient electromagnetic data - A comparative study. Doctoral Thesis, Universität Köln, 2003.

**CONSTABLE ET AL., 1987**

SC Constable, RL Parker & CG Constable: Occam's inversion - a practical algorithm for generating smooth models from electromagnetic sounding data. *Geophysics*, 1987, vol. 52, pp. 289-300.

**COPE ET AL., 2005**

T Cope, BD Ritts, BJ Darby, A Fildani & SA Graham: Late Paleozoic Sedimentation on the Northern Margin of the North China Block: Implications for Regional Tectonics and Climate Change. *Int. Geology Review*, 2005, vol. 47, pp. 270-296.

**CUNNINGHAM ET AL., 1996**

WD Cunningham, BF Windley, D Dorjnamjaa, J Badamgarav & M Saandar: Late Cenozoic transpression in southwestern Mongolia and the Gobi Altai-Tien Shan connection. *Earth and Planetary Science Letters*, 1996, vol. 140, pp. 67-81.



**CUNNINGHAM ET AL., 1997**

WD Cunningham, Windley, Owen, Barry, Dorjnamjaa & Badamgarav: Geometry and style of partitioned deformation within a late Cenezoic transpressional zone in the E Gobi Altai Mountains. *Tectonophysics*, 1997, vol. 277, pp. 285-306.

**DANIELSEN ET AL., 2003**

JE Danielsen, E Auken, F Jørgensen, V Sondergaard & KI Sørensen: The application of the transient electromagnetic method in hydrogeophysical surveys. *Journal of Applied Geophysics*, 2003, vol. 53, pp. 181-198.

**DARBY ET AL., 2005**

BJ Darby, BD Ritts, Y Yue & Q Meng: Did the Altyn Tagh fault extend beyond the Tibetan Plateau? *EPSL*, 2005, vol. 240, pp. 425-435.

**DAUBECHIES, 1994**

I Daubechies: Ten lectures on wavelets. SIAM, 1994.

**DING ET AL., 2004**

G Ding, J Chen, Q Tian, X Shen, C Xing & K Wei: Active faults and magnitudes of left-lateral displacement along the northern margin of the Tibetan Plateau. *Tectonophysics*, 2004, vol. 380, pp. 243-260.

**DRUSKIN & KNIZHNERMAN, 1994**

VL Druskin & LA Knizhnerman: Spectral Approach to solving three-dimensional Maxwell's equations in the time and frequency domain. *Radio Science*, 1994, vol. 29, pp. 937-953.

**EBY, 1992**

GN Eby: Chemical subdivision of the A-type granitoids: Petrogenetic and tectonic implications. *Geology*, 1992, vol. 20, pp. 641-644.

**EFFERSØ ET AL., 1999**

F Effersø, E Auken & KI Sørensen: Inversion of band-limited TEM responses. *Geophysical Prospecting*, 1999, vol. 47, pp. 551-564.

**ESC, 2002**

GeoCover Product Description Sheet - Orthorectified Landsat Thematic Mapper Mosaics. Earth Satellite Corporation, 2002.

[https://zulu.ssc.nasa.gov/mrsid/docs/GeoCover\\_circa\\_1990\\_Product\\_Description.pdf](https://zulu.ssc.nasa.gov/mrsid/docs/GeoCover_circa_1990_Product_Description.pdf)

**ESC, 2004**

GeoCover Product Description Sheet - Orthorectified Landsat Enhanced Thematic Mapper (ETM+) Compressed Mosaics. Earth Satellite Corporation, 2004.

[https://zulu.ssc.nasa.gov/mrsid/docs/GeoCover\\_circa\\_2000\\_Product\\_Description.pdf](https://zulu.ssc.nasa.gov/mrsid/docs/GeoCover_circa_2000_Product_Description.pdf)

**FENG ET AL., 2001**

Q Feng, G Cheng & KN Endo: Towards sustainable development of the environmentally degraded River Heihe basin, China. *Hydrological Sciences*, 2001, vol. 46 (5), pp. 647-658.

**FITTERMAN, 1988**

DV Fitterman: Equivalence Behaviour of three Electrical Sounding Methods as Applied to Hydrogeological Problems. 50th Annual Meeting, EAGS, The Hague, Netherlands, 1988.

**FOURNIER ET AL., 2005**

M Fournier, L Jolivet, P Davy & JC Thomas: Backarc extension and collision: an experimental approach to the tectonics of Asia. *Geophysical Journal International*, 2004, vol. 157, pp. 871-889.

**FRAZIER, 1999**

MW Frazier: An Introduction to Wavelets Through Linear Algebra. Springer, 1999.

**GEOINSTRUMENTS, 1997**

Geoinstruments: LAPTEM - PC Based TEM System - Operator's Manual (V. 2.08), 1997.

**GEYH & GU, 1999**

MA Geyh & W Gu: Isotopically highly enriched shallow groundwater below overlying dry sediments. Proceedings Isotope Techniques in Water Resources Development and Management IAEA, Vienna, 1999.

**GEYH ET AL., 1996**

MA Geyh, W Gu & D Jäkel: Groundwater Recharge Study in the Gobi Desert, China. Geowissenschaften, 1996, vol. 14, pp. 279-280.

**GOLDMAN ET AL., 1994**

M Goldman, L Tabarovsky & M Rabinovich: On the influence of 3-D structures in the interpretation of transient electromagnetic sounding data. Geophysics, 1994, vol. 59, pp. 889-901.

**GPGB, 1981**

The Regional Geological Survey Report (Sogo Nur) - Geological Map (1:200.000, K-47-XVIII). Gansu Provincial Geological Bureau, Chinese Ministry of Geology, 1981.

**GPH, 1990**

Regional Geology of Nei Mongol Autonomous Region - Magmatic Rocks Map (1:2.000.000), 1990, Geological Publishing House, Beijing, China.

**GRAHAM ET AL., 2001**

SA Graham, MS Hendrix, CL Johnson, D Badamgarav, G Badarch, J Amory, M Porter, R Barsbold, LE Webb & BR Hacker: Sedimentary record and tectonic implications of Mesozoic rifting in southeast Mongolia. GSA Bull., 2001, 113, 1560-1579.

**HABER ET AL., 2004**

E Haber, UM Ascher & DW Oldenburg: Inversion of 3D electromagnetic data in frequency and time domain using an inexact all-at-once approach. Geophysics, 2004, vol. 69 (5), pp. 1216-1228.

**HAN ET AL., 1997**

B Han, S Wang, B Jahn, D Hong, H Kagami & Y Sun: Depleted-mantle source for the Ulungur River A-type granites from North Xinjiang, China. Chem. Geol., 1997, vol. 138, pp. 135-159.

**HANSEN, 1994**

PC Hansen: Regularization Tools - A Matlab package for analysis and solution of discrete ill-posed problems. Numerical Algorithms, 1994, vol. 6 (I-II), pp. 1-35.

**HANSTEIN, 1996**

T Hanstein: Digitale Optimalfilter für LOTEM-Daten. In: K Bahr & A Junge (eds.): Elektromagnetische Tiefenforschung - 16. Kolloquium, Burg Ludwigstein, 1996, pp. 320-328.

**HARTMANN, 2003**

K Hartmann: Spätpleistozäne und holozäne Morphodynamik im nördlichen Gaxun Nur Becken, Innere Mongolei, NW China. Dissertation, FU Berlin, 2003.

**HGG, 2007**

HydroGeophysics Group, University of Aarhus, Denmark: EMMA - ElectroMagnetic Model Analysis. <http://www.hgg.au.dk/page198.aspx>.

**HILLER, 2005**

T Hiller: Der Einfluss von geneigten Schichten bei der Interpretation von TEM Daten. Studienarbeit, TU Berlin, 2005.

**HOHMANN, 1988**

GW Hohmann: Numerical Modeling for Electromagnetic Methods of Geophysics. In: MN Nabighian (ed.): Electromagnetic Methods In Applied Geophysics, SEG, 1987, vol. 1.

**HOLT ET AL., 2000**

WE Holt, N Chamot-Rooke, X Le Pichon, AJ Haines, B Shen-Tu & J Ren: Velocity field in Asia inferred from Quaternary fault slip rates and GPS observations. JGR, 2000, vol. 105, pp. 19185-19209.

**HÖLZ ET AL., 2006**

S Hölz, T Hiller & H Burkhardt: Effects of Dipping Layers on TEM 1D-Inversion. Protokoll über das 21. Kolloquium Elektromagnetische Tiefenforschung, 2006, pp. 197-206.

**HÖLZ ET AL., 2007**

S Hölz, D Polag, M Becken, R Fiedler-Volmer, HC Zhang, K Hartmann & H Burkhardt: Electromagnetic and Geoelectric Investigation of the Gurinai Structure, Inner Mongolia, NW China. Tectonophysics, 2007 (accepted).

**HÖLZ, 2007**

S Hölz: Polygon Clipper. Routine on the Matlab File Exchange Server, 2007.

[www.mathworks.com/matlabcentral/fileexchange/loadFile.do?objectId=8818&objectType=FILE](http://www.mathworks.com/matlabcentral/fileexchange/loadFile.do?objectId=8818&objectType=FILE)

**HÖLZ, 2007B**

S Hölz: GetSRTMData. Routine on the Matlab File Exchange Server, 2007.

[www.mathworks.com/matlabcentral/fileexchange/loadFile.do?objectId=5544&objectType=file](http://www.mathworks.com/matlabcentral/fileexchange/loadFile.do?objectId=5544&objectType=file)

**HÖRDT ET AL., 1992**

A Hördt, KM Strack, K Vozoff & PA Wolfgram: Resolving resistive layers using joint inversion of LOTEM and MT data. In: A Vogel, AK Sarwar & R Gorenflo (eds.): Theory and Practice of Geophysical Data Inversion, Vieweg, 1992, 147-158.

**HUANG ET AL., 2001**

B Huang, Y Otofujii, R Zhu, R Shi & Y Wang: Paleomagnetism of Carboniferous sediments in the Hexi corridor: its origin and tectonic implications. EPSL, 2001, vol. 194, pp. 135-149.

**HUANG ET AL., 2002**

B Huang, Y Wang, R Zhu & F Zhang: Paleomagnetism of early Paleozoic volcanic rocks from the Beishan area, Gansu of NW China: Preliminary insight into early Paleozoic kinematics of the Beishan terrane. CSB, 2002, vol. 47, pp. 1561-1567.

**JAHN ET AL., 2000**

BM Jahn, FY Wu & B Chen: Massive granitoid generation in Central Asia: Nd isotope evidence and implication for continental growth in the Phanerozoic. Episodes, 2000, vol. 23 (2), pp. 82-92.

**JÄKEL, 2002**

D Jäkel: The importance of dunes for groundwater recharge and storage in China. Z. Geomorph. N.F., 2002, vol. 126 (Supplement), pp. 131-146.

**JOHANSEN & SØRENSEN, 1979**

HK Johansen & K Sørensen: Fast Hankel transforms, Geophysical Prospecting, 1979, vol. 27, pp. 876-901.

**JOHNSON, 2004**

CL Johnson: Polyphase evolution of the East Gobi basin: sedimentary and structural records of Mesozoic-Cenozoic intraplate deformation in Mongolia. Basin Research, 2004, vol. 16, pp. 79-99.

**KAFRI & GOLDMAN, 2005**

U Kafri & M Goldman: The use of the time domain electromagnetic method to delineate saline groundwater in granular and carbonate aquifers and to evaluate their porosity. Journal of Applied Geophysics, 2005, vol. 57(3), pp. 167-178.

**KAMENETSKY & OELSNER, 2000**

F Kamenetsky & C Oelsner: Distortions of EM transients in coincident loops at short time-delays Geophysical Prospecting, 2000, Vol. 48 (6), pp. 983-994.

**KAPP ET AL., 2003**

P Kapp, A Yin, CE Manning, TM Harrison & MH Taylor: Tectonic evolution of the early Mesozoic blueschist-bearing Qiangtang metamorphic belt, central Tibet. Tectonics, 2003, vol. 22 (4), pp. 17/1-17/11.

**KIRSCH, 2006**

R Kirsch: Groundwater quality - saltwater intrusions In: R Kirsch (ed.): Groundwater Geophysics. Springer-Verlag, 2006, pp. 423-438.

**KIRSCH, 2006B**

R Kirsch: Petrophysical properties of permeable and low-permeable rocks In: Groundwater Geophysics. R Kirsch (ed.): Springer-Verlag, 2006, pp. 1-22.

**KLAASSEN, 2005**

M Klaassen: Gesteine - Entstehung und Eigenschaften. Materialwissenschaften und Werkzeugtechnik, 2005, vol. 36 (8), pp. 344-352.

**KOZLOVSKY ET AL., 2005**

AM Kozlovsky, VV Yarmolyuk, EB Sal'nikova, VM Savatenkov & VI.Kovalenko: Age of bimodal and alkali granite magmatism of the Gobi-Tien Shan rift zone, Tost Range, southern Mongolia. Petrology, 2005, vol. 13 (2), pp. 197-203.

**KRAUSE ET AL., 2005**

HJ Krause, GI Panaitov, Y Zhang & M Bick: Appearance of sign reversal in geophysical transient electromagnetics with a SQUID due to stacking, IEEE Transactions on Applied Superconductivity, 2005, vol. 15 (2), pp. 745-748.

**LAMB ET AL., 1999**

MA Lamb, AD Hanson, SA Graham, G Badarch & LE Webb: Left-lateral sense offset of Upper Proterozoic to Paleozoic features across the Gobi Onon, Tost, and Zuunbayan faults in southern Mongolia. EPSL, 1999, vol. 173, pp. 183-194.

**LAURENT-CHARVET ET AL., 2003**

S Laurent-Charvet, J Charvet, P Monié & L Shu: Late Paleozoic strike-slip shear zones in eastern central Asia (NW China): New structural and geochronological data. Tectonics, 2003, vol. 22 (2), pp. 4/1-4/24.

**LOISELLE & WONES, 1979**

MC Loisel & DR Wones: Characteristics and origin of anorogenic granites. Geological Society of America Abstracts with Programs 11, 1979, p. 468.

**MACNAE ET AL., 1984**

JC Macnae, Y Lamontagne & GF West: Noise processing techniques for time-domain EM systems. Geophysics, 1984, vol. 49 (7), pp. 934-948.

**MAO ET AL., 2005**

J Mao, RJ Goldfarb, Y Wang, CJ Hart, Z Wang & J Yang: Late Paleozoic base and precious metal deposits, East Tianshan, Xinjiang, China: Characteristics and geodynamic setting. Episodes, 2005, vol. 28 (1), pp. 23-36.

**MATHWORKS, 2005**

Wavelet Toolbox - User's Guide. The MathWorks, 2005.

**MATHWORKS, 2006**

Optimization Toolbox - User's Guide. The MathWorks, 2006.

**MCC, 2001**

PC-CARD-DAS 16/16 & PC-CARD-DAS 16/16-AO - User's Manual (Revision 5). Measurement Computing, 2001.

**MCC, 2007**

<http://www.measurementcomputing.com/>

**MEJU, 2005**

MA Meju: Simple relative space-time scaling of electrical and electromagnetic depth sounding arrays: implications for electrical static shift removal and joint DC-TEM data inversion. Geophysical Prospecting, 2005, vol. 53 (4), pp. 463-480.

**MENG ET AL., 2001**

QR Meng, JM Hu & FZ Yang: Timing and magnitude of displacement on the Altyn Tagh fault: constraints from stratigraphic correlation of adjoining Tarim and Qaidam basins, NW China. Terra Nova, 2001, vol. 13, pp. 86-91.

**MENG ET AL., 2003**

QR Meng, JM Hu, JQ Jin, Y Zhang & DF Xu: Tectonics of the late Mesozoic wide extensional basin system in the China-Mongolia border region. *Basin Research*, 2003, vol. 15, pp. 397-415.

**MENG ET AL., 2005**

QR Meng, E Wang & JM Hu: Mesozoic sedimentary evolution of the northwest Sichuan basin: Implication for continued clockwise rotation of the South China block. *GSA Bulletin*, 2005, vol. 117 (3/4), pp. 396-410.

**MEYER ET AL., 1996**

B Meyer, P.Tapponnier, Y Gaudemer, G Peltzer, S Guo & Z Chen: Crustal thickening in Gansu-Qinghai, lithospheric mantle subduction, and oblique, strike-slip controlled growth of the Tibet plateau. *GJI*, 1998, vol. 135, pp. 1-47.

**MISCHKE, 1996**

S Mischke: Sedimentologische Untersuchungen zur Landschaftsgenese der nordwestlichen Badain Jaran Shamo (Innere Mongolei / VR China). Diploma, FU Berlin, 1996.

**MITSUHATA ET AL., 2002**

Y Mitsuhashi, T Uchida & H Amano: 2.5-D inversion of frequency-domain electromagnetic data generated by a grounded-wire source. *Geophysics*, 2002, vol. 67, pp. 1753-1768.

**MOSKOW ET AL. (1999)**

S Moskow, V Druskin, T Habashy, P Lee & S Davdycheva: A Finite Difference Scheme for Elliptic Equations With Rough Coefficients Using a Cartesian Grid Nonconforming to Interfaces. *SIAM JNA*, 1999, vol. 36 (2), pp. 442-464.

**MUNKHOLM & AUKEN, 1996**

MS Munkholm & E Aukien: Electromagnetic Noise Contamination on Transient Electromagnetic Soundings in Culturally Disturbed Environments. *JEEG*, 1996, vol. 1 (2), pp. 119-127.

**MURTA, 2007**

A Murta: GPC - General Polygon Clipper library. 2007.  
<http://www.cs.man.ac.uk/~toby/alan/software>

**NABIGHIAN & MACNAE, 1991**

MN Nabighian & JC Macnae: TEM Prospecting Methods. In: MN Nabighian (ed.): *Electromagnetic Methods in Applied Geophysics - Vol.2*, SEG, 1991.

**NABIGHIAN, 1979**

Nabighian, M.: Quasi-static transient response of a conducting half-space: An approximate representation. *Geophysics*, 1979, vol. 44, pp. 1700-1705.

**NASA, 2006**

<https://zulu.ssc.nasa.gov/mrsid/>

**NELSON, 2005**

TJ Nelson: A remotely-tuned loop receiving antenna for LW and MW. <http://entropy.brneurosci.org/loopantenna.html>.

**NEWMAN & COMMER, 2005**

G Newman & M Commer: New advances in three dimensional transient electromagnetic inversion. *Geophysical Journal International*, 2005, vol. 160, pp. 5-32.

**NOZAKA & LIU, 2002**

T Nozaka & Y Liu: Petrology of the Hegenshan ophiolite and its implication for the tectonic evolution of northern China. *EPSL*, 2002, vol. 202, pp. 89-104.

**OLSEN & HOHMANN, 1992**

K. B. Olsen & G. W. Hohmann: Adaptive noise cancellation for time-domain EM data. *Geophysics*, 1992, vol. 57, pp. 466-469.

**ORISTAGLIO & HOHMANN, 1984**

ML Oristaglio & GW Hohmann: Diffusion of electromagnetic fields into a two-dimensional earth: A finite-difference approach. *Geophysics*, 1984, vol. 49, pp. 870-894.

**PAGANO ET AL., 2003**

G Pagano, A Menghini & S Floris: Electrical tomography and TDEM prospection in the Chianciano thermal basin (Siena, Italy). *Annals of Geophysics*, 2003, vol. 46 (3), pp. 501-512.

**PALACKY, 1987**

GJ Palacky: Resistivity Characteristics of Geologic Targets. In: MN Nabighian (ed.): *Electromagnetic Methods in Applied Geophysics* (Vol. 1), SEG, Tulsa, 1987, pp. 53-129.

**PANAITOV ET AL., 2002**

G Panaitov, M Blick, Y Zhang & HJ Krause: Peculiarities of SQUID magnetometer application in TEM, *Geophysics*, 2002, vol. 67, pp. 739-745.

**PANAITOV ET AL., 2004**

G Panaitov, M Bick, Y Zhang & HJ Krause: Reply by the authors to the discussion by Brian R. Spies (same issue), *Geophysics*, 2004, vol. 69(2), pp. 626-628.

**PEARCE ET AL., 1984**

JA Pearce, NBW Harris & AG Tindle: Trace element discrimination diagrams for the tectonic interpretation of granitic rocks. *Journal of Petrology*, 1984, vol. 25, pp. 956-983.

**PEARCE, 1996**

JA Pearce: Sources and settings of granitic rocks. *Episodes*, 1996, vol. 19, pp. 120-125.

**RABINOVICH, 1995**

M Rabinovich: Errors of 1-D interpretation of 3-D TDEM data in the application of mapping saltwater / freshwater contact. *Journal of Applied Geophysics*, 1995, vol. 34, pp. 23-34.

**RYDESÄTER, 2003**

P Rydesäter: TCP/UDP/IP Toolbox 2.0.5. Routine on the Matlab File Exchange Server, 2003.

[www.mathworks.com/matlabcentral/fileexchange/loadFile.do?objectId=345&objectType=file](http://www.mathworks.com/matlabcentral/fileexchange/loadFile.do?objectId=345&objectType=file)

**SCHAUMANN, 2001**

G Schumann: TEM Messungen auf Mülldeponien - Untersuchung des Einflusses von 3D-Leitfähigkeitsvariationen und 1D-frequenzabhängiger Polarisierbarkeit. Dissertation, Universität Braunschweig, 2001.

**SCHÖN, 1998**

J Schön: Physical Properties of Rocks. In: K Helbig & S Treitel (eds.): *Handbook of Geophysical Exploration, Seismic Exploration*, vol. 18, Pergamon, 1998.

**SHENG, 1996**

Y Sheng: Wavelet Transform In: AD Poularikas (ed.): *The Transforms and Applications Handbook*. CRC Press, 1996, pp. 747-827.

**SMITH & PAINE, 1999**

R Smith & J Paine: Three-Dimensional Transient Electromagnetic Modeling - A User's View. In: M Oristaglio, B Spies & MR Cooper (eds.): *Three-Dimensional Electromagnetics*. SEG, 1999, pp. 103-118.

**SMITH & SANDWELL, 2003**

B Smith & D Sandwell: Accuracy and resolution of shuttle radar topography mission data. *Geophysical Research Letters*, 2003, vol. 30 (9), art.no. 1467.

**SMYTH, 2002**

GK Smyth: Nonlinear Regression. In: AH El-Shaarawi & WW Piegorsch (eds.): *Encyclopedia of Environmetrics*, John Wiley & Sons, 2002, vol. 3, pp. 1405-1411.

**SONG ET AL., 2006**

S Song, L Zhang, Y Niu, L Su, B Song & D Liu: Evolution from Oceanic Subduction to Continental Collision: a Case Study from the N-Tibetan Plateau Based on Geochemical and Geochronological Data. *Jo Petrology*, 2006, vol. 47, pp. 435-455.

**SPIES, 1988**

BR Spies: Local noise prediction filtering for central induction transient electromagnetic sounding. *Geophysics*, 1988, vol. 53 (8), pp. 1068-1079.

**SPIES, 2004**

BR Spies: Discussion on "Peculiarities of SQUID magnetometer application in TEM" by Panaitov et al. (2002), *Geophysics*, 2004, vol. 69 (2), pp. 624-628.

**STEPHAN & STRACK, 1991**

A Stephan & KM Strack: A simple approach to improve the S/N ratio for TEM data using multiple receivers. *Geophysics*, 1991, vol. 56 (6), pp. 863-869.

**STERNBERG ET AL., 1988**

BK Sternberg, JC Washburne & L Pellerin: Correction for the static shift in magnetotellurics using transient electromagnetic soundings. *Geophysics*, 1988, vol. 53 (11), pp. 1459-1468.

**STRACK ET AL., 1989**

KM Strack, TH Hanstein & HN Eilenz: LOTEM data processing for areas with high cultural noise levels. *Physics of the Earth and Planetary Interiors*, 1989, vol. 53, pp. 261-269.

**SUN & McDONOUGH, 1989**

SS Sun & WF McDonough: Chemical and isotopic systematics of oceanic basalts; implications for mantle composition and processes. In AD Saunders & MJ Norry (ed.): *Magmatism in the ocean basins*. *GSL*, 1989, pp. 313-345.

**SUN ET AL., 2003**

G Sun, KJ Ranson, VI Kharuk & K Kovacs: Validation of surface height from SRTM using shuttle laser altimeter. *Remote Sensing of Environment*, 2003, vol. 88, pp. 401-411.

**SYLVESTER, 1996**

D Sylvester: Bearbeitung und Interpretation von Daten transient-elektromagnetischer Tiefensondierungen im Umfeld der KTB unter Berücksichtigung von Anisotropie. Diploma thesis, University of Cologne, 1997.

**TABAROVSKY ET AL., 1995**

LA Tabarovsky, M Goldman, M Rabinovich & K Strack: 2.5D-modeling in electromagnetic methods of geophysics. *Journal of Applied Geophysics*, 1995, vol. 35, pp. 261-284.

**THERN, 1996**

HF Thern: Datenverarbeitung und erste Ergebnisse bei der Auflösung einer ehemaligen Subduktionszone mittels transient elektromagnetischer Tiefensondierung (LOTTEM). Diploma thesis, University of Cologne, 1996.

**TIETZE & SCHENK, 1985**

U Tietze & C Schenk: *Halbleiter-Schaltungstechnik*. Springer Verlag, 1985.

**TOFT, 2001**

MW Toft: Three-dimensional TEM modeling of nearsurface resistivity variations. Thesis, University of Århus, Denmark, 2001.

**TORSVIK & COCKS, 2003**

TH Torsvik & LRM Cocks: Earth geography from 400 to 250 Ma: a palaeomagnetic, faunal and facies review. *Journal of the Geological Society, London*, 2004, vol. 161, pp. 555-572.

**USGS, 2006**

Global GTOPO 30 Data Coverage.

<http://edc.usgs.gov/products/elevation/gtopo30/gtopo30.html>

**USGS, 2007A**

<ftp://e0srp01u.ecs.nasa.gov/srtm/version1/SRTM3>

<ftp://e0srp01u.ecs.nasa.gov/srtm/version2/SRTM3>

**USGS, 2007B**

<ftp://e0srp01u.ecs.nasa.gov/srtm/version2/SRTM30>

**VALENS, 2004**

A Really Friendly Guide to Wavelets. 2004.

[perso.orange.fr/polyvalens/clemens/download/arfgtw\\_26022004.pdf](perso.orange.fr/polyvalens/clemens/download/arfgtw_26022004.pdf)

**VATTI, 1992**

BR Vatti: A Generic Solution to Polygon Clipping. Communications of the ACM, 1992, vol. 35 (7), pp. 56-63.

**VINCENT & ALLEN, 1999**

SJ Vincent & MB Allen: Evolution of the Minle and Chaoshui Basins, China: Implications for Mesozoic strike-slip basin formation in Central Asia. GSA Bulletin, 1999, vol. 111 (5), pp. 725-742.

**VOZOFF & JUPP, 1975**

K Vozoff & DLB Jupp: Joint Inversion of Geophysical Data. Journal of the Royal Astronomical Society, 1975, vol. 42, pp. 977-991.

**WANG & HOHMANN, 1993**

T Wang & GW Hohmann: A finite-difference, time-domain solution for three-dimensional electromagnetic modelling. Geophysics, 1993, vol. 58, pp. 797-809.

**WANG ET AL., 1997**

Z Wang, G Wu & X Xiao: Explanatory Notes for Global Geoscience Transect Golmud - Ejina Transect. China Geological Publishing House, Beijing, 1997.

**WANG ET AL., 2004**

X. Wang, H. Guo, Y. Chang & L. Zha: On paleodrainage evolution in mid-late Eocene based on radar remote sensing in NE Ejina Banner, Inner Mongolia. Journal of Geographical Sciences, 2004, vol. 14 (2), pp. 235-241.

**WARD & HOHMANN, 1987**

SH Ward & DW Hohmann: Electromagnetic theory for geophysical applications. In: MN Nabighian (ed.): EM Methods in Applied Geophysics - Vol. 1. SEG, Tulsa, 1987, pp. 131-311.

**WEBB & JOHNSON, 2006**

LE Webb & CL Johnson: Tertiary strike-slip faulting in southeastern Mongolia and implications for Asian tectonics. EPSL, 2006, vol. 241, pp. 323-335.

**WEBB & ROWSTON, 1995**

M Webb & P Rowston: The geophysics of the Ernest Henry Cu-Au Deposit (N.W.) Qld. Exploration Geophysics, 1995, vol. 26, pp. 51-59.

**WEIDELT, 1984**

P Weidelt: Inversion transient-elektromagnetischer Messungen über geschichteten Untergrund. Technical Report for the Bundesanstalt für Geologie und Rohstoffe, Hannover, 1984.

**WEIDELT, 2000**

P Weidelt: Numerical modeling of transient-electromagnetic fields in three-dimensional conductors: A comparative study. Elektromagnetische Tiefenforschung, Kolloquiumsband zur Tagung in Altenberg, 2000, pp. 216-230.

**WHALEN ET AL., 1987**

JB Whalen, KL Currie & BW Chappell: A-type granites: geochemical characteristics, discrimination and petrogenesis. Contrib. Mineral. Petrol., 1987, vol. 95 (4), pp. 407-419.

**WHITE, 1979**

AJR White: Sources of granitic magmas. Geological Society of America Abstracts with Program 11, 1979, p. 539.



**WU ET AL., 2002**

FY Wu, DY Sun, HM Li, BM Jahn & S Wilde: A-type granites in northeastern China: age and geochemical constraints on their petrogenesis. *Chemical Geology*, 2002, vol. 187 (1-2), pp. 143-173.

**WU ET AL., 2003A**

FY Wu, BM Jahn, SA Wilde, CH Lo, TF Yui, Q Lin, WC Ge & DY Sun: Highly fractionated I-type granites in NE China (I): geochronology and petrogenesis. *Lithos*, 2003, vol. 66, pp. 241-273.

**WU ET AL., 2003B**

FY Wu, BM Jahn, SA Wilde, CH Lo, TF Yui, Q Lin, WC Ge & DY Sun: Highly fractionated I-type granites in NE China (II): isotopic geochemistry and implications for crustal growth in the Phanerozoic. *Lithos*, 2003, vol. 67, pp. 191-204.

**WÜNNEMANN AND HARTMANN, 2002**

B Wünnemann & K Hartmann: Morphodynamics and Paleohydrography of the Gaxun Nur Basin, Inner Mongolia, China. *Z. Geomorph. N. F.*, 2002, vol. 126, pp. 147-168.

**WÜNNEMANN ET AL., 2006**

B Wünnemann, N Altmann, K. Hartmann, HJ Pachur & U Hambach F. Sirocko, M. Clausen & M. Sanchez-Goni (ed.): Glacial and Interglacial fingerprints from lake deposits in the Gobi Desert, NW China (in print), Elsevier, 2006.

**WÜNNEMANN, 1999**

B Wünnemann: Untersuchungen zur Paleohydrographie der Endseen in Badain Jaran- und Tengger Wüste, Innere Mongolei, Nordwest-China. *Habil.*, FU Berlin, 1999.

**XIAO ET AL., 2003**

W Xiao, BF Windley, J Hao & M Zhai: Accretion leading to collision and the Permian Solonker suture, Inner Mongolia, China: Termination of the central Asian orogenic belt. *Tectonics*, 2003, vol. 22 (6), pp. 8/1-8/20.

**YIN & HARRISON, 2000**

A Yin & TM Harrison: Geologic Evolution of the Himalayan-Tibetan Orogen. *Annu. Rev. Earth Planet. Sci.*, 2000, vol. 28, pp. 211-280.

**YOUNG ET AL., 2004**

ME Young, PG Macumber, MD Watts & N Al-Toqy: Electromagnetic detection of deep freshwater lenses in a hyper-arid limestone terrain. *Journal of Applied Geophysics*, 2004, vol. 57 (1), pp. 43-61.

**YUE & LIOU, 1999**

YJ Yue & JG Liou: Two-stage evolution model for the Altyn Tagh fault, China. *Geology*, 1999, vol. 27 (3), pp. 227-230.

**YUE, 1966**

KS Yee: Numerical Solution of initial boundary value problems involving Maxwell's equations in isotropic media. *IEEE Trans. on Antennas and Propagation*, 1966, vol. AP-14, pp. 302-307.

**ZHANG ET AL., 2005**

L Zhang, W Xiao, K Qin, W Qu & A Du: Re-Os isotopic dating of molybdenite and pyrite in the Baishan Mo-Re deposit, eastern Tianshan, NW China, and its geological significance. *Mineralium Deposita*, 2005, vol. 39, pp. 960-969.

**ZHANG, 1990**

Z Zhang: Quaternary Geologic Map of the People's Republic of China and Adjacent Sea Area (1:2500000). China Cartographic Publishing House.

**ZHENG ET AL., 1996**

Y Zheng, Q Zhang, Y Wang, R Liu & SG Wang: Great Jurassic thrust sheets in Beishan (North Mountains) - Gobi areas of China and southern Mongolia. *Journal of Structural Geology*, 1996, vol. 18 (9), pp. 1111-1126.

**ZHOU ET AL., 2004**

MF Zhou, CM Leshner, ZX Yang, JW Li & M Sun: Geochemistry and petrogenesis of 270Ma Ni-Cu-(PGE) sulfide-bearing mafic intrusions in the Huangshan district, E-Xinjiang, NW China. *Chemical Geology*, 2004, vol. 209, pp. 233-257.

**ZHU & HU, 1995**

RX Zhu & XY Hu: Study On The Resistivity Structure Of The Lithosphere Along The Golmud - Ejinaqi Geoscience Transect (Chinese with English abstract). *Acta Geophysica Sinica*, 1995, vol. 38 (Suppl. II), pp. 46-57.

## **Appendix A**

### **LAPTEM - Specifications & Modifications**

All TEM-measurements in China were carried out using the LAPTEM-device, purchased by the TU Berlin in late 1997. The LAPTEM was manufactured by the *Department of Earth Sciences* at Monash University and distributed by *Geoinstruments* (both Australia). Due to the small number of instruments sold - only three were sold in Germany (Theurer (IGM), pers. comm.) - there are only very few scientific articles about the application of the LAPTEM. Articles exist, e.g. in non destructive material testing with HTS SQUID sensors (PANAITOV ET AL., 2002; KRAUSE ET AL., 2003).

Because of a creeping device failure in the years 2002/03, test-measurements were carried out to track down the cause of the failure. With very limited support from the Australian vendor and no circuit diagrams, the error search turned out to be lengthy. Finally, a broken nano-fuse and a slack joint in the parallel port connector were identified as source of error. Subsequently, the experience gained during the repair and testing led to modifications of the LAPTEM hardware and the development of a new control software. This new configuration of soft- and hardware offers advantages over the original configuration.

The specifications of original and new configuration will be described in the following. It should be noted that both configurations are still operational and may be used for measurements. The information in this chapter supplements the LAPTEM documentation for both soft- and hardware and provides additional information needed for a correct interpretation of measured data and may aid in troubleshooting.

#### **A.1 General Mode of Operation**

In this chapter the general mode of operation for the LAPTEM is described for the original and the new configuration. The chapter comprises information about the control software (chap. A.1.1) and the communication between control software and LAPTEM over the parallel port (chap. A.1.2).

### A.1.1 Control Software

#### **Original Configuration**

The original DOS control software exists in several versions (*Laptem30.exe*, *Laptem40.exe* = *Lapnew.exe*, *Laptem50.exe*). The version referred to hereafter as "DOS control software" is *Laptem40.exe*. The results in the following chapters apply to the other versions as well.

Due to the direct access of the control software to the parallel port, it will only work on DOS based operating systems like Windows 98 or older. Newer operating systems (e.g. Windows 2000) prohibit the direct access of the DOS program to the parallel port. Therefore, the control software will not start. The experimental use of virtual device drivers did not remediate the problem. Because the source code for the program was not made available by the vendor of the LAPTEM, there is currently no way to operate the program on an up-to-date operating system. Therefore, the user is forced to have an old operating system installed on the computer used for measuring.

On each start of the program a calibration measurement is performed, which terminates with the display of a *calibration number*. The calibration process is not documented in the device manual (GEOINSTRUMENTS, 1997), but from tests (chap. A.2.2) it is known that the calibration number is somehow related to the speed of the computer's CPU. The calibration procedure is seemingly needed to adjust the software based timing for the triggering of the AD-converter (Fig. A-2) to the predefined sampling frequency of 20kHz. The duration of this calibration is strongly related to the speed of the computer's CPU and may be the cause of subsequent errors (chap. A.2.2). It can take more than one minute with up-to-date computers. Neither the sampling frequency nor the length of the calibration cycle may be altered due to the lacking source code. After the calibration, the program may be used for measuring as described in the manual.

## New Configuration

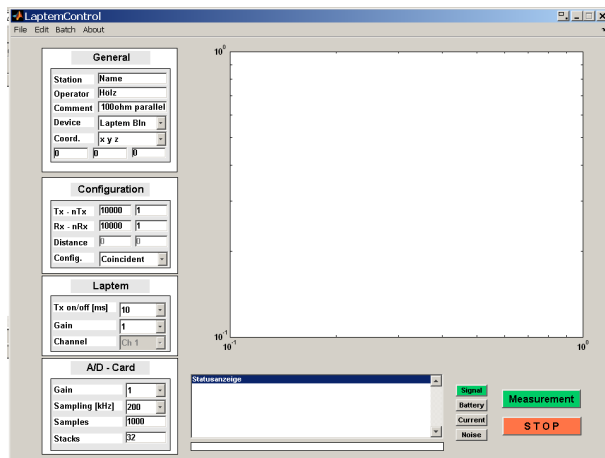


Fig. A-1: LAPTEMControl - GUI.

The new control software LAPTEMControl consists of a collection of Matlab functions and a graphical user interface (GUI, Fig. A-1). In addition, the drivers for the external AD-converter card need to be installed via the program InstaCal (MCC, 2007). LAPTEMControl is platform independent and can be run on any laptop with a PCMCIA slot for the external AD-converter card. It requires Matlab and the Data Acquisition Toolbox (V2.2 or higher) to be installed on the system. Compared to the original configuration, the new configuration offers the following advantages:

- Runs on any operating system with appropriate drivers for the PCMCIA-card.
- Source code is open and can be tested, modified, improved and expanded.
- Measurements are directly available for analysis in Matlab.
- Triggering of AD-conversions is hardware-controlled (chap. A.2.2).
- Transmitter waveform may be measured directly to yield accurate current-amplitudes and ramp times (chap. A.3.2).
- A text batch mode for the automatic setting of measurement parameters and the execution of measurements over simple scripts.

The batch mode is especially useful to avoid errors during field operations. All interactions with the GUI may be included in a text file, which is then just loaded and used during field measurements to initiate a complete measurement cycle. Exemplarily, the following batch-code shows some commands from an actual script contained in a text file:

```

1: comment      75ohm reihe
2: rx_area      10000
3: samples      1000
4: gain_lap     1
5: measurement
6: tx_on        3
7: gain_lap     4
8: measurement
9: message      Thomas, Kabel einholen und umbauen !!!
```

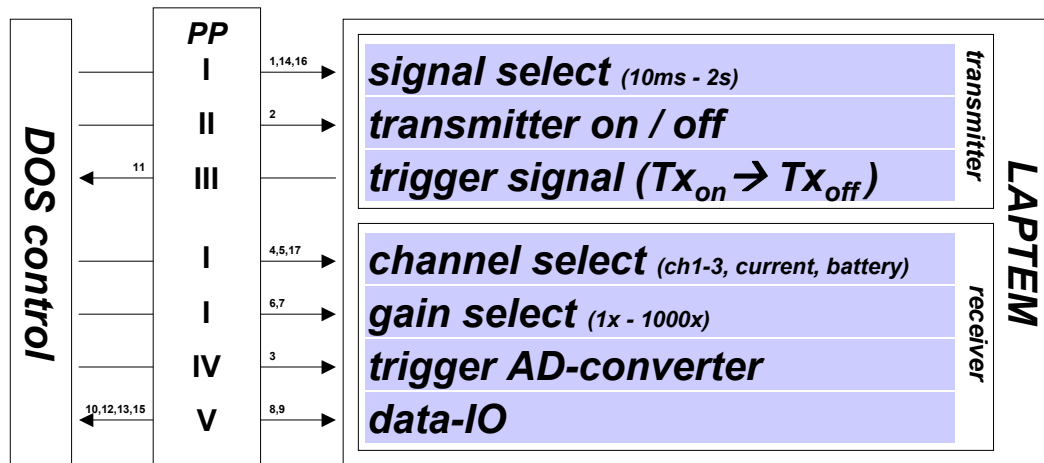


Fig. A-2: Schematic diagram showing the parallel port logic for the communication between the DOS control program and the LAPTEM in the original configuration. Arrows and arabic numerals (1-20) depict the pins used to control various settings and who is controlling them. Roman numerals (I-V) show the chronological succession of switching operations for a measurement (s. text).

10: repeat

Line numbers have been included for reference purposes only and are not contained in the actual file. In lines 1-4, status fields (comment, rx\_area) and measurement parameters (samples, gain\_lap) are automatically set within the GUI before a first measurement is initiated in line 5. After this measurement, parameters (tx\_on, gain\_lap) are changed in line 6-7 and a second measurement is initiated in line 8. After this measurement a message box is displayed, which pauses the execution of the script (line 9). After closing of the message box, the whole measurement cycle is repeated. A complete list of all currently implemented scripting commands is available in the documentation.

### A.1.2 Port Logic

#### Original Configuration

In the original configuration all communication between the DOS-control software and the device is handled via the parallel port (Fig. A-2), which needs to be configured to *Normal Mode* resp. *SPP Mode* in the computer's BIOS settings. The functionality and assignment of the parallel ports' signal lines was determined by using an oscilloscope to monitor the signal levels at the appropriate port pins during test-measurements.

Prior to the actual measurement, the control software once measures the voltage of the accumulators, which are used for the power supply, the current amplitude (chap. A.3.1) and the ramp time (chap. A.3.2). The actual measurement of  $m$  transients, each consisting of  $n$  samples, then uses the following control sequence:

- I. Control program sets the selected signal length (pins 1, 14, 18), measurement channel (pins 4, 5, 17) and gain (pins 6, 7).
- II. Control program starts transmitter of LAPTEM (pin 2).
- III. LAPTEM signals current turn off to control software by changing the trigger state (pin 11) approximately  $10\mu\text{s}$  before turn off.
- IV. Control program initializes AD-conversion (pin 3).
- V. The control program retrieves 16bit of data from the AD-converter in the LAPTEM in four 4bit-packages (pins 10, 12, 13, 15). The packages are selected by the control program over pins 8 and 9.
- VI. a) If less than  $n$  samples have been collected for the current transient, the control program returns to IV after  $\sim 50\mu\text{s}$  and initiates the next conversion.  
 b) If  $n$  samples and less than  $m$  transients have been collected, the control program returns to III and waits for the next trigger edge.  
 c) If  $n$  samples and  $m$  transients have been collected, the control program stops the transmitter of the LAPTEM (pin 2) and exits the measurement.

Looking at this succession of operations and the LAPTEM specifications there are two important points to be noted:

1. The measurements performed by the LAPTEM internal AD-converter are initiated by a software driven trigger over the parallel port (see IV). Therefore, the timing of conversions depends on the performance of the DOS-control software.
2. The sampling rate is a predefined parameter within the control program. It is set to  $50\mu\text{s}$  ( $\hat{=} 20\text{kHz}$ ) and can not be changed, even though the internal AD-converter may be operated with a sampling rate up to  $10\mu\text{s}$  ( $\hat{=} 100\text{kHz}$ ).

### **New Configuration**

In this configuration, the control software LAPTEMControl only uses the status lines of the parallel port for the selection of signal, trigger, gain, and transmitter on/off (Fig. A-3). AD-conversions and data-IO, where timing are critical, are all handled by the external AD-card. The card is synchronized to the LAPTEM's transmitter via a connection to the LAPTEM trigger. This setup offers the following advantages:

- Timing of the AD-conversions is handled hardware based by the AD-card's internal clock with increased accuracy.
- The external AD-card can be sampled with higher sampling rates of up to  $200\text{kHz}$ , which is a 10fold increase in the sampling frequency. Thus, the new configuration enables the LAPTEM to be used with smaller coils, where higher sampling rates are needed to acquire data at early times, i.e. starting at approximately  $10\mu\text{s}$ .

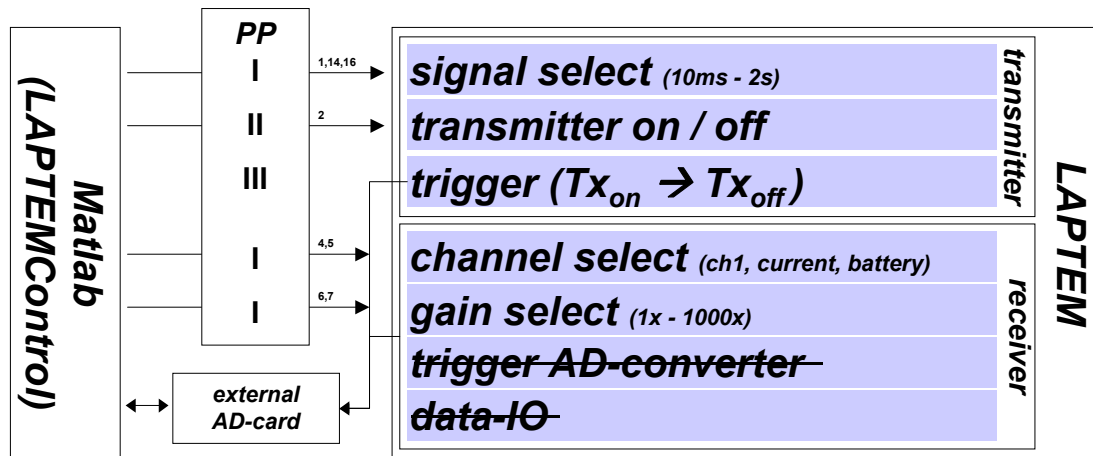


Fig. A-3: Port logic for new configuration: Schematic diagram for the communication between the new Matlab control program (LAPTEMControl) and the LAPTEM device over the parallel port and the external AD-card. Numbers and arrows as in Fig. A-2. The port lines for triggering the AD-converter and for the data-IO are no longer used in this configuration.

## A.2 Specification Receiver

### A.2.1 Offset

The offset is the average internal voltage level measured by the LAPTEM without an external sensor connected to the receiver. The offset level depends on the internal device temperature and may exhibit a drift. During processing the offset cancels out by averaging one positive and one negative transient in each stack (s. Fig. 2-6, p. 15), if it is stable or exhibits a reasonably slow drift. To test the possible influence of the drift on processed data, the positive and negative transients can be investigated prior to the averaging of each stack. Fig. A-4 shows the maximum offset drift found in measurements from China. For each measured stack the voltage of the last sample in each positive and negative transient is plotted (black lines). Since these samples are taken from the signal free part in each stack, the plots referring to samples belonging to the positive respectively negative transients approximately plot on top of each other and can not be distinguished. According to the data fit (grey line & formula in Fig. A-4), the drift is about 400bit/2000stack = 0.2bit/stack. This means that during each measurement cycle (s. Fig. 2-6, p. 15), the offset

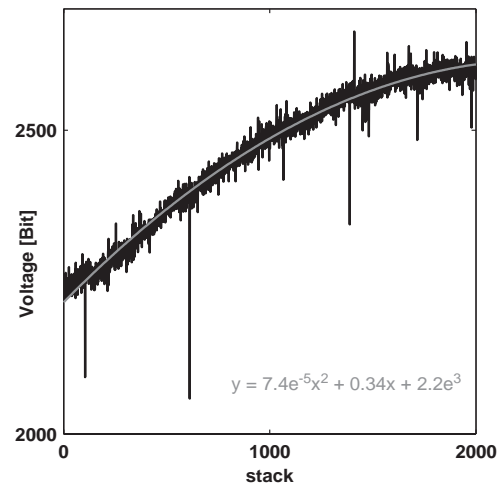


Fig. A-4: Offset drift at station TEM39.



drift is well below one Bit (i.e. the detection limit of the AD-converter) and thus, will be canceled out during processing.

### A.2.2 Precision of Time Scale

#### Original Configuration

As it has been pointed out in chap. A.1.1, the timing of AD-conversions in the original configuration is software controlled. Therefore, the calibration process at the beginning of the DOS control software plays a crucial role. To check the precision of timing, test measurements were taken using two different computers (chap. A.6). A sine-wave of  $1000.00(\pm .01)$  Hz was used as reference input signal for the LAPTEM. A spectral analysis of the measured reference signal was then used to compare the measured sampling frequency to the documented sampling frequency of 20kHz (GEOINSTRUMENTS, 1997).

With the older PCIII computer the calibration process of the DOS control program showed a stable *calibration number* (chap. A.1.1) with a value of 144 (chap. A.1.1). The spectral analysis of the reference signal indicates a sampling frequency of the LAPTEM in conjunction with a Pentium 1 computer of 20.4kHz which is 2% above the documented value.

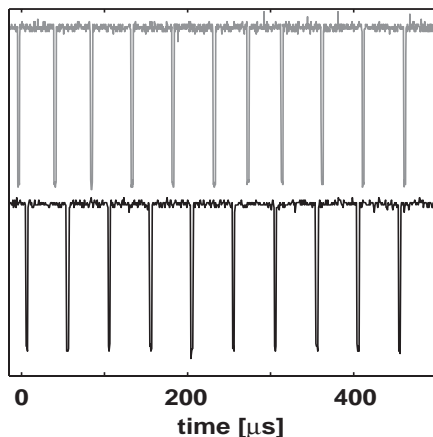


Fig. A-5: Trigger-pulses of DOS-software at the AD-converter (s. text). Curves are shifted for better visibility.

With the newer ASUS computer the calibration process of the DOS control program showed varying *calibration numbers*. In the normal case, when *calibration numbers* with values of 1214 or 1219 were displayed, spectral analysis of the reference signal indicated actual sampling frequencies between 20.4-20.7kHz. The occasional occurrence of smaller *calibration numbers* with values as low as 725 correlated to a significant increase in the actual sampling frequency of up to 27kHz, which is a 35% increase over the documented value.

To verify these findings a second series of test measurements was carried out, where the trigger-pulses from the DOS control software were directly monitored using an oscilloscope at the appropriate pin of the AD-converter (Fig. A-5). Using the older PCIII (Fig. A-5, bottom curve) the pulses to the AD-converter are regular, approximately with the specified sampling frequency of 20kHz. With the newer computer (Fig. A-5, top curve) the pulses to the AD-converter are distinctly higher at ~21.5kHz. Furthermore, the pulses are not evenly spaced, e.g. around 250μs. An extended analysis of the trigger pulses showed that both, inaccuracies of sampling frequency and jitter of the trigger pulses can become quite significant with increasing processor speed.

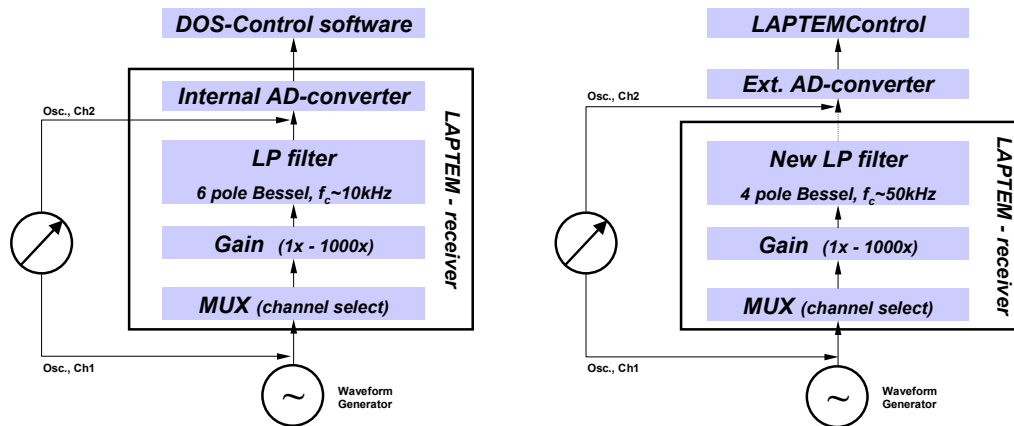


Fig. A-6: Schematic diagrams of the signal path from the signal input to the AD-converter (original configuration: left; new configuration: right). An oscilloscope (Osc.) was used to determine the frequency response of the system (chap. A.2.3).

Concluding, the tests have revealed that the precision of timing is not guaranteed for the original configuration and depends on the kind of computer used. It is a problem for the future use of the device, when suitable laptops may not be available anymore.

### New Configuration

The measurements and the spectral analysis of two sine-waves (1 kHz and 10 kHz) showed no significant difference between the generated and measured frequency. According to the measurements the frequency error is  $<1\%$ , which agrees with the documented frequency accuracy of 50 ppm (MCC, 2001). Due to the fact that the AD-converter in the PCMCIA-card is not directly accessible, no direct measurements were performed.

### A.2.3 Frequency Response

To determine the frequency response a waveform generator was connected to the input of the LAPTEM (Fig. A-6). For input signals in a frequency range between DC-0.3 MHz, input and output were then simultaneously measured with an oscilloscope. Small voltages were realized by in-series resistors as voltage dividers (1:101, 1:1001). The DC voltage was measured with a high precision multimeter. The frequency responses were used to estimate the corner frequencies and group delays of the implemented Bessel filters by fitting the theoretical filter responses after TIETZE & SCHENK (1985) with the coefficient in Tab. A-1 to the magnitude of the measured filter responses.

### Original Configuration

The magnitude of the frequency response for the original configuration shows a virtually constant amplification in the pass band for all gains (Fig. A-7, left). The amplification is about

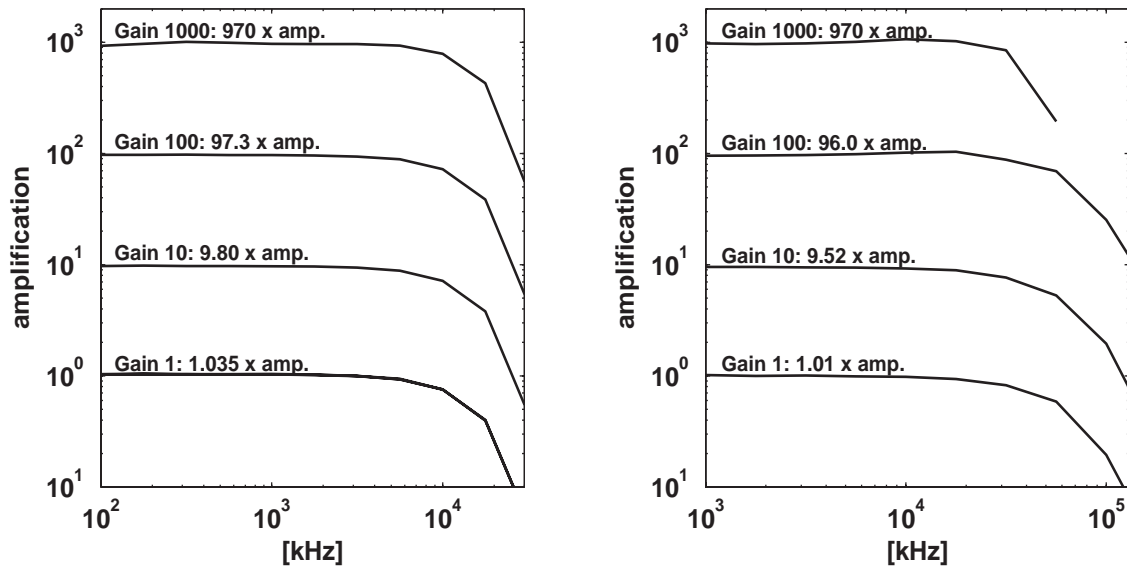


Fig. A-7: Frequency response (mag.) for the original configuration (left) and the new configuration (right).

N	$a_{1...[N/2]}$	$b_{1...[N/2]}$	N	$a_{1...[N/2]}$	$b_{1...[N/2]}$
1	1	0	6	1.2217, 0.9686, 0.5131	0.3887, 0.3505, 0.2756
2	1.3617	0.6180	7	0.5937, 1.0944, 0.8304, 0.4332	0, 0.3395, 0.3011, 0.2381
3	0.7560, 0.9996	0, 0.4772	8	1.1112, .9754, .7202, .3728	0.3162, 0.2979, 0.2621, 0.2087
4	1.3397, 0.7743	0.4889, 0.3890	9	0.5386, 1.0244, 0.8710, 0.6320, 0.3257	0, 0.2834, 0.2636, 0.2311, 0.1854
5	0.6656, 1.1402, 0.6216	0, 0.4128, 0.3245	10	1.0215, 0.9393, 0.7815, 0.5604, 0.2883	0.2650, 0.2549, 0.2351, 0.2059, 0.1665

Tab. A-1: Coefficients used in formula 2-6 (p. 14) from TIETZE & SCHENK (1985).

3.5% above the nominal value for gain 1. For the higher gains the true amplification is about 2.5% below the nominal values in the pass band. For all gains the corner-frequency of the 6pole Bessel filter, as determined by the -3dB point (s. Fig. 2-4, p. 13), is at  $\sim 10$ kHz, with an associated group delay of  $\sim 34\mu\text{s}$ .

### New Configuration

The magnitude of the frequency response for the original configuration shows a virtually constant amplification in the pass band for all gains (Fig. A-7, right). The amplification is about 1% above the nominal value for gain 1. Field tests (chap. A.4) and measurements in China indicate that gain 1 sometimes exhibits some amplification (10-20%), which was not found during laboratory measurements. However, this behavior is easily recognizable and can be corrected by comparing the measurements taken with different gains. For the higher gains the true amplification is about 4% below the nominal value in the pass band.

For gains 1-100 the corner-frequency of the 4pole Bessel filter, as determined by the -3dB point (s. Fig. 2-4, p. 13), is at 50kHz with an associated group delay of 7 $\mu$ s. For gain 1000 the filter characteristics of the gain superimpose the Bessel filter leading to a lower corner-frequency of  $\sim$ 30kHz and a group delay of  $\sim$ 11 $\mu$ s.

### A.3 Specification Transmitter

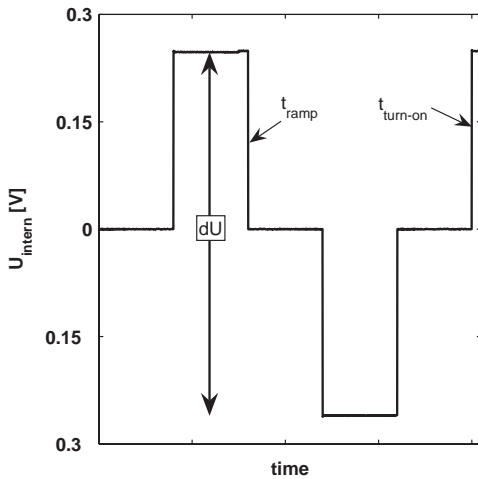


Fig. A-8: LAPTEM current waveform measured over the internal sensor resistor.

The transmitter of the LAPTEM uses a bipolar waveform with 50% duty cycle (Fig. A-8) and repetition frequencies between 0.5-100Hz to generate the primary magnetic field. The voltage  $U_0$  of two accumulators (2x12V or 2x24V), connected in series, is directly used as power supply for the transmitter coil without any regulation. Therefore, the amplitude of the transmitter current depends only on the resistance of the transmitter-coil, the internal resistances of the LAPTEM, and the variable internal resistance of the accumulators. Thus, the device may be tuned to different current amplitudes by varying the resistance of the coil or by using limiting resistors (chap. A.3.2). With estimated values for a 100x100m<sup>2</sup>-coil of  $\sim$ 1mH for the inductance (e.g. KAMENETSKY &

OELSNER, 2000; NELSON, 2005) and  $\sim 4e^{-10}$ F for the capacitance (KAMENETSKY & OELSNER, 2000), the inductive and capacitive resistances are negligible, since the base repetition frequency of the transmitter is at maximum 100Hz. The transmitter's current function is measured over one of the internal channels (Fig. A-2, Fig. A-3) with an internal sensor-resistor of nominal 0.047 $\Omega$ , which is connected in series with the transmitter coil and the power supply.

#### A.3.1 Current Measurement

##### Original Configuration

In this configuration the current is measured by the DOS control software and displayed as parameter after the measurement. The internal procedure of this measurement is not documented and a direct display of the whole current function is not possible. During measurements in China it was noticed that the values for the amplitude of the transmitter current generally yielded implausibly high values. Using a coil with a resistance of 2.5 $\Omega$ , the control software frequently yielded current amplitudes above 10A. However, an estimate of the possible maximum current ( $I_{max}$ ) - assuming reasonable maximum voltages ( $U_{max}$ ) and minimum internal resistance ( $R_{acc}$ ) of the two accumulators - adds up to:

$$I_{max} \leq \frac{U_{max}}{R_{coil} + R_{lap} + R_{acc}} = \frac{2 \cdot 12.7}{2.5 + 0.4 + 2 \cdot 0.05} \text{ A} \sim 8.5 \text{ A} \quad (A-1)$$

Here, the internal resistance of the LAPTEM ( $R_{lap}$ ) is known from direct measurements within the device's electronic. The value assumed for  $R_{acc}$  is reasonable for 65 Ah accumulators with a short circuit current of 250 A. For most measurements in China, smaller accumulators were used (17-28 Ah), which have higher internal resistances ( $\sim 0.1-0.3 \Omega$ ). Thus, the estimate for the maximum current would even be smaller..

Laboratory measurements in which the current was simultaneously measured with external laboratory equipment (chap. A.6) verified that the DOS control software overrates the true current amplitude. Errors were at maximum 50%, but typically in the order of 12-30% for currents around 3 A and 22-35% for currents around 8 A. Since the source code of the control software is not available, the reason for this failure could not be investigated further.

The faulty values for the current amplitude are corrected by using the known voltages for the power supply, i.e. the voltage of the accumulators, which are measured by the control software prior to each measurement. Similar to  $A-1$ , the corrected current amplitude is given by:

$$I_{corr} = \frac{U_0}{R_{coil} + R_{lap} + R_{acc}} \quad (A-2)$$

Some uncertainty remains, since the internal resistances of the accumulators are not known exactly. According to laboratory tests, the error for the corrected current amplitude should not be greater than 5%, which is a great increase in accuracy and, even more important, removes the systematic errors introduced by the DOS control software.

### New Configuration

To calibrate the current measurements for the new configuration, the complete current function was measured over the internal resistance of the LAPTEM (sim. Fig. A-8) and simultaneously over an external sensor resistor. The current amplitude was varied using limiting resistors solely (Fig. A-9, crosses) and with limiting resistors in combination with a 25x25m<sup>2</sup>-coil (Fig. A-9, squares). In both cases, an almost linear relationship was established:

(A-3)

$$I = 0.28(1) + 18.86(5) \cdot dU$$

$$I = 0.26(1) + 19.2(1) \cdot dU - 0.8(2) \cdot dU^2$$

$$[I] = A \quad [dU] = V$$

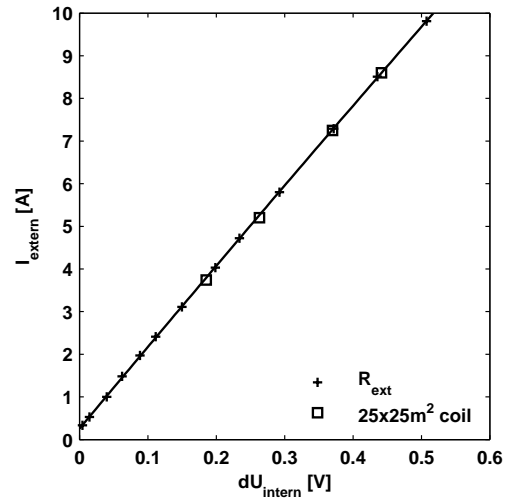


Fig. A-9: Relationship between voltage difference  $dU$  over internal current resistor (Fig. A-8) and externally measured current.

The linear approximation in formula A-3 yields reliable values for current amplitudes between 1-10A, for smaller amplitudes between 0.3-1 A the second order fit is used. The error estimates are <1% for currents above 1 A and <2% for currents between 0.3-1 A.

### A.3.2 Ramp Time

The ramp time (Fig. A-8), i.e. the time from the beginning to the end of the current shut down in the transmitter, has a strong influence especially on the early time gates of the measured transient and is a crucial parameter for the correct data inversion and interpretation. With the original configuration the internal resolution for measurements of the ramp time is limited to the sampling rate of 50μs used in the original DOS control software, which is by no means acceptable for an adequate interpretation of the early time gates. With the new

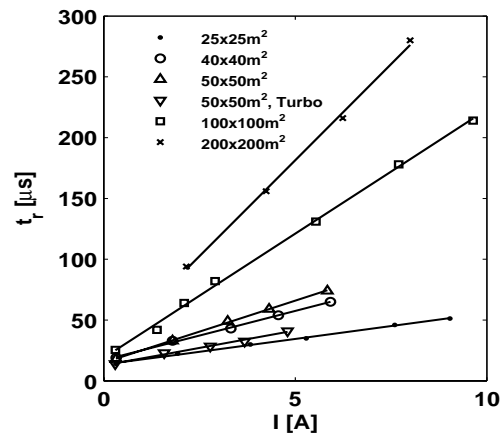


Fig. A-10: Dependency of ramp times ( $t_r$ ) and transmitter currents ( $I$ ) for different loop sizes.

configuration the resolution for measurements of the current ramp is improved to  $5\mu\text{s}$ , which is acceptable for interpretation.

To get reasonable ramp time estimates for field measurements with the original configuration, ramp times were measured using a current clamp respectively a small sensor resistor for various loop sizes and current amplitudes (Fig. A-10). The current amplitudes were varied by changing the resistance of the loops or by limiting resistors connected in series into the transmitter circuit. It is assumed that the ramp time is determined by the loop configuration and has no or only a minor dependency on the physical parameters of the underground. For each loop size, measurements show a linear dependency between current ramp time and transmitter current amplitude (Fig. A-10):

$$t_{ramp} = c_1 + c_2 \cdot I, \quad [t_{ramp}] = \mu\text{s} \quad [I] = \text{A} \quad (A-4)$$

loop size	$c_1$	$c_2$	loop size	$c_1$	$c_2$
25x25m <sup>2</sup>	13.4(6)	4.2(1)	50x50m <sup>2</sup> (turbo)	12.7(9)	5.7(3)
40x40m <sup>2</sup>	17.0(9)	8.1(2)	100x100m <sup>2</sup>	19(2)	20.4(4)
50x50m <sup>2</sup>	15.0(6)	10.2(2)	200x200m <sup>2</sup>	23(6)	32(1)

Tab. A-2: Coefficients with confidence intervals ( $1\sigma$ ) for the above formula.

The residuals for the linear interpolations are small. Therefore, the maximum error for the interpolation of ramp-times with a known current can be estimated to be about  $2\text{-}3\mu\text{s}$ . The linear relationships show that in order to measure early times of a transient, the ramp time may be decreased by using a limiting resistor in the loop to decrease the current amplitude. Another means to reduce the ramp time is the use of an external electronic switch („Turbo“ in Fig. A-10). For the 50x50m<sup>2</sup> coil such an external switch, originally build for the SIROTEM device, was tested during measurement in Århus, Denmark. With this switch the ramp times were reduced by up to 45%. Additionally the switch led to a decrease of the current amplitude. The exact circuit diagram of this switch is not known.

### A.3.3 Turn-On Time

During the turn-on of the transmitter the current function exhibits an exponential behavior. The time before the current reaches its full amplitude is called turn-on time (Fig. A-8, hardly visible). It may have a influence on the measured transient waveform at late times, if its duration is considerable compared to the total duration of the transmitter pulse (Auken, pers. comm.). For the LAPTEM the turn-on time depends on the loop size and the current amplitude and can reach values up to 1.5ms. Model calculations with the program EMMA (HGG, 2007) assuming the maximum turn-on time of 1.5ms and the minimum pulse duration of 10ms have

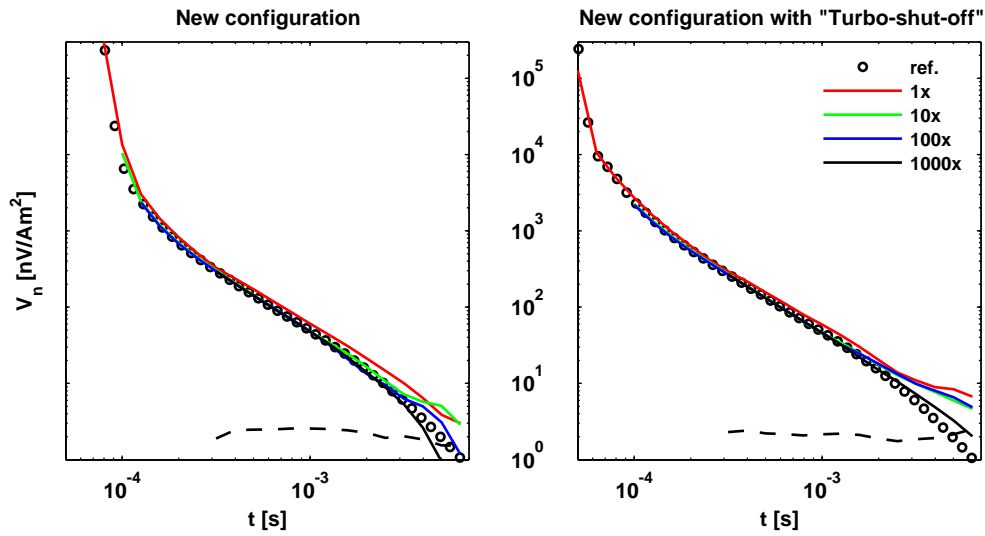


Fig. A-11: Results of calibration measurements in Århus, Denmark, for two different configurations. The reference transients (circles) differ at early times, because of different ramp times for each configuration. Error-floors (dashed lines) are only displayed for gain 1000.

shown that the effect of the turn-on time on measurements is  $<1\%$ . Therefore, it can be neglected for the LAPTEM.

#### A.4 Calibration Measurements in Århus, Denmark

The new configuration of the LAPTEM was tested in cooperation with the HydroGeophysics Group (HGG, University of Århus, Denmark) at a test-site close to Århus, where about 10 TEM-devices (PROTEM and HGG SkyTEM) were previously tested and calibrated with measurements in the inloop configuration ( $40 \times 40 \text{ m}^2$  transmitter coil, inloop receiver). The results of these tests measurements compared well for times between  $10 \mu\text{s}$ -5 ms and were combined to a reference transient and an associated reference 1D model (Auken, pers. comm.). Since measurements with the LAPTEM were carried out with a slightly different configuration (coincident loop,  $50 \times 50 \text{ m}^2$ ), the original reference transient and the LAPTEM measurements may not be compared directly. Instead, an adjusted reference transient was calculated from the 1D reference model for this configuration.

In a first test, which resembles the measurements in China, the transmitter coil was directly connected to the LAPTEM. During a second test the current and ramp time were limited to check the possibility to measure transient data at earlier times using the new configuration. In this test, the current was limited by an external "turbo-shut-off-switch", which was originally built for the SIROTEM-device (chap. A.3.2).

Generally, the comparison of the test measurements are in good agreement with the reference curves (Fig. A-11). They clearly show the influence of the Bessel filter, which leads to a sharp increase of the normalized voltage at early times (comp. Fig. 2-5, p. 14). Measurements



with gains 10-1000 are within 5% of the reference curve between 200ms-3ms. For these gains the deviation at shorter times is somewhat larger, but may also be caused by minor inaccuracies ( $<5\mu\text{s}$ ) in the timescale. For late times ( $>3\text{ms}$ ), the amplitude of the transients drops to the order of the noise level (Fig. A-11, dashed lines), thus, leading to increasing deviations. The measurements with gain 1 show the same general tendencies, but are 10%-20% above the reference curve. This behavior was not encountered during laboratory testing (chap. A.2.3). Consequently, measurements with gain 1 may need an additional adjustment, if they do not align with measurements using the larger gains. The comparison of measurements with respectively without the "turbo-switch" (Fig. A-11, right resp. left) demonstrates that the limiting of the ramp time is possible by the use of external switches and yields reliable results, here down to about  $60\mu\text{s}$ .

Concluding, the test measurements have demonstrated that the new configuration of the LAPTEM is working and fully operational.

## A.5 Summary - LAPTEM

In the original configuration the LAPTEM with the given DOS control software has limitations in both, accuracy and applicability. Summarized, the main problems are:

- Need for an old operating system (Win98 or older)
- Source code for DOS control software not available
- Sampling rate limited to  $50\mu\text{s}$  ( $\approx 20\text{kHz}$ )
- Software controlled sampling rate
- Sampling rate depends, to some extent, on the type of computer used
- Accuracy of ramp time limited to  $\pm 25\mu\text{s}$
- Systematic error in estimation of current amplitude
- Minimum measurable time (first gate) limited to  $\sim 125\text{-}175\text{ms}$ .

The problems are due to the limited sampling speed and the limited accuracy of timing for the AD-conversions. These inaccuracies of the original configuration may be corrected with respect to the laboratory measurements in the previous chapters. A general improvement of the system within the original configuration is not possible, which is in parts due to the lacking source code for the control software.

To overcome these shortcomings a new configuration was designed, implemented and successfully tested during a field test in Århus, Denmark. The new configuration was in parts used during field measurements in the Gurinai Structure (s. chap. 4.3, p. 111) and at the Jingsutu Cliff (s. chap. 4.2, p. 80). In this configuration a new control software LAPTEMControl and an external AD-converter card are used with the following advantages:

- Hardware based AD-conversions with increased accuracy of timing and speed ( $5\text{ }\mu\text{s} \hat{=} 200\text{kHz}$ ),
- Decreased minimum measurable time (currently  $\sim 60\text{ }\mu\text{s}$ ),
- Accurate measurement of current amplitude and ramp time,
- Open source code,
- Independent on operating system (not fully tested).

Work on this new configuration is still an ongoing process. Future improvements may be:

- Use of an external GPS in LAPTEMControl to determine the current position (partially implemented). This would especially be needed for a moving TEM-system.
- Use of generic libraries for the control of AD-converter card instead of the Data Acquisition Toolbox.
- Improvement of the mechanical stability of cables and connectors.
- Compiling of LAPTEMControl into stand-alone application (needs special compiler) to be independent of Matlab.
- Implementation of Bessel filter with higher corner frequency (150-200kHz) - this would be needed to measure with smaller coils at earlier times.

## A.6 List of Laboratory Instruments for Calibration

- Oscilloscope: TekScope THS 710 Std
- Function generator: Feedback SSO 603
- Multimeter: Voltcraft M4660A  
Fluke 8050A
- Frequency counter: TTI PFM 1300
- Current probe: Fluke 80i - 110s AC/DC
- External A/D-card: MCC PC-CARD DAS 16/16
- Computers: ASUS L8400 (Laptop, 850MHz Pentium 3)  
PC III (Laboratory computer, 100MHz Pentium 1)

## Appendix B

### Coefficient Bands in the Wavelet Domain

The analysis of TEM signals with the wavelet decomposition shows that the energy of transient signals for almost arbitrary models of the underground is transformed into stable coefficient bands in the wavelet domain (comp. fig xyz, pabc), i.e. the energy of a transformed signal is always contained in the same coefficients (s. chap. 2.4.3, p. 49ff). In this appendix the coefficient bands are tabulated for 12 different measurement configurations on the following pages. Using the first rows of the table from the next page, the entries are shortly explained:

A=625m <sup>2</sup> ; I=2A; gain=100x; t <sub>0</sub> =25μs; dt=5μs											
Wavelet	cD <sub>1</sub>	cD <sub>2</sub>	cD <sub>3</sub>	cD <sub>4</sub>	cD <sub>5</sub>	cD <sub>6</sub>	cD <sub>7</sub>	cD <sub>8</sub>	cD <sub>9</sub>	cD <sub>10</sub>	cA <sub>max</sub>
bior1.3	1-81	3-107	3-94	3-52	3-28	3-16	3-10	3-7	-	-	2-8
bior1.5	2-86	2-109	2-97	3-55	3-30	3-18	3-12	-	-	-	4-15
...	...	...	...	...	...	...	...	...	...	...	...

The shaded header row contains information about the considered measurement configuration. With these parameters the true, unnormalized voltage can be calculated. For the example above the parameters for the coincident loop are:

- loop area: A=625m<sup>2</sup>
- transmitter current: I=2A.
- receiver-gain: 100x
- sampling rate: dt=5ms
- first sample: t<sub>0</sub>=25ms

The marked cell in the third row and second column exemplarily shows that for the bior1.3 wavelet the detail coefficients 1-81 from the first decomposition level contain relevant signal energy of the transformed transient and are needed for a reconstruction of the signal. Similarly, the listed detail coefficients for the levels 2-8 ( $\Leftrightarrow$  cD<sub>1-8</sub>) and the approximation coefficients of the maximum level (cA<sub>max</sub>=cA<sub>8</sub>) are needed in the reconstruction. Using these coefficients, any transformed transient of an arbitrary 1D underground model can be recovered with an error <1% for all relevant times, i.e. the time range in which the true voltage of the transient is within the resolution limit of the measurement system. The same applies to the other listed wavelets and all tabulated measurement configurations.

# Coefficient Bands in the Wavelet Domain

A=625m <sup>2</sup> ; I=2A; gain=100x; t <sub>0</sub> =25μs; dt=5μs											
Wavelet	cD <sub>1</sub>	cD <sub>2</sub>	cD <sub>3</sub>	cD <sub>4</sub>	cD <sub>5</sub>	cD <sub>6</sub>	cD <sub>7</sub>	cD <sub>8</sub>	cD <sub>9</sub>	cD <sub>10</sub>	cA <sub>max</sub>
bior1.3	1-81	3-107	3-94	3-52	3-28	3-16	3-10	3-7	-	-	2-8
bior1.5	2-86	2-109	2-97	3-55	3-30	3-18	3-12	-	-	-	4-15
bior2.2	1-11	1-11	1-12	1-11	2-11	2-10	2-8	2-6	-	-	2-9
bior2.4	2-12	2-13	2-14	3-13	3-13	3-12	3-11	-	-	-	4-16
bior2.6	3-12	4-15	3-16	3-15	4-15	4-14	4-13	-	-	-	6-18
bior2.8	3-13	5-16	4-17	5-17	5-17	5-16	-	-	-	-	8-31
bior3.1	2-5	2-6	2-6	2-6	2-6	2-5	2-5	2-4	2-3	-	1-5
bior3.3	1-6	1-7	1-7	3-8	3-8	3-7	3-7	3-7	-	-	3-10
bior3.5	2-7	2-9	2-9	4-9	4-9	4-9	4-9	-	-	-	4-17
bior3.7	3-8	3-10	3-11	5-11	5-11	5-11	5-11	-	-	-	7-19
bior3.9	4-9	6-12	4-13	6-13	6-13	6-13	-	-	-	-	8-32
bior4.4	2-6	1-8	2-9	2-9	2-9	2-9	2-9	-	-	-	3-17
bior5.5	2-6	2-9	2-10	3-10	3-10	3-10	2-10	-	-	-	2-19
bior6.8	4-8	5-11	4-12	5-13	5-13	5-13	-	-	-	-	5-33
coif1	1-12	1-15	2-17	2-17	1-17	1-13	1-9	1-6	-	-	1-9
coif2	2-7	3-9	3-10	3-11	3-11	3-11	3-10	-	-	-	2-20
coif3	3-8	5-11	5-13	5-14	6-14	6-15	-	-	-	-	4-34
coif4	4-10	6-14	7-17	7-18	7-18	8-18	-	-	-	-	8-38
db10	1-9	4-14	5-16	6-17	5-18	5-18	-	-	-	-	6-39
db2	1-12	1-16	1-18	1-17	1-16	1-13	1-8	1-5	1-4	-	1-5
db3	1-8	1-10	1-11	1-11	1-11	1-10	1-9	1-6	-	-	1-10
db4	1-7	1-9	1-10	2-10	2-10	2-10	2-9	1-7	-	-	1-12
db5	1-7	2-9	2-10	2-11	2-11	2-11	2-10	-	-	-	2-19
db6	1-7	3-10	3-11	3-12	3-12	3-12	3-11	-	-	-	2-21
db7	1-7	3-11	3-13	3-13	4-13	3-13	4-13	-	-	-	3-23
db8	1-8	3-12	4-14	4-14	4-15	4-15	4-14	-	-	-	4-25
db9	1-9	3-13	5-15	4-16	4-16	4-16	-	-	-	-	5-37
rbio1.3	2-8	2-9	2-9	2-10	2-9	2-9	2-8	2-6	-	-	1-9
rbio1.5	3-7	3-8	4-9	4-9	3-9	3-9	3-9	-	-	-	1-17
rbio2.2	1-16	1-23	2-27	2-30	2-25	2-15	2-9	2-6	-	-	2-10
rbio2.4	2-8	3-10	3-11	3-12	3-11	3-11	3-10	-	-	-	2-18
rbio2.6	3-8	4-10	4-12	4-12	5-12	5-12	4-11	-	-	-	2-20
rbio2.8	4-9	6-12	6-13	6-14	7-14	7-14	-	-	-	-	4-33
rbio3.1	2-194	2-202	2-102	2-52	2-27	2-15	2-9	2-6	2-4	-	1-5
rbio3.3	3-11	3-15	3-17	3-17	3-17	3-15	3-10	3-8	-	-	1-12
rbio3.5	4-8	4-11	4-12	4-13	4-12	4-12	4-11	-	-	-	1-19
rbio3.7	5-9	5-12	5-13	5-14	5-13	5-13	5-13	-	-	-	2-21
rbio3.9	6-10	6-13	7-15	7-15	8-15	7-15	-	-	-	-	3-34
rbio4.4	2-8	2-10	3-11	3-11	2-11	2-10	2-10	-	-	-	2-18
rbio5.5	2-8	2-10	2-11	2-11	2-11	2-11	2-10	-	-	-	3-19
rbio6.8	4-9	5-12	5-13	5-14	5-14	5-14	-	-	-	-	3-33
sym10	4-10	4-13	4-15	5-15	5-16	5-16	-	-	-	-	3-33
sym2	1-12	1-16	1-18	1-17	1-16	1-13	1-8	1-5	1-4	-	1-5
sym3	1-8	1-10	1-11	1-11	1-11	1-10	1-9	1-6	-	-	1-10
sym4	1-7	1-8	1-9	1-9	1-9	1-9	1-8	1-7	-	-	1-10
sym5	2-7	2-8	2-9	2-9	2-9	1-9	1-8	-	-	-	1-17
sym6	2-7	2-9	2-10	2-10	2-10	2-10	2-10	-	-	-	1-18
sym7	2-8	3-10	3-11	3-11	3-12	3-12	3-12	-	-	-	2-21
sym8	3-8	2-11	4-11	3-13	4-13	3-13	3-13	-	-	-	2-20
sym9	3-9	4-12	4-13	4-14	5-14	4-14	-	-	-	-	2-33

Tab. B-1: Coefficient bands for measurement configuration 1.

A=625m <sup>2</sup> ; I=2A; gain=1000x; t <sub>0</sub> =25μs; dt=5μs											
Wavelet	cD <sub>1</sub>	cD <sub>2</sub>	cD <sub>3</sub>	cD <sub>4</sub>	cD <sub>5</sub>	cD <sub>6</sub>	cD <sub>7</sub>	cD <sub>8</sub>	cD <sub>9</sub>	cD <sub>10</sub>	cA <sub>max</sub>
bior1.3	1-89	3-121	3-139	3-127	3-83	3-43	3-24	3-14	3-9	-	2-9
bior1.5	2-92	2-125	2-142	3-130	3-85	3-46	3-26	3-16	-	-	4-18
bior2.2	1-10	1-11	1-12	2-12	2-12	2-12	2-11	2-10	2-8	-	2-10
bior2.4	2-11	2-13	2-14	3-15	3-14	3-14	3-14	3-13	-	-	4-19
bior2.6	3-12	4-15	3-16	4-16	4-16	4-16	4-16	4-15	-	-	6-21
bior2.8	4-13	5-16	4-18	5-19	5-18	5-18	5-18	-	-	-	8-37
bior3.1	2-5	2-6	2-6	2-6	2-6	2-6	2-6	2-6	2-5	2-4	1-6
bior3.3	1-6	1-7	1-7	3-8	3-8	3-8	3-8	3-7	3-7	-	3-11
bior3.5	2-7	2-8	2-9	4-10	4-10	4-10	4-10	4-9	-	-	5-20
bior3.7	3-8	3-10	3-11	5-11	5-12	5-12	5-12	5-11	-	-	7-22
bior3.9	4-9	6-12	4-12	6-13	6-14	6-14	6-14	-	-	-	9-38
bior4.4	2-7	2-8	2-9	2-10	3-10	2-10	2-9	2-9	-	-	3-20
bior5.5	2-7	2-9	2-10	3-10	3-11	2-11	2-10	2-10	-	-	2-22
bior6.8	4-8	4-11	4-12	4-13	5-13	5-13	4-13	-	-	-	5-38
coif1	1-12	1-16	2-19	2-20	1-18	1-20	1-17	1-12	1-8	-	1-11
coif2	2-7	3-9	3-10	3-11	3-11	3-11	3-11	3-10	-	-	2-22
coif3	3-8	5-11	5-13	5-14	6-14	6-15	5-15	-	-	-	5-40
coif4	4-10	6-14	7-17	7-18	7-19	8-19	7-19	-	-	-	7-44
db10	1-10	4-14	5-16	6-18	5-18	5-18	6-18	-	-	-	6-45
db2	1-12	1-17	1-19	1-19	1-19	1-17	1-15	1-11	1-7	1-5	1-6
db3	1-8	1-10	1-11	1-12	1-12	1-11	1-11	1-10	1-8	-	1-11
db4	1-7	1-9	2-10	2-11	2-11	2-11	1-10	1-10	1-8	-	1-13
db5	1-7	2-9	2-10	2-11	2-11	2-11	2-11	2-11	-	-	2-22
db6	1-7	3-10	3-11	3-12	3-13	3-13	3-12	2-12	-	-	2-24
db7	1-8	3-11	3-12	3-13	4-14	3-14	4-13	3-13	-	-	2-26
db8	1-8	3-12	4-14	4-15	4-15	4-15	4-15	3-15	-	-	4-28
db9	1-9	3-13	5-15	5-16	4-17	4-17	5-16	-	-	-	5-43
rbio1.3	2-8	2-9	2-10	2-10	2-10	2-10	2-9	2-9	2-8	-	1-10
rbio1.5	3-7	3-8	4-9	4-10	3-10	3-10	3-9	3-9	-	-	1-20
rbio2.2	1-16	1-25	2-32	2-35	2-36	2-36	2-23	2-13	2-8	-	2-11
rbio2.4	2-8	3-10	3-11	3-12	3-12	3-12	3-12	3-12	-	-	2-21
rbio2.6	3-8	4-10	4-11	5-12	5-12	5-12	4-12	4-12	-	-	2-23
rbio2.8	4-9	6-12	6-13	6-14	7-14	7-14	6-14	-	-	-	3-39
rbio3.1	2-209	2-465	2-325	2-164	2-83	2-43	2-23	2-13	2-8	2-5	1-6
rbio3.3	3-11	3-15	3-17	3-18	3-19	3-19	3-19	3-14	3-9	-	1-13
rbio3.5	4-8	4-11	4-12	4-13	4-13	4-13	4-13	4-12	-	-	1-22
rbio3.7	5-9	5-12	5-13	5-14	5-14	5-14	5-14	5-13	-	-	2-25
rbio3.9	6-10	6-13	7-15	7-16	8-16	7-16	7-16	-	-	-	3-40
rbio4.4	2-7	2-10	3-11	3-12	2-12	2-11	2-11	2-10	-	-	2-20
rbio5.5	2-8	2-10	2-11	3-12	2-12	2-11	2-11	2-11	-	-	3-21
rbio6.8	4-9	5-12	5-13	5-14	5-14	5-14	5-14	-	-	-	3-39
sym10	4-10	4-13	5-15	5-15	5-16	4-16	4-16	-	-	-	2-39
sym2	1-12	1-16	1-19	1-19	1-19	1-18	1-16	1-11	1-7	1-5	1-6
sym3	1-8	1-10	1-11	1-12	1-11	1-11	1-11	1-10	1-8	-	1-11
sym4	2-7	1-8	1-9	1-9	1-9	1-9	1-9	1-9	1-8	-	1-12
sym5	2-7	2-8	2-9	2-9	2-9	2-9	1-9	1-9	-	-	1-20
sym6	2-7	2-9	2-10	3-10	2-11	2-11	2-10	1-10	-	-	1-21
sym7	2-8	3-10	3-11	3-12	3-12	3-12	3-12	2-12	-	-	2-23
sym8	3-8	4-11	4-11	3-13	4-13	3-13	3-13	2-13	-	-	1-23
sym9	3-9	4-12	4-13	4-14	5-14	4-15	4-15	-	-	-	3-38

Tab. B-2: Coefficient bands for measurement configuration 2.

# Coefficient Bands in the Wavelet Domain

A=10000m <sup>2</sup> ; I=0.3A; gain=1x; t <sub>0</sub> =50μs; dt=5μs											
Wavelet	cD <sub>1</sub>	cD <sub>2</sub>	cD <sub>3</sub>	cD <sub>4</sub>	cD <sub>5</sub>	cD <sub>6</sub>	cD <sub>7</sub>	cD <sub>8</sub>	cD <sub>9</sub>	cD <sub>10</sub>	cA <sub>max</sub>
bior1.3	1-72	3-92	3-69	3-36	3-20	3-12	3-8	-	-	-	2-9
bior1.5	2-74	2-95	3-71	4-38	3-22	3-14	-	-	-	-	4-17
bior2.2	1-9	1-9	2-10	2-10	2-10	2-9	2-7	-	-	-	2-10
bior2.4	2-10	2-11	2-12	3-12	3-12	3-11	-	-	-	-	4-18
bior2.6	3-11	4-13	4-14	4-14	4-14	4-13	-	-	-	-	6-20
bior2.8	4-12	6-14	5-15	5-16	5-16	-	-	-	-	-	8-35
bior3.1	2-4	2-5	2-5	2-5	2-5	2-5	2-5	2-4	-	-	1-5
bior3.3	3-5	1-6	1-7	3-7	3-7	3-7	3-7	-	-	-	2-11
bior3.5	4-6	2-8	2-8	4-9	4-9	4-9	-	-	-	-	4-19
bior3.7	5-7	5-9	5-10	5-11	5-11	5-11	-	-	-	-	6-21
bior3.9	6-7	7-11	6-12	6-13	6-13	-	-	-	-	-	8-36
bior4.4	2-5	2-7	2-8	3-9	3-9	3-9	-	-	-	-	3-19
bior5.5	2-5	4-8	3-9	3-9	4-10	3-10	-	-	-	-	2-21
bior6.8	4-6	5-10	5-11	5-12	5-12	-	-	-	-	-	5-37
coif1	1-10	2-13	2-16	2-16	2-15	1-11	1-7	-	-	-	1-11
coif2	2-5	3-8	3-9	3-10	4-10	3-10	-	-	-	-	3-22
coif3	3-6	5-10	6-12	5-13	7-13	-	-	-	-	-	6-39
coif4	4-8	7-13	8-15	8-16	8-17	-	-	-	-	-	9-43
db10	1-7	4-13	6-15	6-16	6-17	-	-	-	-	-	8-43
db2	1-10	1-13	1-16	1-15	1-14	1-10	1-6	1-4	-	-	1-6
db3	1-6	1-9	1-9	1-10	1-10	2-9	1-7	-	-	-	1-11
db4	2-5	1-8	2-9	2-9	2-9	2-9	2-8	-	-	-	1-13
db5	1-5	2-8	2-9	2-10	3-10	2-10	-	-	-	-	2-21
db6	1-5	3-9	3-10	3-11	3-11	3-11	-	-	-	-	3-23
db7	1-6	3-10	3-11	4-12	4-13	4-12	-	-	-	-	4-25
db8	1-7	3-11	4-13	5-14	4-14	5-14	-	-	-	-	5-27
db9	1-7	4-11	5-14	5-15	5-15	-	-	-	-	-	6-41
rbio1.3	2-6	2-8	2-8	2-9	2-8	2-8	2-7	-	-	-	1-10
rbio1.5	3-5	3-7	4-8	4-9	4-9	3-9	-	-	-	-	1-19
rbio2.2	1-13	2-19	2-25	2-26	2-19	2-11	2-7	-	-	-	1-11
rbio2.4	2-6	3-9	3-10	3-11	4-11	3-10	-	-	-	-	2-20
rbio2.6	3-6	4-9	4-11	4-11	5-11	5-11	-	-	-	-	2-22
rbio2.8	4-7	6-11	6-12	6-13	7-13	-	-	-	-	-	4-38
rbio3.1	2-172	2-135	2-69	2-36	2-19	2-11	2-7	2-5	-	-	1-6
rbio3.3	3-9	3-13	3-14	3-16	3-15	3-12	3-8	-	-	-	1-12
rbio3.5	4-7	4-10	4-11	4-11	4-12	4-11	-	-	-	-	1-21
rbio3.7	5-7	5-11	5-12	5-13	6-13	5-13	-	-	-	-	2-23
rbio3.9	6-9	6-12	7-14	7-15	8-15	-	-	-	-	-	4-39
rbio4.4	2-6	2-9	3-9	3-10	3-10	3-10	-	-	-	-	2-20
rbio5.5	2-6	3-9	3-10	3-10	3-10	3-10	-	-	-	-	3-21
rbio6.8	4-7	6-11	5-12	6-13	7-13	-	-	-	-	-	4-38
sym10	5-9	5-11	5-13	6-14	6-14	-	-	-	-	-	3-38
sym2	1-10	1-13	1-16	1-15	1-14	1-10	1-6	1-4	-	-	1-6
sym3	1-6	1-9	1-9	1-10	1-10	2-9	1-7	-	-	-	1-11
sym4	2-5	2-7	1-8	1-8	1-8	1-8	1-7	-	-	-	1-11
sym5	2-5	2-7	3-8	2-8	1-8	1-8	-	-	-	-	1-19
sym6	3-5	2-8	2-9	3-9	2-10	2-9	-	-	-	-	1-20
sym7	2-6	3-9	3-10	4-10	5-11	3-11	-	-	-	-	2-23
sym8	4-7	4-10	4-11	4-11	4-12	4-12	-	-	-	-	2-23
sym9	4-8	5-11	4-13	5-13	6-12	-	-	-	-	-	2-37

Tab. B-3: Coefficient bands for measurement configuration 3.

A=10000m <sup>2</sup> ; I=0.3A; gain=10x; t <sub>0</sub> =50μs; dt=5μs											
Wavelet	cD <sub>1</sub>	cD <sub>2</sub>	cD <sub>3</sub>	cD <sub>4</sub>	cD <sub>5</sub>	cD <sub>6</sub>	cD <sub>7</sub>	cD <sub>8</sub>	cD <sub>9</sub>	cD <sub>10</sub>	cA <sub>max</sub>
bior1.3	1-80	3-119	3-114	3-107	3-55	3-29	3-17	3-10	3-7	-	2-7
bior1.5	2-83	2-123	3-116	4-109	3-57	2-32	2-19	2-12	-	-	4-13
bior2.2	1-8	1-10	2-11	2-11	2-12	2-11	2-10	2-9	2-6	-	2-8
bior2.4	2-9	2-12	2-12	3-13	3-14	3-13	3-12	3-11	-	-	4-14
bior2.6	3-9	4-13	4-14	4-15	4-16	4-15	4-14	4-13	-	-	6-16
bior2.8	4-10	6-14	5-16	5-17	5-18	5-17	5-16	-	-	-	8-27
bior3.1	2-4	2-4	2-5	2-6	2-6	2-6	2-6	2-5	2-5	2-3	1-4
bior3.3	3-5	1-6	1-7	3-7	3-7	3-8	3-8	3-7	3-7	-	3-9
bior3.5	4-6	2-7	2-8	4-9	4-9	4-9	4-9	4-9	-	-	5-15
bior3.7	3-7	5-9	5-10	5-11	5-11	5-11	5-11	5-11	-	-	6-17
bior3.9	4-8	7-10	6-12	6-13	6-13	6-13	6-13	-	-	-	8-28
bior4.4	2-5	2-7	2-8	3-9	3-9	3-9	2-9	2-9	-	-	3-15
bior5.5	2-5	4-8	3-9	3-10	4-10	3-10	3-10	3-10	-	-	2-17
bior6.8	4-6	5-10	5-11	5-12	5-13	5-13	5-13	-	-	-	5-29
coif1	1-10	2-14	2-16	2-18	2-18	1-16	1-14	1-9	1-6	-	1-8
coif2	2-5	3-8	3-9	3-10	3-10	3-11	3-10	3-10	-	-	2-18
coif3	3-6	5-10	6-12	5-13	7-14	6-14	6-14	-	-	-	5-31
coif4	4-8	7-13	8-15	8-16	8-18	8-18	8-18	-	-	-	8-35
db10	1-7	4-12	5-16	6-17	6-17	6-18	6-18	-	-	-	7-35
db2	1-9	1-15	1-17	1-18	1-18	1-16	1-14	1-8	1-6	1-4	1-5
db3	1-6	1-8	1-10	1-11	1-11	2-11	1-10	1-9	1-6	-	1-9
db4	2-5	1-7	2-9	2-10	2-10	2-10	2-9	2-9	1-8	-	1-11
db5	1-5	2-8	2-10	2-10	3-11	2-11	2-10	3-10	-	-	2-17
db6	1-5	3-9	3-11	3-11	3-12	3-12	3-12	3-11	-	-	2-19
db7	1-6	3-10	3-12	4-13	4-13	4-13	4-13	4-13	-	-	4-21
db8	1-7	3-11	4-13	5-14	4-14	5-15	5-14	5-14	-	-	4-23
db9	1-7	4-12	5-14	5-15	5-16	5-16	5-16	-	-	-	5-33
rbio1.3	2-5	2-7	2-9	2-9	2-9	2-9	2-8	2-8	2-6	-	1-8
rbio1.5	3-5	3-7	4-8	4-9	4-9	3-9	3-9	3-9	-	-	1-15
rbio2.2	1-13	2-21	2-27	2-34	2-31	2-28	2-16	2-9	2-6	-	2-9
rbio2.4	2-6	3-9	3-11	4-11	4-12	3-12	3-11	3-11	-	-	2-16
rbio2.6	3-5	4-9	4-11	5-11	5-12	5-12	5-12	4-11	-	-	2-18
rbio2.8	4-7	6-11	6-12	6-13	7-14	7-14	7-14	-	-	-	4-29
rbio3.1	2-215	2-370	2-212	2-107	2-55	2-29	2-16	2-9	2-6	2-4	1-5
rbio3.3	3-8	3-14	3-16	3-17	3-19	3-17	3-16	3-11	3-8	-	1-10
rbio3.5	4-7	4-10	4-12	4-12	4-12	4-13	4-12	4-12	-	-	1-17
rbio3.7	5-7	5-10	5-12	5-13	6-13	5-13	5-13	5-13	-	-	2-19
rbio3.9	6-9	6-12	7-14	7-15	8-15	7-15	7-15	-	-	-	3-31
rbio4.4	2-6	2-8	3-10	3-11	2-11	2-11	2-10	2-10	-	-	2-16
rbio5.5	2-6	3-9	3-10	3-11	3-11	3-11	3-11	2-10	-	-	3-17
rbio6.8	4-7	6-11	5-12	6-13	7-13	6-14	5-14	-	-	-	3-29
sym10	5-9	7-11	5-13	6-14	6-14	5-15	5-15	-	-	-	3-29
sym2	1-9	1-15	1-17	1-18	1-18	1-16	1-14	1-8	1-6	1-4	1-5
sym3	1-6	1-8	1-10	1-11	1-11	2-11	1-10	1-9	1-6	-	1-9
sym4	2-5	2-7	2-8	1-8	1-9	1-9	1-8	1-8	1-7	-	1-9
sym5	2-5	2-7	3-8	2-9	1-9	1-9	1-9	1-8	-	-	1-15
sym6	3-5	2-8	2-9	3-10	2-10	2-10	2-10	2-9	-	-	1-16
sym7	2-6	3-9	4-10	4-11	5-11	4-11	3-11	3-11	-	-	2-19
sym8	4-7	4-10	4-11	4-12	4-12	4-13	3-13	3-13	-	-	2-18
sym9	4-8	5-11	5-13	5-13	6-13	5-14	4-14	-	-	-	3-29

Tab. B-4: Coefficient bands for measurement configuration 4.

# Coefficient Bands in the Wavelet Domain

A=10000m <sup>2</sup> ; I=0.3A; gain=100x; t <sub>0</sub> =50μs; dt=5μs											
Wavelet	cD <sub>1</sub>	cD <sub>2</sub>	cD <sub>3</sub>	cD <sub>4</sub>	cD <sub>5</sub>	cD <sub>6</sub>	cD <sub>7</sub>	cD <sub>8</sub>	cD <sub>9</sub>	cD <sub>10</sub>	cA <sub>max</sub>
bior1.3	1-92	3-135	3-124	3-129	3-123	3-66	3-34	3-18	3-10	-	2-10
bior1.5	2-93	2-140	3-127	3-131	3-128	3-68	3-36	3-21	-	-	4-20
bior2.2	1-9	1-10	2-11	2-12	2-12	2-12	2-10	2-10	2-9	-	2-11
bior2.4	2-9	2-12	2-14	3-15	3-15	3-15	3-13	3-12	-	-	4-21
bior2.6	3-10	4-14	4-15	4-17	4-16	4-16	4-15	4-15	-	-	6-23
bior2.8	4-11	6-15	5-17	5-19	5-18	5-18	5-17	-	-	-	8-41
bior3.1	2-3	2-5	2-5	2-6	2-6	2-6	2-6	2-17	2-9	2-4	1-6
bior3.3	3-4	1-6	1-7	3-8	3-8	3-8	3-35	3-20	3-12	-	3-12
bior3.5	4-5	2-7	2-9	4-9	4-10	4-10	4-37	4-22	-	-	5-22
bior3.7	5-6	5-9	3-10	5-11	5-12	5-12	5-39	5-24	-	-	6-24
bior3.9	4-7	6-10	6-12	6-13	6-13	6-14	6-41	-	-	-	8-42
bior4.4	2-5	2-7	2-9	3-9	3-10	3-10	2-10	2-9	-	-	3-22
bior5.5	2-5	4-8	3-9	3-10	4-11	3-11	3-11	2-21	-	-	2-25
bior6.8	4-7	5-10	4-11	5-13	5-13	5-13	5-13	-	-	-	5-43
coif1	1-10	2-15	2-18	2-19	2-21	1-17	1-18	1-18	1-11	-	1-12
coif2	2-5	3-8	3-10	3-11	4-11	3-11	3-11	3-10	-	-	2-25
coif3	3-6	5-10	5-12	5-13	7-14	6-14	6-15	-	-	-	5-46
coif4	4-8	7-13	7-15	7-17	8-18	8-18	8-19	-	-	-	8-50
db10	1-7	4-13	6-16	6-17	6-18	6-18	6-18	-	-	-	7-50
db2	1-10	1-15	1-18	1-19	1-20	1-17	1-34	1-18	1-10	1-6	1-6
db3	1-6	1-9	1-11	1-11	1-12	2-12	1-10	1-19	1-11	-	1-12
db4	2-5	1-8	2-10	2-10	2-10	2-11	2-10	2-10	1-10	-	1-14
db5	1-5	2-8	2-10	2-11	3-11	2-12	2-11	2-20	-	-	2-24
db6	1-5	3-9	3-11	3-12	3-12	3-13	3-12	3-21	-	-	2-26
db7	1-6	3-10	3-12	4-13	4-14	4-14	4-13	4-22	-	-	4-28
db8	1-7	3-11	4-13	5-15	4-15	5-15	5-15	4-25	-	-	4-30
db9	1-7	4-12	5-15	5-16	5-16	6-17	5-16	-	-	-	5-48
rbio1.3	2-5	2-8	2-9	2-10	2-10	2-10	2-34	2-19	2-11	-	1-12
rbio1.5	3-5	3-7	4-9	4-9	4-10	4-10	3-36	3-21	-	-	1-23
rbio2.2	1-14	2-22	2-30	2-33	2-34	2-66	2-35	2-19	2-11	-	2-12
rbio2.4	2-6	3-9	3-11	4-12	4-12	3-13	3-12	3-11	-	-	2-23
rbio2.6	3-6	4-9	5-11	5-12	5-12	5-12	4-12	4-12	-	-	2-27
rbio2.8	4-7	6-11	6-13	6-14	7-14	7-14	7-14	-	-	-	4-44
rbio3.1	2-235	2-481	2-513	2-257	2-129	2-65	2-33	2-17	2-9	2-5	1-6
rbio3.3	3-9	3-14	3-16	3-19	3-19	3-68	3-36	3-20	3-12	-	1-14
rbio3.5	4-7	4-10	4-12	4-13	4-13	4-13	4-38	4-22	-	-	1-25
rbio3.7	5-7	5-11	5-13	6-14	6-14	5-14	5-39	5-24	-	-	2-28
rbio3.9	6-9	6-12	7-14	7-15	8-16	7-16	7-41	-	-	-	3-45
rbio4.4	2-6	2-9	3-10	3-11	3-11	2-12	2-11	2-10	-	-	2-23
rbio5.5	2-6	3-9	3-11	3-11	3-12	3-12	3-11	2-10	-	-	3-24
rbio6.8	4-7	6-11	5-13	5-14	6-14	6-14	5-14	-	-	-	4-44
sym10	5-9	5-11	5-14	6-15	6-16	6-16	5-16	-	-	-	3-44
sym2	1-10	1-15	1-18	1-19	1-20	1-17	1-34	1-18	1-10	1-6	1-6
sym3	1-6	1-9	1-11	1-11	1-12	2-12	1-10	1-19	1-11	-	1-12
sym4	2-5	2-7	2-8	1-9	1-9	1-9	1-9	1-8	1-12	-	1-13
sym5	2-5	2-7	3-8	2-9	2-9	1-9	1-9	1-20	-	-	1-23
sym6	3-6	2-8	2-9	3-10	2-10	2-10	2-10	2-22	-	-	1-24
sym7	2-6	4-9	3-10	4-11	4-12	3-12	3-38	3-23	-	-	2-27
sym8	4-7	4-10	4-11	4-12	4-13	4-13	3-13	2-24	-	-	2-26
sym9	4-8	5-11	5-13	5-13	6-14	5-14	4-14	-	-	-	3-43

Tab. B-5: Coefficient bands for measurement configuration 5.



A=10000m <sup>2</sup> ; I=0.3A; gain=1000x; t <sub>0</sub> =100μs; dt=50μs											
Wavelet	cD <sub>1</sub>	cD <sub>2</sub>	cD <sub>3</sub>	cD <sub>4</sub>	cD <sub>5</sub>	cD <sub>6</sub>	cD <sub>7</sub>	cD <sub>8</sub>	cD <sub>9</sub>	cD <sub>10</sub>	cA <sub>max</sub>
bior1.3	1-89	3-115	3-118	3-67	3-35	3-19	3-12	3-8	-	-	2-8
bior1.5	2-91	2-119	2-120	3-69	3-37	3-21	3-14	-	-	-	4-16
bior2.2	1-10	1-11	1-12	1-12	2-11	2-11	2-10	2-7	-	-	2-9
bior2.4	2-11	2-13	2-14	3-14	3-13	3-13	3-12	-	-	-	4-17
bior2.6	3-12	4-15	3-16	3-16	4-15	4-15	4-13	-	-	-	6-19
bior2.8	3-13	5-16	4-18	5-18	5-17	5-17	-	-	-	-	8-33
bior3.1	2-5	2-6	2-6	2-6	2-6	2-6	2-5	2-5	2-4	-	1-5
bior3.3	1-6	1-7	1-8	3-8	3-8	3-7	3-7	3-7	-	-	3-10
bior3.5	2-7	2-9	2-9	4-10	4-9	4-9	4-9	-	-	-	5-18
bior3.7	3-8	3-10	3-11	5-12	5-11	5-11	5-11	-	-	-	6-20
bior3.9	4-9	6-11	4-13	6-13	6-13	6-13	-	-	-	-	8-34
bior4.4	2-7	1-8	2-9	2-10	2-9	2-9	2-9	-	-	-	3-18
bior5.5	2-7	2-9	2-10	3-10	3-10	2-10	2-10	-	-	-	2-20
bior6.8	4-8	5-11	4-12	4-13	4-13	5-13	-	-	-	-	5-34
coif1	1-12	1-16	2-17	1-18	1-17	1-17	1-11	1-7	-	-	1-10
coif2	2-7	3-9	3-10	3-11	3-11	3-10	3-10	-	-	-	2-20
coif3	3-8	5-11	5-13	5-14	6-14	6-15	-	-	-	-	5-36
coif4	4-10	6-15	7-17	7-18	7-18	8-19	-	-	-	-	8-40
db10	1-10	4-14	5-16	6-17	5-18	5-18	-	-	-	-	5-41
db2	1-12	1-17	1-17	1-17	1-18	1-16	1-10	1-6	1-4	-	1-5
db3	1-8	1-10	1-11	1-11	1-11	1-11	1-10	1-7	-	-	1-10
db4	1-7	1-9	1-10	2-10	2-10	2-10	1-10	1-8	-	-	1-12
db5	1-7	2-9	2-11	2-11	2-11	2-10	2-10	-	-	-	2-20
db6	1-7	3-10	3-12	3-12	3-12	3-12	2-12	-	-	-	2-22
db7	1-8	3-11	3-13	3-13	4-13	3-13	3-13	-	-	-	3-24
db8	1-8	3-12	4-14	4-15	4-15	4-15	4-15	-	-	-	4-26
db9	1-9	3-13	5-15	4-16	4-16	4-16	-	-	-	-	5-39
rbio1.3	2-8	2-9	2-10	2-10	2-10	2-9	2-9	2-7	-	-	1-9
rbio1.5	3-7	3-8	4-9	4-10	3-9	3-9	3-9	-	-	-	1-18
rbio2.2	1-16	1-22	2-27	2-31	2-31	2-19	2-11	2-7	-	-	2-10
rbio2.4	2-8	3-10	3-12	3-12	3-12	3-11	3-11	-	-	-	2-19
rbio2.6	3-8	4-10	4-12	5-12	5-12	4-12	4-12	-	-	-	2-21
rbio2.8	4-9	6-12	6-13	6-14	7-14	7-14	-	-	-	-	3-35
rbio3.1	2-190	2-259	2-130	2-66	2-34	2-18	2-10	2-6	2-4	-	1-5
rbio3.3	3-11	3-15	3-17	3-17	3-18	3-18	3-12	3-9	-	-	1-12
rbio3.5	4-9	4-11	4-12	4-13	4-13	4-12	4-12	-	-	-	1-20
rbio3.7	5-9	5-12	5-13	5-14	5-14	5-13	5-13	-	-	-	2-22
rbio3.9	6-10	6-13	7-15	7-16	8-16	7-15	-	-	-	-	3-36
rbio4.4	2-8	2-10	2-11	3-11	2-11	2-10	2-10	-	-	-	2-18
rbio5.5	2-8	2-10	2-11	2-11	2-11	2-11	2-10	-	-	-	3-19
rbio6.8	4-9	5-12	4-13	5-14	5-14	5-14	-	-	-	-	3-35
sym10	4-10	4-14	4-15	5-15	5-16	4-16	-	-	-	-	3-35
sym2	1-12	1-17	1-17	1-17	1-18	1-16	1-10	1-6	1-4	-	1-5
sym3	1-8	1-10	1-11	1-11	1-11	1-11	1-10	1-7	-	-	1-10
sym4	1-7	1-8	1-9	1-9	1-9	1-8	1-8	1-7	-	-	1-11
sym5	1-7	2-8	2-9	2-9	1-9	1-9	1-9	-	-	-	1-18
sym6	2-7	2-9	2-10	3-10	2-10	2-10	2-10	-	-	-	1-19
sym7	2-8	3-10	3-11	3-12	3-12	3-12	3-12	-	-	-	2-21
sym8	3-9	4-11	4-11	3-13	4-13	3-13	2-13	-	-	-	2-21
sym9	3-9	4-12	3-13	4-14	5-14	4-14	-	-	-	-	2-34

Tab. B-6: Coefficient bands for measurement configuration 6.

# Coefficient Bands in the Wavelet Domain

A=10000m <sup>2</sup> ; I=3A; gain=1x; t <sub>0</sub> =100μs; dt=50μs											
Wavelet	cD <sub>1</sub>	cD <sub>2</sub>	cD <sub>3</sub>	cD <sub>4</sub>	cD <sub>5</sub>	cD <sub>6</sub>	cD <sub>7</sub>	cD <sub>8</sub>	cD <sub>9</sub>	cD <sub>10</sub>	cA <sub>max</sub>
bior1.3	1-65	3-44	3-24	3-14	3-9	-	-	-	-	-	2-10
bior1.5	2-68	2-45	2-25	3-16	-	-	-	-	-	-	4-18
bior2.2	1-12	1-10	1-10	1-9	2-8	-	-	-	-	-	2-10
bior2.4	2-13	2-12	2-12	2-12	-	-	-	-	-	-	4-19
bior2.6	3-13	4-14	3-14	3-13	-	-	-	-	-	-	6-21
bior2.8	3-14	5-15	4-16	-	-	-	-	-	-	-	8-37
bior3.1	2-6	2-6	2-6	2-5	2-5	2-4	-	-	-	-	1-6
bior3.3	1-7	1-8	1-7	3-7	3-7	-	-	-	-	-	2-11
bior3.5	2-8	2-9	2-9	4-9	-	-	-	-	-	-	4-20
bior3.7	3-9	3-11	3-11	5-11	-	-	-	-	-	-	6-22
bior3.9	4-10	6-12	4-12	-	-	-	-	-	-	-	8-38
bior4.4	2-7	1-9	2-9	2-9	-	-	-	-	-	-	3-20
bior5.5	2-7	2-9	2-10	3-10	-	-	-	-	-	-	2-22
bior6.8	4-9	4-11	4-12	-	-	-	-	-	-	-	5-38
coif1	1-13	1-14	1-14	1-12	1-8	-	-	-	-	-	1-11
coif2	2-7	3-10	2-10	3-10	-	-	-	-	-	-	3-23
coif3	3-8	4-11	4-13	-	-	-	-	-	-	-	5-40
coif4	4-11	6-14	6-16	-	-	-	-	-	-	-	9-44
db10	1-10	4-14	4-16	-	-	-	-	-	-	-	5-44
db2	1-13	1-14	1-14	1-11	1-7	1-5	-	-	-	-	1-6
db3	1-9	1-9	1-9	1-9	1-8	-	-	-	-	-	1-11
db4	1-7	1-9	1-9	2-9	2-8	-	-	-	-	-	1-13
db5	1-7	2-9	2-10	2-10	-	-	-	-	-	-	2-22
db6	1-8	3-10	2-11	3-11	-	-	-	-	-	-	3-24
db7	1-8	3-11	3-12	3-12	-	-	-	-	-	-	3-26
db8	1-9	3-12	4-13	3-14	-	-	-	-	-	-	5-27
db9	1-9	3-13	5-14	-	-	-	-	-	-	-	5-42
rbio1.3	2-8	2-9	2-9	2-8	2-7	-	-	-	-	-	1-11
rbio1.5	3-7	3-9	4-9	3-9	-	-	-	-	-	-	1-20
rbio2.2	1-15	1-20	1-21	2-13	2-8	-	-	-	-	-	1-11
rbio2.4	2-8	3-10	3-10	3-11	-	-	-	-	-	-	2-21
rbio2.6	3-8	4-11	4-11	4-11	-	-	-	-	-	-	3-23
rbio2.8	4-9	6-12	6-13	-	-	-	-	-	-	-	3-39
rbio3.1	2-83	2-43	2-23	2-13	2-7	2-5	-	-	-	-	1-6
rbio3.3	3-12	3-14	3-14	3-13	3-9	-	-	-	-	-	1-13
rbio3.5	4-9	4-11	4-11	4-11	-	-	-	-	-	-	1-22
rbio3.7	5-9	5-12	5-12	5-13	-	-	-	-	-	-	2-24
rbio3.9	6-11	6-13	6-14	-	-	-	-	-	-	-	2-40
rbio4.4	2-8	2-10	2-10	3-10	-	-	-	-	-	-	2-21
rbio5.5	2-9	2-10	2-10	2-10	-	-	-	-	-	-	3-22
rbio6.8	3-9	5-12	4-13	-	-	-	-	-	-	-	3-39
sym10	3-10	3-13	4-14	-	-	-	-	-	-	-	2-39
sym2	1-13	1-14	1-14	1-11	1-7	1-5	-	-	-	-	1-6
sym3	1-9	1-9	1-9	1-9	1-8	-	-	-	-	-	1-11
sym4	1-7	1-9	1-8	1-8	1-8	-	-	-	-	-	1-12
sym5	1-7	1-9	2-8	2-8	-	-	-	-	-	-	1-20
sym6	2-8	2-9	2-9	2-9	-	-	-	-	-	-	1-21
sym7	2-8	3-10	3-11	3-11	-	-	-	-	-	-	2-24
sym8	3-9	2-11	3-11	3-12	-	-	-	-	-	-	2-23
sym9	3-10	3-12	3-13	-	-	-	-	-	-	-	3-38

Tab. B-7: Coefficient bands for measurement configuration 7.

A=10000m <sup>2</sup> ; I=3A; gain=10x; t <sub>0</sub> =100μs; dt=50μs											
Wavelet	cD <sub>1</sub>	cD <sub>2</sub>	cD <sub>3</sub>	cD <sub>4</sub>	cD <sub>5</sub>	cD <sub>6</sub>	cD <sub>7</sub>	cD <sub>8</sub>	cD <sub>9</sub>	cD <sub>10</sub>	cA <sub>max</sub>
bior1.3	1-70	3-97	3-53	3-28	3-16	3-10	3-7	-	-	-	2-7
bior1.5	2-72	2-98	2-54	3-30	3-19	3-13	-	-	-	-	4-14
bior2.2	1-10	1-11	1-11	2-10	2-10	2-9	2-6	-	-	-	2-8
bior2.4	2-11	2-13	2-13	3-12	3-12	3-11	-	-	-	-	4-15
bior2.6	3-12	4-15	3-15	4-14	4-14	4-13	-	-	-	-	6-17
bior2.8	4-13	5-16	4-17	5-16	5-16	-	-	-	-	-	8-28
bior3.1	2-5	2-6	2-6	2-6	2-5	2-5	2-5	2-3	-	-	1-5
bior3.3	1-6	1-7	1-7	3-8	3-7	3-7	3-7	-	-	-	3-9
bior3.5	2-7	2-8	2-9	4-9	4-9	4-9	-	-	-	-	4-15
bior3.7	3-8	3-10	3-11	5-11	5-11	5-11	-	-	-	-	6-17
bior3.9	4-9	6-11	4-13	6-13	6-12	-	-	-	-	-	8-28
bior4.4	2-6	1-8	2-9	2-9	3-9	2-9	-	-	-	-	3-15
bior5.5	2-7	2-9	2-10	3-10	3-10	3-10	-	-	-	-	2-17
bior6.8	4-8	5-11	4-12	5-13	5-13	-	-	-	-	-	5-29
coif1	1-12	1-16	2-16	2-16	1-14	1-9	1-6	-	-	-	1-9
coif2	2-7	3-9	3-10	3-10	3-10	3-10	-	-	-	-	2-18
coif3	3-8	5-11	5-13	5-14	6-14	-	-	-	-	-	5-31
coif4	4-10	6-14	7-16	7-17	7-18	-	-	-	-	-	8-35
db10	1-10	4-14	5-16	6-17	5-17	-	-	-	-	-	7-36
db2	1-12	1-15	1-15	1-15	1-13	1-8	1-5	1-4	-	-	1-5
db3	1-8	1-10	1-11	1-10	1-10	2-9	1-6	-	-	-	1-9
db4	1-7	1-9	2-10	2-10	2-9	2-9	2-8	-	-	-	1-11
db5	1-7	2-9	2-10	2-10	2-10	2-10	-	-	-	-	2-17
db6	1-7	3-10	3-11	3-11	3-11	3-11	-	-	-	-	2-19
db7	1-8	3-11	3-12	3-13	4-13	3-13	-	-	-	-	4-21
db8	1-8	3-12	4-14	4-14	4-14	4-14	-	-	-	-	5-23
db9	1-9	3-13	5-15	4-15	4-16	-	-	-	-	-	5-34
rbio1.3	2-7	2-9	2-10	2-9	2-8	2-8	2-6	-	-	-	1-8
rbio1.5	3-7	3-8	4-9	4-9	3-9	3-9	-	-	-	-	1-16
rbio2.2	1-16	1-22	1-25	2-27	2-15	2-9	2-6	-	-	-	2-9
rbio2.4	2-8	3-10	3-11	3-11	3-11	3-11	-	-	-	-	2-16
rbio2.6	3-8	4-10	4-11	5-12	5-11	5-11	-	-	-	-	2-18
rbio2.8	4-9	6-12	6-13	6-14	7-13	-	-	-	-	-	4-30
rbio3.1	2-177	2-102	2-52	2-27	2-15	2-9	2-6	2-4	-	-	1-5
rbio3.3	3-11	3-15	3-16	3-16	3-15	3-11	3-8	-	-	-	1-10
rbio3.5	4-8	4-11	4-12	4-12	4-12	4-12	-	-	-	-	1-18
rbio3.7	5-9	5-12	5-13	5-13	5-13	5-13	-	-	-	-	2-19
rbio3.9	6-10	6-13	7-15	7-15	8-15	-	-	-	-	-	3-31
rbio4.4	2-8	2-10	3-11	3-10	2-10	2-10	-	-	-	-	2-16
rbio5.5	2-8	2-10	2-11	2-11	2-10	3-10	-	-	-	-	3-17
rbio6.8	4-9	5-12	5-13	5-13	5-13	-	-	-	-	-	3-30
sym10	4-10	4-13	4-14	5-15	5-15	-	-	-	-	-	3-30
sym2	1-12	1-15	1-15	1-15	1-13	1-8	1-5	1-4	-	-	1-5
sym3	1-8	1-10	1-11	1-10	1-10	2-9	1-6	-	-	-	1-9
sym4	1-7	1-8	1-9	1-8	1-8	1-8	1-7	-	-	-	1-9
sym5	2-7	2-8	2-9	2-9	2-8	1-8	-	-	-	-	1-15
sym6	2-7	2-9	2-10	2-10	2-9	2-9	-	-	-	-	1-16
sym7	2-8	3-10	3-11	3-11	3-11	3-11	-	-	-	-	2-19
sym8	3-9	2-11	4-11	3-12	4-12	3-13	-	-	-	-	2-18
sym9	3-9	4-12	4-13	4-14	5-14	-	-	-	-	-	3-29

Tab. B-8: Coefficient bands for measurement configuration 8.

# Coefficient Bands in the Wavelet Domain

A=10000m <sup>2</sup> ; I=3A; gain=100x; t <sub>0</sub> =100μs; dt=50μs											
Wavelet	cD <sub>1</sub>	cD <sub>2</sub>	cD <sub>3</sub>	cD <sub>4</sub>	cD <sub>5</sub>	cD <sub>6</sub>	cD <sub>7</sub>	cD <sub>8</sub>	cD <sub>9</sub>	cD <sub>10</sub>	cA <sub>max</sub>
bior1.3	1-90	3-103	3-109	3-63	3-34	3-19	3-11	3-7	-	-	2-8
bior1.5	2-93	2-107	2-114	3-66	3-36	3-21	3-14	-	-	-	4-16
bior2.2	1-12	1-12	1-12	1-12	2-12	2-10	2-9	2-7	-	-	2-9
bior2.4	2-13	2-14	2-14	2-14	3-14	3-12	3-11	-	-	-	4-17
bior2.6	3-14	4-16	3-16	3-16	4-16	4-15	4-13	-	-	-	6-19
bior2.8	3-15	5-17	4-18	4-18	5-18	5-17	-	-	-	-	8-33
bior3.1	2-6	2-6	2-6	2-6	2-6	2-6	2-5	2-5	2-4	-	1-5
bior3.3	1-7	1-8	1-8	3-8	3-8	3-8	3-7	3-7	-	-	3-10
bior3.5	2-8	2-9	2-10	4-10	4-10	4-10	4-9	-	-	-	5-18
bior3.7	3-9	3-11	3-11	5-11	5-12	5-12	5-11	-	-	-	6-20
bior3.9	4-10	6-12	4-13	6-13	6-14	6-13	-	-	-	-	8-34
bior4.4	2-7	1-9	2-10	2-10	2-10	2-9	2-9	-	-	-	3-18
bior5.5	2-7	2-9	2-10	3-11	3-11	2-10	2-10	-	-	-	2-20
bior6.8	4-8	4-11	3-12	4-13	4-13	4-13	-	-	-	-	5-34
coif1	1-14	1-17	1-19	1-18	1-17	1-17	1-10	1-7	-	-	1-10
coif2	2-7	3-10	3-11	3-11	3-11	3-10	3-10	-	-	-	2-20
coif3	3-9	4-12	4-14	4-14	6-14	6-15	-	-	-	-	5-36
coif4	4-11	6-15	6-17	7-18	6-19	7-19	-	-	-	-	7-40
db10	1-10	4-15	4-17	5-18	5-18	5-18	-	-	-	-	6-41
db2	1-14	1-17	1-19	1-19	1-16	1-16	1-9	1-6	1-4	-	1-5
db3	1-9	1-11	1-11	1-12	1-12	1-10	1-9	1-7	-	-	1-10
db4	1-7	1-9	1-11	2-10	2-11	1-10	1-9	1-8	-	-	1-12
db5	1-7	2-10	2-11	2-11	2-11	2-11	2-10	-	-	-	2-20
db6	1-8	3-11	2-12	3-12	3-12	2-12	2-12	-	-	-	2-22
db7	1-8	3-11	3-13	3-13	4-14	3-13	3-13	-	-	-	3-24
db8	1-9	3-12	4-14	4-15	4-15	4-15	3-14	-	-	-	3-26
db9	1-9	3-14	5-15	4-16	4-16	4-16	-	-	-	-	4-39
rbio1.3	2-8	2-10	2-10	2-10	2-10	2-9	2-8	2-6	-	-	1-9
rbio1.5	3-7	3-9	4-10	3-10	3-10	3-9	3-9	-	-	-	1-18
rbio2.2	1-18	1-25	2-29	2-29	2-26	2-18	2-10	2-7	-	-	2-10
rbio2.4	2-8	3-11	3-12	3-12	3-12	3-11	3-11	-	-	-	2-19
rbio2.6	3-8	4-11	4-12	4-12	5-12	4-12	4-12	-	-	-	2-21
rbio2.8	4-9	6-12	6-14	6-14	7-14	7-14	-	-	-	-	3-35
rbio3.1	2-189	2-245	2-124	2-63	2-33	2-18	2-10	2-6	2-4	-	1-5
rbio3.3	3-12	3-16	3-17	3-18	3-17	3-16	3-12	3-8	-	-	1-12
rbio3.5	4-9	4-12	4-13	4-13	4-13	4-12	4-12	-	-	-	1-20
rbio3.7	5-9	5-12	5-14	5-14	5-14	5-13	5-13	-	-	-	1-22
rbio3.9	6-11	6-14	6-15	6-16	8-16	7-15	-	-	-	-	3-36
rbio4.4	2-8	2-11	2-11	3-11	2-11	2-10	2-10	-	-	-	2-18
rbio5.5	2-9	2-11	2-11	2-11	2-11	2-11	2-10	-	-	-	3-19
rbio6.8	3-9	5-12	4-14	5-14	5-14	5-14	-	-	-	-	3-35
sym10	4-10	4-14	4-15	4-16	5-16	4-16	-	-	-	-	2-35
sym2	1-14	1-17	1-19	1-19	1-16	1-16	1-9	1-6	1-4	-	1-5
sym3	1-9	1-11	1-11	1-12	1-12	1-10	1-9	1-7	-	-	1-10
sym4	1-7	1-9	1-9	1-9	1-9	1-9	1-8	1-7	-	-	1-11
sym5	1-7	1-9	2-9	2-9	2-9	1-9	1-9	-	-	-	1-18
sym6	2-8	2-9	2-10	3-10	2-10	2-10	2-10	-	-	-	1-19
sym7	2-8	3-10	3-11	3-12	3-12	3-12	2-12	-	-	-	2-21
sym8	3-9	3-11	3-12	3-13	4-13	2-13	2-13	-	-	-	2-21
sym9	3-10	3-12	3-14	4-14	5-14	4-14	-	-	-	-	3-34

Tab. B-9: Coefficient bands for measurement configuration 9.

A=10000m <sup>2</sup> ; I=3A; gain=1000x; t <sub>0</sub> =100μs; dt=50μs											
Wavelet	cD <sub>1</sub>	cD <sub>2</sub>	cD <sub>3</sub>	cD <sub>4</sub>	cD <sub>5</sub>	cD <sub>6</sub>	cD <sub>7</sub>	cD <sub>8</sub>	cD <sub>9</sub>	cD <sub>10</sub>	cA <sub>max</sub>
bior1.3	1-95	3-130	3-135	3-127	3-106	3-54	3-29	3-16	3-10	-	2-10
bior1.5	2-100	2-133	2-137	3-130	3-108	3-56	3-31	3-18	-	-	4-19
bior2.2	1-11	1-12	1-13	1-13	2-12	2-12	2-11	2-10	2-9	-	2-11
bior2.4	2-12	2-14	2-15	3-15	3-15	3-14	3-13	3-13	-	-	4-20
bior2.6	3-13	4-16	3-17	3-17	4-16	4-16	4-15	4-15	-	-	6-22
bior2.8	3-14	5-17	4-19	5-19	5-19	5-19	5-17	-	-	-	8-39
bior3.1	2-5	2-6	2-6	2-6	2-6	2-6	2-6	2-6	2-5	2-4	1-6
bior3.3	1-6	1-7	1-8	3-8	3-8	3-8	3-8	3-8	3-7	-	3-12
bior3.5	2-7	2-9	2-10	4-10	4-10	4-10	4-10	4-9	-	-	5-21
bior3.7	3-8	3-10	3-11	5-12	5-12	5-12	5-12	5-11	-	-	7-23
bior3.9	4-9	6-12	4-13	6-13	6-14	6-14	6-14	-	-	-	8-40
bior4.4	2-7	2-8	2-9	2-10	2-10	2-10	2-10	2-9	-	-	3-21
bior5.5	2-7	2-9	2-10	3-11	3-11	2-11	2-11	2-10	-	-	2-23
bior6.8	4-8	4-11	4-12	5-13	5-13	5-13	4-13	-	-	-	5-41
coif1	1-13	1-16	1-19	1-20	1-19	1-18	1-18	1-15	1-9	-	1-11
coif2	2-7	3-9	3-11	3-11	3-11	3-11	3-11	3-11	-	-	2-24
coif3	3-8	4-11	4-13	4-15	6-15	6-15	5-15	-	-	-	4-42
coif4	4-11	6-14	6-17	7-18	7-19	7-20	7-20	-	-	-	7-46
db10	1-10	4-14	4-17	6-18	5-18	5-18	6-18	-	-	-	6-47
db2	1-13	1-17	1-20	1-20	1-19	1-18	1-16	1-14	1-8	1-6	1-6
db3	1-8	1-10	1-12	1-12	1-12	1-11	1-11	1-10	1-9	-	1-12
db4	1-7	1-9	1-11	2-11	2-11	1-10	1-10	1-10	1-9	-	1-14
db5	1-7	2-10	2-11	2-11	2-12	2-11	2-11	2-11	-	-	2-23
db6	1-7	3-10	2-12	3-12	3-13	3-12	2-12	2-12	-	-	2-25
db7	1-8	3-11	3-13	3-14	3-14	3-14	3-14	3-13	-	-	2-27
db8	1-8	3-12	4-14	4-15	4-15	4-15	4-15	3-15	-	-	3-29
db9	1-9	3-13	5-15	5-16	4-17	4-17	5-17	-	-	-	4-45
rbio1.3	2-8	2-9	2-10	2-10	2-10	2-10	2-9	2-9	2-8	-	1-11
rbio1.5	3-7	3-8	4-10	3-10	3-10	3-10	3-10	3-9	-	-	1-21
rbio2.2	2-17	2-26	2-33	2-34	2-35	2-37	2-28	2-16	2-10	-	2-12
rbio2.4	3-8	3-11	3-12	3-13	3-13	3-12	3-12	3-11	-	-	2-22
rbio2.6	4-8	4-10	4-12	5-12	5-13	4-12	4-12	4-12	-	-	2-24
rbio2.8	5-9	6-12	6-13	6-14	7-14	7-14	6-14	-	-	-	3-41
rbio3.1	2-232	2-457	2-416	2-209	2-106	2-54	2-28	2-15	2-9	2-5	1-6
rbio3.3	3-11	3-16	3-18	3-20	3-20	3-19	3-19	3-16	3-11	-	1-13
rbio3.5	4-9	4-11	4-13	4-13	4-14	4-13	4-13	4-12	-	-	1-23
rbio3.7	5-10	5-12	5-13	5-14	5-14	5-14	5-14	5-13	-	-	1-25
rbio3.9	6-11	6-14	6-15	7-16	8-16	7-16	6-16	-	-	-	3-42
rbio4.4	2-8	2-10	2-11	3-11	2-12	2-11	2-11	2-10	-	-	2-22
rbio5.5	2-9	2-10	2-11	2-12	2-12	2-11	2-11	2-10	-	-	3-23
rbio6.8	4-9	5-12	4-13	5-14	5-14	5-14	5-14	-	-	-	3-41
sym10	4-10	4-13	4-15	5-16	5-16	4-16	4-16	-	-	-	3-41
sym2	1-13	1-17	1-20	1-20	1-19	1-18	1-16	1-14	1-8	1-6	1-6
sym3	1-8	1-10	1-12	1-12	1-12	1-11	1-11	1-10	1-9	-	1-12
sym4	1-7	1-8	1-9	1-9	1-10	1-9	1-9	1-9	1-8	-	1-12
sym5	1-7	1-8	2-9	2-9	2-10	1-9	1-9	1-9	-	-	1-22
sym6	2-7	2-9	2-10	3-11	2-11	2-11	2-10	1-10	-	-	1-22
sym7	2-8	3-10	3-11	3-12	3-12	3-12	2-12	2-12	-	-	2-25
sym8	3-9	2-11	3-12	3-13	4-13	3-13	2-13	2-13	-	-	2-24
sym9	3-9	3-12	3-13	4-14	5-15	4-15	3-15	-	-	-	2-41

Tab. B-10: Coefficient bands for measurement configuration 10.

# Coefficient Bands in the Wavelet Domain

A=10000m <sup>2</sup> ; I=10A; gain=1000x; t <sub>0</sub> =100μs; dt=50μs											
Wavelet	cD <sub>1</sub>	cD <sub>2</sub>	cD <sub>3</sub>	cD <sub>4</sub>	cD <sub>5</sub>	cD <sub>6</sub>	cD <sub>7</sub>	cD <sub>8</sub>	cD <sub>9</sub>	cD <sub>10</sub>	cA <sub>max</sub>
bior1.3	1-87	3-124	3-147	3-139	3-125	3-66	3-34	3-18	3-10	-	2-10
bior1.5	2-90	2-127	2-151	3-142	3-131	3-68	3-36	3-21	-	-	4-20
bior2.2	1-10	1-11	1-12	2-12	2-12	2-12	2-12	2-11	2-10	-	2-11
bior2.4	2-11	2-13	2-14	3-14	3-14	3-14	3-14	3-13	-	-	4-21
bior2.6	3-12	4-15	3-16	4-16	4-17	4-16	4-17	4-15	-	-	6-23
bior2.8	4-13	5-16	4-18	5-18	5-19	5-18	5-19	-	-	-	8-41
bior3.1	2-5	2-6	2-6	2-6	2-6	2-6	2-6	2-17	2-9	2-4	1-6
bior3.3	1-6	1-7	1-7	3-8	3-8	3-8	3-35	3-20	3-12	-	3-12
bior3.5	2-7	2-8	2-9	4-10	4-10	4-10	4-37	4-22	-	-	5-22
bior3.7	3-8	3-10	5-11	5-11	5-12	5-12	5-39	5-24	-	-	7-24
bior3.9	4-9	6-11	6-13	6-13	6-14	6-14	6-41	-	-	-	9-42
bior4.4	2-6	2-8	2-9	2-10	3-10	2-10	2-10	2-10	-	-	3-22
bior5.5	2-7	2-9	2-10	3-10	3-11	3-11	2-11	2-21	-	-	2-25
bior6.8	4-8	5-11	4-12	5-13	5-13	5-13	4-14	-	-	-	5-43
coif1	1-12	1-16	2-18	2-19	2-19	1-20	1-18	1-18	1-11	-	1-12
coif2	2-7	3-9	3-10	3-11	3-11	3-11	3-11	3-11	-	-	2-25
coif3	3-8	5-11	5-13	5-14	6-14	6-15	5-15	-	-	-	5-46
coif4	4-10	7-14	7-17	7-18	7-19	8-20	7-20	-	-	-	7-50
db10	1-8	4-14	5-16	6-18	5-18	5-18	6-18	-	-	-	6-50
db2	1-12	1-17	1-18	1-20	1-19	1-19	1-34	1-18	1-10	1-6	1-6
db3	1-8	1-10	1-11	1-11	1-12	2-11	1-12	1-19	1-11	-	1-12
db4	1-7	1-9	2-10	2-10	2-11	2-11	2-11	1-10	1-10	-	1-14
db5	1-7	2-9	2-10	2-11	2-11	2-11	2-11	2-20	-	-	1-24
db6	1-7	3-10	3-11	3-12	3-12	3-12	2-12	2-21	-	-	2-26
db7	1-8	3-11	3-13	3-13	4-14	3-14	4-14	3-22	-	-	3-28
db8	1-8	3-12	4-14	4-15	4-15	4-15	4-15	3-25	-	-	3-30
db9	1-9	4-13	5-15	4-16	4-17	4-17	5-17	-	-	-	4-48
rbio1.3	2-7	2-9	2-10	2-10	2-10	2-10	2-34	2-19	2-11	-	1-12
rbio1.5	3-7	3-8	4-9	4-10	3-10	3-10	3-36	3-21	-	-	1-22
rbio2.2	2-16	2-25	2-30	2-34	2-40	2-66	2-35	2-19	2-11	-	2-12
rbio2.4	3-8	3-10	3-11	3-12	3-12	3-12	3-12	3-12	-	-	2-23
rbio2.6	4-8	4-10	4-11	5-12	5-12	4-12	4-12	4-12	-	-	2-27
rbio2.8	5-9	6-12	6-13	6-14	7-14	7-14	6-14	-	-	-	3-44
rbio3.1	2-228	2-473	2-513	2-257	2-129	2-65	2-33	2-17	2-9	2-5	1-6
rbio3.3	3-11	3-15	3-17	3-19	3-19	3-68	3-36	3-20	3-12	-	1-14
rbio3.5	4-8	4-11	4-12	4-13	4-13	4-13	4-38	4-22	-	-	1-25
rbio3.7	5-9	5-12	5-13	5-14	5-14	5-14	5-39	5-24	-	-	2-28
rbio3.9	6-10	6-13	7-15	7-16	8-16	7-16	7-41	-	-	-	3-46
rbio4.4	2-8	2-10	3-11	3-11	2-11	2-11	2-11	2-11	-	-	2-23
rbio5.5	2-8	2-10	2-11	3-11	2-11	2-11	2-11	2-11	-	-	3-24
rbio6.8	4-9	6-12	5-13	5-14	5-14	5-14	5-14	-	-	-	3-44
sym10	4-10	4-13	4-15	5-15	5-16	4-16	4-16	-	-	-	3-44
sym2	1-12	1-17	1-18	1-20	1-19	1-19	1-34	1-18	1-10	1-6	1-6
sym3	1-8	1-10	1-11	1-11	1-12	2-11	1-12	1-19	1-11	-	1-12
sym4	2-7	1-8	1-9	1-9	1-9	1-9	1-9	1-9	1-12	-	1-13
sym5	2-7	2-8	2-9	2-9	2-9	1-9	1-9	1-20	-	-	1-23
sym6	2-7	2-9	2-10	3-10	2-10	2-10	2-10	1-22	-	-	1-24
sym7	2-8	3-10	3-11	3-12	3-12	3-12	3-38	2-23	-	-	2-27
sym8	4-9	2-11	4-11	3-13	4-13	3-13	3-13	2-24	-	-	2-26
sym9	3-9	4-12	4-13	4-14	5-14	4-15	4-15	-	-	-	2-43

Tab. B-11: Coefficient bands for measurement configuration 11.

A=10000m <sup>2</sup> ; I=20A; gain=1000x; t <sub>0</sub> =100μs; dt=50μs											
Wavelet	cD <sub>1</sub>	cD <sub>2</sub>	cD <sub>3</sub>	cD <sub>4</sub>	cD <sub>5</sub>	cD <sub>6</sub>	cD <sub>7</sub>	cD <sub>8</sub>	cD <sub>9</sub>	cD <sub>10</sub>	cA <sub>max</sub>
bior1.3	2-94	3-137	3-155	3-152	3-129	3-66	3-34	3-18	3-10	-	2-10
bior1.5	2-95	2-141	2-158	3-154	3-131	3-68	3-36	3-21	-	-	4-20
bior2.2	2-11	2-11	2-12	2-12	2-13	2-13	2-12	2-12	2-10	-	3-11
bior2.4	2-11	2-13	2-14	3-15	3-15	3-15	3-15	3-13	-	-	4-21
bior2.6	3-12	4-15	3-16	3-16	4-17	4-17	4-17	4-15	-	-	6-23
bior2.8	3-13	5-16	4-18	5-18	5-19	5-19	5-19	-	-	-	8-41
bior3.1	2-5	2-6	2-6	2-6	2-6	2-6	2-6	2-17	2-9	2-4	1-6
bior3.3	3-6	3-7	3-8	3-8	3-8	3-8	3-35	3-20	3-12	-	3-12
bior3.5	2-7	2-8	2-9	4-10	4-10	4-10	4-37	4-22	-	-	5-22
bior3.7	3-8	3-10	3-11	5-11	5-12	5-12	5-39	5-24	-	-	7-24
bior3.9	4-9	6-11	4-13	6-13	6-14	6-14	6-41	-	-	-	8-42
bior4.4	2-6	2-8	2-9	2-10	2-10	2-10	2-10	2-10	-	-	3-23
bior5.5	3-7	2-9	2-10	3-10	3-11	2-11	2-11	2-21	-	-	2-25
bior6.8	4-8	4-11	4-12	4-13	4-13	5-13	5-14	-	-	-	5-44
coif1	2-12	1-15	1-18	1-20	1-21	1-21	1-19	1-19	1-11	-	1-12
coif2	2-7	3-9	3-11	3-11	3-11	3-11	3-11	3-11	-	-	2-25
coif3	3-8	5-11	4-13	4-14	6-14	6-15	5-15	-	-	-	4-46
coif4	4-11	6-15	7-17	7-18	7-19	8-20	7-20	-	-	-	7-50
db10	2-10	4-14	5-17	6-18	5-18	5-19	6-19	-	-	-	6-50
db2	2-12	1-17	1-18	1-19	1-20	1-20	1-34	1-18	1-10	1-6	1-6
db3	2-8	1-10	1-11	1-11	1-12	1-12	1-12	1-19	1-11	-	1-12
db4	2-7	1-9	1-10	2-10	2-11	2-11	1-11	1-11	1-10	-	1-14
db5	2-7	2-10	2-11	2-11	2-11	2-12	2-12	2-20	-	-	1-24
db6	2-7	3-10	3-12	3-12	3-12	2-13	2-13	2-21	-	-	2-26
db7	2-8	3-11	3-13	3-13	3-14	3-14	3-14	3-22	-	-	2-28
db8	2-8	3-12	4-14	4-15	4-15	4-15	4-16	3-25	-	-	4-30
db9	2-9	3-13	5-15	5-16	5-17	4-17	5-39	-	-	-	5-48
rbio1.3	3-7	2-9	2-10	2-10	2-10	2-10	2-34	2-19	2-11	-	1-12
rbio1.5	4-7	3-8	4-9	4-10	3-10	3-10	3-36	3-21	-	-	1-23
rbio2.2	3-17	2-24	2-31	2-38	2-40	2-66	2-35	2-19	2-11	-	2-12
rbio2.4	4-8	3-10	3-12	3-12	3-13	3-13	3-13	3-12	-	-	2-23
rbio2.6	5-8	4-10	4-12	5-12	5-12	4-13	4-13	4-12	-	-	2-27
rbio2.8	6-9	6-12	6-13	6-14	7-14	7-14	6-15	-	-	-	3-44
rbio3.1	2-250	2-512	2-513	2-257	2-129	2-65	2-33	2-17	2-9	2-5	1-6
rbio3.3	3-11	3-15	3-17	3-19	3-20	3-68	3-36	3-20	3-12	-	1-14
rbio3.5	4-9	4-11	4-13	4-13	4-13	4-14	4-38	4-22	-	-	1-25
rbio3.7	5-9	5-12	5-13	5-14	5-14	5-14	5-39	5-24	-	-	1-28
rbio3.9	6-10	6-13	7-15	7-16	8-16	7-16	7-41	-	-	-	3-45
rbio4.4	3-7	2-10	2-11	3-11	2-12	2-12	2-12	2-11	-	-	2-23
rbio5.5	2-8	2-10	2-11	3-11	2-12	2-12	2-12	2-11	-	-	3-24
rbio6.8	4-9	5-12	5-13	5-14	5-14	5-14	5-14	-	-	-	3-44
sym10	4-10	4-13	4-15	4-16	5-16	4-16	4-16	-	-	-	3-44
sym2	2-12	1-17	1-18	1-19	1-20	1-20	1-34	1-18	1-10	1-6	1-6
sym3	2-8	1-10	1-11	1-11	1-12	1-12	1-12	1-19	1-11	-	1-12
sym4	2-7	1-8	1-9	1-9	1-9	1-9	1-9	1-20	1-12	-	1-13
sym5	2-7	2-8	2-9	2-9	2-9	1-10	1-10	1-20	-	-	1-23
sym6	2-7	2-9	2-10	3-10	2-10	2-11	2-11	1-22	-	-	1-24
sym7	2-8	3-10	3-11	3-12	4-12	3-12	3-38	2-23	-	-	2-27
sym8	3-9	3-11	3-11	3-13	4-13	2-13	2-14	2-24	-	-	1-26
sym9	3-9	3-12	4-13	4-14	5-15	4-15	4-15	-	-	-	2-43

Tab. B-12: Coefficient bands for measurement configuration 12.





## Appendix C

### Data Fits & Additional Inversion Results

This appendix summarizes additional information about the modeling and inversion results. For better visibility and comparability, all measured and calculated transients are not displayed in terms of their normalized voltage, but rather as late time apparent resistivities. The standard deviations of the processed measurements is generally very small ( $<1\%$ ) and may slightly exceed 10% at the latest times in each measurement only. Therefore, the associated error bars are usually minute and are not displayed.

#### C.1 Jingsutu Structure

Data fits for the 1D smooth inversions along Profile N are summarized in Fig. C-1. At each station, all runs were inverted simultaneously. Measurements at most stations were conducted with different current amplitudes and, thus, varying ramp times (s. chap. A.3.2, p. 144). This leads to deviations of the according runs, which is especially significant at early times (e.g. 1900m in Fig. C-1).

Inversion results for the 1D smooth inversions along Profile S are summarized in Fig. C-1. The deviations caused by varying ramp times are less pronounced along this profile, because measurements were just carried out with Gain 1 and Gain 1000 and the according transients only have a small overlap along the time axis.

The section of models according to the 1D block inversions along Profile N is depicted in Fig. C-3. Several westward dipping boundaries are indicated by dashed lines. The angles of inclination for possible interfaces (dashed lines) are about  $3-5^\circ$  and  $15-22^\circ$  for the shallow and deeply dipping interfaces, respectively. These inclinations have to be considered rough estimates, since they are subjective to a certain degree and depend on the interpreters choice of interfaces. The resulting data fits of the 1D block inversions are approximately similar to the fits of the 1D smooth inversion (Fig. C-1). Therefore, they are not depicted separately.

Final results for the 2.5D modeling of transients measured along Profile N are summarized in Fig. C-4. The 2.5D modeling was performed in comparison to 1D reference transients, which were calculated by using the 1D models of the 1D smooth inversion for forward calculations with *TEMIDmod*. In the forward calculations all parameters, which depend on the acquisition or the measurement device - i.e. ramp time, internal lowpass filter, and repetition frequency of the transmitter - were excluded or set to zero. Therefore, Fig. C-4 and Fig. C-1 are not directly comparable.

## Data Fits & Additional Inversion Results

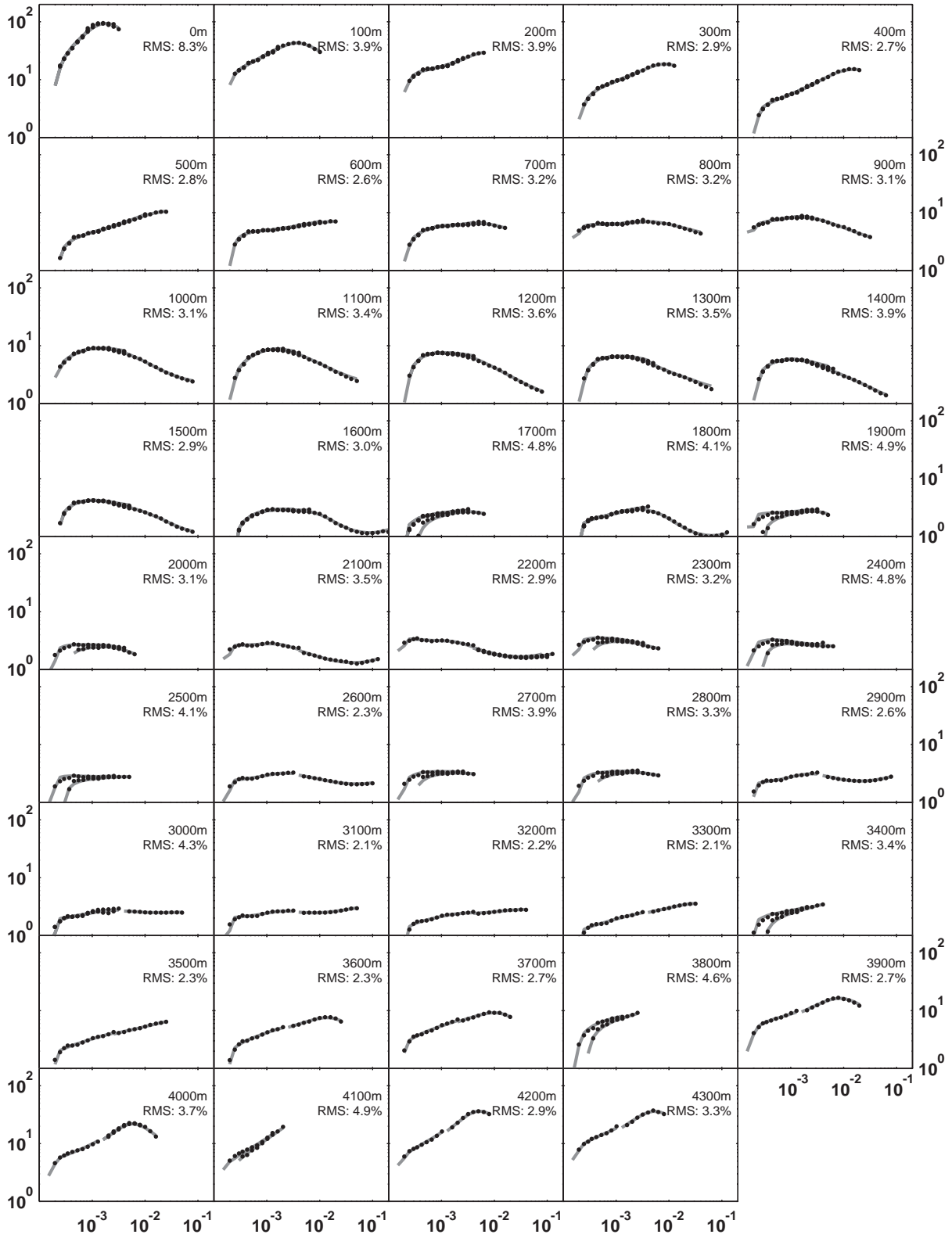


*Fig. C-1:* Final results of the 1D smooth inversion along Profile N in the Jingsutu Structure. Measured runs (dotted lines) and inversion result (gray lines) are displayed as late time apparent resistivities. All axes share the same x- and y-limits.

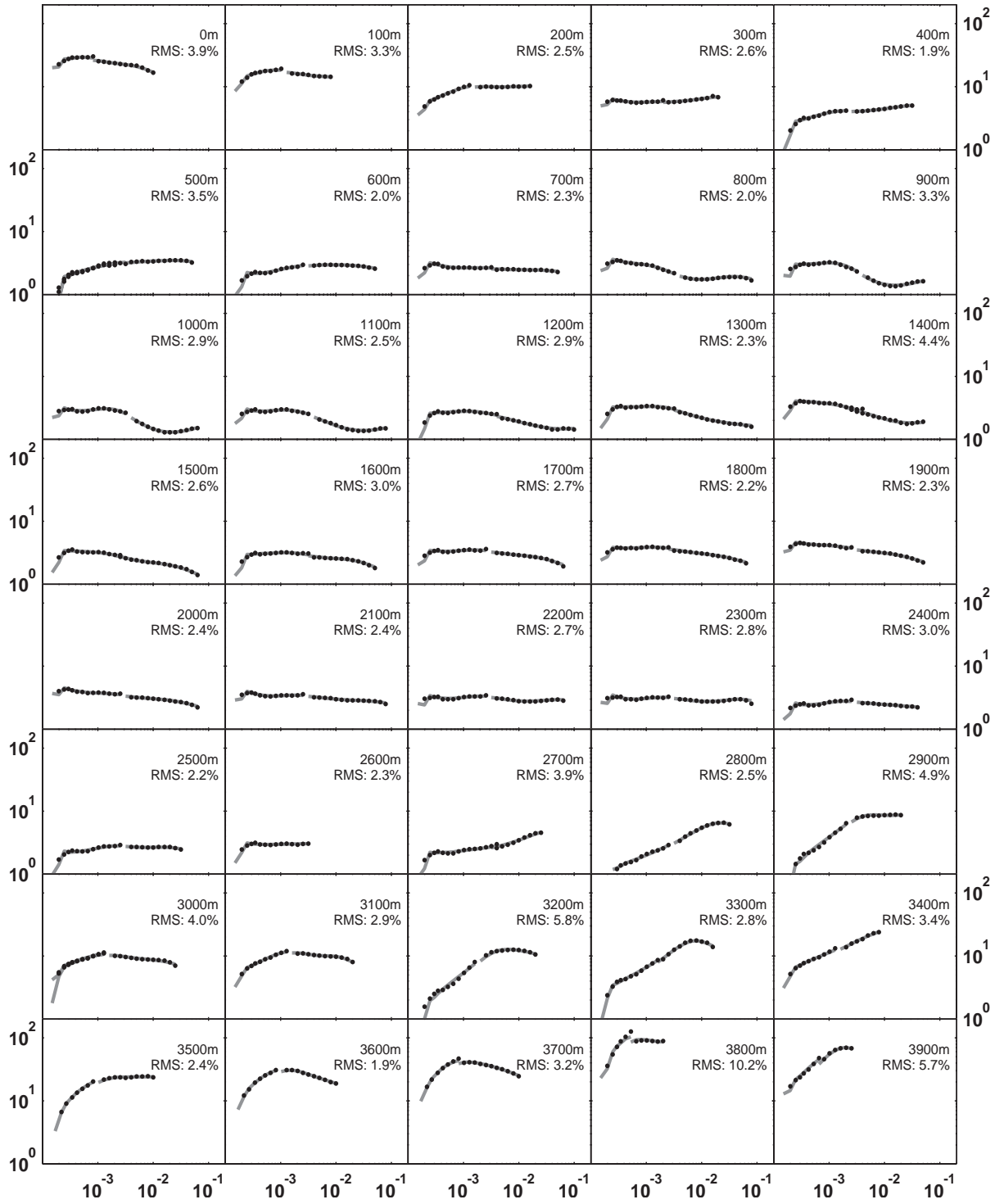
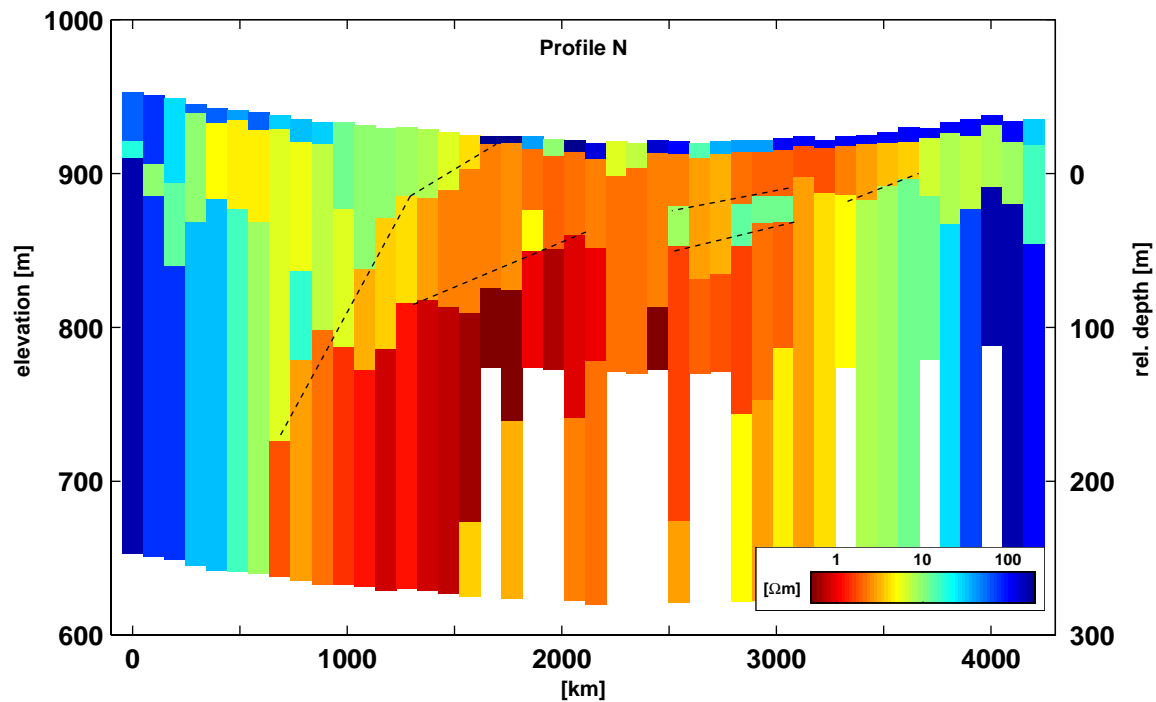


Fig. C-2: Final results of the 1D smooth inversion along Profile S in the Jingsutu Structure. Measured runs (dotted lines) and inversion result (gray lines) are displayed as late time apparent resistivities. All axes share the same x- and y-limits.



*Fig. C-3:* Models of 1D block inversions displayed as section along Profile N (s. Fig. 4-16, p. 95). The models are plotted with respect to the true elevation of stations. The vertical exaggeration of the section is about 7:1. Several westward dipping boundaries are indicated by dashed lines.

## C.2 Gurinai Structure

On the following pages the results of the Joint 1D inversion are summarized.

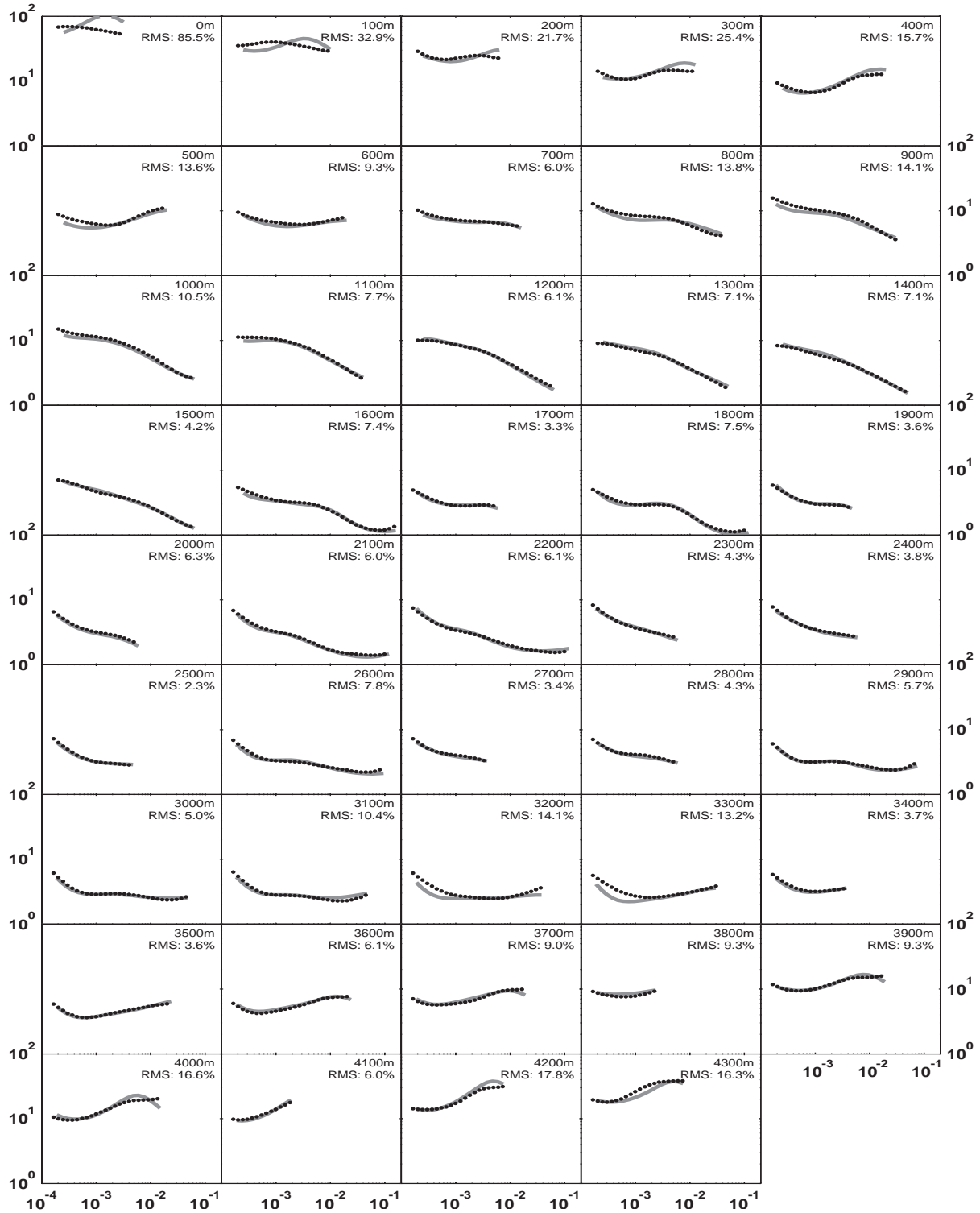


*Fig. C-4:* Final results of 2.5D modeling along Profile N in the Jingsutu Structure. Modeling results (dotted lines) are displayed together with reference transients referring to the models of the 1D smooth inversion (gray lines) as late time apparent resistivities. Note that because all acquisition-dependent parameters (e.g. ramp time) are removed from the reference transients, this figure may not directly be compared with Fig. C-1. All axes share the same x- and y-limits.

## Data Fits & Additional Inversion Results

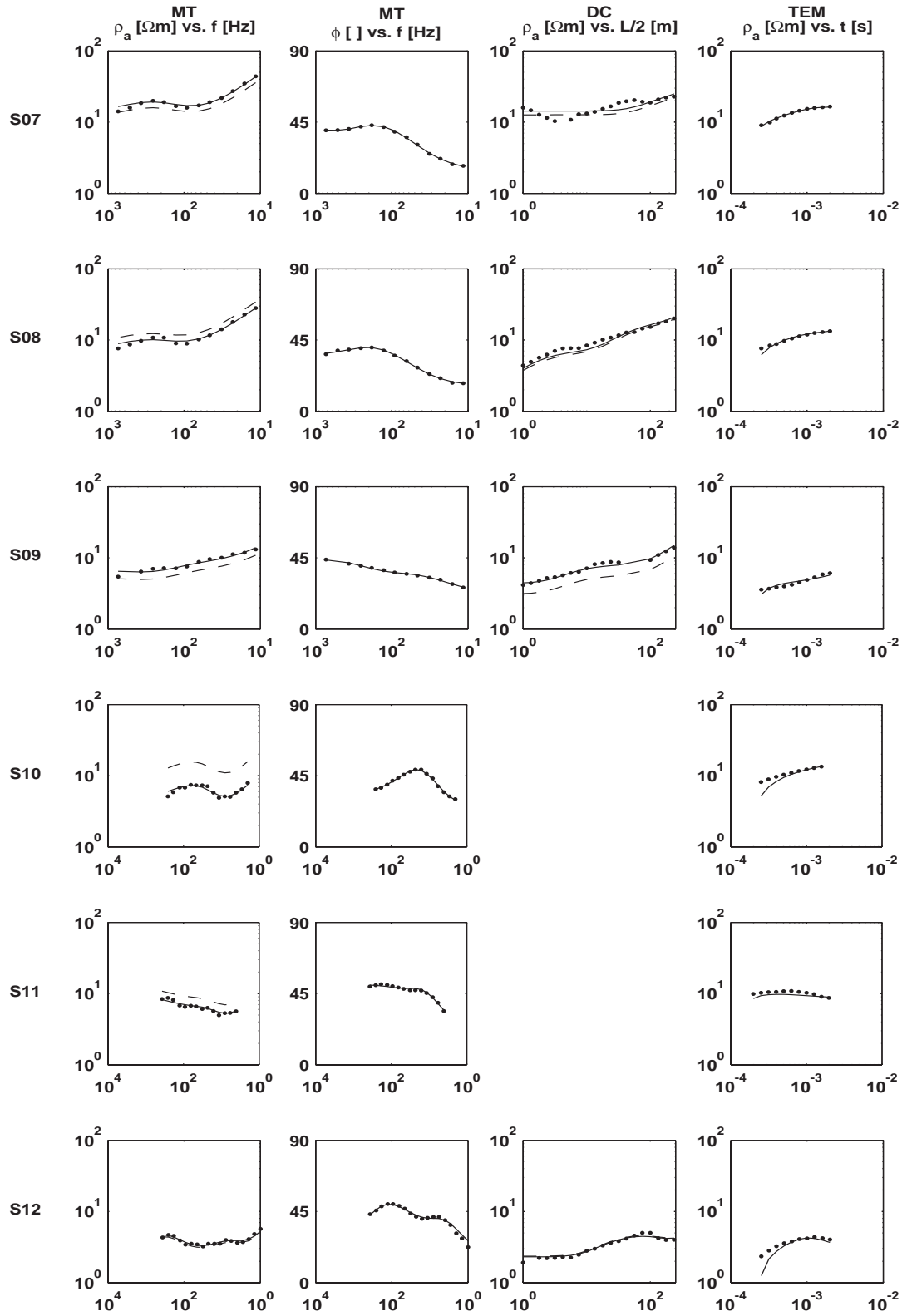


Fig. C-5: Data fits of the 1D joint inversion of MT-, DC- and TEM-data at stations S07-S12 in the Gurinai Structure (comp. Fig. C-7). At stations S10 & S11 no DC data was measured.

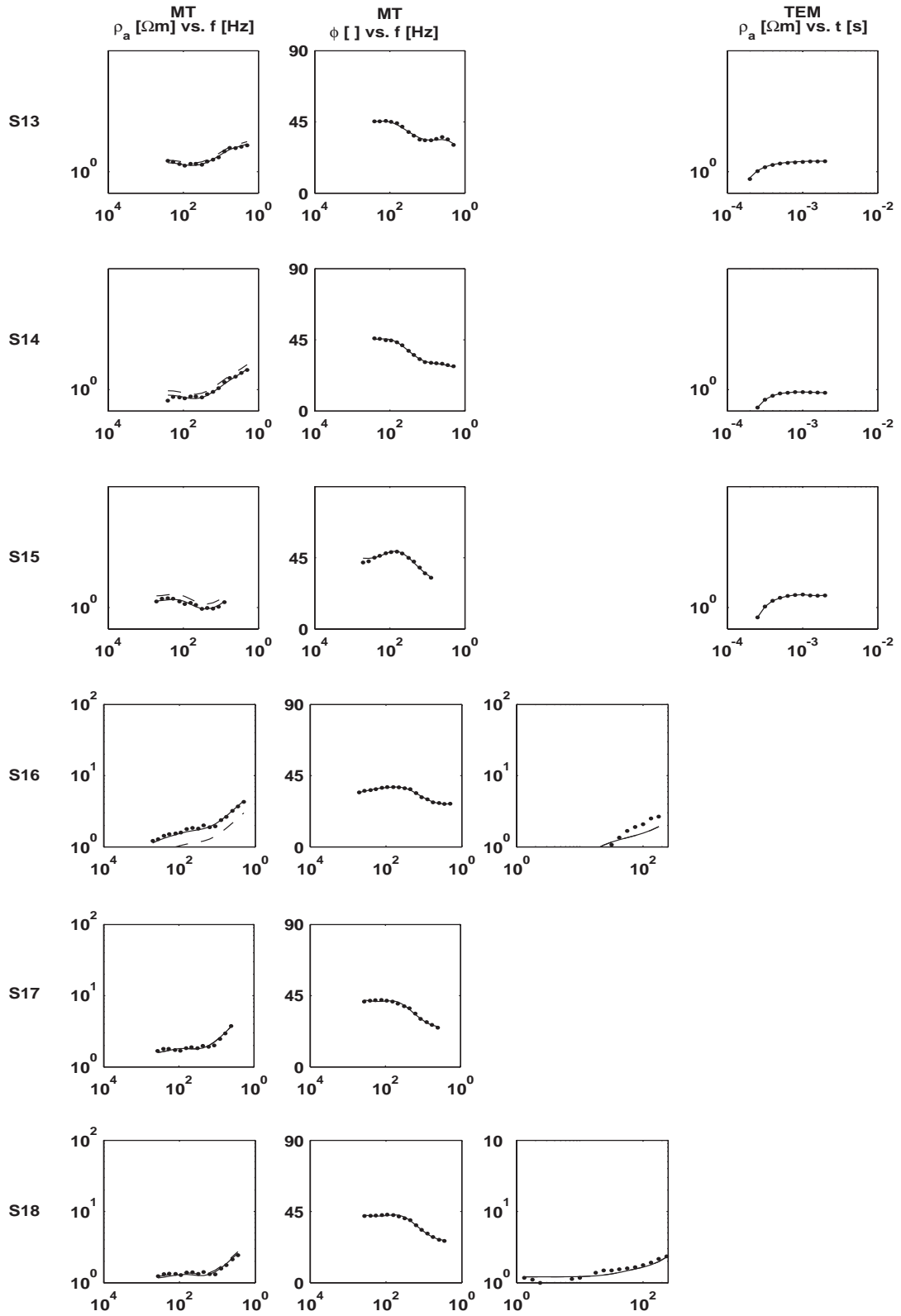


Fig. C-6: Data fits of the 1D joint inversion of MT-, DC- and TEM-data at stations S13-S18 in the Gurinai Structure (comp. Fig. C-7). At stations S13-S15 & S17 and at stations S16-S18 no DC and TEM data was measured, respectively.

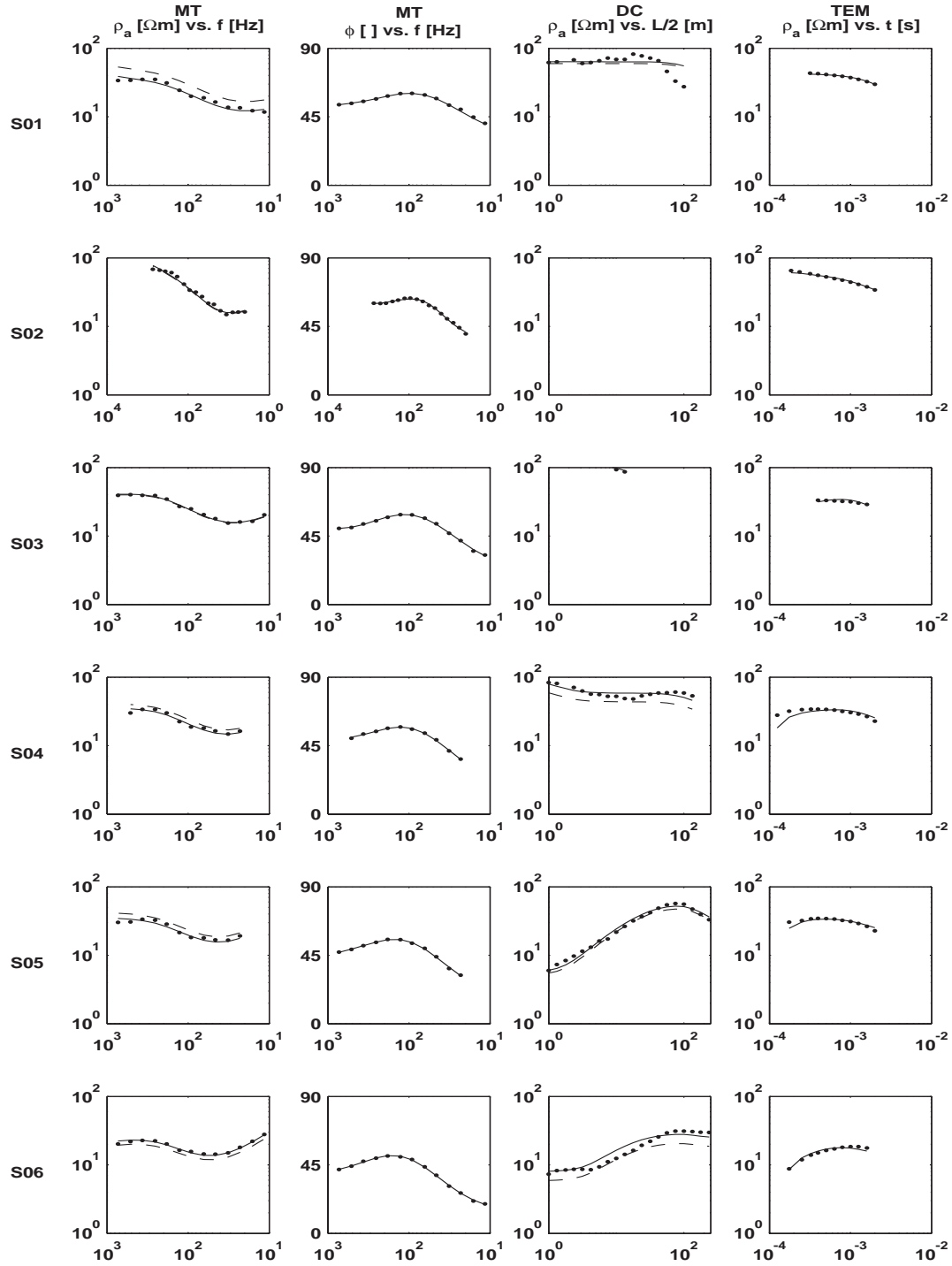


Fig. C-7: Data fits (solid lines) of the 1D joint inversion of MT-, DC- and TEM-data (dots) at stations S01-S06 in the Gurinai Structure. The data fit without static shift correction for MT and DC apparent resistivities is displayed by dashed lines. For locations refer to Fig. 4-27 (p. 114).



## Curriculum Vitae & List of Publications

Sebastian Georg Otto Hölz  
Stephanstr. 12  
D-10559 Berlin  
+49-30-39877120  
hoelz@geophysik.tu-berlin.de

Date of Birth: 10.08.1972

Place of Birth: Berlin

Citizenship: German

Employment: December 2005 - March 2007

Freelancer in the DFG-project "Geophysikalische Untersuchungen von Beckenstrukturen und Sedimentinventar in der nördlichen Badain Jaran Shamo, NW-China"

May 2001 - November 2005

Research associate of the Technical University of Berlin in the DFG-project "Geophysikalische Untersuchungen von Beckenstrukturen und Sedimentinventar in der nördlichen Badain Jaran Shamo, NW-China"

Education: October 1993 - May 2001

Diploma in geophysics at the Free University of Berlin

1985 -1993

Walther-Rathenau-Gymnasium, Berlin, Germany

1990 -1991

Mathomedi-High School, Minnesota, USA

### **Papers**

- Hölz S., Polag D., Becken M., Fiedler-Volmer R., Zhang H.C., Hartmann K. & Burkhardt H.: Electromagnetic and Geoelectric Investigation of the Gurinai Structure, Inner Mongolia, NW China. *Tectonophysics* 2007 (in print).
- Becken M., Hölz S., Fiedler-Volmer R., Hartmann K., Wünnemann B. & Burkhardt H.: The electrical resistivity image of the Jingsutu Graben at the NE margin of the Ejina basin (NW China) and implications for the basin development. *GRL*, 2007, vol. 34 (9).

### **Proceedings**

- Hölz S., Hiller T. & Burkhardt H.: Effects of Dipping Layers on TEM 1D-Inversion. *EMTF* 2005.

### **Presentations**

- Hölz S., Becken M., Fiedler-Volmer R., Hiller T., Polag D., Burkhardt H.: Elektromagnetische und geologische Untersuchungen im Ruoshui - Becken, Innere Mongolei, NW-China. *DGG* 2005.
- Hölz S. & Burkhardt H.: Signal Processing Of TEM-Signals By Means Of The Wavelet Transformation. *Int. Induction Workshop* 2004.
- Hölz S., Becken M., Polag D., Fiedler-Volmer R. & Burkhardt H.: Electromagnetic investigations in the Gaxun Nur Basin, Inner Mongolia, China. *Rachad* 2003.
- Hölz, S. & Burkhardt, H.: Praktische Aspekte bei der Datenbearbeitung und Bewertung von äquivalenten 1D-Modellen von TEM-Daten. *DGG* 2003.
- Hölz S., Becken M., Pfaffhuber A., Schenk A., Fiedler-Volmer R. & Burkhardt, H.: AMT- und TEM-Untersuchungen zur Beckencharakterisierung in der Wüste Gobi, NW-China. *DGG* 2002.
- Hölz S., Becken M., Burkhardt H., Fiedler-Volmer R., Kroupa M. & Pfaffhuber, A.: Characterization of the sedimentary inventory of a basin in the Badain Jaran Shamo using electromagnetic and electrical sounding methods. *Rachad* 2001.
- Polag D., Hölz S., Becken M., Fiedler-Volmer R., Schenk A. & Burkhardt H.: Elektromagnetische und Geoelektrische Untersuchungen in der Gurinai Struktur, Innere Mongolei, VR China. *DGG* 2005.
- Polag D., Hölz S., Becken M., Fiedler-Volmer R. & Burkhardt H.: Elektromagnetische und Geoelektrische Untersuchungen in der Gurinai Struktur, Innere Mongolei (VR China). *EMTF* 2005.
- Becken M., Hölz S. & Burkhardt H.: 1D Dünne-Schicht Modelle in der TEM - quasianalytische Transformation in den Zeitbereich und Vergleich mit optimierten Hankelfilterlängen. *DGG* 2003.
- Becken M., Burkhardt H., Fiedler-Volmer R., Hölz S., Kroupa M. & Pfaffhuber A: Geophysical Investigation of a basin structure in the Badain Jaran Shamo using electromagnetic and electrical sounding methods. *Rachad* 2001.